Site selectivity of specific reaction steps important for catalysis

CO dissociation on ruthenium surfaces

Nielsen, Kenneth

Publication date:
2011

Document Version
Publisher's PDF, also known as Version of record

Center for Individual Nanoparticle Functionality

DTU

SITE SELECTIVITY OF SPECIFIC REACTION STEPS IMPORTANT FOR CATALYSIS

CO DISSOCIATION ON RUTHENIUM SURFACES

CENTER FOR INDIVIDUAL NANOPARTICLE FUNCTIONALITY
DEPARTMENT OF PHYSICS
TECHNICAL UNIVERSITY OF DENMARK
KENNETH NIELSEN
AUGUST 2011

Front cover: Central image is a derivative STM image of the Ru(0 1 54) surface after cooling down the sample in the amount of CO that was present in the chamber after a TPD. See section 3.4.

PhD thesis
Department of Physics
Center For Individual Nanoparticle Functionality (CINF)
The Technical University of Denmark (DTU)

Site selectivity of specific reaction steps important for catalysis

-

CO dissociation on ruthenium surfaces

Kenneth Nielsen
August 2011

Preface

The work presented in thesis has been carried out at the Center for Individual Nanoparticle Functionality (CINF) at the Institute of Physics at the Technical University of Denmark (DTU) from September 2008 to August 2011. The project has been carried out with Professor Jane H. Nielsen as a supervisor. This thesis is submitted in partial fulfillment of the requirements for the PhD degree from DTU.

As this project is coming to an end, there are a few people I would to thank. First and foremost I would like to thank my fiance and family for their encouragement and support. Second, thanks to my supervisor, the faculty and all my colleagues, for providing a stimulating and fun work environment, this is one of the things that I have really appreciated during the years at DTU. A large thank you to all the people who have helped my acquire new skills, especially Yann Tison, Lone Bech, Robert Jensen and Thomas Andersen. Thanks also to all the theoriticians that I have collaborated with, and especially Duncan J. Mowbray, for good collaboration and fruitful discussions. Finally a big thanks to Yann Tison and Christian Strebel for proofreading this thesis.

Lyngby, August 31st 2011

_____

Kenneth Nielsen
s021749

Abstract

This thesis presents the results of two different projects, both focused on catalysis. The main part is about the investigation of the structure sensitivity of the CO dissociation reaction with STM on a Ru(0 1 54) single crystal and the second part concerns the STM structure study of the Bi/Pt(111) overlayer system.

In the STM study of the structure sensitivity of the CO dissociation reaction on the Ru(0 1 54) sample, it was determined that after cooling the sample from 700 K to 400 K in 10^{-8} Torr of CO or in the CO that was left after a TPD, the sample displayed periodic decorations on every other of the geometrically alternating step. In some cases these decorations also extended into a hexagonal structure on the step and in both cases had a periodicity of 0.55 ± 0.05 nm. They were identified as originating from atomic oxygen and the presence of these patches along with the presence of carbon in the amount of 0.014-0.020 ML (determined by oxygen titration), which is close to the concentration of one kind of step (0.02 ML), lead to the conclusion that CO dissociation takes place on only one kind of step. Furthermore, from experiments with a 10 L CO dose at different constant temperatures and a 10 L post-saturation dose at 400 K, it was determined that only for the 500 K dose was the oxygen structure observed. From this we conclude that a temperature between 450 K and 500 K is required to activate the CO dissociation on the steps and at higher temperatures recombination is activated.

From comparison of our results with simulated STM images and DFT based reaction energy level calculation, it was furthermore determined that it is the B-step configuration that is active for the CO dissociation and that a configuration with the oxygen atom occupying the hcp 3-fold hollow site on top of the step, right next to the dissociation site, is the most stable configuration after dissociation.

Preliminary results where the sample was exposed to high doses of CO, at a CO pressure of 10^{-5} Torr and a temperature of 550 K (dissociation conditions) indicated that especially every other step had a very rough appearance after 7 min exposure. After the 14 min exposure they had straightened out again and after 60 min exposure something, most probably carbon species, was observed to grow from the bottom of one kind of step and from under-coordinated atoms on the other step.

In an collaborative ruthenium related extra-project it was determined that it was possible to shift the CO TPD behavior of different systems. It was showed that for the Ru(0 1 54) sample it was possible to shift the TPD shape from the single crystal type to the nano-particle type by sputtering the sample for 300 s. It was also showed that for a system consisting of a PVD nano-particle film it was possible to shift its TPD behavior from the nano-particle type to the single crystal type by annealing it for 600 s at 900 K.

In the Bi/Pt(111) side project samples was prepared by PVD of bismuth on a Pt(111) single crystal, after which the sample was subjected to successively increasing heat treatments and characterized with XPS and STM. From the experiments it was determined that the 500°C 3 min heat treatment was sufficient to evaporate the bismuth in excess of 1 ML from the sample. Furthermore, two small shifts was observed in the XPS binding energy of the Bi $4f_{7/2}$ peak. The first 0.08±0.02 eV shift up is likely due to the ordering of the overlayers after the first heat treatment at 300°C 3 min. The second 0.10±0.02 eV shift down after the heat treatment to 500°C for 30 min could be due to the evaporation of the excess bismuth layers or to alloying of the bismuth into the platinum surface. The STM images showed a rough surface after deposition, a crystalline island structure after the 300°C 3 min heat treatment and a flat surface with step heights comparable to the substrate after the 500°C 3 min heat treatment. At higher heat treatments the surface layer is observed to break up, either due to evaporation or alloying, in a manner where holes are formed until these become so abundant that they become interconnected and the bismuth that is left appears as particles. On the 500°C 3 min sample a hexagonal 1.05-1.07×1.07-1.08 nm 62.2-65.8° structure was observed indicative of the p(4×4) overlayer structure. Also in preliminary results from the 300 °C 3 min sample and the high temperature particles, periodicities was observed but these need further confirmation.

Resumé

Denne afhandling handler om arbejde på to forskellige projekter. Hovedparten omhandler undersøgelsen af strukturfølsomheden af CO-dissociationsreaktionen med STM på en Ru(0 1 54)-enkeltkrystal and den anden del handler om STM-strukturstudiet af Bi/Pt(111)-overlagssystemet.

I STM-studiet af strukturfølsomheden af CO-dissociationsreaktionen på Ru(0 1 54)-prøven, blev det fastlagt at efter nedkøling af prøven fra 700 K til 400 K i 10^{-8} Torr CO, eller i den CO der var tilbage i kammeret efter en TPD, vil prøven have periodiske dekorationer på hvert andet af de geometrisk skiftende trin. I nogle tilfælde strakte disse dekorationer sig også ind på trinnet i en heksagonal struktur og i begge tilfælde havde de en periodicitet på 0.55 ± 0.05 nm. De blev identificeret som stammende fra atomart ilt og tilstedeværelsen af disse, sammen med tilstedeværelsen af kulstof i en mængde af 0.014-0.020 ML (bestemt vha. ilttitrering), hvilket er tæt på koncentrationen af én type trin på overfladen (0.02 ML), førte til konklusionen at CO-dissociation kun finder sted på en type trin. Ydermere blev det med eksperimenter med 10 L dose ved forskellige konstante temperaturer og en 10 L post-mætningsdose ved 400 K, bestemt at kun 500 K-prøven indeholdt iltstrukturerne. Fra dette blev det konkluderet at en temperatur mellem 450 K og 500 K er nødvendig for at aktivere dissociationen af CO ved trin og at ved højere temperaturer vil rekombinering blive aktiveret.

Fra sammenligningen af vores resultater med simulerede STM-billeder, samt DFT-baserede reaktionsenergi-niveauudregninger, blev det bestemt at det er B-trinnet der er aktivt for CO-dissociation og at en konfiguration hvor iltatomet sidder i hcp 3-folds-hulstedet på toppen af trinnet, lige ved siden af dissociationstedet, er den mest stabile konfiguration efter dissociation.

Foreløbige resultater hvor prøven blev udsat for store doser af CO, ved et 10^{-5} Torr CO-tryk ved 550 K (dissociationsbetingelser) indikerer, at specielt hvert andet trin har en meget ru fremtoning efter 7 min-dosen. Efter 14 min-dosen er de blevet mere glatte igen og efter 60 min-dosen ser det ud som om noget (med al sandsynlighed en form for kulstof) gror fra bunden af hvert andet trin og fra underkoordinerede atomer på det andet trin.

I et ekstra ruthenium-relateret samarbejdsprojekt blev det påvist at det var muligt at ændre TPD-opførslen for forskellige systemer. Det blev demonstreret, at med Ru(0 1 54)-prøven var det muligt at ændre dens TPD-form fra enkeltkrystal-typen til nanopartikle-typen ved at sputtere den i 300 s. Det blev også demonstreret at for et system bestående af PVD nanopartikle-film var det muligt at ændre dens TPD-opførsel fra nanopartikletypen til enkeltkrystaltypen ved at anneale den 600 s ved 900 K

I Bi/Pt(111)-sideprojektet blev prøver dannet ved PVD af bismut på en Pt(111)-enkeltkrystal, hvorefter prøven blev udsat for på hinanden følgende, kraftigere, varmebehandlinger, samt karakterisering med XPS og STM. Fra disse eksperimenter blev det vist at en opvarmning til 500°C 3 min var rigeligt til at fordampe den overskydende bismut over 1 ML. Ydermere blev der observeret to små skift i XPS-bindingsenergien for Bi $4f_{7/2}$-toppen. Det første skift op på 0.08±0.02 eV skyldes sandsynligvis en ordning af overlagene efter den første opvarmning til 300°C 3 min. Det andet 0.10±0.02 eV skift ned kan skyldes fordampning af de ekstra overlag ud over det første eller dannelsen af en legering af bismut ind i platinoverfladen. STM-billederne viser at overfladen er ru efter deponering, efter opvarmning til 300°C 3 min dannes en krystallinks ø-struktur og efter opvarmningen til 500°C 3 min er der en flad overflade med trinhøjder som er sammenlignelige med underlagets. Ved kraftigere varmebehandlinger kunne det observeres at overfladelaget brydes op, enten på grund af fordampning eller legering, på en måde hvor huller formes indtil disse bliver så mange, at der dannes forbindelse mellem dem, og den tilbageværende bismut observeres som partikler. På 500°C 3 min-prøven kan en heksagonal 1.05-1.07×1.07-1.08 nm 62.2-65.8° struktur observeres, som er indikator for p(4 × 4)-overlagsstrukturen. Også på foreløbige resultater fra 300 °C 3 min-prøven og på højtemperaturpartiklerne kunne der observeres periodiciteter, men disse kræver yderligere bekræftelse.

Contents

List of abbreviation xiii

List of figures xv

1 Introduction 1
- 1.1 Heterogeneous catalysis . . . 1
- 1.2 Surface science and reactivity . . . 3
- 1.3 Tailoring surface reactivity . . . 5
- 1.4 STM in catalysis research . . . 7
- 1.5 The gaps in the surface science approach . . . 8
- 1.6 Thesis outline . . . 10

2 Experimental methods 11
- 2.1 The experimental setup . . . 11
- 2.2 The samples . . . 13
- 2.3 Scanning Tunneling Microscopy (STM) . . . 13
  - 2.3.1 Theory of STM . . . 15
  - 2.3.2 The Århus STM . . . 17
  - 2.3.3 Image processing and analysis . . . 18
- 2.4 X-ray Photoelectron Spectroscopy (XPS) . . . 19
  - 2.4.1 General principle . . . 19
  - 2.4.2 Features and artifacts in the XPS spectra . . . 21
  - 2.4.3 Quantitative analysis . . . 23
  - 2.4.4 XPS data processing . . . 26
  - 2.4.5 XPS on ruthenium . . . 26
- 2.5 Mass Spectrometry . . . 26
  - 2.5.1 General principle . . . 26
  - 2.5.2 Gas analysis . . . 28
  - 2.5.3 Temperature Programmed Desorption (TPD) . . . 28
  - 2.5.4 Carbon uptake experiments . . . 29

3 CO dissociation on ruthenium 31
- 3.1 Introduction . . . 31
  - 3.1.1 Structure of species on ruthenium surfaces . . . 32
  - 3.1.2 Structure sensitivity . . . 35
- 3.2 The sample . . . 41
- 3.3 Cleaning the sample . . . 42
  - 3.3.1 Cleaning procedure and XPS checks . . . 42
  - 3.3.2 Graphene overlayers . . . 44
  - 3.3.3 Sub-surface argon bubbles . . . 45
- 3.4 CO dose while cooling after TPD . . . 46

3.5 CO dose at constant pressure . . . 49
3.6 CO dose at constant temperature and pressure . . . 49
3.7 Assignment of the observed features . . . 52
3.8 Comparison of STM images with calculations . . . 57
3.8.1 Simulated STM images . . . 58
3.8.2 CO dissociation energy levels . . . 61
3.9 Discussion of low CO dose experiments . . . 62
3.10 Large CO doses at 550 K . . . 64
3.11 Structure cross-over . . . 68
3.12 Summary . . . 72

4 Bi/Pt(111) 75
4.1 Introduction . . . 75
4.2 Experimental details . . . 77
4.3 Results and discussion . . . 78
4.3.1 XPS results . . . 78
4.3.2 STM results . . . 80
4.4 Summary . . . 84

5 Summary and outlook 87

Bibliography 89

Included papers 95

List of Abbreviations

DFT	Density Functional Theory
HOPG	Highly Ordered Pyrolytic Graphite
LEED	Low Energy Electron Diffraction
ML	Monolayer
PVD	Physical Vapor Deposition
QMS	Quadrupole Mass Spectrometer
STM	Scanning Tunneling Microscopy
TPD	Temperature Programmed Desorption
UHV	Ultra High Vacuum
XPS	X-ray Photoelectron Spectroscopy

List of Figures

1.1 Basic principle of catalysis 2
1.2 Volcano curve for methanation 4
1.3 Interaction of molecule with sp-band and d-band 5
1.4 Au/Ni(111) and Bi/Pt(111) surface alloys 6
1.5 Step site activity for N_2 dissociation on Ru(0001) 7
1.6 H_2 evolution of MoS_2 nanoparticles 8
1.7 Length scales of catalysis 9

2.1 Images of the setup 12
2.2 Schematic illustration of an STM 13
2.3 STM theory geometric model 16
2.4 N.D. Lang STM model system 17
2.5 Apparent height in STM 18
2.6 The Århus type STM 19
2.7 Photoelectric effect 20
2.8 Electron mean free path 21
2.9 Coverage models for XPS overlayer quantification 25
2.10 XPS spectrum of Ru $3d$ doublet 27
2.11 General principle of the QMS 27
2.12 Example Ru(0 1 54) TPD 29

3.1 $(\sqrt{3} \times \sqrt{3})R30°$ CO on Ru(001) STM image 33
3.2 STM images of oxygen structures on Ru(001) 33
3.3 STM images of oxygen and nitrogen structures on Ru(001) 34
3.4 Methanation activity on nickel single crystals and supported catalysts 36
3.5 UHV carbide formation and high pressure methanation structure dependence on nickel 37
3.6 CO TPDs on Ru(109) as function of initial coverage 37
3.7 Isotopic scrambling and carbon blocking of active sites by ethylene decomposition on Ru(109) 38
3.8 β-peak area and carbon uptake on a Ru(0 1 54) crystal after carbon deposition by CO dissociation 39
3.9 Ball model of the Ru(0 1 54) surface and illustration of the Ru(109) double step reconstruction 41
3.10 STM images of a clean Ru(0 1 54) surface 42
3.11 Cleaning procedure and carbon contamination development 43
3.12 XPS overview spectrum of Ru(0 1 54) 44
3.13 Short description 45
3.14 Sub-surface argon bubbles 46
3.15 Steps after a CO TPD 47
3.16 Steps after CO TPD extended 48

3.17 Cooling in constant pressures of CO 49
3.18 Constant temperature with finger structure at the steps 50
3.19 Constant temperature but with no oxygen fingers at the steps 51
3.20 Consecutive CO TPDs and comparison to controlled CO exposure . . 53
3.21 Oxygen titration after dose at constant pressure 55
3.22 Model of the step analysis 55
3.23 Step determination from STM image 56
3.24 Tilt effect on projected distances over steps 57
3.25 Simulated STM images of various species on steps 59
3.26 Simulated STM images of carbon at bottom of steps 60
3.27 DFT energy reaction diagram 61
3.28 7 min CO dose at 550 K, 10^{-5} Torr 65
3.29 14 min CO dose at 550 K, 10^{-5} Torr 66
3.30 60 min CO dose at 550 K, 10^{-5} Torr 67
3.31 STM images correlated with β-peak area 67
3.32 Cross over in CO TPD behavior 70

4.1 EC-STM images of Bi-modified Pt(111) surface 76
4.2 LEED structure study of Bi overlayers on Pt(111) 77
4.3 Bi to Pt XPS ratio 79
4.4 Overview images of the Bi/Pt(111) system after different heat treatments 81
4.5 Atomic resolution STM images of Bi/Pt(111) after the 300°C 3 min and 500°C 3 min heat treatments 83
4.6 Near-atomic resolution STM images of the high temperature Bi particles in the Pt(111) surface 84

Chapter 1

Introduction

The main theme in this PhD thesis is to obtain detailed information about catalytic processes at the atomic level by the use of Scanning Tunneling Microscopy (STM). The motivation for choosing this approach to catalysis research will be explained in the following sections with an introduction to heterogeneous catalysis and an overview of the surface science approach to catalysis research.

1.1 Heterogeneous catalysis

A catalyst, by definition, is a compound that can increase the overall reaction rate of a reaction, without being consumed in the process. The field of catalysis is subdivided into homogeneous and heterogeneous catalysis depending on the phase of the reactants/products and the catalyst. In heterogeneous catalysis, the reactants and the products are usually in a gas or liquid phase whereas the catalyst is a solid. Since catalysis is a surface phenomenon, catalysts are often found in the form of supported nanoparticles, in an attempt to optimize their specific area. To facilitate a continued reaction the involvement of the catalyst needs to be circular, in a manner where it can both let the reactants adsorb and react and the products desorb, as illustrated in figure 1.1(a). A catalyst acts by lowering the activation barrier of one or more reaction steps (figure 1.1(b)), hence increasing the reaction rate. The reaction step with the highest barrier (or the lowest rate) limits the overall reaction rate; it is therefore called the rate limiting step. It is this particular reaction step that should be targeted by the catalyst. Part of the challenge is to identify this step and to understand why its barrier is high. This rate limiting step is often believed to be the dissociation of one of the reactant molecules and here the catalyst function by lowering the strength of the internal bond in the molecule, thereby making it easier to dissociate.

The simple principle described above can have a large influence on the energy consumption of a chemical production and thereby also its economy. For instance catalysts are involved in 85-90% of all chemical production[1, chapter 1]. One very important example is the synthesis of ammonia by means of the Haber-Bosch process:

$$N_2 + 3H_2 \rightarrow 2NH_3 \tag{1.1}$$

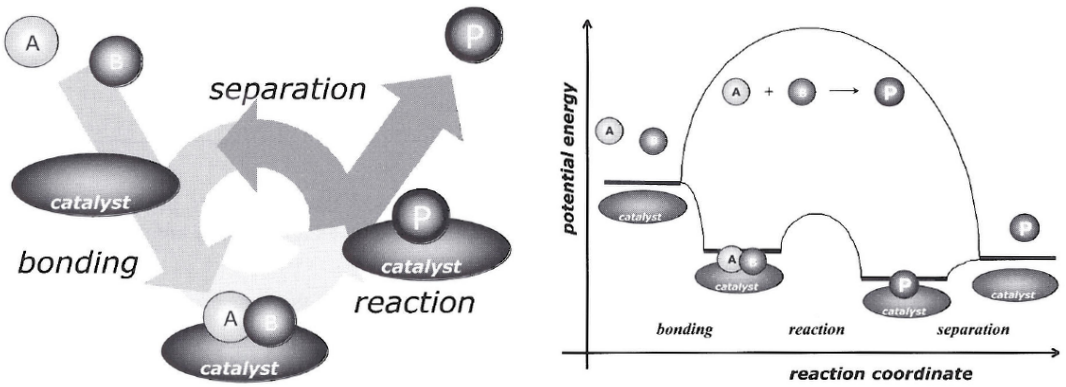

(a) (b)

Figure 1.1: The basic principle of catalysis. Figure **(a)** illustrates the circular role of the catalyst. Reactants adsorb on the surface, react and then desorb thereby preparing the surface for the next reaction. Figure **(b)** shows how the presence of the catalyst lowers the potential energy barrier of the reaction, compared to the non-catalyzed reaction. Both figures are adapted from [1, chapter 1].

Without the continuous and sufficient production of ammonia by means of this process, it would not be possible to produce the incredible amounts of fertilizer, that is required to produce enough food, to sustain the worlds population at its present level. But the production of ammonia is only one out of many of the processes where catalysts are used for optimization. Not only is a catalyst used in the actual Haber-Bosch process, but ammonia production also requires large amounts of hydrogen, which is produced cheapest from methane by use of two other catalyzed processes, the steam reforming process, equation (1.2), and the water gas shift reaction, equation (1.3).

$$CH_4 + H_2O \rightarrow CO + 3H_2 \tag{1.2}$$

$$CO + H_2O \rightarrow CO_2 + H_2 \tag{1.3}$$

Besides ammonia synthesis catalysts are also involved in the production of organic chemicals like ethylene and propylene, plastics like polyethylene and polystyrene, hydro cracking in oil refineries and finally in processes for environmental and health protection such as the removal of sulfur species from crude oil and for cleaning flue gas and exhaust gas from cars[1, chapter 1]. Furthermore, catalysts are also predicted to play a central part in future applications within production, conversion and storage of renewable energy. As apparent from this list of applications, heterogeneous catalysis has large influence on vital aspects of our society such as the economy, population size, health and the environment. It is this impact, that makes catalysis a field that historically has been, and probably will continue to be, an active subject of research.

1.2 Surface science and reactivity

Due to the wide application and economic importance of catalysis, there is always a demand for finding better catalysts. When Ultra High Vacuum (UHV) entered into catalysis research, the possibility arose to study very well defined systems with surface science techniques. It was made possible to study atomically clean well-defined surfaces interacting with controlled amounts of clean gas for several hours before the system is polluted by the residual gas in the UHV chamber.

In another area, developments within computer calculation capabilities has made first-principles calculations able to contribute with knowledge about reactions at the atomic level. These developments are first and foremost Density Functional Theory (DFT), which dramatically reduces the calculation complexity per system size thereby making it possible to perform calculations on larger systems. The second development is the increase in available computer calculation power. The gathering of fast single computers into super computers has made it possible to perform even very complex calculations within a manageable time frame. The combination of these two advances means that it is now possible to directly calculate catalytically relevant quantities such as binding energies and reaction energies, on model surfaces comparable to the model surfaces being used in UHV.

The combination of the advances within UHV and DFT has allowed to pursue a direction of research, in which the objective is to obtain detailed information at the atomic level about a few systems, from which it is possible to draw general trends that can then govern the search for better catalysts. This approach is very different from the one that has historically governed catalysis research. The efforts ware largely guided by a form of parallel screening with guided trial and error[2] in which large number of compounds were synthesized and tested and positive results were carried on to the next batch. This method presents the advantage of allowing to search large pools of compounds in short time. It does however also have several disadvantages, the largest of which perhaps is that the pool of candidates to test, in order to include all the different combinations of different compounds and synthesis methods is impractically large, and it is therefore entirely possible to miss a good candidate, while still thinking that it should have been covered by the parameter search.

Returning to the new approach it is evident that, it is necessary to understand the basic principles of catalysis, in order to know what to look for in the testing of a catalytic system, by surface science methods (or computer calculations). As previously mentioned the role of the catalyst is circular; the reactants adsorb on the surface where they react with lower barriers, and finally the products need to desorb from the surface. This means that the binding to the surface is necessary in order to affect the reaction, which in turn means that it is a necessity that the surface binds the reactants strongly enough to sufficiently alter the reaction barriers. On the other hand it cannot bind the products too strongly, because they need to be able to leave the surface and free up the reaction site for another turn over. The consequence is that the highest turn over frequency exist at an optimum intermediate value for the binding energy. This is known as the Sabatier principle[1, chapter 1 and 6]. For systems where a single parameter (usually the dissociative adsorption energy

of one of the reactants) governs the overall reactivity, plotting the reactivity as a function of this parameter will results in a curve similar to the one in figure 1.2. The

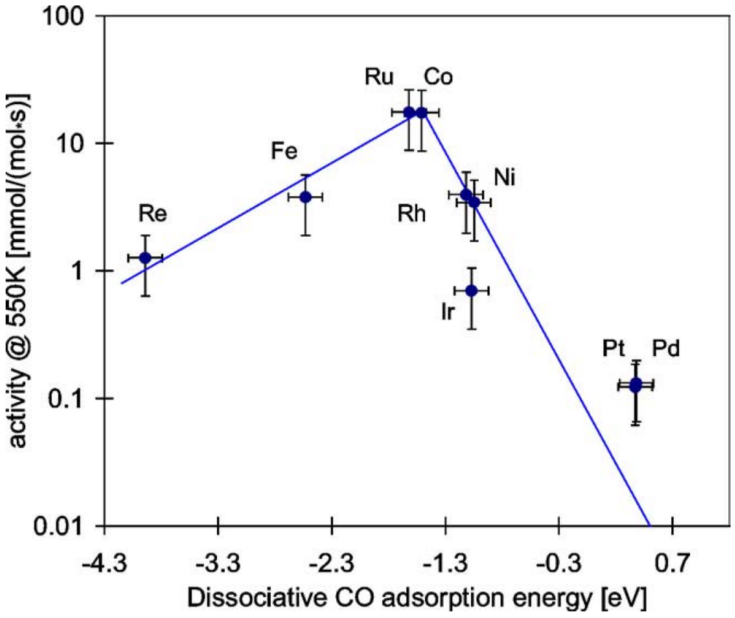

Figure 1.2: The methanation activity for a series of transition metals as a function of the dissociative CO adsorption energy. Adapted from [3].

shape of such curves illustrating something similar to the Sabatier principle[1] is often referred to as volcano curves due to their shape. The volcano plot in figure 1.2 is for the methanation reaction and it shows the experimentally determined methanation reaction activity for a group of transition metals as a function of the dissociative adsorption energy of CO, which is found to be a good descriptor for the catalytic activity for methanation. In fact it has been shown in the work by T. Bligaard *et al.*[3] (source of previously mentioned figure), that assuming simple reaction kinetics and no desorption barrier for the products, the dissociative adsorption energy of the key reactant is a good indicator for the overall catalytic activity[3].

From relations such as the one illustrated in the volcano curve in figure 1.2, it is possible to extract information about what the ideal value should be for some parameter (e.g. the dissociative adsorption energy) in order to have the best catalytic activity. However, if this optimum if not located on one of the common surfaces of pure metals it is necessary to look into how one can tailor the catalytic activity towards this value. The properties governing the catalytic properties of a material can be understood in terms of the Newns-Anderson model. This model allows to clarify the strength of the bond between a surface and a molecule (reactant) and its effect on the reaction barrier for dissociation. The Newns-Andersson model is an approximation based on a quantum mechanical treatment of the problem. In qualitative terms the model can be understood from figure 1.3. The figure illustrates the electronic bands and levels of a transition metal (on the left) and an adsorbing molecule (on the right). When the molecule approaches the surface the interaction

[1] This kind of curve, based on DFT calculations and micro kinetic modeling may differ from those based purely on the Sabatier principle, but they both resemble a volcano and both illustrate the same qualitative correlation[3].

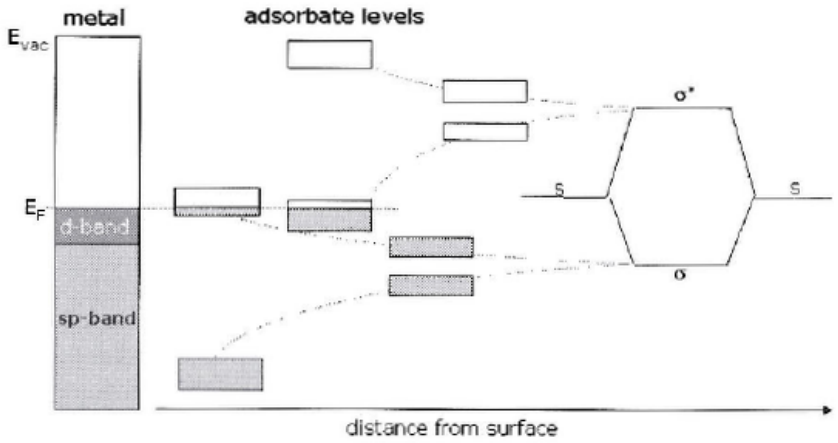

Figure 1.3: This figure schematically illustrates the effects that the electronic bands of a transition metal has on the electronic levels of an adsorbing molecule. Adapted from [1].

with the sp-band will lead to a broadening and lowering of the electronic states of the molecule facilitating the binding to the surface. The d-band however will induce the splitting of the electronic levels of the molecule up into one level moving upwards in energy and one moving down, (similar to the effect seen in the electronic interaction between two atoms forming a diatomic molecule), leading to the formation of the downwards moving bonding orbitals and upwards moving anti-bonding orbitals. The close proximity to the surface means that the filling of electronic levels will level out to the Fermi level of the surface. As a consequence, the level splitting may lead to a binding orbital of the molecule moving up in energy past the Fermi level, meaning that its electrons will spill over to the metal and it will be partially or fully drained. Similarly, one of the anti-bonding orbitals of the molecule may move enough down in energy for it to be partially or fully filled. Both effects lead to a weakening of the intermolecular bond, lowering the energy barrier for dissociation. The parameters of the surface that has influence on the effects described in this section are the filling level of the d-band and the position of the center of the d-band. Both these parameters can be influenced by e.g. the inter-atomic distance and the number and type of neighboring atoms[1, chapter 6][4].

1.3 Tailoring surface reactivity

The understanding of the parameters affecting the catalytic properties of a material can be used to propose different ways to modifying them (see e.g. reference [5]). Perhaps the most obvious option is to make an alloyed surface. By changing the nature of some of the surface atoms the d-band filling, shape and position will change. A few well-known examples of this effect are the Au in Ni(111) (figure 1.4(a)) and Bi in Pt(111) (figure 1.4(b)) surface alloys. In the Au/Ni(111) image the Ni atoms neighboring the Au atom appear brighter in the STM image, indicating that its electronic states have changed (see section 2.3.1), leading to different catalytic properties[6]. In the Bi/Pt(111) case the figure shows the increased hydrogen evolution reaction rate compared to the pure Pt(111) surface and to a system where Bi is present on

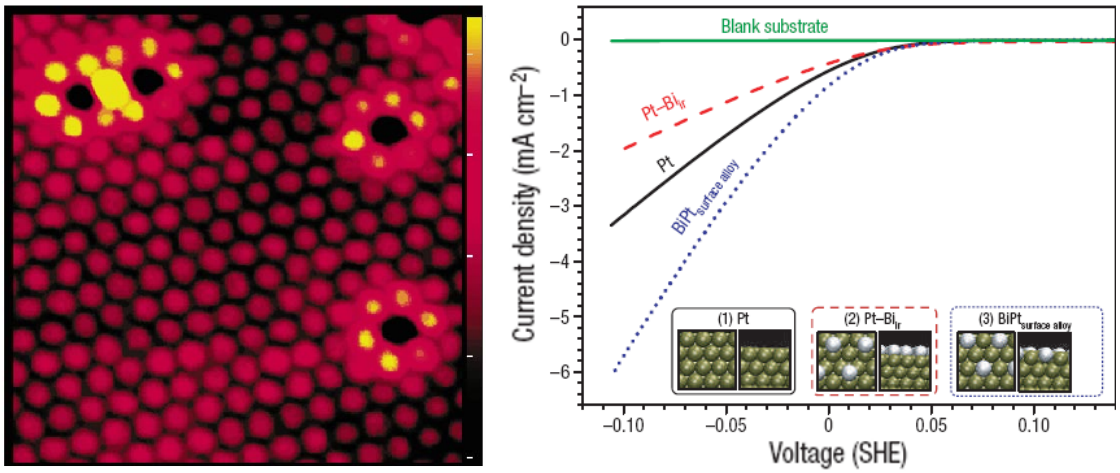

(a) (b)

Figure 1.4: (a) shows an STM image of a 2% of a monolayer Au alloyed into a Ni(111) surface. The Au atoms are the dark spots surrounded by bright spots. Image adapted from [6]. **(b)** shows the hydrogen evolution activity of the Bi/Pt(111) surface alloy system, compared to the clean Pt(111) surface and the Bi overlayer on Pt(111) system (structure models in the inset). Adapted from [7].

Pt(111) as an overlayer. Also in this case the alloying changed the electronic states of the surface, which changed the adsorption energy of H_2, which in turn changed the activity[7].

Another way to modify the catalytic properties of a surface is to stretch or compress the atomic structure. The change in the inter-atomic distances will be accompanied by a change in the width and position of the d-band. An example of such modification is the effect straining overlayers of Cu on Pt(111) has on the stability of adsorbed formate and on hydrogenation of carbonate, which is presented in [8]. For a more general theoretical description of the effects of straining overlayers, see the work by Mavrikakis *et al*[9].

Finally, and most interestingly for this project, one can optimize the reactivity by changing the density of surface sites with special geometries, i.e. specific numbers of nearest neighbors. Atoms located at steps or kinks on the surface have a different number of nearest and next nearest neighbors and will therefore have (sometimes dramatically) different catalytic properties. Figure 1.5 shows an Arrhenius plot of the thermal sticking coefficient of N_2 on the Ru(0001) surface, both in the case where the crystal was unmodified and in the case where the step sites on the surface was blocked with Au. Clearly the blocked surface show much lower activity than the unmodified surface. In fact, it was shown that for the N_2 dissociation the step sites on the closed packed Ru(0001) surface are up to nine orders of magnitude more active than the terrace sites[10].

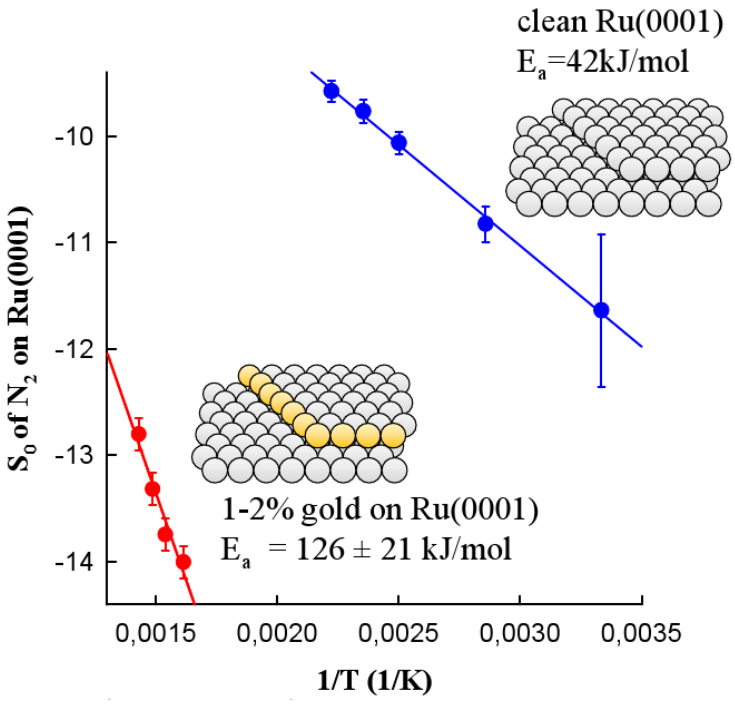

Figure 1.5: An Arrhenius plot of the thermal sticking coefficient of N_2 on the Ru(0001) surface, unmodified and with the steps blocked by Au. Modified version adapted from lecture notes of Professor Ib Chorkendorff. Originally from [10].

1.4 STM in catalysis research

The last section demonstrates the importance of surface modifications on the catalyst's activity. Therefore, it is necessary to be able to study surfaces in a controlled environment. In this regard, the surface science methods in general have been used to make large contributions to the knowledge surrounding catalysis, and of particular interest for this project, there has also been several significant contributions where STM has played a key role. A few such examples are e.g. the study of the Au in Ni(111) previously mentioned (figure 1.4(a)). In this study STM was instrumental in obtaining information about the nature of the modification Au made when alloyed into the Ni(111) surface. Knowledge that ultimately made it possible to propose this modification as a way of preventing deactivation of Ni catalysts by graphite formation when used for steam reforming[6]. Another example where STM studies have provided unique insight are in the studies of MoS_2 nanoparticles, where sites associated with the edge of these flat triangular or hexagonal particles have been shown to contain or be neighbor to the active sites. This is the case for both the hydrodesulfurization process[11] and the hydrogen evolution reaction[12][included article IV]. In the latter case, STM images such as the ones shown in the top of figure 1.6 were used to measure the basal plane areas and edge lengths of the MoS_2 nanoparticles, supported on a Au(111) single crystal. After this quantification, the same samples were characterized electrochemically to determine the hydrogen evolution activity. The correlation curves between the activity and the basal plane area and edge lengths respectively are shown in the bottom of the figure. They show a

clear correlation between the activity and the edge lengths, thus strongly suggesting that they represent the active site. It was furthermore shown, that only one kind of edge was active. This information makes it possible to try and tailor particles with more of the active edge, thus providing a better catalyst. For more examples of the contributions of STM to catalysis research, see e.g. the review article by Professor Michal Bowker[13].

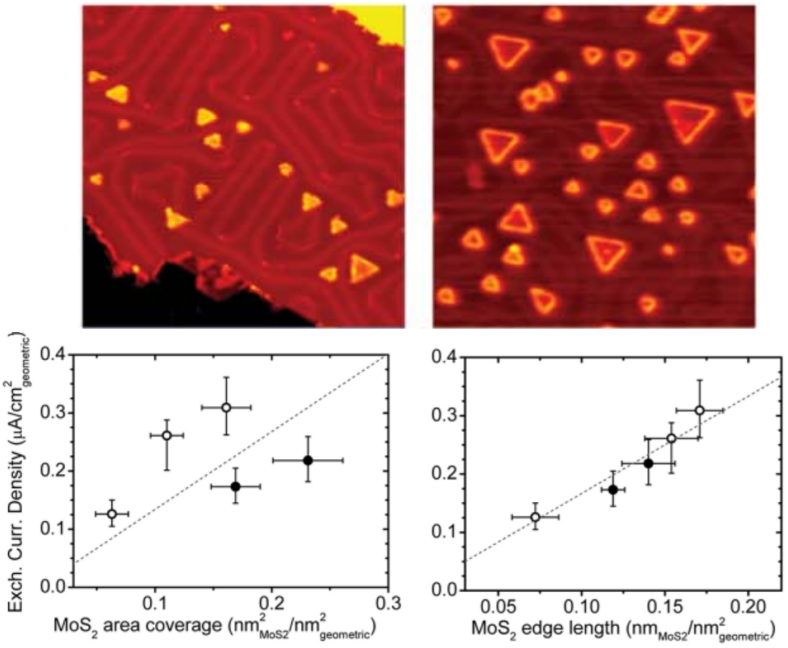

Figure 1.6: STM images of MoS_2 nanoparticles supported on Au(111) from which the edge lengths and areas of the particles were measured. Below the correlation of the exchange current density to particle area (bottom left) and edge length (bottom right). Adapted from [12].

1.5 The gaps in the surface science approach

As illustrated above the surface science approach has its virtues, but there are also drawbacks with this approach. The main drawback is that the model system which is investigated can be quite unrealistic, compared to the catalyst in reaction conditions. Therefore, it is very challenging to apply the knowledge gained directly. This is evidenced by figure 1.7 which shows that, in industry, the catalyst is in the form of nanoparticles supported on a porous substrate. This substrate is shaped into pellets which are embedded into a reactor. On the other hand, the model system is often one of the compact surfaces of a single crystal, a macroscopic version of one of the surfaces present on a nanoparticle. The other surfaces, the kinks and corners, as well as the influence of the substrate are neglected. This is know as the structure and material gap. Furthermore, there can be more than 12 orders of magnitude in pressure of difference between the reaction conditions and surface science measurements in UHV, this is the pressure. Lastly one has to mention the

temperature gap since the temperature can vary between the model experiment and the industrial conditions. These major differences are what has become known as the gaps in the surface science approach to catalysis: The structure and material gap, the pressure gap and the temperature gap.

The large difference between model and real system is inconvenient, but it is the price we have to pay in order to be able to get truly fundamental atomic level insight into the systems and mechanisms we are interested in. It should be mentioned in this context that many different approaches are being pursued in order to try and bridge these gaps. This has for instance been done by adding high pressure cells to experimental setups, making it possible to study the system with surface science techniques in UHV, before and after the system was exposed to high pressures of the reactant gasses in the high pressure cell. The latest tendency in this effort is to make use of so called *in situ* techniques. These make it possible to study the same kind of well defined systems, with surface science techniques, but under more realistic reaction conditions. This is an area, that at present date is in fast development, and it will without a doubt make large contributions to the field in the future as it has already done.

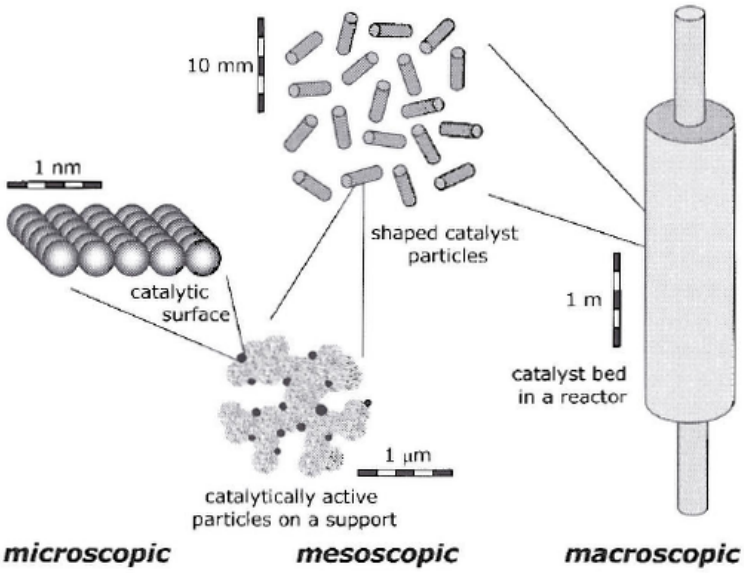

Figure 1.7: The figure shows the many length scales of catalysis, all the way from the industrial reactor to the microscopic surface of the catalytic particles. Adapted from [1].

1.6 Thesis outline

This first chapter was an introduction to heterogeneous catalysis, the surface science approach to catalysis including examples of the contributions that has been made with this approach.

Chapter 2 contains a description of the experimental setup, equipment and the experimental methods that have been used throughout this project.

Chapter 3 will start out with an introduction to the samples and the reactions we wish to investigate and the related literature. Then comes our study of where CO dissociation takes place on a stepped Ru surface and at which temperature. It will then continue with a short look at the self blocking mechanisms of this reaction and on experiments that will help relate the conclusions from single crystal studies to those from nano-particle studies.

Chapter 4 describes the results of a small side project about the structures of Bi overlayers on a Pt(111) crystal. It will also start with an introduction to this system and related literature. Then proceed into the presentation of the spectroscopy and microscopy results for this system.

Finally chapter 5 will sum up the main conclusions for the two studies.

Chapter 2

Experimental methods

This chapter describes the experimental setup and the samples. And then follows an introduction to the different experimental methods used and a few examples of data treatment.

2.1 The experimental setup

The experimental setup used for this project is a UHV chamber targeted towards single crystal research. It has a base pressure of 10^{-10} Torr, pumped by three turbo molecular pumps, one ion pump and a titanium sublimation pump. It is equipped with a manipulator that allows for height translation, rotation and tilt and in which the sample can be heated by electron bombardment. A wobble stick is used to transfer the sample from the manipulator to the STM, which is an Århus type STM[14]. For the X-ray Photoelectron Spectroscopy (XPS) a Specs system was used, consisting of a Specs RQ 20/38 X-ray gun and a 100 mm Phoibos hemispherical electron energy analyzer. It also includes a focussed ion source which is used for Ar^+ sputtering. Bi is deposited from a resistively heated crucible doser and gasses are dosed with leak valves into the whole chamber. In figure 2.1 are two images of the setup where the components are highlighted according table 2.1.

#	Description	#	Description
1a	Electron/Ion energy analyser	7b	Electro engines for manipulator
1b	Iris setting on 1a	8	Garage
2	Ion source	9a	STM
3	Wobble stick	9b	STM electronics box
4	Mass spectrometer	10	Hydrogen gas cleaning
5	Leak valve	11	X-ray source
6	Gas handling system	12	Pressure gauge
7a	Rotation platform for manipulator	13	Fitting for load lock

Table 2.1: List of the different parts on the setup, as shown in figures 2.1(a) and 2.1(b). Adapted from [15] and updated.

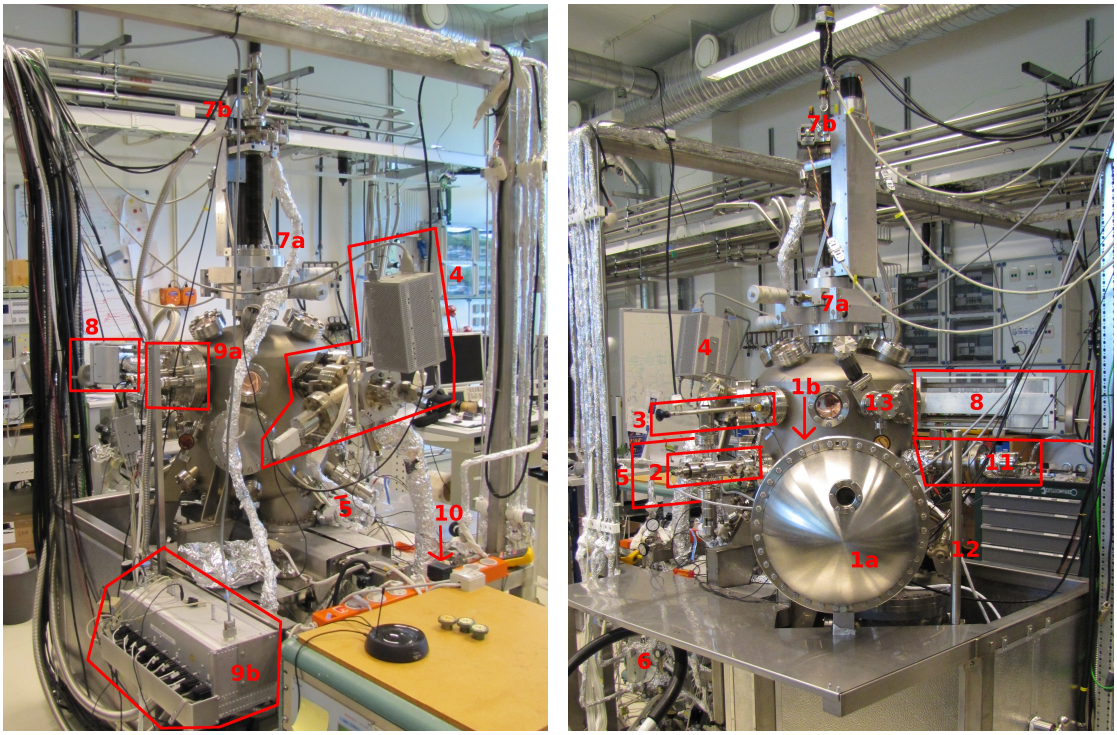

(a) (b)

Figure 2.1: Images of the setup from two different directions. Components are described in table 2.1.

2.2 The samples

The sample used in the experiments described in chapter 3 is a vicinal Ru(0 1 54) single crystal. The sample is bought with this crystal orientation from Mateck, GmbH. A more detailed description of the characteristics of this surface will be given in section 3.2.

The sample used in chapter 4 is a Pt(111) single crystal, likewise bought from Mateck, GmbH. It is of 4N purity and has a miscut angle compared to the (111) orientation better than 0.4°.

Both samples are hat shaped and mounted in Mo sample plates. On the back of the samples a K-type thermol couple is mounted for temperature measurements.

2.3 Scanning Tunneling Microscopy (STM)

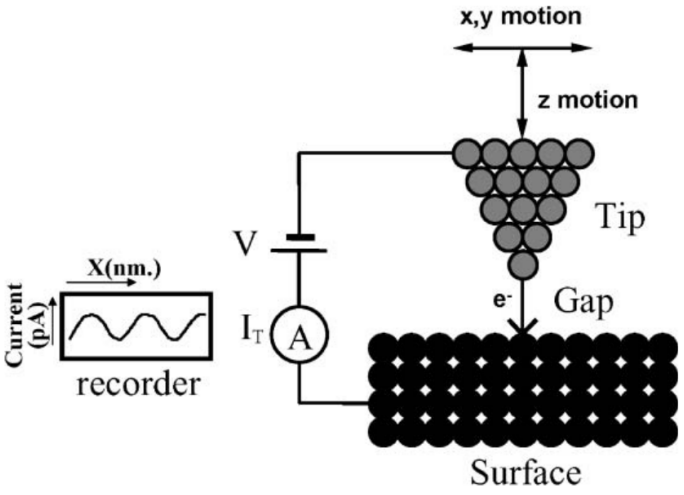

Figure 2.2: Schematic illustration of an STM. The tip moves over the surface by use of a piezo actuated xy-motion. The tunneling current I_T, resulting from the tip bias V, is either directly measured or used as feedback for the z-motion. Adapted from [13].

The general principle of an STM[16] is illustrated in figure 2.2. A metal tip is brought close to a conducting surface (but without forming contact), while the tip is biased compared to the surface. When the distance between the tip and the surface is small enough, it will be possible for electrons to tunnel from one part to the other, giving rise to a tunneling current. This tunneling current will depend exponentially on the distance between the tip and the surface. To form an image the tip is then rastered over the surface whereby it is possible to obtain tunneling in different positions in a grid. To obtain atomic resolution being able to move the tip with sub-nanometer precision is necessary. For this purpose piezoelectric elements are used, since they allow for expansions and contractions in this size regime. Besides the use of the piezoelectric elements (and the specialized high speed, low noise electronics used for their voltage oscillations and the feed back loop) for translation, it is also required that the entire STM must be efficiently mechanically isolated from the main chamber

to damp vibrations from the surroundings. This is achieved by suspending the entire STM in a two level spring system[16].

The STM can be run in two different modes depending on the nature of the scan. In the constant current mode the tunneling current is kept constant by adjusting the height of the tip via a feed back loop in the electronics which reacts to the tunneling current. What forms the image is then the height of the tip (measured as the voltage over the z-piezo element). The other mode is the constant height mode, in which the voltage over the z-piezo element is kept constant and the image is formed by the magnitude of the tunneling current. The constant height mode should be able to give the best resolution and the highest scanning speeds, but is has the large disadvantage that it can only be used on surfaces with height variations less than the tip-to-surface distance, which means that in practice the constant current mode is often the favored one. The images that are presented in this thesis have all been obtained in the constant current mode.

Before the advent of the STM it was common to use the Low Energy Electron Diffraction (LEED) technique for atomic structure information. This technique however gives a reciprocal space image of the surface, which must be transformed back for the real space information and furthermore it is a averaging technique which means that it was not possible to get local information with it. The data recorded in an STM image is a response to the surface corrugation in real space as the tip moves over the surface. As such, STM was one of the first techniques[1] that made it possible to actually "see" the individual atoms and to get local real space information about the atomic structure of a surface on a wide range of samples[13]. Besides the advantages of the STM, there are however also several disadvantages that must be taken into account. Since STM is based on the tunneling current, the imaged surface must be conducting. This restricts the range of the samples to metals, possibly with very thin layers of semiconductor or insulators grown on top. The second disadvantage is the height range. Since the height is controlled by a piezoelectric element, the height range is limited by the range of motion of this element, or what is often the limiting factor, the voltage range of the electronics that control the piezo element. This means that in practice only very flat surfaces on the nanometer range can be imaged. Another disadvantage pertains to the shape of the tip. It is aspired to make the tip as sharp as possible, ideally a cone shape ending in a single atom. But in reality the tip that is being used for the scanning consist of a few atoms sticking out from a much broader tip. This has no effect on the tunneling, but it will result in tip convolution effects, which means that fine details located next to larger features can be lost from the image. Finally it should be mentioned that the STM images does not directly reveal chemical information, which otherwise could be extremely useful.

[1]Before the STM the Field Emission Microscopy (FEM) and Field Ion Microscopy (FIM) also gave real space atomic information. However, today the STM is applied much more widely than any of these two previous techniques.

2.3.1 Theory of STM

In 1983 and 1985 J. Tersoff and D.R. Hamann presented a theory for the tunneling current in an STM[17, 18], which makes it possible to better understand what is being imaged in an STM. This theory has the advantage of being reasonably simple, yet advanced enough to describe many systems with good accuracy. Following the derivation given in [18] the tunneling current can to the first order be written as:

$$I = \frac{2\pi e}{\hbar}\sum_{\mu,\nu} f(E_\mu)[1 - f(E_\mu - eV)]|M_{\mu,\nu}|^2\delta(E_\mu - E_\nu). \tag{2.1}$$

where $f(E) = \frac{1}{exp\left(\frac{E-E_F}{k_BT}\right)+1}$ is the Fermi function, V is the bias between the tip and the surface, $|M_{\mu,\nu}|$ is the tunneling matrix element between the states of the tip ψ_μ and the surface ψ_ν and E_μ is the energy of state ψ_μ without any tunneling. If we assume low temperature and bias, then $eV \approx 0$ and the Fermi function turns into a step function which is 1 below the Fermi energy and 0 above. Following these approximations the expression for the tunneling current can now be reduced to

$$I = \frac{2\pi}{\hbar}e^2V\sum_{\mu,\nu}|M_{\mu,\nu}|^2\delta(E_\nu - E_F)\delta(E_\mu - E_F). \tag{2.2}$$

According to Bardeen's approximation[19], the tunneling matrix is expressed as

$$M_{\mu,\nu} = \frac{\hbar^2}{2m}\int d\vec{S}\cdot(\psi_\mu^*\vec{\nabla}\psi_\nu - \psi_\nu\vec{\nabla}\psi_\mu^*), \tag{2.3}$$

which is integrated over any surface S, placed in the vacuum region separating the two sides. Expanding the wave function for the surface with a Block expansion this is written as

$$\psi_\nu = \frac{1}{\Omega_S^{\frac{1}{2}}}\sum_G a_G \exp[(\kappa^2 + |\vec{\kappa}_G|^2)^{\frac{1}{2}}z]\exp(i\vec{\kappa}_G\cdot\vec{x}) \tag{2.4}$$

where Ω_S is the sample volume, $\kappa = \frac{\sqrt{2m\phi}}{\hbar}$ is the inverse of the decay length of the wave function in the vacuum, ϕ is the work function, $\vec{\kappa}_G = \vec{\kappa}_\parallel + \vec{G}$, and here $\vec{\kappa}_\parallel$ is the Block wave vector for the surface and $\vec{G}$ is the reciprocal lattice vector. The state of the tip is unknown, but assuming, as illustrated in the figure 2.3, that it is a spherically symmetric wave function, centered at r_0, with radius R and nearest distance to the surface d it can be written in the following form:

$$\psi_\mu = \Omega_t^{-\frac{1}{2}}c_t\kappa Re^{\kappa R}(\kappa|\vec{r} - \vec{r}_0|)^{-1}e^{-\kappa|\vec{r}-\vec{r}_0|}, \tag{2.5}$$

A Block expansion, similar to that performed for the surface wave function leads to evaluate the tunneling matrix element as

$$M_{\mu,\nu} = \frac{\hbar^2}{2m}4\pi\kappa^{-1}\Omega_t^{-\frac{1}{2}}\kappa Re^{\kappa R}\psi_\nu(\vec{r}_0). \tag{2.6}$$

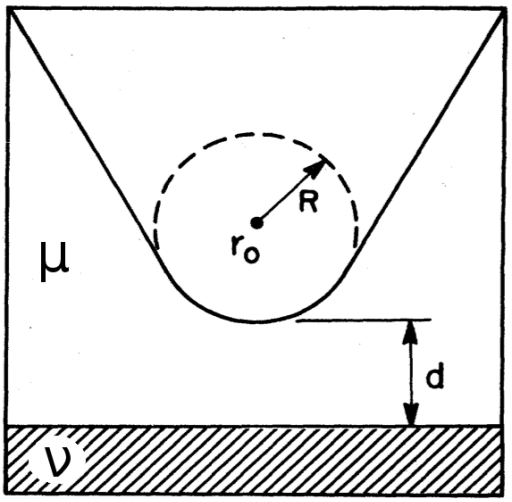

Figure 2.3: The geometry used in the STM theory derivation by J. Tersoff and D.R. Hamann. The wave function of the tip, μ is formed by assuming a spherical form of the wave function for the tip, centered at r_0, with radius R and nearest distance to the surface d. The surface wave function is dubbed ν. Adapted from [18].

where $\vec{r_0}$ is the center of the tip wave function. Inserting equation (2.6) into (2.2) we finally end up with this expression for the current:

$$I = 32\pi^3\hbar^{-1}e^2V\phi^2D_t(E_F)R^2\kappa^{-4}e^{2\kappa R} \times \sum_{\nu}|\psi_\nu(\vec{r_0})|^2\delta(E_\nu - E_F). \tag{2.7}$$

where $D_t(E_F)$ is the density of the states of the probe tip per unit volume.

Inserting typical metallic values (κ of $\sim 0.4\,\text{Å}^{-1}$, ϕ of $\sim 4\,\text{eV}$, V of $\sim 10\,\text{mV}$ and a sperical volume for $D_t(E_F)$ with radius 9 Å) into equation (2.7) it simplifies into

$$\sigma \approx \quad 0.1R^2e^{2\kappa R}\rho(\vec{r}_0, E_F), \tag{2.8}$$

$$\rho(\vec{r}_0, E) \equiv \quad \sum_{\nu}|\psi(\vec{r}_0)|^2\delta(E_\nu - E). \tag{2.9}$$

In this expression for the tunneling current it is noted that $|\psi_\nu(\vec{r_0})|^2$ is proportional to $e^{-2\kappa(R+d)}$. This means that after this derivation one finds the exponentially decreasing correlation between the distance between tip-to-surface distance and the tunneling current: $\sigma \propto e^{-2\kappa d}$ (the same relation found for simple tunneling between flat conducting surfaces separated by a vacuum region). Second it is noted that $\rho(\vec{r}, E)$ is the local density at the surface of states around the Fermi level. This means, that what the STM records in constant current mode, is not a contour plot of heights in the traditional sense, but a contour of $\rho(\vec{r}, E)$.

The point about what is actually being imaged in STM was further illuminated in 1986 by N.D. Lang. He conducted a series of calculations, in which he calculated the distance that would be required in order to maintain constant current for a simplistic test setup (figure 2.4). The setup consisted of two metal surfaces, with an atom on each. The surfaces was modeled with the jellium model. One atom, which

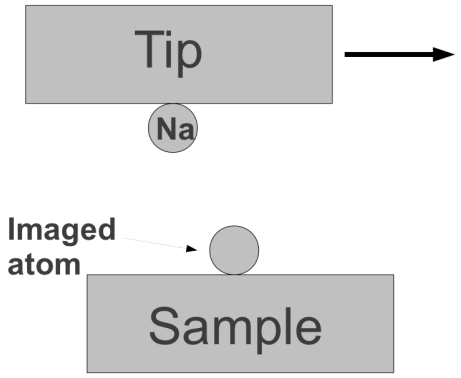

Figure 2.4: Drawing to illustrate the model system used by N.D. Lang to model the STM. Described in the text.

was always Na was used as the STM tip and the atom on the other surface, the one being imaged, was either Na, S or He. The tunneling current was calculated as the difference between the total tunneling minus the tunneling between the two surfaces without the tip atom, in order to rule out contributions for the current flowing from the imaged atom to the surface the tip atom sits on. The result is shown in figure 2.5(a). Here it is shown how S is imaged shallower than Na, partly because it is located closer to the surface and partly because it has a lower density of states close to the Fermi level (the bias was kept low in these simulations so only the states just below the Fermi level was imaged). Furthermore, it shows quite surprisingly, how He is imaged as a small hole, even though it is located on the surface, because it has a very low density of states at the Fermi level. These results show how interpreting STM can be difficult due to the convolution of the surface height and the density of states and highlights how data from other techniques, or possibly simulated STM images, can be helpful in such interpretations. The STM image in figure 2.5(b) is an STM image from earlier work within the group, that shows a very clear example of how differences in density of states can affect the appearance of the object being imaged. The images shows MoS_2 particles on a Au(111) crystal. These particles consist of a completely flat layered structure, but in the image it looks like the particles have a ridge at the edge. This is caused by a special electronic state that forms at the edge of these nano-particles, that increases the density of states at the Fermi level. Incidentally it is also this special edge state that is responsible for the catalytic abilities of these nano-particles.

2.3.2 The Århus STM

The STM used throughout this work is an variable temperature Århus type STM[14]. Figure 2.6(a) shows an image of the STM located in our setup. The actual STM is located in the end to the right of the large aluminum block behind the spring. The design of the STM is very compact, that combined with placing it in a large aluminum block helps to keep the resonance frequency very high. The aluminum block is hanging from a spring suspension system which has a very low resonance frequency. This combination helps to keep the STM very resilient to vibrations

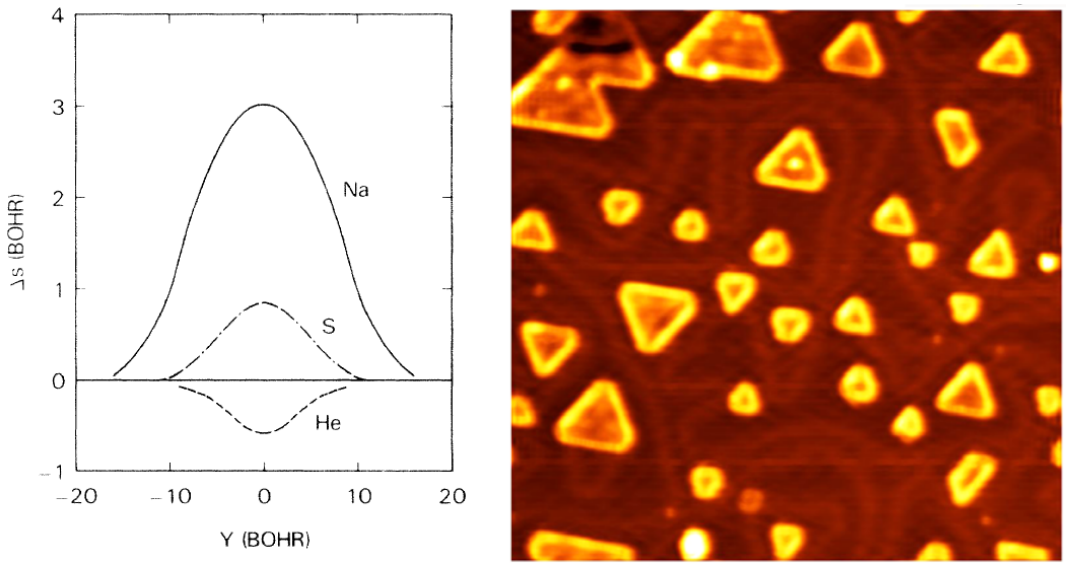

(a) (b)

Figure 2.5: (a) shows the appearent height measured by the STM as calculated by N.D. Lang. Adapted from [20]. **(b)** is an STM image of MoS_2 nanoparticles on a Au(111) surface. The rim of the particles appear higher, even though it has the same geometrical height as the center region of the particles. From included article IV

from the outside. Figure 2.6(b) shows a schematic drawing of the central parts of the STM. The rest of this paragraph explains the parts in this illustration and is partially copied from my masters thesis[15]. The sample (1), is located in a Ta or Mo sample plate (2), which can be slided into the STM under two blade springs (3). At the core of the STM is the tip (4), it is attached to the scanning tube (6) via a piece of macor (5). The scanning tube is fastened to a rod (7) going into the piezo tube (9) which is fastened to the STM body with a macor ring (8). The STM is electrically and thermally insulated from the aluminum block with quarts balls (10). For temperature control the STM has Zener diodes (11) which can be used for counter heating against cooling[21].

2.3.3 Image processing and analysis

All image processing and analysis in this thesis was performed with the Scanning Probe Image Processor (SPIP) software package version 5.1.5 from Image Metrology A/S[22]. The steps typically included in the image processing are calibration, plane correction to remove global tilt, outlier correction typically by use of a median filter to remove single points or lines of noise e.g. originating from unstable scanning conditions, might also include removal of periodic noise by Fourier filtering. The Z-calibration was obtained by measuring the step height on a Au(111) sample and was controlled by measuring the heights of the steps on the clean Ru(0 1 54) and Pt(111) single crystals. The XY calibration was found either from atomically resolved images of the samples themselves, or of other samples who are easier to

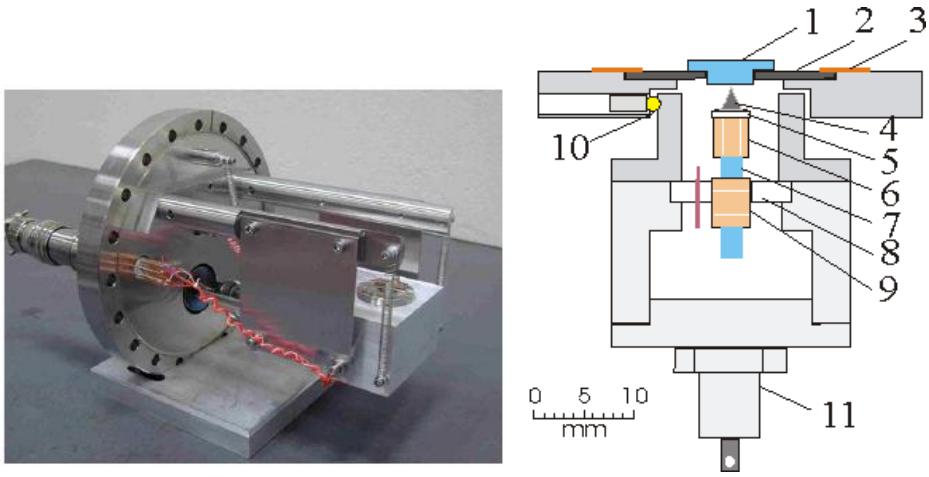

(a) (b)

Figure 2.6: The Århus type STM. **(a)** is an image of the STM and **(b)** is a schematic drawing of the inner parts of the STM. The details of the drawing is explained in section 2.3.2. The drawing is from the website of the Århus University SPM group[21].

resolve like the Au(111) sample or a HOPG sample, or in some special cases for the work on Ru(0 1 54), by use of images of the well defined $(\sqrt{3} \times \sqrt{3})R30°$ overlayer structure as an internal reference. XY correction factors are generally found to be in the range from 1.18 to 1.38.

2.4 X-ray Photoelectron Spectroscopy (XPS)

2.4.1 General principle

The method of XPS[1][23, p. 171-175] is based on the principle of the photoelectric effect (as illustrated in figure 2.7). From this technique it is possible to obtain information about the composition of a sample, and the oxidation state of the constituents. The general principle of the technique is that the surface is irradiated with mono-chromatic X-rays with the energy $h\nu$. These X-rays will, with a certain probability, excite electrons from the core levels of the atoms in the surface, overcoming the binding energy of this particular level $E_{binding}$. If the kinetic energy of these electrons is large enough to overcome the work function, they will leave with a kinetic energy given by this expression

$$E_{kin} = h\nu - E_{binding} - \phi_{sample} \tag{2.10}$$

The kinetic energy of the electrons can be measured with an electron energy analyzer, and the energy of the X-ray photon is fixed. This means that with the exception of the work function of the sample, it is now possible to calculate the binding energy

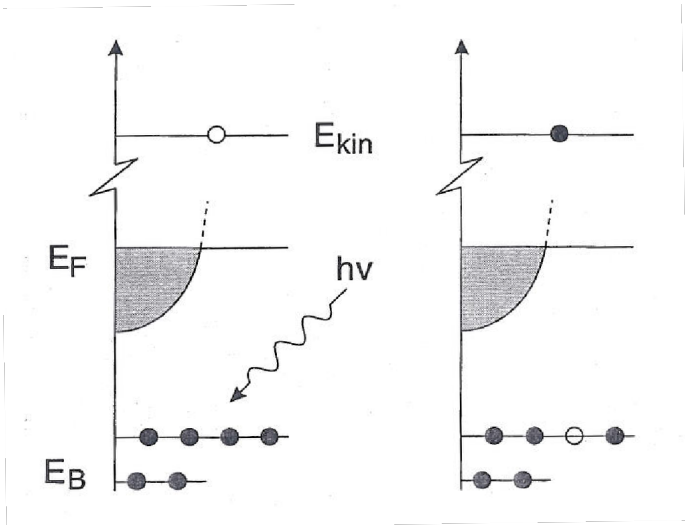

Figure 2.7: The photoelectric effect. An incoming photon with sufficient energy excites an electron out of the material it was located in. The electron ends up in the vaccum level with a kinetic energy that corresponds to the energy left from the photon after the excitation process. Adapted from [24].

of the energy levels of the surface, yielding the binding energy fingerprint necessary to figure out what the surface consists of.

In equations (2.10) the work function of the sample is present. This is inconvenient, since these might change during experimentation, if the surface is modified, and therefore it would be necessary to measure it at all stages in the experimentation. By setting the sample and the analyzer to the same potential their Fermi levels will align, and that makes it possible to make a correlation between the two in the following manner

$$E'_{kin} + \phi_{analyser} = E_{kin} + \phi_{sample} \tag{2.11}$$

where E'_{kin} is the kinetic energy of the electron as measured by the analyzer. Inserting equation (2.10) into equation (2.11) it is now possible to eliminate the work function[23, p. 171-175]

$$E'_{kin} = h\nu - E_{binding} - \phi_{analyser} \tag{2.12}$$

and the result is that we now have the desired correlation between the measured kinetic energy and the binding energy and since the work function of the analyzer does not change it only has to be measured once.

An XPS spectrum is obtained by measuring the number of electrons at a specific energy $N(E)$, and consecutively doing this for a number of energies within the desired energy range. Even though it is the kinetic energy that is measured, such spectra are often plotted as a function of the binding energy, since that is the quantity that carries the relevant information. Such a spectrum is then analyzed

by comparing the position and the magnitude of the peaks, to reference values and spectra such as those found e.g. in [25, 26].

The output from XPS originates only from the surface region of the sample, which means that it is a surface sensitive technique. The reason for this, and the depth of the region the technique probes, can be extracted from figure 2.8, which shows the mean free path of electrons in different materials as a function of their energy (the so-called "standard curve"). The X-rays have a large penetration depth, and

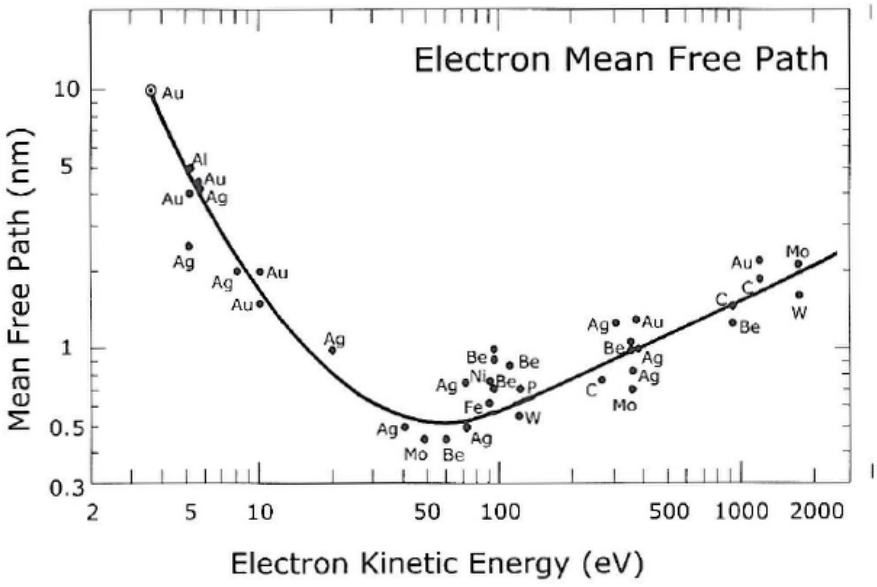

Figure 2.8: The mean free path of electrons in different materials as a function of their energy. Adapted from [1], originally from G.A. Somorjai, *Chemistry in Two Dimensions, Surfaces* (1981), Cornell University Press, Ithaca.

will therefore excite electron deep down into the sample. However, the distance an electron can travel in a solid is limited, as per figure 2.8. Therefore only the electrons that are close to the surface will escape the sample and contribute to the spectra. The energy of the X-rays used in this project is 1253.6 eV, so the energies of the excited electrons will be in the range from a few eV's and up to this value. From the standard curve it is seen that the mean free path of these electrons will be less than 2 nm and the technique will therefore not probe any deeper than this.

2.4.2 Features and artifacts in the XPS spectra

Doing an XPS spectrum of the entire available energy range is called a broad spectrum. Examples of such broad spectra can be seen in section 3.3.1. A broad spectrum is good for getting an overview of the composition and for looking for contaminants. However, for precise measurements of the peak positions and magnitudes, spectra are usually made in a narrow energy window around the particular peak, and these peaks are then made with higher resolution and more counts.

An XPS spectrum consist of a series of peaks super imposed on a background. The background consist of scattered electrons and therefore it increases towards higher binding energies (lower kinetic energy). The background will also be slightly higher on the high binding energy side of peak due to a small continuous loss. The peaks that originate from the binding energy levels (the relevant ones for XPS) are unfortunately not the only ones present in the spectrum. In order to be able to distinguish these from the rest, it is necessary to understand where they come from. The extra peaks that might be present in an XPS spectrum are ghost peaks, satellite peaks, energy loss peaks and Auger peaks, which are explained in the following sections after an explanation of the naming of the binding energy peaks.

The binding energy peaks are named after the quantum state of the level they originate from. The first denotation is a number that corresponds to the level. The angular momentum l is denoted with a letter, so that an angular momentum of (0,1,2,3,...) is attributed the letters (s,p,d,f,...). The spin is included by noting the total angular momentum $j = l + s$. This means that a peak originating from a state with 0 angular momentum will be denoted $1s$ and it is referred to as a singlet. Peaks that originate from states with higher angular momentum will be split into two peaks according to the spin. Such two peaks could then e.g. be denoted $4f_{7/2}$ and $4f_{5/2}$ and they are called a doublet. The intensity ratio between the two peaks corresponds to the multiplicity $2j + 1$ of the levels[1]. The ratio between the $4f_{7/2}$ and $4f_{5/2}$ peaks is therefore given as

$$2\frac{7}{2} + 1 : 2\frac{5}{2} + 1 \Rightarrow 4 : 3 \tag{2.13}$$

The so-called ghost peaks originate from X-rays that comes from another element then the one intended. All XPS in this work is done with the Mg K$\alpha_{1,2}$ radiation, but when X-rays are generated in other compounds they will have a different energy, than the one used in equation (2.12) and therefore the binding energy peaks will be shifted. The extra X-rays can e.g. be generated in the other anode in a dual anode X-ray gun, which in our case is of Al, or it can be generated in oxygen if the anode has been slightly oxidized. The relevant ghost peak shifts and their sources are listed in table 2.2.

Contaminating radiation	Mg anode. Energy shift up in binding energy [eV]
O (Kα)	**728.7**
Al (Kα)	-233.0

Table 2.2: A table with the relative position of the ghost peaks that are possible with the present setup. The most predominant peaks are in bold font. The values are from [25] and the table is adapted from [15].

Satellite peaks are also generated by different X-rays. But in this case they are not generated from another element, but from different transitions within the same element[24]. For Mg the other relevant X-ray transitions, their observed energy shifts and relative heights are listed in table 2.3.

		$\alpha_{1,2}$	α_3	α_4	α_5	α_6	β
Mg	energy shift down [eV]	0	**8.4**	**10.2**	17.5	20.0	48.5
	relative height	100	8.0	4.1	0.55	0.45	0.5

Table 2.3: The relative position and intensity of the satellite peaks for a Mg anode. The largest peaks are in bold font. The values are from [25] and the table is adapted from [15].

An energy loss peaks is formed when an XPS electron experiences a loss due to a surface plasmon. The result is a shift down in kinetic energy, which leads to a shift up in observed binding energy. In order to be able to attribute a peak to this mechanism the energy shift must correspond to the energy of a surface plasmon, but since these are different from surface to surface they are not always known. In that case one can still hypothesize that a peak is an energy loss peaks, if a shift of the same size (which does not correspond to any of the other fixed shifts) is present at more than one of the large peaks and has a size within the range expected for surface plasmons.

The last contribution to the XPS spectrum are Auger peaks[24]. Auger electrons are formed by a different electronic process. When an X-ray photon has excited an electron out of an atom, that leaves a hole in one of the core levels. This will immediately be filled by an electron from a higher level. The difference in energy from this transition can be used to excite a third electron, possible enough to make it leave the sample. This process is called the Auger process, only normally an electron source is used to make a core level hole instead of an X-ray source. Since the excited electron has a kinetic energy that is directly related to the energy difference between two levels in an atom, this can also be used for a spectroscopy method which is called Auger Electron Spectroscopy (AES). AES peaks in an XPS binding energy spectrum does however not make any sense, since here the kinetic energy is subtracted from the energy of the X-ray photon, which for the case of AES has nothing to do with the energy of the measured electron. However, if one plots the intensities in the XPS spectrum as a function of kinetic energy, then it is possible to find the appropriate AES energies, which makes it possible to identify them from reference literature. If in doubt about whether a particular peak in an XPS binding energy spectrum is an XPS or an Auger peak, this can be checked by choosing a different X-ray source. This will shift the position of the AES peak while if it is an XPS peak it will remain at the same energy.

The binding energy of XPS peaks may also be shifted by up to a few eV's depending on their chemical environment. This is one of the really nice features of XPS, since it in some cases allow for e.g. monitoring of whether a certain reaction has taken place.

2.4.3 Quantitative analysis

Comparing the intensity of the peaks in the XPS spectra allows to quantify the different elements involved, provided the structure is known. The intensity is the

area of the peaks which is calculated as the area under a peak after background subtraction. The intensity of such a peak can be described as follows

$$I_{xk} = P_{xk} F_{h\nu} T(E_{xk}) \tag{2.14}$$

where I_{xk} is the intensity of the peak from level k of element x, P_{xk} is the probability of emission per incoming photon, $F_{h\nu}$ is the intensity of photons and $T(E_{xk})$ is the analyzer transmission function. The probability of emission can be written as

$$P_{xk} = \sigma_{xk} N_x \lambda_{xk} \tag{2.15}$$

where σ_{xk} is the cross section of the electrons in level k of element x, N_x is the concentration of element x, λ_{xk} is the probed area, which in this case is the mean free path of the electrons. Combining equations (2.14) and (2.15) gives

$$I_{xk} = \sigma_{xk} N_x \lambda_{xk} F_{h\nu} T(E_{xk}) \tag{2.16}$$

which can be simplified into

$$I_{xk} = S_{xk} N_x F_{h\nu} \tag{2.17}$$

where S_{xk} is the sensitivity factor. It should be noted that in the last simplification the analyzer transmission function was included in the sensitivity factor, which means that in principle it is setup dependent. However, it is often the assumption that the differences in sensitivity factors between setups is merely a linear scaling, which means that any ratios between sensitivity factors remains the same across setups, because in that case the scaling drops out. This also means, that as long as only ratios are compared, any set of constants that has the right internal ratio can work as sensitivity factors. One commonly used set of sensitivity factors sets the sensitivity of the C 1s peak to 1 and scales all other sensitivity factors to this. The ratio of two peak intensities can be written as

$$\frac{I_{xk}}{I_{yl}} = \frac{S_{xk} N_x}{S_{yl} N_y} \tag{2.18}$$

This makes it possible to calculate the composition of any compound where the constituents are homogeneously mixed, as follows

$$\frac{N_x}{N} = \frac{\frac{I_{xk}}{S_{xk}}}{\sum_n \frac{I_n}{S_n}} \tag{2.19}$$

where the sum is only over one peak per element[24].

From XPS intensities it is also possible to calculate layer thicknesses by including the exponential damping of the electrons in the material. It is however necessary to have some knowledge about the structure of the system. Assuming that a smooth

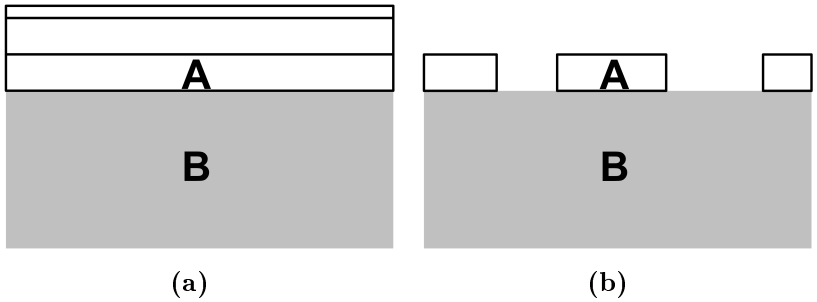

Figure 2.9: Illustrations of the overlayer models used to calculated XPS coverages. **(a)** is used in the multilayer case and assumes that layers grow evenly over the whole surface. **(b)** is the single monolayer model. Here, a layer with a fixed thickness covers only parts of the surface.

film of A is deposited in B (see figure 2.9(a)), the intensity of the overlayer can be written as

$$I_{\mathrm{A}}(n \cdot l_{\mathrm{A}}) = I_{\mathrm{A}}^{\infty}(1 - \exp(-n \cdot l_{\mathrm{A}}/\lambda_{\mathrm{A}})), \tag{2.20}$$

where I_{A}^{∞} is the intensity from a infinitely thick layer of A, l_{A} is the layer thickness of A, n is the number of layers (note that fractional layers by this model are still spread out evenly over the entire area, even though that is not possible) and finally λ_{A} is the mean free path of electrons from A. The intensity of the substrate can be written as

$$I_{\mathrm{B}}(n \cdot l_{\mathrm{A}}) = I_{\mathrm{B}}^{\infty} \exp(-n \cdot l_{\mathrm{A}}/\lambda_{\mathrm{B}}), \tag{2.21}$$

where I_{B}^{∞} is the intensity from an infinitely thick layer of B and λ_{B} is the mean free path of electrons from B. Combining equations (2.20) and (2.21) results in the following equation, from which it is possible to calculate the layer thickness

$$\frac{I_{\mathrm{A}}(n \cdot l_{\mathrm{A}})}{I_{\mathrm{B}}(n \cdot l_{\mathrm{A}})} = \frac{I_{\mathrm{A}}^{\infty}}{I_{\mathrm{B}}^{\infty}} \frac{(1 - \exp(-n \cdot l_{\mathrm{A}}/\lambda_{\mathrm{A}}))}{\exp(-n \cdot l_{\mathrm{A}}/\lambda_{\mathrm{B}})} \tag{2.22}$$

In this equation $\frac{I_{\mathrm{A}}^{\infty}}{I_{\mathrm{B}}^{\infty}}$ is simply the ratio between the sensitivity factors.

It is also possible to form an expression to calculate the sub-monolayer coverage Θ_{A} of A on B, in the case where this layer has a fixed thickness in the area it covers and then only covers part of the surface (see figure 2.9(b)). Using the same variables as before the intensity of the overlayer can be written as

$$I_{\mathrm{A}}(\Theta_{\mathrm{A}}) = I_{\mathrm{A}}^{\infty}\Theta_{\mathrm{A}}(1 - \exp(-l_{\mathrm{A}}/\lambda_{\mathrm{A}})) \tag{2.23}$$

and the intensity of the substrate can be written as[24]

$$I_{\mathrm{B}}(\Theta_{\mathrm{A}}) = I_{\mathrm{B}}^{\infty}\left((1 - \Theta_{\mathrm{A}}) + \Theta_{\mathrm{A}} \exp(-l_{\mathrm{A}}/\lambda_{\mathrm{B}})\right). \tag{2.24}$$

And combining the two the expression from which it is possible to calculate the coverage is

$$\frac{I_{\mathrm{A}}(\Theta_{\mathrm{A}})}{I_{\mathrm{B}}(\Theta_{\mathrm{A}})} = \frac{I_{\mathrm{A}}^{\infty}}{I_{\mathrm{B}}^{\infty}} \frac{\Theta_{\mathrm{A}}(1-\exp(-l_{\mathrm{A}}/\lambda_{\mathrm{A}}))}{((1-\Theta_{\mathrm{A}})+\Theta_{\mathrm{A}}\exp(-l_{\mathrm{A}}/\lambda_{\mathrm{B}}))} \tag{2.25}$$

where, as before, $\frac{I_{\mathrm{A}}^{\infty}}{I_{\mathrm{B}}^{\infty}}$ is the ratio between the sensitivity factors.

2.4.4 XPS data processing

XPS peaks are fitted with a combination of Gaussian and Lorentzian peaks shapes containing an asymmetric component when fitting metals. This asymmetric component is due to the electrons in the conduction band screening the hole after excitation, this creates a continuous loss feature in the high binding energy side of the peaks. In this work the background was always fitted with a Shirley background and in all cases was the energies calibrated by means of a table value for a peak that does not change during the experiments.

2.4.5 XPS on ruthenium

Looking for carbon impurities on a ruthenium crystal with XPS is tied in with some difficulty. The problem is that the C 1s peak is located at ∼284 eV and it overlaps with the Ru $3d_{3/2}$ peak located at approximately the same energy (figure 2.10). Because of this conflict, the only way to determine if the surface is free of carbon, is to check whether the ratio between the Ru 3d doublet peaks has the value it is supposed to. In this particular spectrum the ratio is 1:1.47 and therefore is relatively close to the theoretical value of 1:1.50. It should however be mentioned that this method is not nearly as accurate as when the peaks do not overlap, and therefore can only be used to look for carbon down to a certain level.

2.5 Mass Spectrometry

2.5.1 General principle

Gas compositional analysis is performed with a Quadrupole Mass Spectrometer (QMS). The general principle of the QMS is illustrated in figure 2.11. The sample gas is ionized by an electron filament. The ions are then accelerated towards the quadrupole mass filter, which consist of four rods forming the electrodes. These electrodes are biased with a high frequency AC signal, which is superimposed on a DC bias. This creates an alternating field within the rods, that only ions with a particular mass to charge ratio has a stable trajectory through. By changing the DC bias, the accepted mass to charge ratio is changed thus making it possible to form a spectrum. After passing through the quadrupole the filtered ions enter a sequential electron multiplier, where their signal is amplified into an measurable electron pulse.

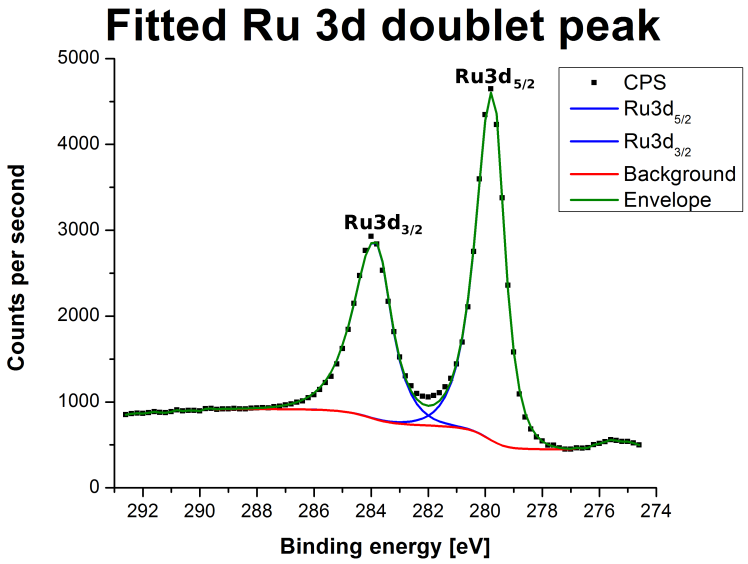

Figure 2.10: XPS spectrum of the Ru $3d$ doublet. Notice how the Ru $3d_{5/2}$ peak is located precisely at the position of the C $1s$ peak at ∼284 eV.

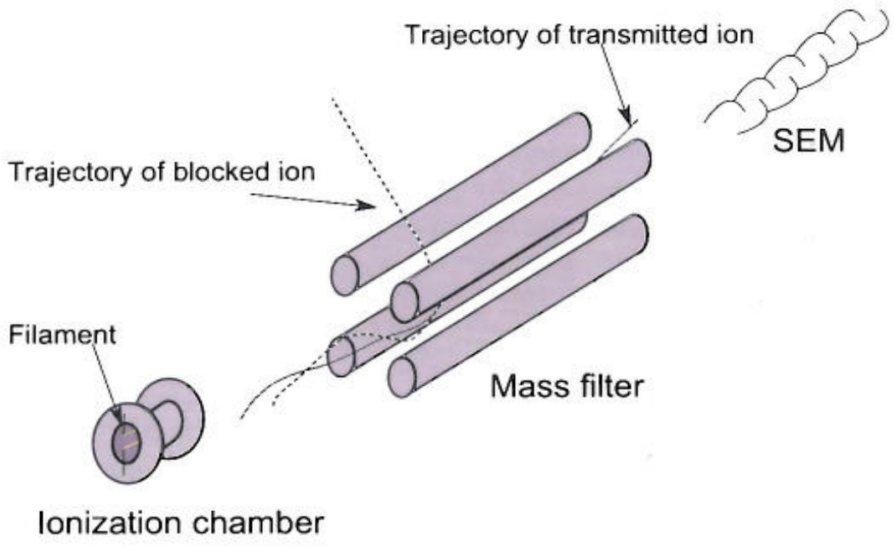

Figure 2.11: The general principle of the QMS. The sample gas is ionized in the ionization chamber, filtered in the quadrupole mass filter, multiplied in the sequential electron multiplier and finally detected. Adapted from [27].

2.5.2 Gas analysis

The QMS is usually used either to make a spectrum where a certain range of masses is scanned or to continuously track a number of masses of particular interest over time. As indicated above, the principle of mass spectrometry is relatively simple, it is however complicated by several issues. First of all there might be an overlap in the masses one wishes to track. This could e.g. be between CO and N_2 who both have molecular mass 28 amu. Another complication is that the ions might become double of even triple ionized by the electron filament, but in the conversion from mass per charge to mass it is assumed that the charge is one. This will results in e.g. Ar having not only a peak at 40 amu but also at mass 20 amu and possibly even 13.33 amu. Another complication is that the electron filament induces the dissociation of a fraction of the molecules. This will lead to e.g. CO having not only a peak at 28 amu, but also at 12 amu and 16 amu corresponding to C and O. Luckily the multiple ionization and the splitting up of molecules happens with well defined probabilities, yielding a fingerprint of mass intensities for any given molecule (the probabilities for breaking the molecule up are called cracking patterns). This helps solving the problem with molecules having the same mass, as there will always be differences in the cracking patterns and multiple ionization probabilities.

2.5.3 Temperature Programmed Desorption (TPD)

Temperature programmed desorption is a surface science technique that makes use of the QMS. The technique simply consist of dosing an amount of gas on a sample, heating the sample along a linear heating ramp and then monitoring the amount of different kinds of gasses that desorb from the surface as a function of temperature. If we ignore re-adsorption then the rate of desorption can be written as

$$r = -\frac{d\theta}{dt} = \nu(\theta)\theta^n exp\left(-\frac{E_{des}(\theta)}{RT}\right) \tag{2.26}$$

$$T = T_0 + \beta t \tag{2.27}$$

where r is the rate of desorption, θ is the adsorbate coverage, n is the order of desorption which can be either 0, 1 or 2, ν is the pre-exponential factor, E_{des} is the desorption energy, R is the gas constant, T is the temperature which is ramped up with a rate β[1].

For the project concerning Ru(0 1 54), an example CO TPD is shown in figure 2.12 from a crystal similar to ours but not taken on our setup[2]. As seen in the figure the TPD has three distinct features, two α-peaks and a β-peak. The lowest temperature α-peak, located at 390 K, originate from the CO adsorbed on the terraces in excess of 1/3 of a monolayer. Above 1/3 ML the CO form an disordered overlayer on the terraces, but below this coverage it forms patches of or a complete ordered $(\sqrt{3}\times\sqrt{3})R30°$ structure. This is more stable and therefore the second α-peak, which

[2]Our TPD's have a temperature shift which means that they do not correlate to those in literature. This TPD is obtained by Søren B. Vendelbo as a part of a collaboration around this project.

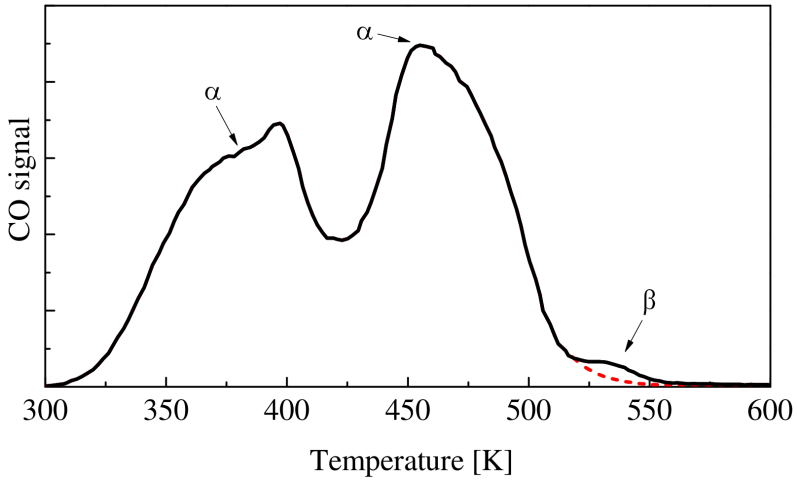

Figure 2.12: Example CO TPD from a Ru(0 1 54) crystal. The TPD has three features. Two α-peaks located at 390 K and 460 K and a β-peak located between 500 K and 550 K. The dashed line is an exponential function fitted to the tail of the α-peak to be able to evaluate the magnitude of the β-peak. Adapted from [28].

originate from the last 1/3 ML, is located at a higher temperature 460 K[29, 30]. At between 500 K and 550 K a third much smaller feature appear, referred to as the β-peak. It has previously been show that the CO that desorbs at this temperature has been dissociated[31, 32] and that the recombination and desorption take place at the steps of the surface[28, 33].

2.5.4 Carbon uptake experiments

These experiments are performed to quantify even small (sub-monolayer) amounts of carbon species present on a surface. The experiment is performed by exposing the surface to a constant pressure of oxygen, initially introduced as a step function, while the sample is kept at a constant temperature. Meanwhile the species desorbing from the surface is monitored with the QMS. For the case with carbon on the surface the CO signal in the QMS will be indicative of the amount of C present on the surface. This amount can then be quantified by comparing the CO area with that of a CO TPD. One difficulty arises during these experiments and that is that in the presence of oxygen the electron filament in the mass spectrometer evolves significant amounts of CO. Subtraction of the QMS contribution to the CO signal is done based on the shape of the signal.

Chapter 3

CO dissociation on ruthenium

In this chapter we will discuss various results concerning the influence of the structure on the catalytic abilities of ruthenium. The ongoing ruthenium reactivity research at the Center for Individual Nanoparticle Functionality (CINF) involves many different approaches. The purpose is to bring insights that might otherwise be missed if only a single sample type or only the techniques of a single setup were employed. The various ties of collaboration and the people we have collaborated with will be described as the results are presented, but it is helpful at this point with a little overview of the scope of the results presented in the different sections. Sections 3.4 to 3.9 of this chapter concern the research carried out as a part of our (the subgroup belonging to the UHV STM setup) approach to the problem, which is a UHV single crystal study, in collaboration with theoreticians (section 3.8). In section 3.10 we will compare some preliminary results of ours with structure sensitivity and reactivity studies from another setup, but also on a single crystal sample. Finally in section 3.11 reactivity and structure results from no less than three different setups, utilizing very different samples will be presented in order to shed some light on the effects of structure and the possibility to draw lines between results obtained with different model system.

First however, this chapter will start with an introduction to the subject. It will begin with motivations, continue into a summary of literature concerning the structure and appearance of the different species we might observe on the sample and conclude with a literature walk-through of the most important results concerning the structure sensitivity of the relevant reactions.

3.1 Introduction

The presented results are about catalytic CO dissociation on ruthenium catalysts. While CO dissociation (equation 3.1) is a relative simple process, it is important because it is the rate limiting step in other reactions with more industrial importance like the Fisher-Tropsch synthesis process (equation 3.2) and also under certain conditions the methanation reaction (equation 3.3).

$$\mathrm{CO} \rightarrow \mathrm{C} + \mathrm{O} \tag{3.1}$$

$$(2n+1)\mathrm{H_2} + n\mathrm{CO} \rightarrow \mathrm{C_nH_{(2n+2)}} + n\mathrm{H_2O} \tag{3.2}$$

$$\mathrm{CO} + 3\mathrm{H_2} \rightarrow \mathrm{CH_4} + \mathrm{H_2O} \tag{3.3}$$

The Fisher-Tropsch process is the last reaction step involved in making heavier hydrocarbons like gasoline or diesel from either lighter hydrocarbons like methane (through the steam reforming process) or from coal (through gasification). While at present, the real world implementations of this method of producing transport fuels is limited, it is likely to play a more important role in the future[34] as the present source for transportation fuel (oil), is likely to become a scarce resource much sooner than gas or coal. While ruthenium in itself is probably too expensive and to scarce for large scale implementation for any of these catalytic reactions, it is the most active catalyst for them and as such the understanding of why exactly that is, might lead to the development of more efficient catalysts with cheaper materials.

But studying CO dissociation is not only important because it is a key part of these larger more important reactions, but also because it is a reaction step that is relative simple. This makes it the ideal choice as a probe reaction, to test and gain insight into the origin of the reactivity. Due to these reasons CO dissociation on ruthenium and the structure of CO adsorbed on ruthenium surfaces has been studied extensively in the past and the next section will serve as an introduction to this work.

3.1.1 Structure of species on ruthenium surfaces

Adsorbing CO onto a close packed ruthenium surface will lead to a few different structures, as already briefly mentioned in section 2.5.3. Up to 1/3 monolayer (ML) CO coverage (with respect to the number of ruthenium atoms), it will form patches of a $(\sqrt{3} \times \sqrt{3})R30°$ structure until these patches grow into a complete $(\sqrt{3} \times \sqrt{3})R30°$ overlayer at precisely 1/3 ML coverage[30, 35, 36, 37]. CO will adsorb in a upright geometry with respect to the surface and will adsorb preferentially on the atop sites[36]. Above 1/3 ML the behavior depends on the adsorption temperature. When adsorbing CO at 110 K it will start to form an ordered $(2\sqrt{3} \times 2\sqrt{3})R30°$ structure up to a coverage of 0.58 ML[35, 37]. At room temperature however it is not possible for CO to form any more ordered layers above 1/3 ML. Instead it will start to fill in the gaps in the $(\sqrt{3} \times \sqrt{3})R30°$ structure in a non-ordered fashion (due to a large repulsion in between the molecules) thus leading to a non-ordered overlayer structure for coverages between 1/3 ML and up to the saturation coverage of $\approx$0.58 ML[35, 37]. These structure studies has mainly been performed with LEED, but the $(\sqrt{3} \times \sqrt{3})R30°$ structure has also been reported in STM studies[38, 39](See figure 3.1 for an example STM image of the $(\sqrt{3} \times \sqrt{3})R30°$ CO overlayer structure on Ru(001) from ref [38]), where it was also found that the overlayers were difficult to resolve above 1/3 ML coverage due to weak corrugation.

While studying the dissociation of a molecule on a surface, it is of course important to know, not only the structure of that molecule on the surface, but also the components it breaks down into and any species that might form unintended. Starting out with the structures of oxygen on closed packed ruthenium surfaces reference [40] reports a number of periodic structures depending of coverage. Starting with the lower coverages the oxygen adopts a $p(2 \times 2)$ structures at coverages below 0.35 ML. The structure is perfect at the appropriate coverage of 0.25 ML (see figure 3.2(a)). Increasing the coverage a $p(2 \times 1)$ structure starts to appear until the saturation

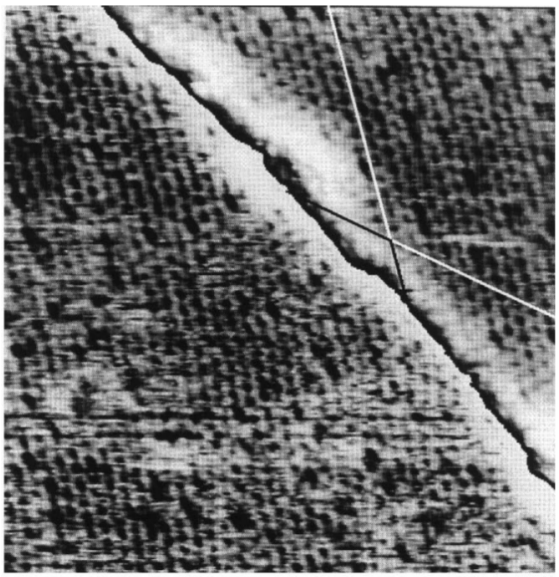

Figure 3.1: 15×15 nm STM image of the $(\sqrt{3} \times \sqrt{3})R30°$ CO overlayer structure on Ru(001). It is rotated 30° with respect to the ruthenium lattice and the periodicity was reported to approximately 0.41 nm and is assigned to the $(\sqrt{3} \times \sqrt{3})R30°$ structure. Adapted from [38].

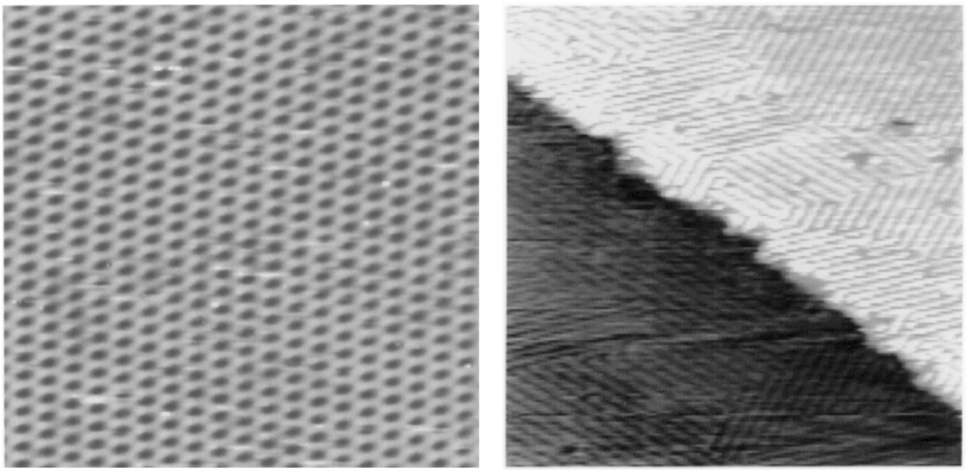

(a) $9{\times}14\,\mathrm{nm}^2$ **(b)** $15{\times}15\,\mathrm{nm}^2$

Figure 3.2: Images of different oxygen structures on Ru(001). Figure **(a)** is an STM image of the p(2×2) overlayer structure, adapted from [41]. Figure **(b)** is an STM image of p(2×1) domains in the vicinity of a step, with a characteristic striped structure. Adapted from [40].

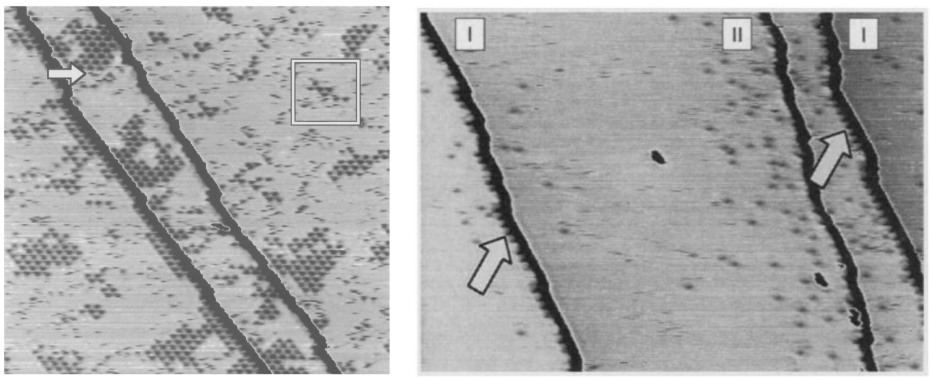

(a) $20\times30\,\mathrm{nm}^2$ **(b)** $24\times19\,\mathrm{nm}^2$

Figure 3.3: (a) is an STM image of oxygen on a Ru(001) surface. Single oxygen atoms are imaged as little stripes as they are moved by or under the tip. If they form patches or are located at steps, they are less mobile and therefore have a different appearance. Adapted from [41]. **(b)** is an STM image of a Ru(001) surface after dissociative adsorption of ∼0.1 ML NO. Grey spots are N, rows of black spots at terraces (marked with arrows) and dashes are O. Adapted from [43].

coverage of 0.5 ML. An example STM image of the p(2×1) structure in the vicinity of a step is shown in figure 3.2(b). Notice the different domains and the striped p(2×1) structure. Menzels group investigated the adsorption of oxygen on a Ru(001) surface that contains regions where the lattice is slightly stretched due to sub-surface argon bubbles (more about this phenomenon in section 3.3.3). It was shown that oxygen preferentially adsorbs in the regions with the expanded lattice and that this tendency was valid for all coverages[39, 42].

A series of interesting observations about the behavior of adsorbed oxygen, alone and in the presence of nitrogen, has also made in the STM studies by Wintterlin, Zambelli, Ertl *et al*[41, 43, 44]. For the case where only oxygen was adsorbed on the surface it resulted in a situation like the one showed in figure 3.3(a). Here it is seen, that when an oxygen atom has no neighbors, it is highly mobile on the surface and it is therefore imaged as dashes along the scan direction. However, when an oxygen atom moves close to other oxygen atoms on the terraces or moves close to the steps, the mobility is reduced and it is then imaged as triangles. When in this configuration, oxygen atoms form a (2×2) periodicity compared to the ruthenium surface. The last thing to notice is that the tendency for oxygen to sit at steps in this configuration is much more pronounced on every other step, which correlates with the Ru(001) surface having two different geometric configurations[1][41]. In the case of co-adsorbed oxygen and nitrogen from small amounts of dissociatively adsorbed NO it resulted in a surface like the one shown in figure 3.3(b). In this image gray spots are nitrogen atoms and they are observed to be on the terrace with a decreasing concentration as the distance from the steps increase. As before black dashes and rows of black spots at the steps are oxygen atoms. As was the case

[1]The step geometry on the Ru(001) surface alternate between two different configurations on every other step.

when only oxygen was present, the rows of oxygen atoms mainly decorate one type of steps and in this case it is the conclusion, that the oxygen that sits at the top of the step will remain there and deactivate that step, so it is the other steps that are responsible for the continued dissociation of NO[43]. Regarding the appearance of oxygen atoms on closed packed ruthenium surfaces by STM, the literature is not entirely clear. In the studies just mentioned (references [41, 43, 44]), where the STM imaging was performed at room temperature, the oxygen atoms were assigned an appearance of lower apparent height than the surrounding ruthenium atoms. In the work by Corriol *et al.*, where room temperature STM images were compared to DFT simulated STM images, it was concluded that there is a contrast inversion. They concluded that oxygen appear as depressions at all coverage below a full monolayer (in a (1×1) overlayer configuration) and only at this coverage as a protrusion[45]. In the work by Meinel *et al.* the oxygen atoms are imaged on Ru(001) as protrusions in a p(2×2) structure at room temperature and it is suggested that the differences in appearance of oxygen atoms on closed packed ruthenium surfaces originate from the scanning conditions[40].

Carbon on the surface, as is the case after CO dissociation, also gives rise to a range of possible structures. In 2008 Shimizu *et al.* presented some beautiful low temperature STM images of hydro carbon species on a Ru(001) surface. These hydrocarbon species was formed from small amounts of carbon impurities and added hydrogen or water[46]. The presence of solely carbon on the ruthenium surfaces has been shown to form graphene sheets on the surfaces of several transition metals, including ruthenium, leading to a hexagonal Moiré pattern with a periodicity of approximately 3 nm[47, 48](image of this phenomenon in section 3.3.2). While these graphene layers often appear as an annoying side effect of insufficient cleaning, it has also been shown that the Moiré patterns can serve a useful purpose. It was demonstrated that the depressions in these patterns can be used as a regular pattern of nucleation centers for nano-particle growth by physical vapor deposition[49, 50].

3.1.2 Structure sensitivity

Having now been through the structures and appearances of the species relevant for this project, this section will return to the central subject of the project, namely the structure sensitivity of the catalytic abilities of ruthenium. This subject has already been the focus of other research groups and this section will go through some of the more important works in some detail.

In early studies by Goodman and Kelley[51, 52] an innovative approach was taken to try and bridge the gap between single crystal studies and the studies on supported catalysts. The research focused on investigating the structure dependence of the methanation reaction on nickel surfaces. This was done by measuring the specific activity (activity per site) of two different single crystal nickel surfaces and a supported nickel catalysts, at high pressure (120 Torr). The result of these measurements are shown in figure 3.4. The plot shows an Arrhenius plot of the specific activity of the methanation reaction over Ni(111) and Ni(100) single crystals and a supported catalyst Ni/Al_2O_3, measured at 120 Torr. As it can be seen, all of the data closely follows the same trend line and since the different data sets represent

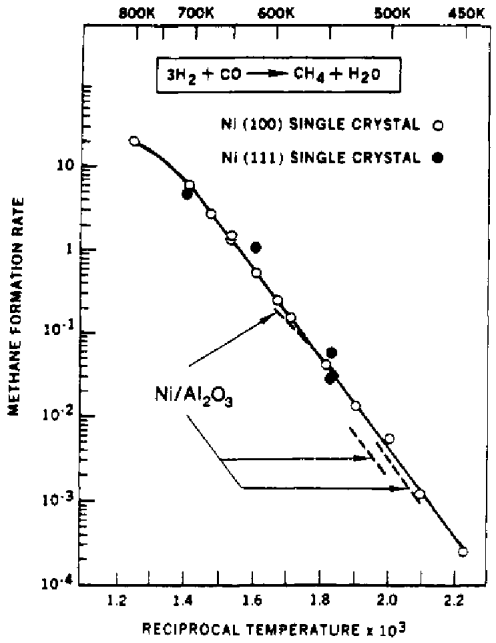

Figure 3.4: Arrhenius plot of the specific methane formation rate measured at 120 Torr on Ni(111) and Ni(100) and a supported nickel catalyst Ni/Al_2O_3. Adapted from [51].

different ruthenium structures, it was concluded that the methanation reaction is structure insensitive on nickel[51]. This conclusion was later expanded to include ruthenium as well[52].

In 2008 Andersson *et al.* performed a series of DFT calculations and performed experiments both under UHV and high pressure conditions, to further investigate the structure sensitivity of the methanation reaction on nickel[53]. Under UHV conditions it was shown that the CO dissociation (which is the rate limiting step under these conditions) could be completely suppressed on a stepped Ni(14 13 13) crystal by dosing sulfur on it in an amount comparable to the amount of steps on the surface. Furthermore, by STM on a Ni(111) single crystal after different doses of CO, it was observed that a form of carbide formed from the deposited carbon, but only at the steps (figure 3.5(a)). These two results strongly suggest that the CO dissociation at UHV conditions only take place at steps, in correspondence with the DFT calculations. In the high pressure case, the methanation activity relative to the amount of nickel present was measured for a series of supported catalysts. From the graph in figure 3.5(b) it can be seen that the best fit for this data, indicate that this reaction takes place at steps and kinks, but not on the facets of the particles, also in correspondence with the DFT calculations[53].

As highlighted by the previous sections, there are some results pertaining to the structure sensitivity of methanation related reactions that seem contradictory. In the case of ruthenium this question was addressed further by Zubkov *et al.* in a series of reaction rate measurements, including isotopic scrambling and blocking of certain sites on a Ru(109) single crystal[32, 54]. Figure 3.6 shows a series of CO TPDs from the Ru(109) crystal as a function of increasing initial coverage. These TPDs contain the same basic features as was explained in section 2.5.3. Note, that at

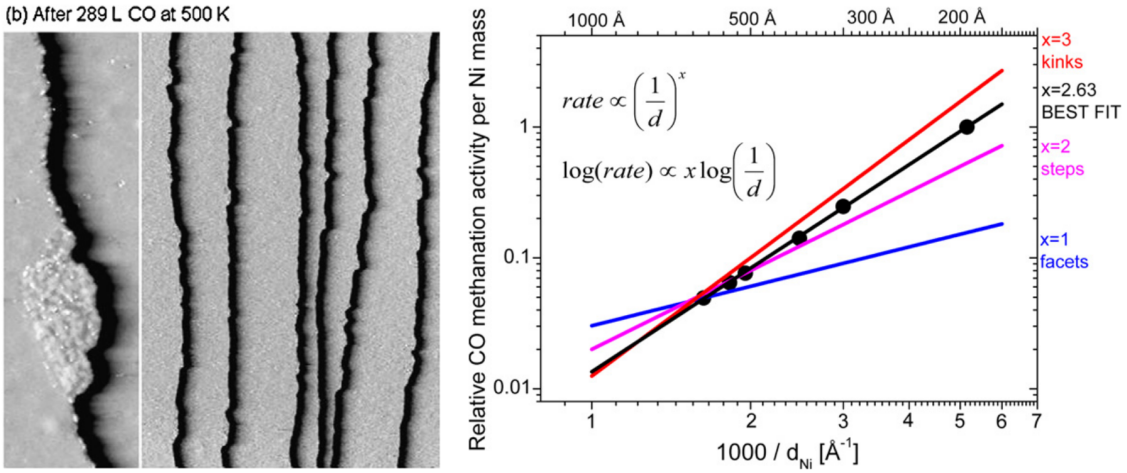

(a) $22\times70\,\mathrm{nm}^2$, $340\times500\,\mathrm{nm}^2$ **(b)**

Figure 3.5: Figure **(a)** shows two STM images of the nickel surface after CO exposure. The images show the growth of nickel carbide at the step of a Ni(111) crystal, indicating that CO dissociation takes place there. **(b)** shows the correlation between inverse particle diameter and methanation activity relative to particle mass. The correlation lines corresponding to facets, steps and kinks are drawn in and the nickel nano-particle correlation lies in between steps and kinks. Both figures are adapted from [53].

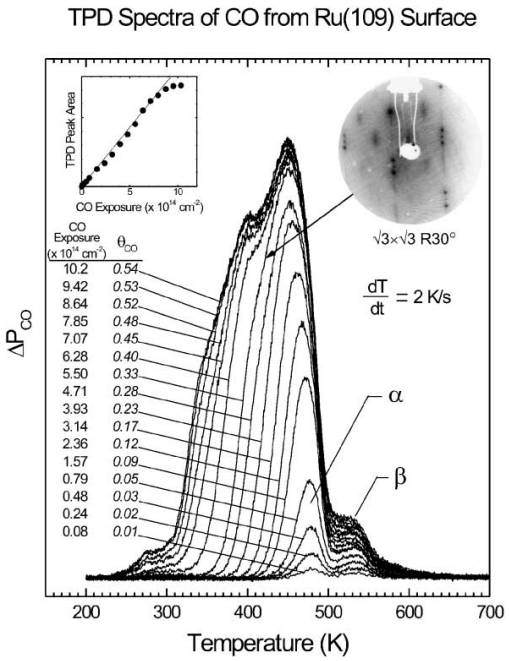

Figure 3.6: CO TPDs from the Ru(109) surface as a function of initial coverage. The α-peaks are assigned to CO desorbing from the terraces and the β-peak to that desorbing from the steps. The left inset indicate total CO exposure and the right inset is the LEED image of the $(\sqrt{3}\times\sqrt{3})R30°$ structure. Adapted from [32].

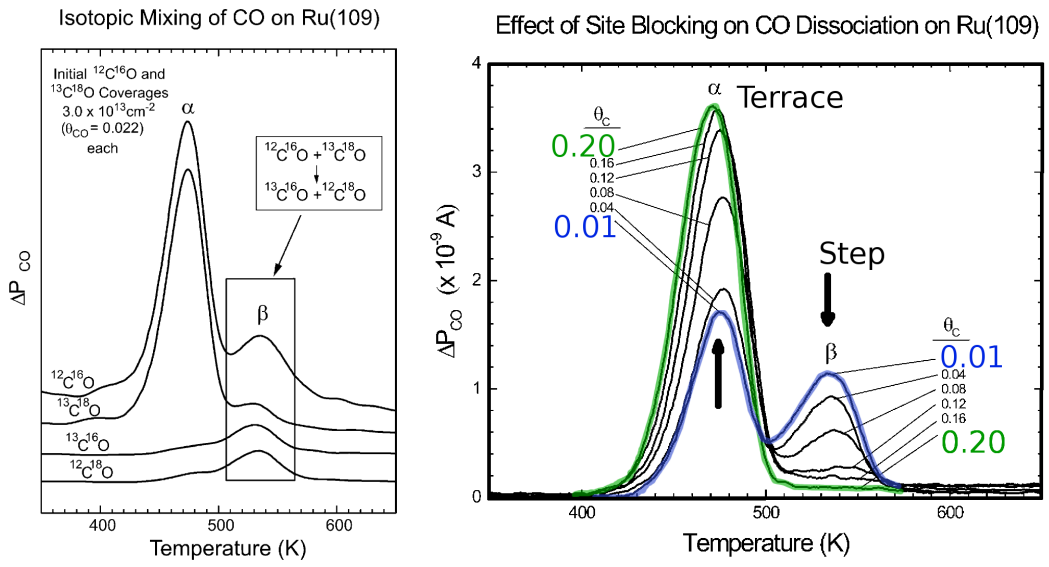

Figure 3.7: (a) shows the TPD signals of all four possible isotopologues that can be achieved after dosing $^{12}C^{16}O$ and $^{13}C^{18}O$. **(b)** shows the CO TPD results after depositing carbon on the surface. The β-peak area decrease and the α-peak area increase as the carbon coverage increase. Both figures are adapted from [32].

the low coverages the β-peak area makes up for a large portion of the total amount of CO, indicating that CO will desorb preferentially from the steps at these coverages. At some point the β-peak saturates and the α-peaks continue to grow making the relative β-peak part smaller. In order to figure out if there is a correspondence between the CO that desorbs from the different regions of the crystal and CO that has been dissociated, the authors also performed isotopic scrambling experiments. They dosed equal amounts of $^{12}C^{16}O$ (mass 28) and $^{13}C^{18}O$ (mass 31) and measured the amounts of both of these and the two mixed isotopologues[2] $^{12}C^{18}O$ (mass 30) and $^{13}C^{16}O$ (mass 29) leaving the crystal, figure 3.7(a). Apparent from this figure is, that from the terraces only the original isotopologues desorb, but in the peak that desorbs from the steps, all four are present in equal amount. This means that only the CO that desorbs from the steps have recombined from carbon and oxygen that have been able to move around and mix. Finally, to see if the dissociation of CO can be deactivated, small amounts of carbon is dosed on the surface by ethylene decomposition, figure 3.7(b), and thereafter CO is dosed up to a coverage of 0.095. The amount of CO that desorbs is approximately the same in all the curves, but the ratio of β-peak goes down and α-peak area goes up, as the deposited carbon amount increase. Finally the β-peak is gone entirely at a carbon coverage of 0.2 relative to the ruthenium atoms, indicating that dissociation sites are present in an amount less than this. This led them to conclude that CO dissociates at the steps and associatively desorbs also from the steps at around 530 K.

[2]The original articles says "isotopomers", but that means molecules with the same composition that differs only in their structure. Whereas "isotopologue" means molecules that differ only due to their isotope compositions, which must be the correct term here.

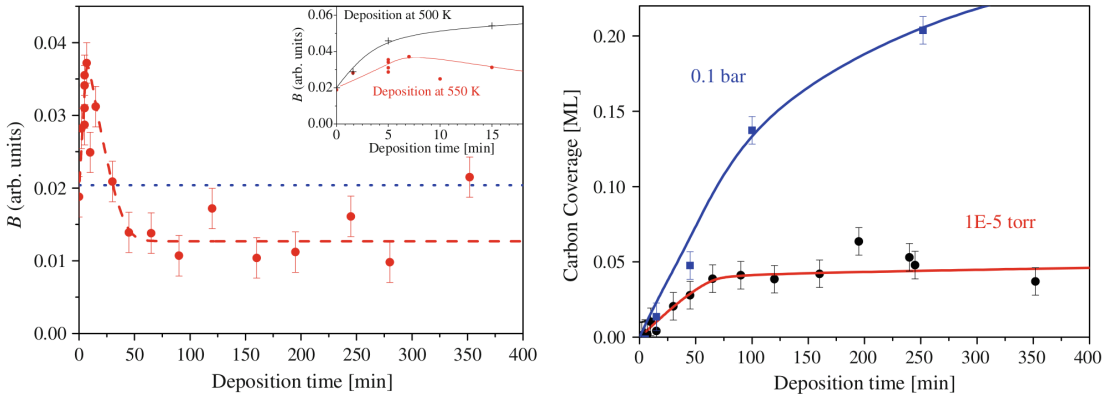

Figure 3.8: Figure **(a)** shows the β-peak area as a function of carbon deposition time at 550 K. The area increase from 2% to ~4% and the decrease to less than 2%. The inset shows both the curves for deposition at 550 K and 500 K and it is seen that carbon uptake leading to blocking is less in the 500 K case. Figure **(b)** shows the carbon update both for the UHV experiments and for high pressure experiments. At UHV the carbon increase is nearly linear up to 4% and then levels out. At high pressures it continue to grow. Both figures are adapted from [33].

Vendelbo *et al.* investigated this further. In an elaborate set of experiments, supported by DFT calculations, the amount of CO dissociated at the steps was studied as an effect of blocking of the steps with carbon from dissociated CO. These experiments were carried out on a vicinal Ru(0 1 54) single crystal which has about 4% steps on the surface and two different step configurations (more about that in section 3.2). The experiments consisted of four steps and started out with quantifying the amount of step sites, from which CO could desorb, by use of a CO TPD. Then followed a carbon deposition step, where the sample was exposed to 10^{-5} Torr of CO at 500 K or 550 K (which is above the dissociation temperature) for a variable amount of time. After this a second TPD was made, to once again quantify the amount of step sites from which CO could desorb and finally the amount of carbon on the surface was quantified by oxygen titration. The ratio of the β-peak area in the second TPD to the total area of the first TPD, as a function of deposition time, is shown in figure 3.8(a). Figure 3.8(b) shows the amount of carbon on the surface as quantified by oxygen titration[3]. As the amount of deposited carbon increase, the β-peak area starts at around 2%, then increase to about 4% and then decrease to a constant level lower than the start value. At the same time the amount of deposited carbon is seen to increase nearly linearly while the β-peak area changes and then level out at roughly the same time as the β-peak area levels out. The starting value of 2% for the β-peak area suggest, that only one of the step configurations, which is present in exactly this amount, is involved in the CO dissociation at this point. It is speculated that the increase in the β-peak area might be due to a surface roughening, possible a CO induced reconstruction that creates more steps sites with the appropriate configuration. The correspondence between the deposition time where

[3]Performed by exposing the sample to 1.8×10^{-6} Torr oxygen at 550 K

the two graphs level out, which is at 4% carbon coverage, the same as the total step density, shows that the steps can be blocked with carbon in the same amount and shows that CO dissociates at the steps and stays there and blocks them from facilitating further CO dissociation. The second line in figure 3.8(b) is the carbon uptake in a set of similar experiments, but where the carbon deposition was done at high pressures, and from this curve it is apparent, that at high pressures CO will continue to dissociate even beyond the 4% coverage point. In summary this work also strongly supports that idea that CO dissociation is structure sensitive and even suggest that only one of the two kinds of steps sites present on the Ru(0 1 54) surface is active for the reaction under these conditions. Furthermore, it also shows that CO dissociation can be self-blocked by carbon deposition from CO dissociation[33]. Vendelbo *et al.* also continued to present results that strongly supports the idea that also the methanation reaction is structure sensitive on ruthenium[55].

As it is apparent from the literature results presented above, the question of the structure sensitivity of CO dissociation and methanation is not fully clarified with studies evidencing a strong influence of step sites and others suggesting insensitivity. Several authors have suggested, that the explanation for this apparent conflict is, that these reactions are in fact so structure sensitive that the reaction takes place only on few very active sites. This means that if these special sites are present in comparable amounts, even on different surfaces, then they will dominate the reaction producing similar activities and it will then appear as is the reactions are structure insensitive[53, 55, 56].

It should be mentioned in this context, that it has previously been shown that other reactions are extremely structure sensitive on ruthenium surfaces. In the work of Dahl *et al.* already mentioned in chapter 1, it was demonstrated that the step sites are more than nine orders of magnitude more active for ammonia synthesis than the terrace sites in a Ru(001) crystal. In DFT calculations in this work it was also revealed that a special site, referred to as the B5 site, has a significantly higher activity than the rest of the sites[10, 57]. In later work these conclusion was also extended to supported nanoparticles, work that lead to the identification of the ideal particles size[58].

The purpose of the present study is to observe the results of CO dissociation by STM and from these observations gain insight into the mechanisms at play. In particular, we wish to address the question of structure sensitivity with this approach thus hopefully shedding further light on the matter. Since in particular the under-coordinated sites at steps and kinks are suspected of being the active sites, we will devote special attention to those regions. By the choice of a sample that has alternating steps with two different step configurations separated by closed packed terraces (described in more detail in the next section), of which one of these configuration is the B5 site, we hope to be able to tell whether there is a difference in activity between these two configurations. We will also make use of DFT calculations and simulated STM images based on DFT calculations to help in the interpretation of the results. Finally we will relate some of our measurements to structure vs. reactivity measurements on other kinds of samples to see if it possible to draw lines in trends between the different structures.

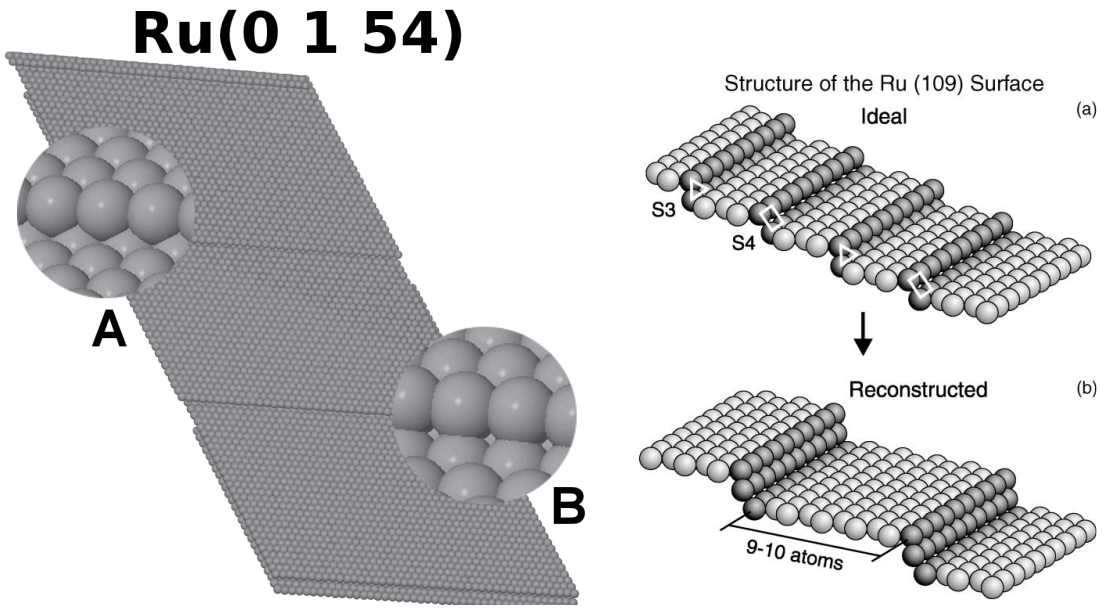

(a) (b)

Figure 3.9: Figure **(a)** is a ball model illustration of the Ru(0 1 54) surface used in the experiments in this report. The steps are in average 27 atomic rows apart. The magnifications show the two different step configurations. The figure is from included article I. **(b)** shows a ball model of the Ru(109) surface, adapted from ref [32], which also has the same alternating step configuration as the Ru(0 1 54) surface and the reconstruction that makes the alternating steps disappear.

3.2 The sample

Keeping the experimental purpose outlined in the previous section in mind, it is desirable to get at sample that allows for the investigation of different steps between otherwise closed packed surfaces. The higher the amount of steps the easier it is to see the effects of them in averaging techniques, however it is also important that the steps are far enough apart to ensure that events on one step does not affect the next one. To meet these requirements a vicinal Ru(0 1 54) crystal was bought from Mateck, GmbH. A ball model of this surface is shown in figure 3.9(a). This surface consist on average of 27 atom rows wide closed packed terraces ($\sim$6.3 nm wide) separated by mono-atomic steps. The steps alternate between two different configurations, as highlighted in the figure. Step type A has a three-fold symmetry and are sometimes referred to as triangle steps, whereas step type B has four-fold symmetry and are sometimes referred to as square steps.

The parameters previously mentioned for the desired sample, would also be fulfilled by the Ru(109) sample that Zubkov and co-workers worked with. But in this case the surface reconstructed as shown in figure 3.9(b)[32]. With this reconstruction the difference between the steps disappear, and it is therefore no longer possible to study different steps, nor of course to study mono-atomic steps. Figure 3.10(a) shows a set of images of the clean Ru(0 1 54) surface from our studies. On the left is a $50\times50\,\mathrm{nm}^2$

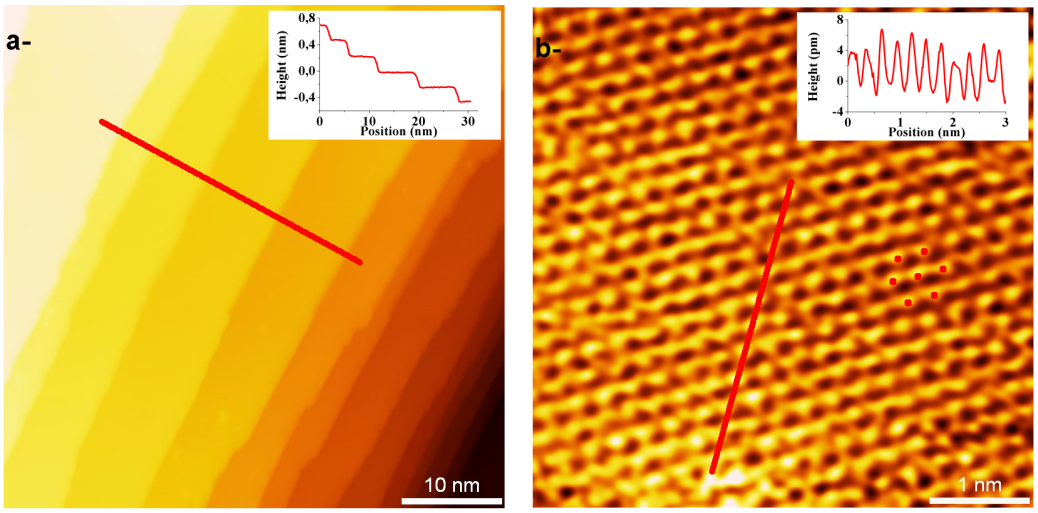

(a) $50\times50\,\mathrm{nm}^2$ **(b)** $5\times5\,\mathrm{nm}^2$

Figure 3.10: (a) is an STM image of the clean surface, plane corrected so that each terrace is level. The image parameters are 0.020 V and 1.01 nA. The inset presents a line profile illustrating a step height of 0.21±0.01 nm. **(b)** is an STM image of the Ru(0 1 54) surface with atomic resolution. The image parameters are 0.010 V and 2.42 nA. The inset shows a line profile along the red line and the red dots are inserted to highlight the hexagonal structure. Both figures are from included article I.

image showing the general structure. The inset is a line profile taken at the red line, from which the step heights are measured to 0.21±0.01 nm. This value is consistent with the bulk plane distance of 0.214 nm and hence these are mono-atomic steps. The terrace widths vary between 4 nm and 10 nm also consistent with the expected average value of 6.3 nm. The image in figure 3.10(b) shows an atomically resolved images of the surface, confirming the expected closed packed structure.

3.3 Cleaning the sample

3.3.1 Cleaning procedure and XPS checks

Due to its high reactivity cleaning ruthenium can be troublesome. The standard procedure is sputtering, oxidation of carbon species and a flash anneal to get rid of the excess oxygen. Unfortunately our setup does not allow us to reach as high temperatures as is necessary to desorb all of the oxygen, both due to the use of K-type thermocouple and due to the capacity of the electron bombardment heater. Therefore it was necessary to add an extra step to the cleaning cycle (illustrated in figure 3.11(a)), which all in all consist of the following:

- 1 keV, Ar^+ ion sputtering at an argon pressure of 2×10^{-7} Torr, 800 K for 30 min

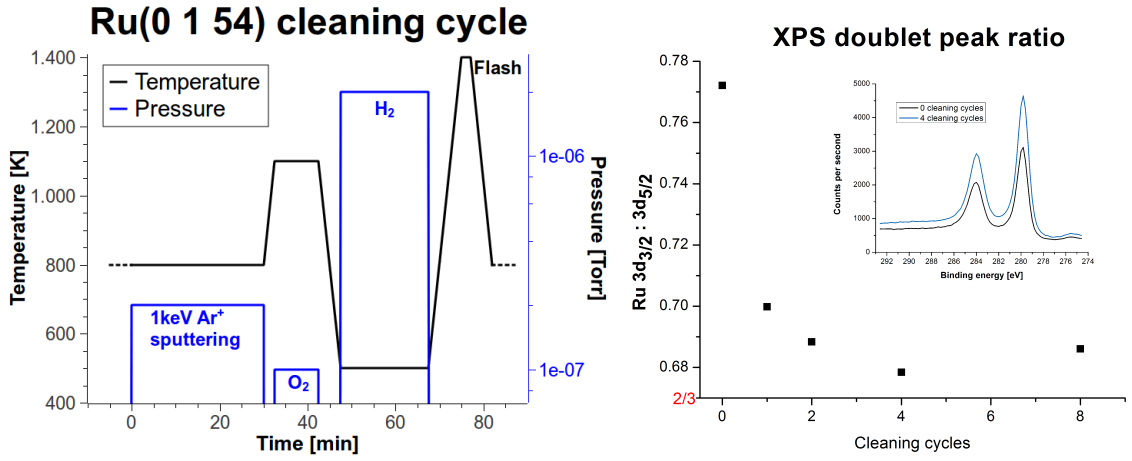

(a) (b)

Figure 3.11: **(a)** illustrates the cleaning procedure for the Ru(0 1 54) sample as described in the text. **(b)** shows the evolution in the Ru $3d$ doublet ratio as a function of number of cleaning cycles. The closer this ration gets to 2/3 the less carbon is present on the sample. The inset shows the raw graphs for the ruthenium curves with the highest and the lowest carbon content.

- Oxidation of carbon species with 1×10^{-7} Torr O_2 at 1100 K for 10 min
- Reduction of excess oxygen with 2×10^{-6} Torr H_2 at 500 K for 20 min
- Flash anneal to 1400 K for 2 min

By far the most problematic part of the cleaning is to get rid of carbon species on the surface. One of the possible sources of carbon species is as a pollutant in the hydrogen that is used during the cleaning cycle. To prevent this, the hydrogen is cleaned by passing it through a palladium/silver membrane. This membrane allows only hydrogen to pass through and any other species are caught on the surface. As described in section 2.4.5 it is possible to get a rough estimate of how clean of carbon the surface is by examining the Ru $3d$ doublet ratio. This is the case since the Ru $3d_{5/2}$ contains the carbon $1s$ peak and it will therefore disturb the ratio away from its theoretical value of 2:3. Figure 3.11(b) shows the evolution of this peak ratio after a bake out, where the sample has been exposed to normal atmosphere while the chamber was opened and chamber atmosphere at elevated pressures during the bake out. The graph shows that getting the carbon concentration low takes many cycles, in fact, after a bake out it will generally require somewhere between 30 and 40 cleaning cycles before it is clean. The accuracy of this method of evaluating carbon cleanliness is however limited and therefore after this method no longer shows any carbon, the cleanliness has to be confirmed by STM.

Besides carbon, which is by far the most predominant possible impurity source, we also checked thoroughly for nickel, to make sure that we did not form any nickel carbonyl with CO in the stainless steel gas tubing. In none of the spectra was there any indication of any nickel present (data not shown). Besides the "expected" impurity sources, which was checked for with spectra with high resolution and statistics, we also made broad scans to look for any other impurities (figure 3.12). As it can

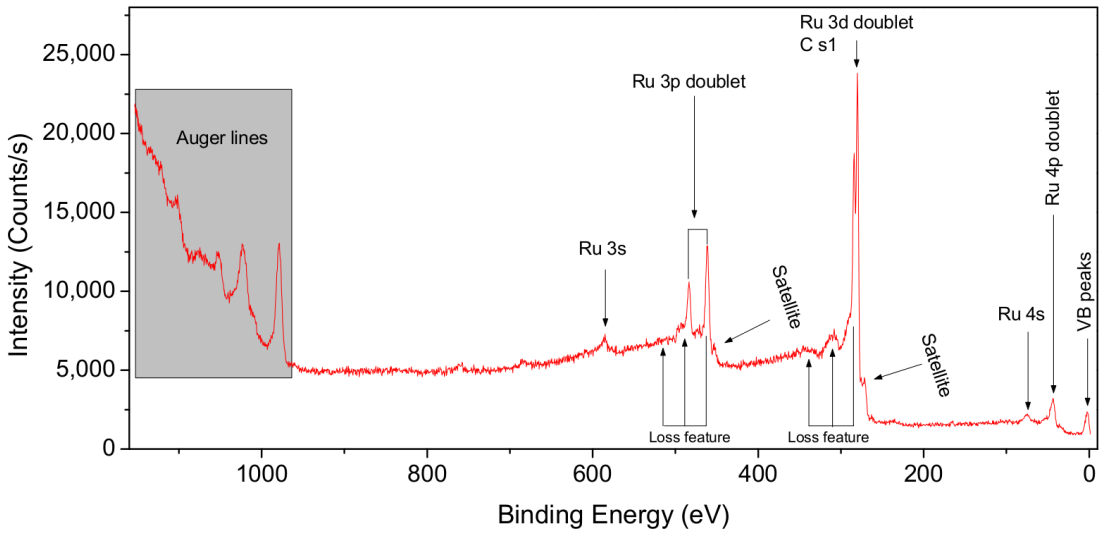

Figure 3.12: An XPS overview spectrum of the Ru(0 1 54) sample. The main singlet and doublet peaks, their energy loss features, satellites and Auger peaks are all marked. Adapted from [59].

be seen from the figure, the majority of the peaks are accounted for as either energy levels peaks or artifacts (as described in section 2.4.2) from ruthenium. It consist of the main singlet and doublet lines of ruthenium, where the Ru $3d_{3/2}$ peak overlaps with the C $1s$ peak as described earlier. Besides that, there are also two energy loss features originating from surfaces plasmons at slightly higher values than the primary peaks. There is also a satellite peak originating form the α_3 X-rays located around 8 eV below the primary peaks and a set of Auger peaks at high apparent binding energies. Besides the ruthenium related peaks there are two very small peaks at ∼682 eV and ∼758 eV that are difficult to interpret. The closest match to the peak at 682 eV is the F $1s$ peak located at 684.9 eV[25], but that is almost 3 eV of and we have no reason to suspect the presence of fluorine. The second peak at 758 eV does not correspond to any peaks in the reference material[25, 26] and it is possible that this peak, or both of them, are some kind of artifact.

3.3.2 Graphene overlayers

In the early stages of cleaning, or in the case where there are impurities of carbon species in one of the gasses used during cleaning, there can be enough carbon on the Ru(0 1 54) surface to form graphene layers. As seen in figure 3.13, these graphene overlayers form a large super-structure known as a moiré pattern. The moiré patterns on the closed packed ruthenium surfaces are formed as a superposition of the distance from 12 times the bulk lattice spacing of graphite (12×0.246 nm=2.95 nm) and the distance from 11 times the inter-atomic distance on the ruthenium surface (11×0.271 nm=2.98 nm)[48]. This length corresponds nicely with the observed periodicities, all-though the patterns are not always completely regular, possible due to interruption from the steps that are always near by.

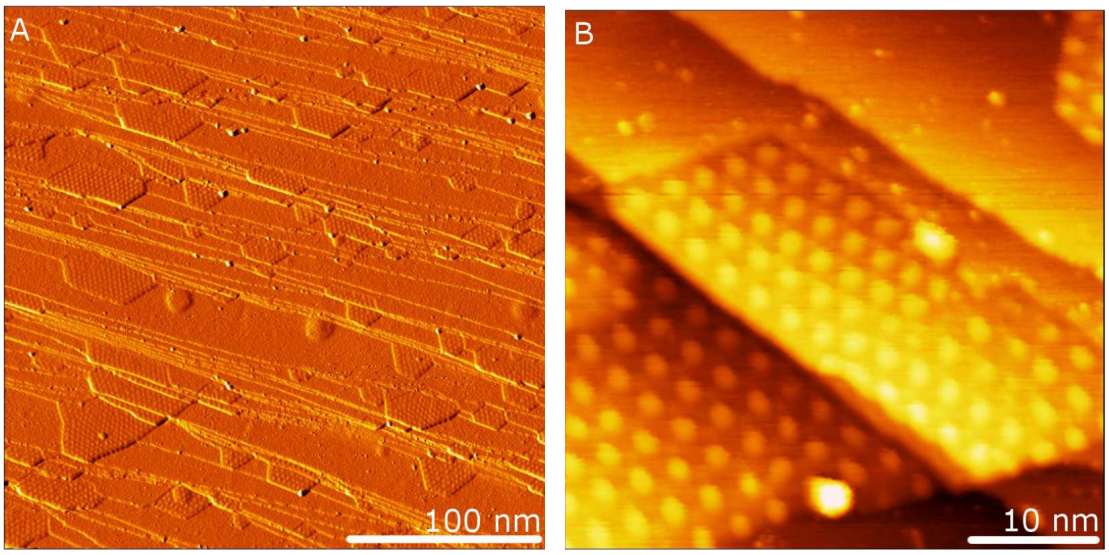

(a) $276 \times 276\,\mathrm{nm}^2$ **(b)** $42 \times 42\,\mathrm{nm}^2$

Figure 3.13: (a) is a gradient overview STM image of the Ru(0 1 54) surface covered partially by graphene overlayers. Image parameters are 0.508 V and 0.08 nA. **(b)** is an STM images that shows the moiré pattern that graphene forms with the ruthenium substrate. Image parameters are 0.106 V and 0.05 nA. Both images are adapted form [59].

3.3.3 Sub-surface argon bubbles

Sub-surface argon bubbles is a phenomenon that is formed, when several hundreds of argon atoms[39] get trapped in a pocket below the surface. This causes the surface to bulge up and form a protrusion, roughly 5-10 nm in diameter[39, 42]. This is consistent with our observations from images such as the ones in figure 3.14 and it is therefore concluded that when we see protrusions like this on the surface it is due to such bubbles. It has previously been shown that such protrusion will stretch the periodicity of the lattice on top of it and compress it at the rim. This will alter the reactivity of the surface[39, 42] in correspondence with the expectations from d-band theory applied to stretched or compressed lattices[9]. Since it is our intention to study the activity of sites with special reactivity at steps, compared to the terrace steps it is obviously not desirable to have other sites present with an altered reactivity compared to the normal terrace sites, especially not if the alteration is large. In order to minimize the amount of such argon bubbles, the sputtering angle has been adjusted until the concentration was reasonably low. For microscopy the precautions above are sufficient, since due to the low coverage it is possible to simply ensure that the imaged region does not contain any bubbles, since it is known that the distortions relaxes after about 1-2 nm[39] this should ensure that the effects observed in these regions are not affected. For the averaging techniques however, it will be necessary to have an estimate of how large the changes in reactivity is at these bubbles. In references [39, 42] it is reported that the expansions on top of such bubbles and the compression right next to them are less than 3%. We measure a compression of ∼6% and a expansion of ∼11% of the CO overlayer on top of the protrusions. Taking

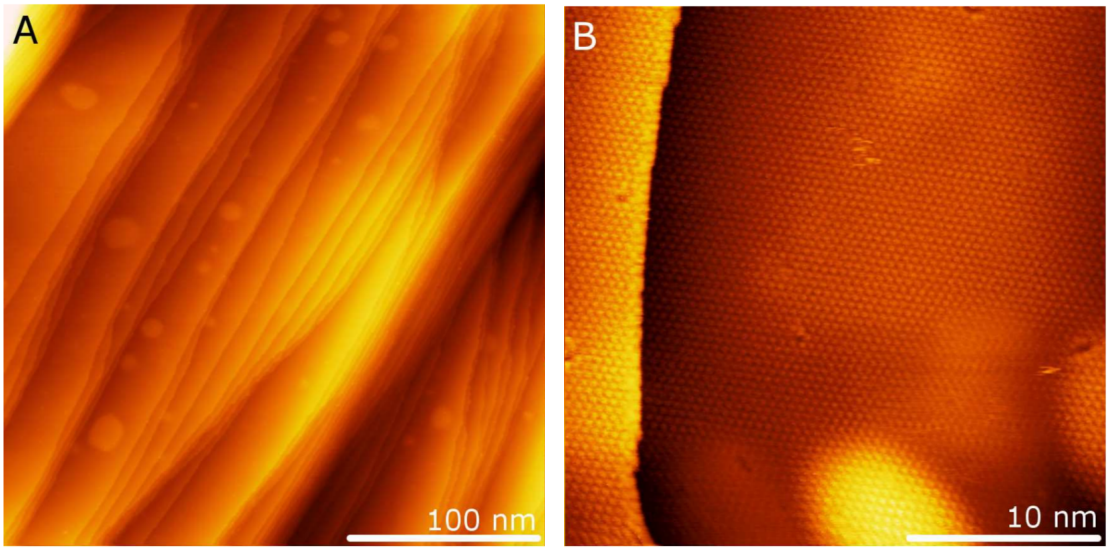

(a) 275×275 nm^2 **(b)** 28×28 nm^2

Figure 3.14: **(a)** is an overview STM image that shows protrusion on several steps in the otherwise clean surface. Image parameters are 0.020 V and 0.49nA. **(b)** is a zoom in on one of the protrusions. Image parameters are 0.038 V and 1.16 nA. These protrusions are assigned to sub-surface argon bubbles. Adapted from [59].

into consideration that the top of the CO molecule is located at least 0.31 nm above the surface (0.11 nm C-O bond length[9] and 0.20 nm Ru-C bond length[36]) and the fact that the height of the bubbles are around 0.3-0.4 nm there is bound to be a significant over-estimation of both the expansion and the compression when they are measured on top of the CO, which mean that as large upper estimates these correspond roughly with literature value. In reference [9] the change in transition state energy during CO dissociation was calculated by DFT to be about 0.15 eV per % expansion of the lattice, leading thus to an upper estimate for the changes in CO dissociation energy of 0.45 eV (for the 3% literature value). In reference [33] the difference in activation energy of CO dissociation between the terrace and the steps was calculated also by DFT to be about 1 eV. Taking these numbers, the exponential dependence of the reaction rate on the activation energy and the lower concentration of bubble sites as compared to steps sites into account, we estimate that the influence on averaging techniques will be negligible.

After, in the previous sections, having gone through the literature, described the sample and how to prepare it, the next sections will present the results, relate them to theory and discuss them in connection with literature.

3.4 CO dose while cooling after TPD

The experiments in this and the following two sections are all centered around the purpose of trying to identify the active site for CO dissociation on the Ru(0 1 54)

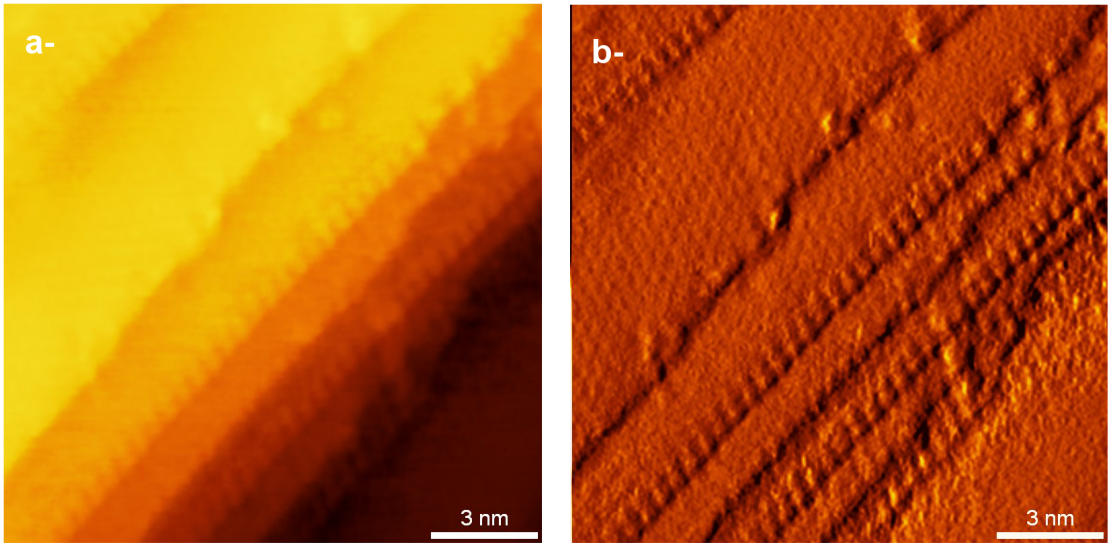

(a) $20\times20\,\mathrm{nm}^2$ **(b)** $20\times20\,\mathrm{nm}^2$

Figure 3.15: (a) is an STM image taken after a CO TPD. Image parameters are 0.020 V and 1.07 nA. **(b)** is a gradient version of **(a)** which makes it easier to observe the features at the steps and on the terraces. Both images are from included article I.

surface by means of STM. The section contain results obtained after different experimental sample preparations.

The following STM images was obtained on the sample, after it had been exposed to the remaining pressure of CO, that was present in the chamber after a TPD and at the varying temperatures the sample was at, when cooling down after a TPD. In figure 3.15(a) it is possible to identify a kind of decoration on the steps, that is not there on a clean surface. Making a gradient version of this image (figure 3.15(b)) they become much easier to distinguish. It is observed, that the top of every other step is decorated with a periodic striped pattern, which in the following will be referred to as "fingers" (because they look a bit like fingers grabbing a hold of the edge). The distance between these fingers was measured to $0.55\pm0.05\,\mathrm{nm}$. Also apparent from the gradient image is a faint pattern on the terraces with a smaller periodicity than the distance between the fingers. The pattern is regular and hexagonal with a periodicity of $0.47\pm0.03\,\mathrm{nm}$.

Figure 3.16 show STM images of two different regions of the surface after this treatment. In figure 3.16(a) once again the fingers are observed on top of every other step, highlighted in the images by the green dots. In figure 3.16(b) they are also present but in this case they extend into the terraces forming a hexagonal pattern with the same periodicity, likewise highlighted by green dots. In both images a faint periodicity is observed on the rest of the terraces, highlighted by blue dots. While these first results are very interesting, it is unfortunate that the experimental conditions, namely the CO pressure the surface is exposed to and the temperatures of exposure, are not well defined. The experiments in the next sections are designed to remedy that.

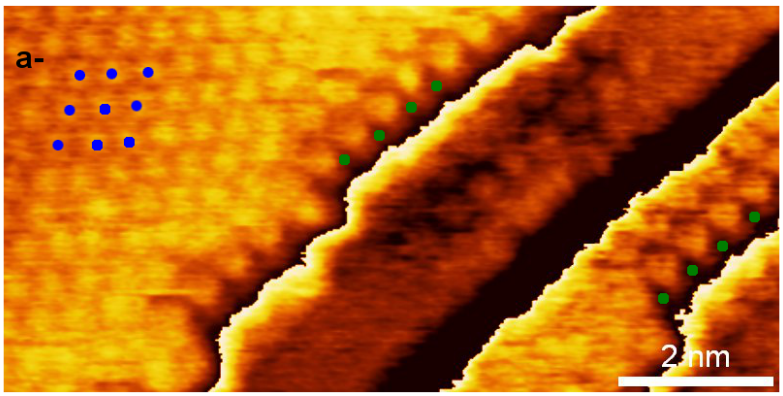

(a) $10\times5\,\mathrm{nm}^2$

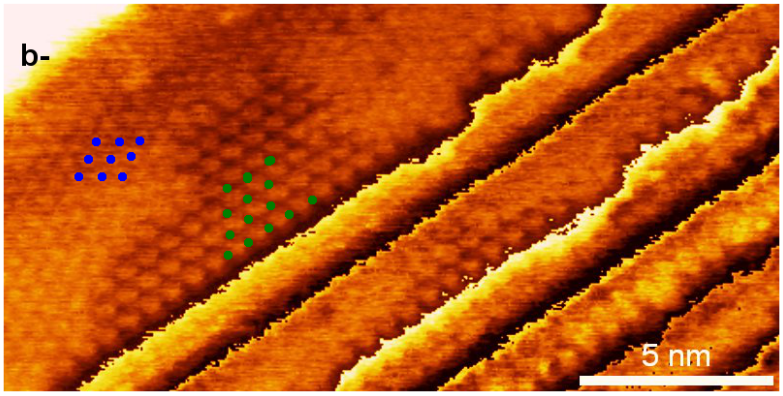

(b) $20\times10\,\mathrm{nm}^2$

Figure 3.16: STM images of two different regions of the surface obtained after a CO TPD. Image parameters are 0.020 V and 3 nA for **(a)** and 0.022 V and 3 nA for **(b)**. Both images show the fingers at every other step highlighted in **(a)** with green dots, and in the **(b)** the fingers extend into the terrace into a hexagonal pattern, likewise highlighted with green dots. Both images also show a hexagonal pattern on the terraces highlighted with blue dots. A periodic color scale has been used in order to highlight the periodicities on several terraces without making a gradient image. Both images are from included article I.

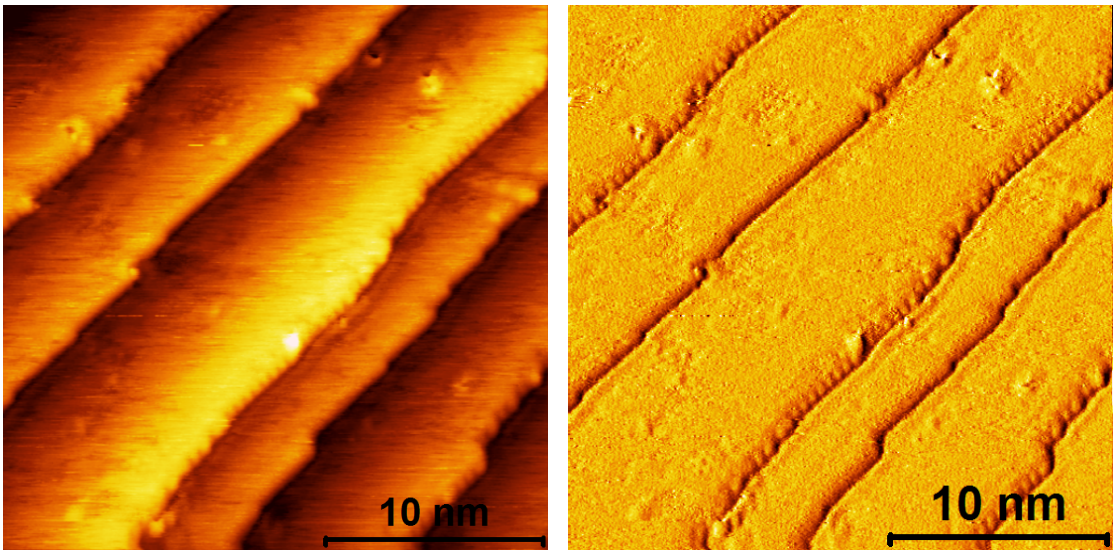

(a) $25 \times 25\,\mathrm{nm}^2$ **(b)** $25 \times 25\,\mathrm{nm}^2$

Figure 3.17: STM images of the surface after cooling the sample at a fixed pressure of CO. Image parameters are 0.052 V and 0.53 nA.

3.5 CO dose at constant pressure

In these experiments, instead of exposing the sample to the CO pressure present in the chamber after a TPD, the temperature of the sample was raised and then lowered along a cooling ramp in 8×10^{-8} Torr of CO from 700 K to 400 K (roughly 1000 s). An example STM image of the surface after such a treatment is shown in figure 3.17. Once again, the fingers are observed on every other step, especially visible in the gradient image (figure 3.17(b)), thus confirming that we can recreate them under more controlled CO pressures. It should however be noted, that in none of the images we obtained with this procedure, did we see the fingers extend into the terrace like in the previous experiments. Since we suspect that the step decoration originates from dissociation of CO, it is also interesting to determine the temperature dependence of the formation of these structures. This is the subject of the next section.

3.6 CO dose at constant temperature and pressure

These experiments were performed by exposing the clean crystal to a fixed dose of CO at different fixed temperatures. The dosing temperature was varied in 50 K intervals between 400 K and 600 K. At this specific temperature the sample was exposed to 10^{-7} Torr of CO for 100 s, corresponding to a dose of 10 L. After this the sample was cooled to 400 K at which temperature it was exposed to another 10 L of CO at the same pressure. The purpose of the last dose is to make sure that the surface is covered with CO in the $(\sqrt{3} \times \sqrt{3})R30°$ structure.

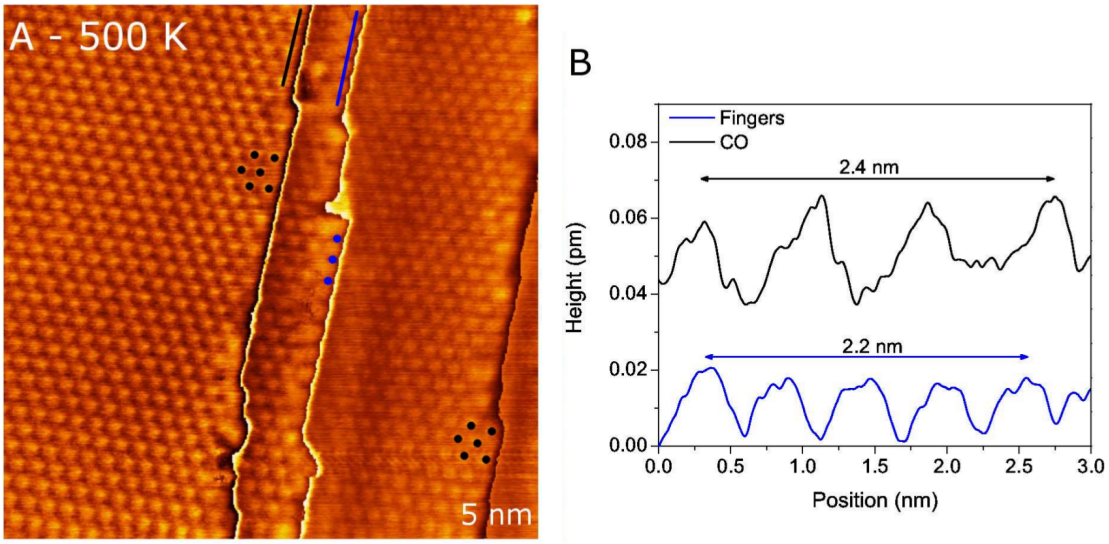

(a) $14\times14\,\mathrm{nm}^2$ **(b)**

Figure 3.18: (a) is an STM image of the surface where the first 10 L dose was performed at 500 K. The fingers are highlighted by blue dots and the structure on the terraces by black dots. Image parameters are 0.038 V and 1.09 nA. In figure **(b)** line profiles are shown from along the blue and black lines in **(a)**. Both figures are adapted from [59].

Figure 3.18(a) shows an example image of the surface, as it looks when the first 10 L CO dose is performed at 500 K. In this image once again the fingers can be observed on the top of every other step and a structure with a smaller periodicity on the terraces. Figure 3.18(b) shows a line profile from each of the two kinds of steps. Along the black line where no fingers are observed, the periodicity at the step is measured to $\frac{2.4\,\mathrm{nm}}{3} = 0.80\,\mathrm{nm}$. This value corresponds very well with the distance between the two next nearest neighbors in the $(\sqrt{3}\times\sqrt{3})R30°$ structure, which is $\sqrt{3}\sqrt{3}\cdot 0.27\,\mathrm{nm} = 0.81\,\mathrm{nm}$. Along the blue line, where the fingers are observed, the periodicity is measured to $\frac{2.2\,\mathrm{nm}}{4} = 0.55\,\mathrm{nm}$, which is very close to two times the inter-atomic distance on the (001) surfaces ($2\times 0.27\,\mathrm{nm} = 0.54\,\mathrm{nm}$).

Figure 3.19 shows STM images of the surface as it looks after the first CO dose has been performed at the four other temperatures in the range, i.e. 400 K, 450 K, 550 K and 600 K. In none of the images was there any indication of oxygen fingers on top of any steps and only the structure on the terraces is visible.

In the experiments presented in this section, and the last two, a lot of the same structures are observed. In the next sections it will be attempted to determine what they represent by comparing their appearance to literature and to theoretical calculations.

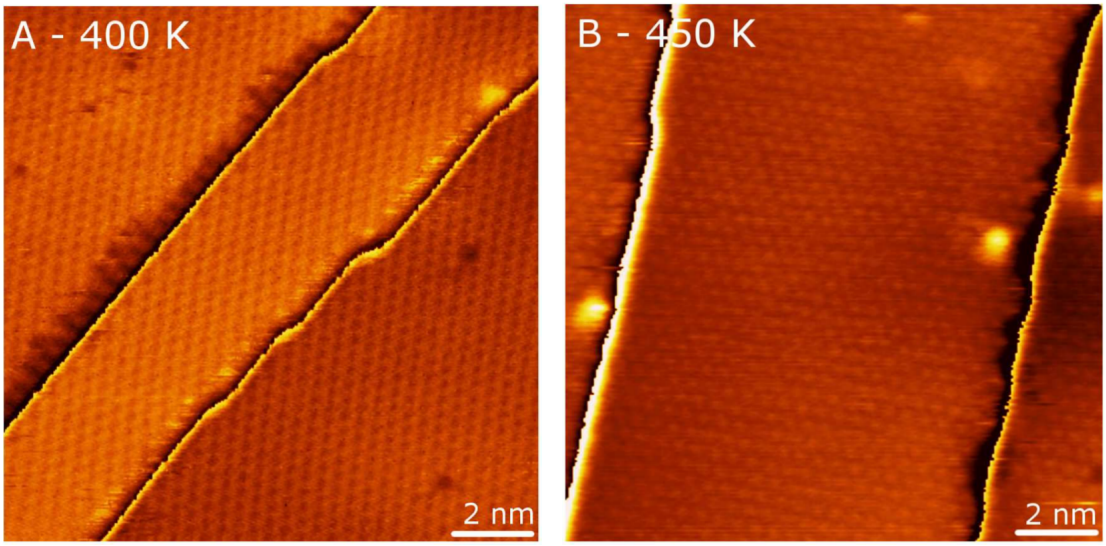

(a) $14 \times 14\,\mathrm{nm}^2$ (b) $14 \times 14\,\mathrm{nm}^2$

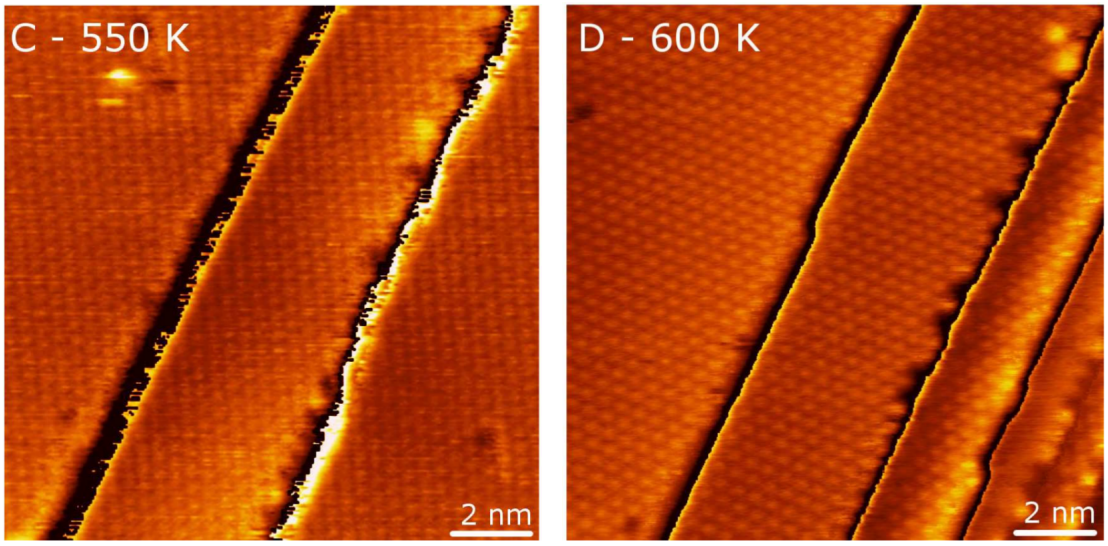

(c) $14 \times 14\,\mathrm{nm}^2$ (d) $14 \times 14\,\mathrm{nm}^2$

Figure 3.19: Images of the surface after a first CO dose at the four other temperatures in the range. The temperatures and the images parameters are: **(a)** 400 K, 0.045 V and 0.88 nA. **(b)** 450 K, 0.030 V and 1.01 nA. **(c)** 550 K, 0.046 V and 1.06 nA. **(d)** 600 K, 0.048 V and 0.09 nA. Adapted from [59].

3.7 Assignment of the observed features

From the images in the previous sections a pattern emerge. On the terraces a regular hexagonal patterns is observed that has a periodicity of 0.47±0.03 nm. On the top of every other step the finger pattern is observed. The spacing between the fingers is 0.55±0.05 nm. In some occasions the finger structures at the steps extend into the terrace and in this case it forms a regular hexagonal pattern with a periodicity of 0.55 nm. To identify these structures we look back at the literature presented in the introduction.

The first most natural thing to look for is CO, since it is dosed. CO is known from several sources[37, 38, 39] to form a $(\sqrt{3} \times \sqrt{3})R30°$ overlayer structure at coverages below 0.33 ML. The length of the unit cell vector is $\sqrt{3} \times 0.27\,\text{nm} = 0.47\,\text{nm}$, which is exactly the size measured for the periodicity on the terraces. The coverage is determined from TPDs. The black curve in figure 3.20, which is a regular TPD after a saturation dose of CO, has the same main features as reported in literature. The two peaks originating from molecular CO desorption has maxima around 430 K and 490 K and the re-association shoulder lie between 550 K and 600 K. These values are higher then those values reported in literature due to a diffusion induced temperature gradient between the temperature probe and the sample surface in our setup, that we have been unable to get rid of. It does however, not affect the constant temperature measurements nor does it affect the comparison of intensities between different TPDs. From the red curve in figure 3.20, which is an example of a second TPD, we can estimate the amount of CO present on the surface at these conditions, by comparing it to the black curve. The area of the second TPD is roughly 0.22 the area of the first TPD (from a saturated surface) which corresponds to 0.58 ML. This means that the coverage must be about $0.22 \times 0.58\,\text{ML} = 0.13\,\text{ML}$. The blue curve in figure 3.20 is an example of a TPD after a constant pressure CO dose while cooling the crystal down. Relating the area of this TPD to the full TPD a coverage of around 0.36 ML is found. This means that both of these coverages, within measuring uncertainty, are in the range where CO is know to form the $(\sqrt{3} \times \sqrt{3})R30°$ structure, which is also confirmed by the fact that only the high temperature α-peak is visible. Furthermore, comparing the unit cell from these terrace structures with the clean atomically resolved Ru(0 1 54) surface, we see that the terrace structure is in fact rotated by 30°. Summing up, the following is known:

- The surface will be exposed to CO at temperatures where it can be adsorbed as molecular CO, due to the remaining pressure of CO in the chamber after a CO TPD or during a fixed dose of CO in the "cooling in CO" or "constant temperature" experiments
- For the "after TPD" experiments the coverage has to be somewhat lower than saturation coverage, since only a fraction of the CO that desorbs during a TPD (which is exactly a saturated overlayer) will re-adsorb. For this type of experiment the coverage is measured to about 0.13 ML. For the "cooling in CO" experiments the coverage was measured to 0.36 ML.
- Both the periodicity, the rotation and the coverage is consistent with a $(\sqrt{3} \times \sqrt{3})R30°$ overlayer structure

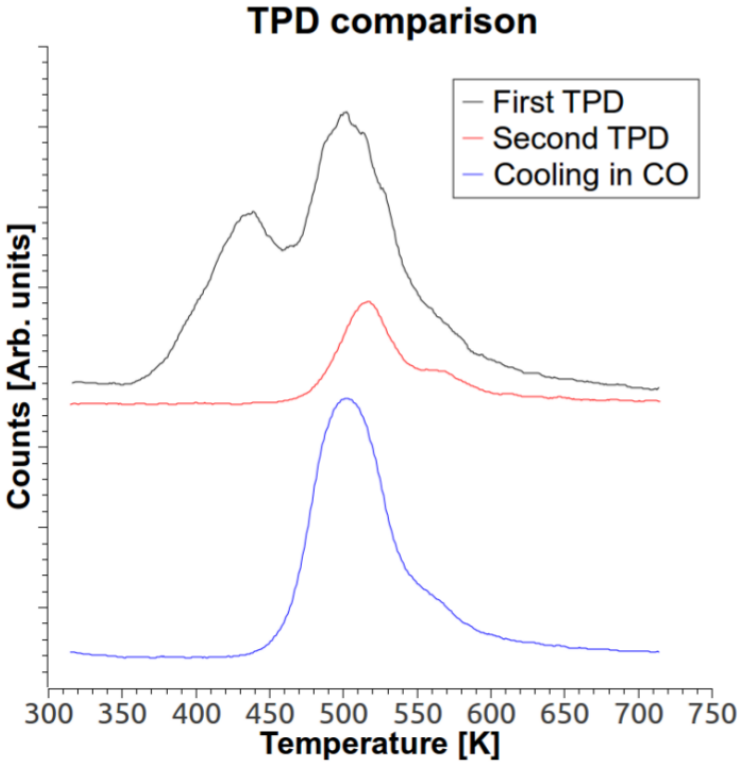

Figure 3.20: The black curve is a CO TPD taken after a 20 L dose of CO at 310 K. The red curve is a second TPD taken immediately after the first without adding any CO to the chamber. The blue curve shows the CO TPD obtained after an exposure to 8×10^{-8} Torr CO between 700 K and 400 K (section 3.5). Figure is from supplementary material for included article I.

- No other species that we might expect to be present on the surface is known to form the $(\sqrt{3} \times \sqrt{3})R30°$ overlayer structure

From these observations we assign the hexagonal 0.47 nm structure on the terraces to molecularly adsorbed CO.

The next step is to look at the possible dissociation species. From literature[41] it is known that oxygen is supposed to be very mobile on the surface at low coverages, and only be imaged in STM as dashes in the scanning direction, with two notable exceptions. 1) Oxygen atoms coming into close vicinity on the terraces can form a cluster adopting a p(2×2) structure, occupying the 3-fold hollow hcp-sites[39, 40, 42]. 2) Oxygen atoms that comes into vicinity of a step may occupy the 3-fold hollow hcp-sites right next to the steps and form a line of oxygen atoms with a distance of 2 times the inter-atomic ruthenium distance[41, 43, 44]. Due to these observations, we propose that the ×2 structure we observe at the steps and the p(2×2) structure we observe extending from the steps, are due to atomic oxygen adsorbed in the 3-fold hollow sites. Since no oxygen was present on the surface before the CO doses, we hypothesize that it comes from dissociated CO. It should be noted, that we do not observe any mobile oxygen on the surface, in the form of dashes in the STM images, but that was also only observed with a low coverage of oxygen and nothing else present. It is very likely, that the CO overlayer that was either formed before or after the CO dissociation, either keeps the oxygen in the place where it was dissociated or pushes oxygen around on the terraces until they form a cluster or a line at the steps.

Having identified the finger structure as oxygen, it is important to discuss the fate of the carbon atoms. Sufficient amounts of carbon is known to form graphene[47, 48] but no periodicity is observed that indicates that this is the case. From oxygen titration experiments, like the one presented in figure 3.21, it is confirmed that there is carbon on the surface in the amount of 0.014-0.020 ML. This is similar to the observations made by Vendelbo *et al.* for the same kind of surface[33], and in this case that carbon was attributed to CO dissociating at the steps. If the carbon that originates from dissociated CO at the steps, is left at the bottom of the step and stays there, due to the CO layer blocking the terrace, it is very likely that we will not observe it due to tip convolution effects.

The oxygen fingers are only observed on every other step and the carbon coverage found by oxygen titration is also close to the coverage of one kind of step (total step density is 4%, for one kind of step it is 2%). Both of these observations points to, that the dissociation of CO only takes place at one kind of step, but it has still not been shown which of the two step configuration it takes place at. Revisiting the geometric model for this surface, it is found that it should in principle be possible to distinguish between the different kinds of steps by observations on the CO overlayer as follows. The distance d between lines of nearest neighbor atoms in a closed packed surface with nearest neighbor distance s is given by $d = \sqrt{3}/2 \cdot s = \sqrt{3}/2 \cdot 0.271\,\text{nm} = 0.235\,\text{nm}$. Due to the stacking order of the ruthenium crystal, there is a difference between the distance between rows of atoms, measured in parallel with the terraces, when crossing a step, as illustrated in figure 3.22(a). When going down an A-step the rows on the lower terrace should be translated by $\frac{1}{3}d$ and when going down a B-step they should be translated by $\frac{2}{3}d$. In our images we do however not have access

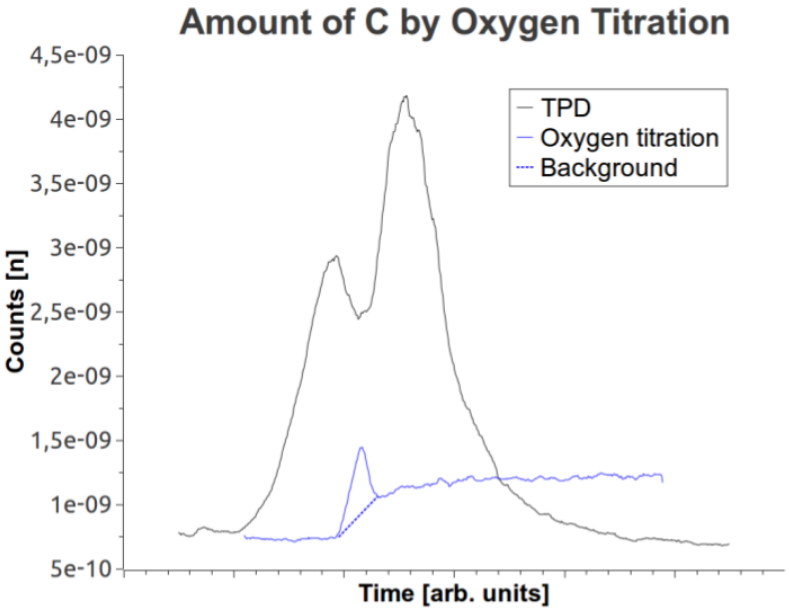

Figure 3.21: Oxygen titration experiment (blue line). The oxygen titration peak is located on a background of CO, which is evolved in the mass spectrometer. The carbon amount can be quantified by comparing it to a TPD (black line), which is the first TPD from figure 3.20. Figure is from supplementary material for included article I.

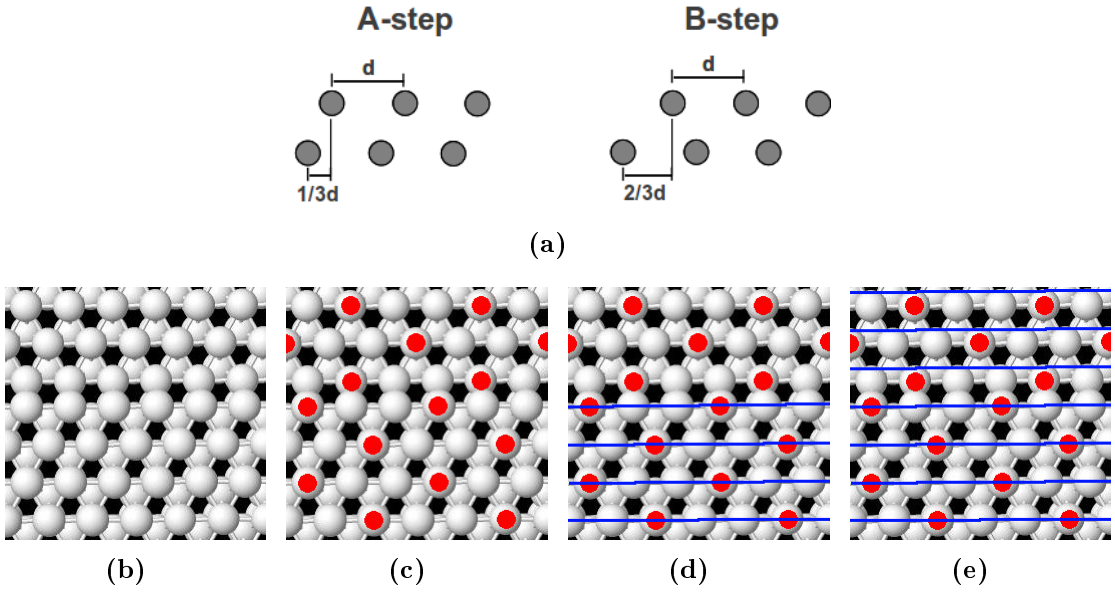

Figure 3.22: Model description of the distinction between steps. **(a)** is a side view model of the two kinds of steps. Due to the stacking the rows of atoms are shifted $\frac{1}{3}d$ at A-steps and $\frac{2}{3}d$ at B-steps. Figures **(b)** through **(e)** illustrate the steps in the data processing that is required to identify the steps, described in the text.

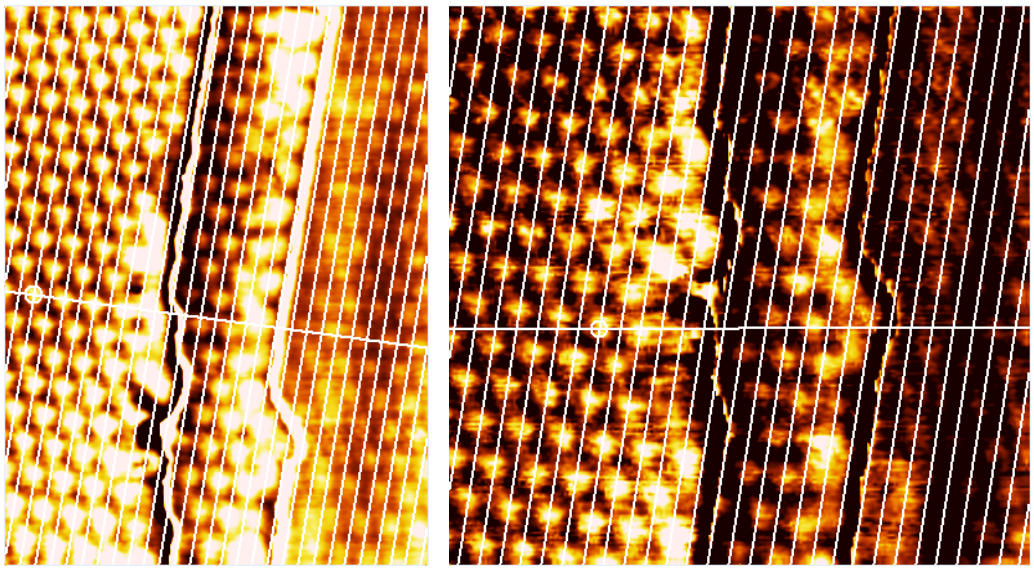

(a) (b)

Figure 3.23: STM images with the lines drawn through next nearest neighbors in the CO overlayer on the top terrace extended out over the two lower terraces.

directly to the atomic configuration of the ruthenium atoms to measure this distance on, since the surface is always covered by a $(\sqrt{3} \times \sqrt{3})R30°$ layer of CO. However, it should in principle still be possible to discern enough of the underlying structure from the structure of the CO overlayer to make the distinction. The procedure is illustrated in a set of top view 3D models in figures 3.22(b) through 3.22(e) for a B-step. Figure 3.22(b) is the clean surface. The atomic configuration of the ruthenium is hidden by the $(\sqrt{3} \times \sqrt{3})R30°$ CO overlayer (figure 3.22(c)), but fortunately the rows of nearest neighbors in the ruthenium surface can be recreated from the CO overlayer by drawing lines between next nearest neighbors as illustrated in figure 3.22(d). By extending these equidistantly placed lines out over the steps (figure 3.22(e)) it is observed that the lines of next nearest neighbors of CO molecules on the lower terrace is translated by $\frac{2}{3}d$, as viewed in the directions of going down the step. Hence it is a B-step.

In figure 3.23 two images are presented that this analysis has been performed on. In figure 3.23(a) CO atoms on the second step might appear to be translated a little, but not quite $\frac{1}{3}d$ which would seem the most obvious with a small translation. Moving down to the third step the CO atoms here are placed close to $\frac{1}{2}d$, but at this point it was supposed to be translated back in registry with the top step. Image 3.23(b) seems to fit better, with close to a $\frac{1}{3}d$ translation from first to second step and back in registry at the bottom, but this image has quite a bit of noise which makes it difficult to really access the fit. Unfortunately the tendencies in the analysis from the two images are general, which means that we cannot conclude on the step type directly from this kind of measurement. As a last measure to see if it was possible to make this analysis more consistent, we considered if the error brought into the distance measurement over steps due to sample tilt, might be the culprit. The principle is

illustrated in figure 3.24 and all the variables are described in the figure text. The

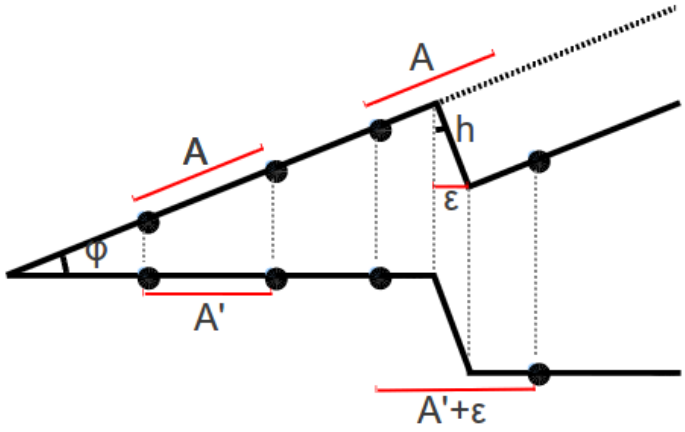

Figure 3.24: Figure that illustrates how projected distances between objects on two different steps will be over or under estimated due to tilted imaging. The top profile is the measured profile, the bottom profile is the measurement after plane correction fitted to the left terrace as indicated by the dashed line extended from it. A is a characteristic distance. A' is the distance A turns into after tilt correction. h is the step height. ϕ is the angle of the tilt of the top terrace and ϵ is the error induced in A' due to the tilt.

point is that due to the tilt of the sample, xy distances measured over steps will include an over or under estimation (depended on whether the sample tilt upwards as steps go down or the other way around) given by $\sin(\theta) \times$ h. Calculating this, including a correction due to the xy calibration that the image is also subjected to, we find that the distances over steps in our images are overestimated by 0.008 nm. This is only 3.4% of d and it is therefore not enough to explain why the analysis does not yield consistent results.

Having not been able to decide which step is the active site directly from experiment, we will now compare our results with a series of simulated STM images and DFT calculations of reaction and transitions state energies to help with the interpretation.

3.8 Comparison of STM images with calculations

In the following section we will compare our results with a set of calculations that has been performed in the theoretical group CAMd as a part of a collaboration around this project. The calculations consist of simulated STM images and reaction and transition state energy level calculations and they have been performed by the following people: Duncan J. Mowbray, Federico Calle Vallejo, Kirsten Andersen, Jens J. Mortensen and Karsten W. Jacobsen

The most important calculation details are as follows: All the structure optimization and total energy calculations were performed with the DACAPO plane wave DFT code[60]. The exchange-correlation functional used was the RPBE functional[61]. The ionic cores were represented by ultra soft pseudo potentials[62]. The Brillouin

zone was sampled with a $4 \times 1 \times 1$ Monkhorst-Pack grid. The surface was modeled using a 4 layer slab, which was separated by at least 1.2 nm and dipoles were corrected in the vacuum. Atoms in the top most layer was relaxed until the maximum remaining force between atoms was below $0.5\,\mathrm{eV\,nm^{-1}}$. The simulated STM images was made by use of the Tersoff-Hamann method where the tip was modeled by a *s*-orbital. For further details see the "Methods" section included in article I.

3.8.1 Simulated STM images

In this section a series of simulated STM images of different species adsorbed in different configurations at steps will be presented. The system chosen for these simulations is a Ru(109) surface. As previously mentioned this surface has the same features of close packed terraces separated by steps with alternating A- and B-step configuration. While this system is not identical to our experimental surface, it does have the advantage of having a significantly smaller unit cell, which lead to much shorter calculation times. At the same time it was determined, that the narrower terrace width does not form a problem in the sense of one step interfering with the calculations on the next. Furthermore, the experimental problem with this surface of step reconstruction[32], is not a problem in the calculations where the surface was fully relaxed and still retained its original structure.

For the purpose of comparing our images with simulations, the different ad-species configurations relevant for CO dissociation have been simulated. These simulations are gathered in figures 3.25a-f and 3.26a-b. Figure 3.25a shows the clean surface and from this we can see that beside from a slightly more curved appearance at the A-step, the two steps look very much alike and they do not show anything similar to the experimentally observed finger pattern. Image 3.25b is an image of CO adsorbed molecularly on the B-step. CO adsorption was tested in different configuration and the conclusion was that CO adsorbed at the bridge site of the step edge was the most stable configuration. The CO molecule adsorbs with the carbon atom binding to the surface and in the adsorption geometry the CO molecule tilts down towards the lower terrace. As it can be seen from the figure, the appearance of the CO molecule is a large, almost spherical protrusion at the step. The image for CO adsorbed molecularly at the A-step is not shown as it is very similar to the image from the B-step. For the A-step the CO molecule also adsorb on the bridge site of the step edge and is tilted down towards the lower terrace. These adsorption geometries are in good agreement with the observations made in reference [31]. Considering the magnitude and shape of the protrusions these images are not very similar to the step fingers structure we observe, where the structure has a more elongated shape.

In figures 3.25c-d the situation with separate carbon and oxygen after the dissociation of CO is depicted on the A- and B-step respectively. In the case of CO dissociation on the A-step the carbon atom occupies the fcc 3-fold hollow site next to the step on the lower terrace and the oxygen atom occupies the fcc 3-fold hollow next to the step on the top terrace. For CO dissociation on the B-step the most stable configuration corresponds to the carbon atom occupying the 4-fold site at the lower step site and the oxygen atoms occupying the hcp 3-fold hollow site on top of the step but translated one site over from the CO adsorption site (on the

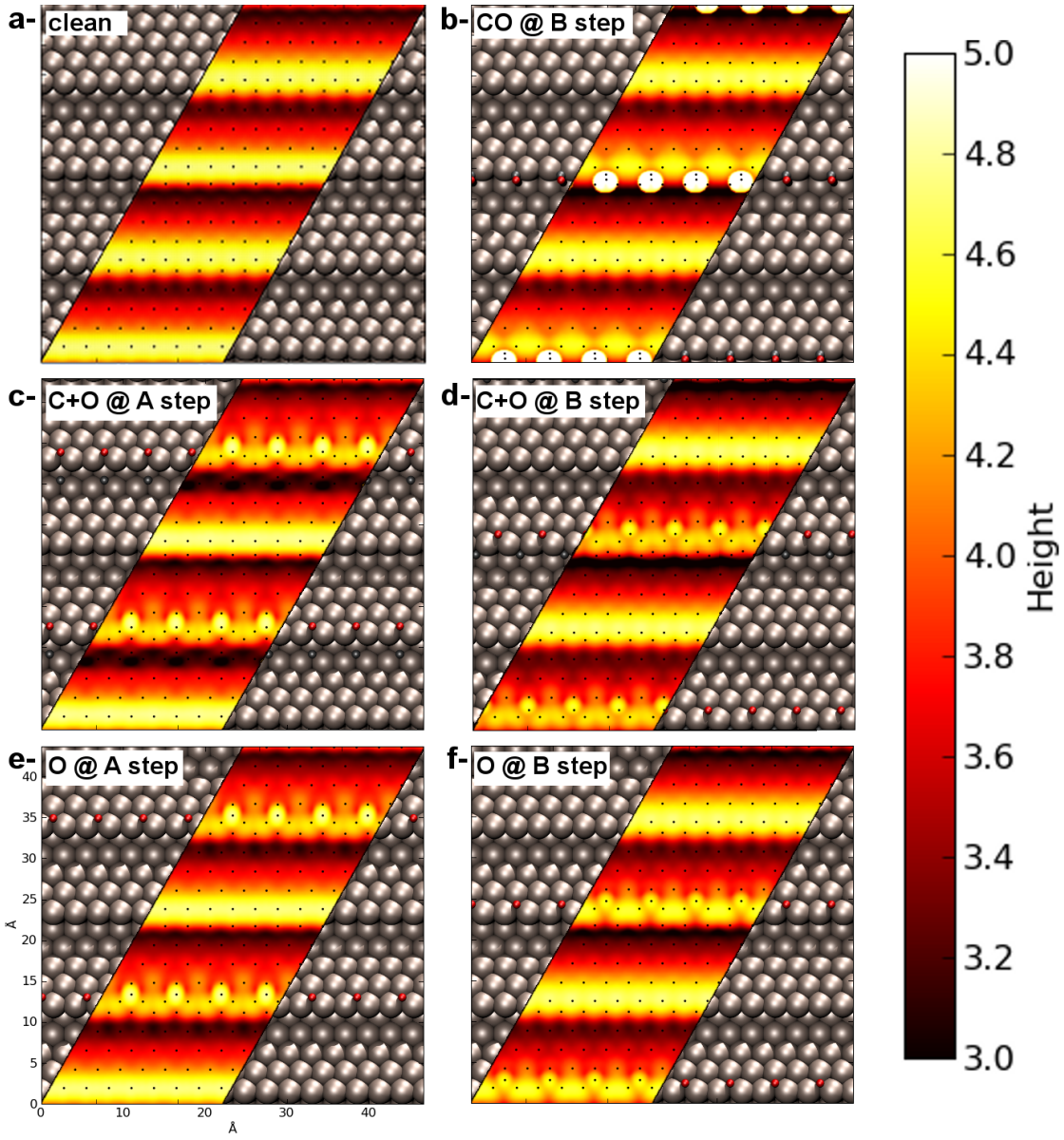

Figure 3.25: Six simulated STM images next to ball models of the configuration. A is a clean surface. B is CO at the B-step. C and D are dissociated CO at the A- and B-step respectively. In D the oxygen atom is placed at the hcp 3-fold hollow site next to the step in between the two hcp 3-fold hollow sites just above the dissociation sites. E and F is of oxygen on top of a A- and B-step respectively. In the ball models silver balls are ruthenium atoms, gray balls are carbon atoms and red balls are oxygen atoms. The red-to-yellow height scale shows apparent height in the STM images in Å and is zeroed at the bottom of the cell. Figure is from included article I.

image it can be described as being located on the top site located in between the two dissociation sites). This configuration might not by the most obvious one to consider, but it is the most stable, more stable e.g. than the configuration where the oxygen atom occupies the hcp 3-fold hollow site right above the carbon atom. In fact the latter configuration was less stable than molecular CO in its adsorption site and thus there would be no energy gain by dissociation. The images also show the effects of the oxygen atom partially depleting the density of states near the Fermi level of the neighboring ruthenium atoms, which are depicted with less intensity that in the images of the clean surface. The appearance of the dissociated CO has an elongated shape into the step, which is similar to our STM images. Unfortunately the simulated STM images of CO dissociated at the A- and the B-step are too similar to be used to distinguish the type of steps observed in STM.

Figures 3.25e-f shows the situation where oxygen is present in the same location as in the "after dissociation" images, but in this case there is no carbon present. These images are very similar to the images after dissociation, which indicates that by far the largest influence on the appearance after dissociation comes from the oxygen. As previously mentioned, while presenting the experimental results, it is necessary

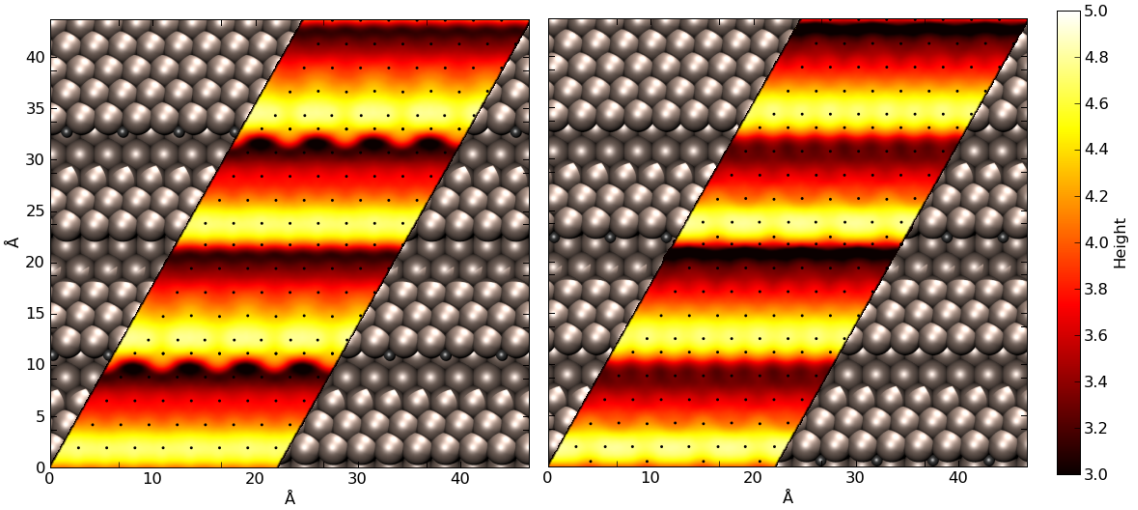

Figure 3.26: Simulated images of carbon at the A-steps (left) and the B-step (right). Color assignment in the ball models and color scale in the simulated image are the same as in figure 3.25. Figure is from supplementary material for included article I.

to ascertain the fate of the carbon atoms, since they are not directly visible in the STM images. One possibility mentioned was that the carbon atoms stay at the bottom of the steps and not be visible in the images either due to the atomic and geometric configuration or due to tip convolution effects. In figure 3.26 simulated images are presented, of the case where the carbon atoms is located in the sites they occupy after dissociation, but without any oxygen present. The appearance of these images are very similar to those of the clean surface, except for a slightly more curved appearance of the A-step, and the simulations therefore indicate that carbon atoms adsorbed at the bottom of the steps do not affect the STM images to the degree present in the real STM images.

From the simulated STM images it is confirmed that the fingers structure we have

observed at the steps, could originate from atomic oxygen adsorbed there after dissociation. Unfortunately they did not help in the identification of which type of steps they are located at. To try and determine this, it will be necessary to look into the energetics of the reaction on different locations presented in the next section.

3.8.2 CO dissociation energy levels

In order to determine the energetics of CO dissociation on different sites on ruthenium surfaces, a series of calculations was performed describing the different steps in the dissociation and on different sites.

The results are presented in figure 3.27. The black dotted lines represent dissociation

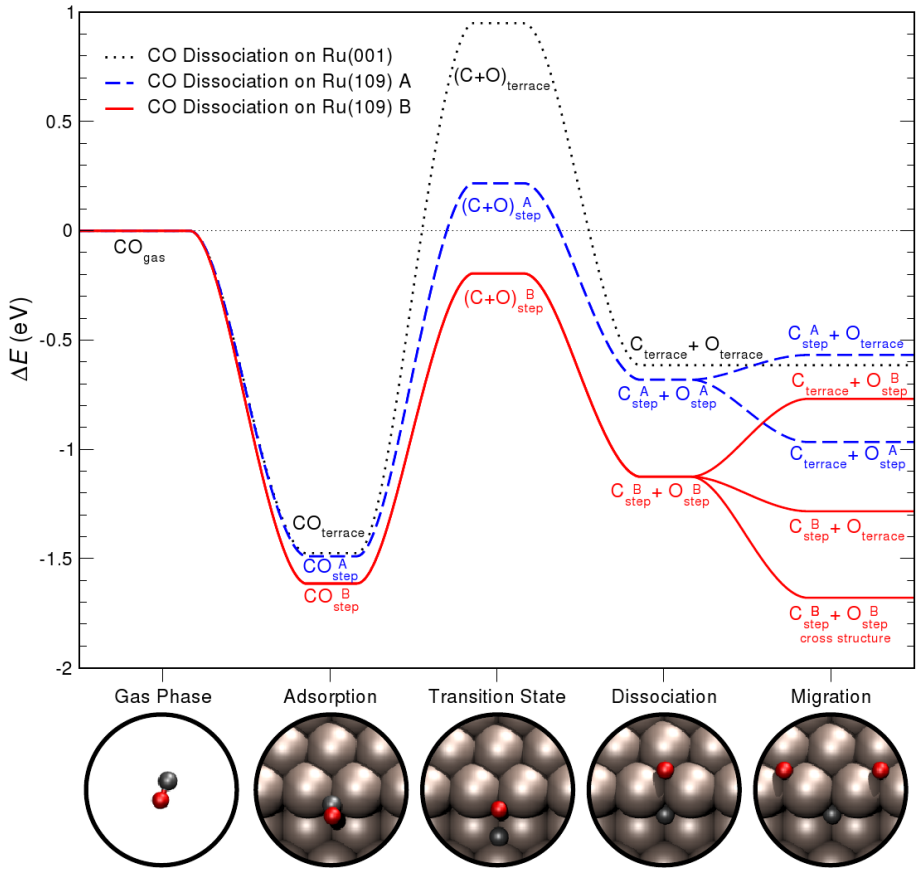

Figure 3.27: Reaction energy diagram for CO dissociation in three different site configurations based on DFT calculations. The diagram shows the energy of the system relative to CO in the gas phase for five stages; gas phase, adsorption, transition state, dissociation and migration. The black dotted curve represents dissociation of the terraces, the blue dashed on the A-step and the red full curve on the B-step. Figure is from included article I.

on the terrace, the blue dashed line on the A-step and the solid red line on the B-step, and going from left to right represents the different stages in the reaction. Starting from the left is the case with just the surface and the CO molecule present in gas phase, this energy level is set as the zero level for all the remaining calculations. In the adsorption step we see that the adsorption energy is almost the same on

the terrace and on the A-step at about 1.5 eV, while adsorption on the B-step is about 0.1 eV more stable. The transition state for the reaction differ greatly (a spread of about 1.2 eV) depending on the site. In general both step sites have a lower dissociation barrier than the terrace site, but what is more interesting is that the transition state level lies above the gas phase level for both the A-step and the terrace site. This means that on these two sites the molecule would rather desorb than dissociate and therefore points strongly towards the B-step being the active site for dissociation. This means that the first levels in the calculations support the observations that only one of the steps are active and suggest that it is the B-step.

After the transition state the levels of the most stable configuration of atomic positions after dissociation is calculated. Again the terrace and the A-step levels are close and the B-step level is lower. It is however not lower than the initial adsorption state, which would indicate that if the there were no other options, dissociation would be out-competed by re-association. However, if the possibility of the atoms migrating away from the reaction site (the last column) is considered, the situation is different. At the A-site the configuration with carbon migrating out into the terrace and the oxygen staying at the step is more stable than the other way around. For the B-site it is the other way around, here oxygen migrating out into the terrace is the more stable configuration. But, even more stable is the situation on the B-step where the oxygen migrates into the hcp 3-fold hollow site right next to the dissociation site (the cross structure, shown in the structure illustration below the diagram). The stability of the cross structure fixes the problem with re-associations, since this level actually is lower than the adsorption level. It also corresponds nicely with our results where a row of oxygen was observed on one of the step types. Without the cross structure the most stable configuration for the oxygen atoms is to migrate into the terrace, but with the cross structure it is more likely that the oxygen will stay at the step and if it has migrated into the step, then if it comes close to a B-step it is more likely to stay there.

3.9 Discussion of low CO dose experiments

The purpose of the presented results was to illuminate the structure sensitivity question by use of STM and to identify the active site. From the STM images we have obtained after CO exposure we clearly see that the steps act differently from the rest of the surface and we therefore have very clear indications that for the CO dissociation there is indeed a structure sensitive effect, in correspondence with literature references [32, 33, 54].

What was also apparent, was that the special step behavior was only present on every other step, and since the Ru(0 1 54) has a step configuration that alternates between A and B-step, it was therefore clear that only one type of step was involved in the CO dissociation. This observation also corresponds nicely with the results of Vendelbo *et al.* that showed that the amount of carbon left on the surface by exposing it to small amounts of CO was about 0.02 ML[33], which is the same as the coverage of one kind of step sites. Even though theoretically possible, it was however not possible to show which step configuration was the active one from experiments only. But after comparison of our results with simulated STM images and DFT

calculations it was possible to determine that the active site is the B-site. This result corresponds well with other theoretical work that concluded that the B5 site is the site with the lowest energy barrier for CO dissociation[63], as it is also the case on nickel[53] and rhodium[56]. Another interesting piece of information that originates from the calculations, is that after dissociation, the oxygen prefers to occupy the fcc site on top of the A-step and the hcp site on top of the B-step. As previously mentioned oxygen always prefer the hcp site on the terraces. This means that if these site occupation preferences hold, then in the case where the oxygen structure extend into the steps there should be a lattice mismatch at the A-step and there should not be a lattice mismatch at the B-step. We observe a pattern where the row of oxygen atoms at the step continuously extend into the terrace without any such lattice mismatch and this therefore supports the idea that dissociation takes place at the B-step.

From the DFT calculations it was also shown that the most stable configuration of the atoms after dissociation, was one where the oxygen atoms is located in the hcp 3-fold hollow site shifted one site over from the carbon atom (the cross structure). This fits well with the observations from isotopic scrambling experiments in literature, where it was found that the CO that desorbs from steps conform of mixed isotopologues consistent with random mixing[31, 32, 54]. Since the calculations show that it is energetically favorable for the oxygen atoms to move away from the carbon atoms they originated from, that makes it a plausible mixing mechanism. The cross structure also makes an appealing configuration for further reactions with other components, since both the oxygen atom and the carbon have plenty of free sites around them for other reactants to approach from, both on the terrace and on the steps.

From STM studies by Jakob *et al.* of co-adsorption of CO and O on ruthenium surfaces it was found that CO preferentially occupies sites at, or close to, steps whereas oxygen preferentially forms patches on the terraces. It was proposed that this behavior is due to a local compression of the ruthenium lattice in the vicinity of the step, which makes the $(\sqrt{3} \times \sqrt{3})R30°$ structure of CO more favorable whereas the oxygen p(2×2) structure prefers an non-altered or slightly expanded lattice[39], in correspondence with previous theoretical work[9]. We observed oxygen preferentially at the steps. However, this apparent conflict can however be explained by the different dosing procedures. In our case the CO overlayer was already formed before the oxygen appeared whereas in the work by Jakob *et al.* the species was co-adsorbed. This interpretation, that oxygen is formed at the steps after the CO layer is formed, and the fact that these formed oxygen structures are only observed on every other step, is also consistent with the idea that CO only dissociates at every other steps.

In the introduction it was mentioned that there is some disagreement in literature about the appearance of the oxygen atoms in the simulated and the real STM images. Some sources report that oxygen atoms are imaged as depressions[41, 43, 44], some report that they are imaged as both dependent on coverage[45] and some report that they are imaged as protrusions and hypothesizes that the difference in appearance reported in literature depend on scanning conditions[40]. In the simulated STM images we have presented, the oxygen atoms are imaged as protrusions and from the real STM images we are not able to tell. It is possible that the reason

for the difference between our simulated images and the ones published in literature reference [45], are different modeling conditions such as the bias or different calculation method such as the tip model. The determination of this would however require a large theoretical study and is outside the scope of this work. The bottom line is that our real images of the oxygen structure are reminiscent of the simulated STM images and that none of the conclusions we have based purely on the appearance of the real STM images rely of such an assignment of the appearance of the oxygen atoms.

The constant temperature experiments showed that only with the CO dose at 500 K was the finger structure associated with dissociated oxygen observed. Comparing this with the TPDs e.g. from references [32] and [28] this is right at the onset of the β-peak. That no oxygen fingers are observed at higher temperatures, is then due to the re-association that is known to take place at the steps at temperatures above 500 K. That no oxygen fingers are present in the experiments at 400 K and 450 K, indicates that these temperatures are not high enough to activate the dissociation of CO at the steps and these experiments therefore points to an onset of CO dissociation at the steps in between 450 K and 500 K, in correspondence with the approximately 500 K reported in reference [31] and approximately 480 K reported in reference [32, 54].

As it is clear from the presented results and the discussion above, there are now quite clear answers to the questions about structure sensitivity of the CO dissociation reaction and the catalytically active site for this reaction. There are however also questions that have not yet been addressed. One of these questions is the matter of whether CO can induce a step reconstruction that can activate the other step, a question raised in the work by Vendelbo *et al.*(presented in the introduction). This is a question we will look into in the next section with a set of preliminary results. Another question that also still stands is whether or not it is possibly to carry the conclusions made from this single crystal study over to more complex structures. This question will be addressed by a group of joint experiment over several different structures in section 3.11.

3.10 Large CO doses at 550 K

In this section a set of preliminary results will be presented where the sample has been exposed to large CO doses at an elevated pressure (10^{-5} Torr) at 550 K. These experiments are similar, both in the sample, the cleaning procedure and the CO exposure conditions to the ones carried out by Vendelbo *et al.* (summarized in the introduction, section 3.1.2). From these experiments it was observed, that as a function of increasing dose, the β-peak area was initially 2% of a monolayer, which is the same as the amount of one type of step, it then increased to almost 4% of a monolayer, which is the same as the total amount of steps and then decreased again to a level below the initial level. As a possible explanation for this behavior it was proposed that maybe the CO induced a reconstruction of the inactive step, thereby activating it. In order to shed some light on this matter, some initial STM experiments have been performed with surfaces that have received a treatment, that is identical to the one used in Vendelbo's experiments.

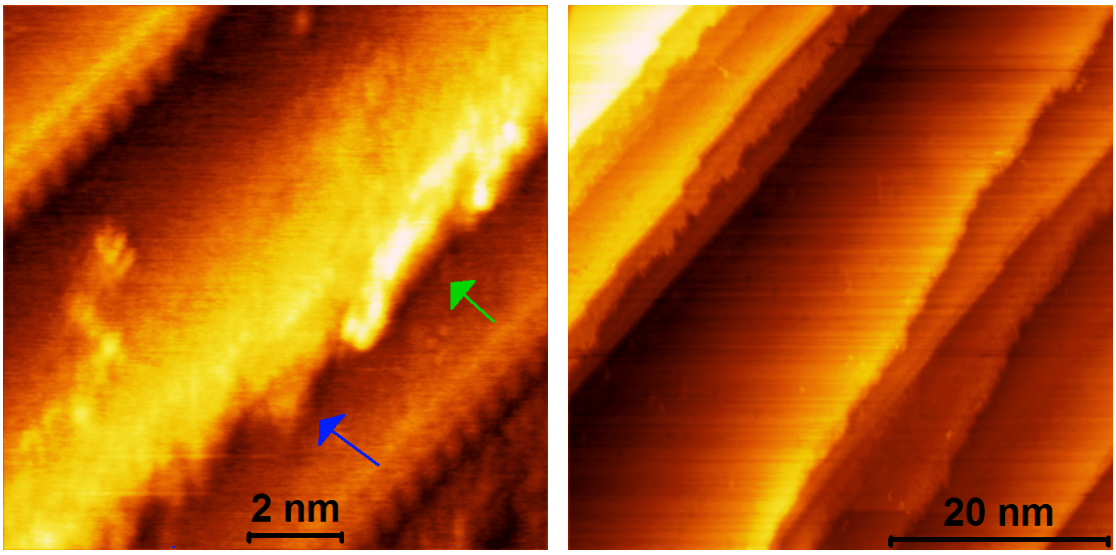

(a) $11.8 \times 11.8\,\mathrm{nm}^2$ **(b)** $50 \times 50\,\mathrm{nm}^2$

Figure 3.28: Images after 7 min CO dose at 550 K, 10^{-5} Torr. The images show clearly differing appearance at the two steps types and one of the steps are quite rough as compared to the clean sample. Image parameters are 0.010 V, 0.47 nA for **(a)** and 0.011 V 2.01 nA for **(b)**.

Images of the clean surface has already been presented in section 3.2. It is reiterated that the clean surface presents itself with smooth, straight, parallel steps without any difference in appearance between the two different step configurations. Figure 3.28 shows images of the surfaces after a 7 min CO dose at 550 K, 10^{-5} Torr, which was the exact exposure that showed the largest β-peak in Vendelbo's experiments. On the right (figure 3.28(b)) is shown a $50 \times 50\,\mathrm{nm}^2$ overview image. As in the previous experiments it is once again observed, that the appearance is different on every other step in consistency with the alternating step configuration. One type of step appears very smooth and in a few places seem to expand one or a few atomic rows in a small jump. On the other hand, the other step appears quite rough. It has many small jags in it and is not as smooth as the clean surface. In the smaller $11.8 \times 11.8\,\mathrm{nm}^2$ image (figure 3.28(a)) there are more details on the steps. The straight step shows a structure that is very reminiscent of the oxygen fingers structure, but it was not possible to confirm that it had the exact same periodicity due to a calibration problem. On the other step the roughness is observed to not have any periodic structure or angled edges usually associated with on ordered structure. Furthermore it is observed in some areas, that there is a lower layer next to the step (marked with a blue arrow) and in other areas that there is a layer that is higher then the steps (marked with a green arrow).

Figure 3.29 shows the images obtained after 14 min exposure under the same conditions. Starting once again with the overview image (figure 3.29(b)) the surface is now very different from the 7 min exposure. There does not appear to be any particularly rough steps and it would therefore appear that they have straightened out. The surface is however not quite like the clean surface, there are still more little protrusions at or on the steps and on the terrace. Zooming in (figure 3.29(a)) it is

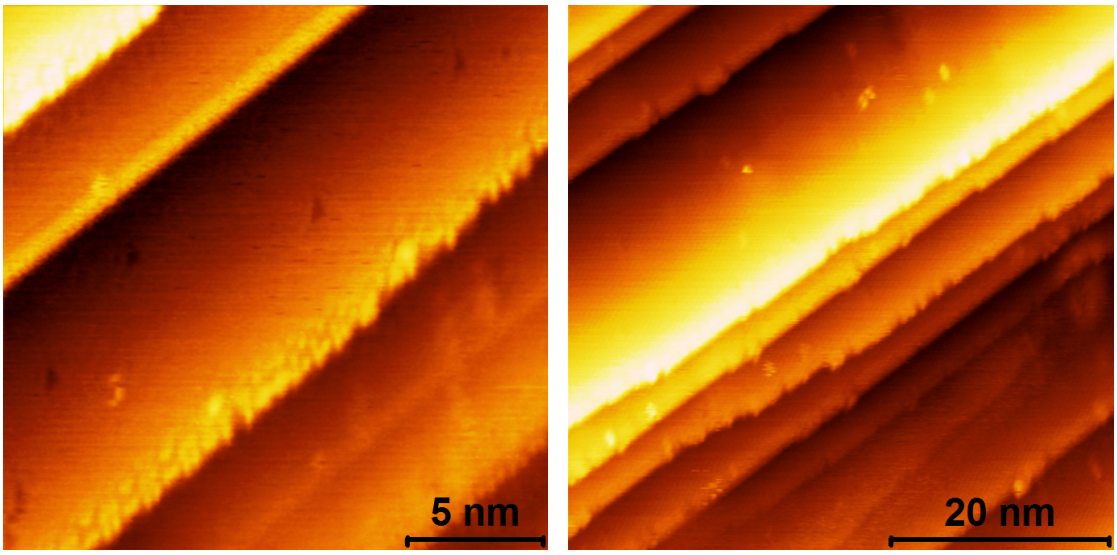

(a) $20{\times}20\,\mathrm{nm}^2$ **(b)** $50 \times 50\,\mathrm{nm}^2$

Figure 3.29: 14 min CO dose at 550 K, 10^{-5} Torr. Image **(b)** shows smooth looking steps but in the smaller image **(a)** it is observed that one of the steps has a decoration on top of it. Image parameters are 0.110 V, 0.97 nA for **(a)** and 0.999 V, 0.92 nA for **(b)**.

clear that the surface is indeed still modified. The steps both have a very straight form, but one of them has a decoration on top of it. The decoration appear to not be in the form of an ordered structure such as the oxygen fingers was and they also extend more into the surface. Looking closer at the other step, it might also have a modification that appears as a bright rim at the edge, but it is difficult to see this clearly.

Extending the CO exposure all the way up to 60 min at the same conditions the result is a surface as presented in figure 3.30. From the large image (figure 3.30(b)) it appears that one of the steps are quite rough and the other one is a little rough and with small dents in it. A closer look reveals that something is present at the bottom of primarily every other step. It appears as if it is extending out from the steps. From the small image (figure 3.30(a)) it is observed that indeed the growth is present primarily on every other step and at under coordinated sites on the other step.

One of the purposes of these experiments was to try and explain the activation-deactivation behavior reported by Vendelbo *et al.* from the β-peak area. Relating the STM images to the appropriate points in the β-peak area graph from reference [33] results in figure 3.31. As it can be seen, the 7 min exposure is at the top of the β-peak area and remembering that at this exposure there was decorations of both steps, this could be in line with the hypothesis of a reconstructive activation of the A-steps. The 14 min exposure corresponds to a point on the curve on the way down from the maximum. At this exposure we still observed some roughness in the images and one or both of the steps has an altered appearance. This means that at this exposure there is also modifications to the steps, but to a lesser degree

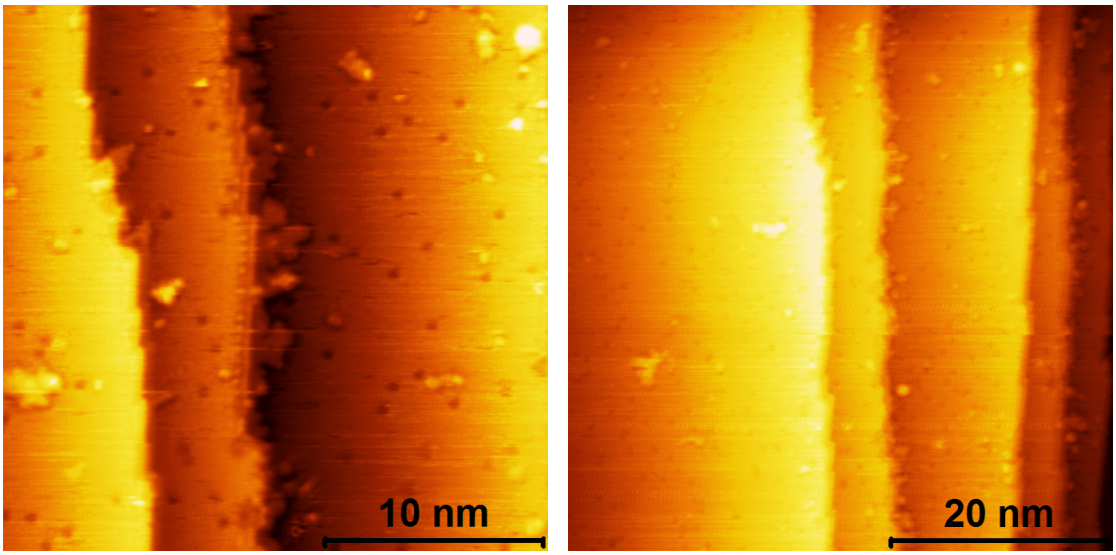

(a) $25 \times 25\,\mathrm{nm}^2$ (b) $50 \times 50\,\mathrm{nm}^2$

Figure 3.30: 60 min CO dose at 550 K, 10^{-5} Torr. In both images it appear as if a structure is "growing" from primarily every other step. In the small image however it is observed that this also happen on the other kind of step at under-coordinated step sites. Image parameters are 0.020 V, 0.71 nA for **(a)** and 0.020 V, 0.96 nA for **(b)**.

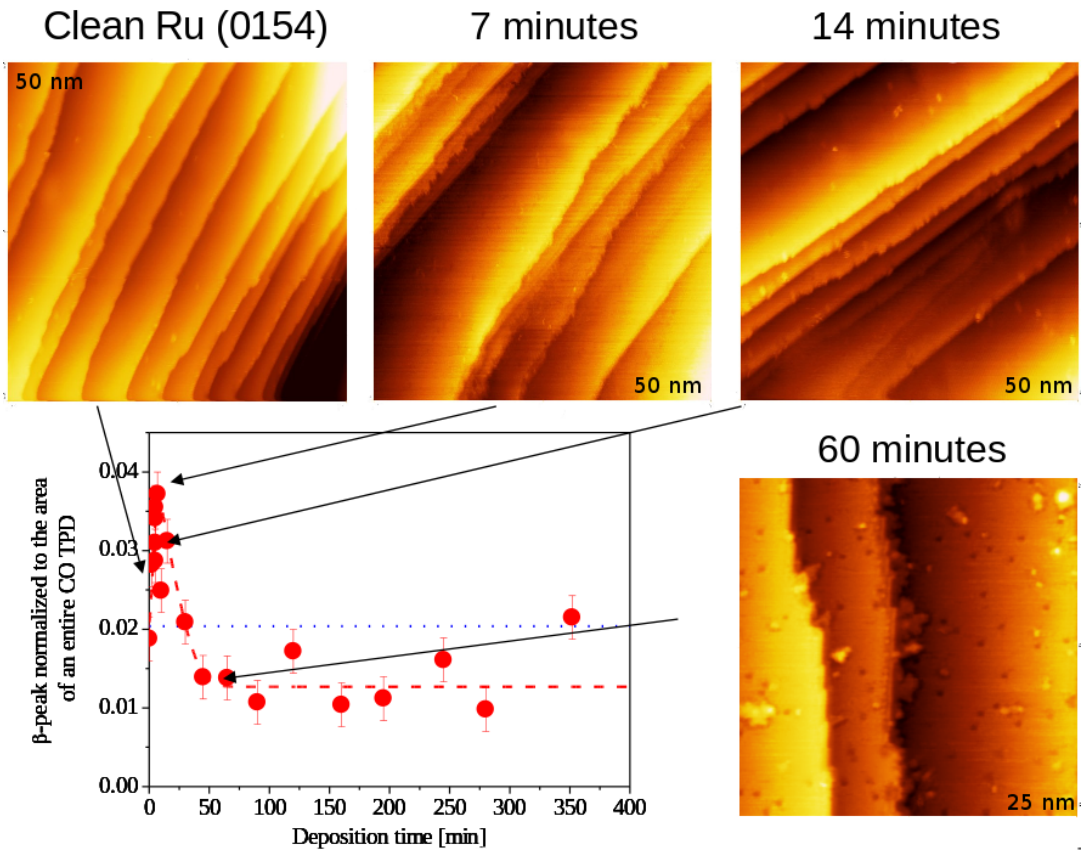

Figure 3.31: The presented STM images correlated to the β-peak area graph from reference [33].

than for the 7 min exposure. This could also fit in with the previously mentioned hypothesis, if it is assumed that the reconstruction disappears after the CO that induced it has been dissociated. In the 60 min images it is evident that patches was forming at the bottom of the steps. From the measurements of Vendelbo *et al.* it is known that carbon from dissociated CO accumulates on the surface and that the 60 min exposure marks the point where carbon only accumulates very slowly with further exposure. This means that these images certainly support the previous conclusions that one type of step is the primary source of CO dissociation sites, since the carbon growth is primarily seen on one type of step. It is however not clear if these images also match with the hypothesis above, since that would require the ability to resolve a single line of carbon atoms present on the less active step. This is not visible and from the simulated STM presented in section 3.8.1 it was seen that a single row of carbon atoms at the bottom of steps does not significantly change the appearance. However, one really intriguing aspect of these images is the way that they directly show the effects of under-coordinating atoms at the steps, and shows that it is possible to active the other step by this under-coordination. It should however be re-iterated that these results are preliminary so until they have been properly reproduced, the interpretations above are restricted to being speculations.

Step roughening by exposure to CO has previously been observed in high pressure (1.25 bar total pressure) *in situ* STM measurements in Frenken's group[64]. Even though these measurement were performed at high pressures, and our experiments are restricted to large CO doses under UHV conditions, it does lend some credence to the idea of CO induced step roughening, but does not give any clues as to whether it is due to a reconstruction of the step. In the same study by Frenken's group it was also observed that by exposure to carbon monoxide and oxygen, clusters were formed all over the surface up to 70% coverage, including on the terraces. It was also possible to partially remove these clusters by exposure to hydrogen, which lead to the conclusion that they were carbonaceous species. This means, that it is a possibility, that the reason that Vendelbo *et al.* did not find any carbon coverage saturation in his high pressure experiments, the way he observed it for the UHV experiments, might be that at higher pressures the terraces become activated for CO dissociation as well or less likely that the higher pressure increase the mobility of the carbon atoms which allow them to move away from the steps. In any case it is certainly a subject that we will continue to investigate, both with the high dose UHV experiments and possible also in the future with *ex situ* high pressure experiments.

3.11 Structure cross-over

This section is about the comparative study of CO desorption on ruthenium model systems with different structures. The study involves different model systems and therefore also different setups and the people that work with these setups. The collaborative roles of the people in the experimental work are as follows: The nanoparticle and thin film work was done by S. Murphy, C. Strebel and R.M. Nielsen, the single crystal TPD measurements was performed by S. B. Vendelbo and C.

Conradsen, the single crystal STM measurements was performed by Y. Tison, L. Bech and myself and the supervision was done by I. Chorkendorff, J.H. Nielsen and M. Johansson.

The systems that have been studied are size selected ruthenium nano-particles supported on highly ordered pyrolytic graphite (HOPG), Physical Vapor Deposited (PVD) ruthenium nano-particle films grown on HOPG and the Ru(0 1 54) single crystal surface described in section 3.2. The size selected nano-particles and the PVD nano-particle films have been studied in a multichamber UHV system with a base pressure below 10^{-10} mbar. The Ru(0 1 54) single crystal TPD measurements were performed in an UHV system with a base pressure below 10^{-10} mbar and the Ru(0 1 54) single crystal STM measurements were performed on our setup (described in section 2.1).

All of the work previously presented in this thesis has only concerned single crystal work, but as already mentioned in the introduction, the structure of this kind of model system is far away from the industrial catalytic system consisting of supported nano-particles. The so-called structure gap is one of the large challenges for the surface science approach to catalysis research. Single crystals are comparatively simple enough for us to understand, but the knowledge gained is not always easily transferable to the real catalysts. One step up the complexity ladder towards the real system, is size selected nano-particles supported on well defined surfaces. This system is closer to the real system, and is compatible with most surface science techniques. Non the less, with this small step upwards in complexity it can be a great challenge to properly resolve the structure, which puts a limit in what kind of information can be obtained.

The results presented in this sections will show how it is possible to relate CO TPDs to specific surface morphologies across the structure gap. It will also show how it is possible to shift the behavior of two model systems from the single crystal like behavior to the nano-particle like behavior or the other way around.

The main results from this study are presented in figure 3.32. The top row contain the single crystal results. Image a is an STM image of the clean sample, such as has been presented before. Image b is an STM image of the surface after it has been sputtered for 300 s with 1 keV Ar^+ ions, which results in a very rough surface. In between the two images are shown a set of TPDs. The top one is the TPD corresponding to the un-sputtered surface. It has the two main α-peaks located at 390 K and 460 K and the β-peak shoulder at around 535 K, as described earlier. The bottom one is the TPD corresponding to the surface after 300 s of sputtering. This TPD now has a single quite broad feature around 420 K and a large tail extending towards $\sim$600 K. All the spectra in between shows the TPDs after different intermediate sputtering durations. From these it can clearly be seen that the change in the TPD shape is gradual as a function of the sputtering time. The high temperature α-peak from the un-sputtered crystal TPD gradually lowers in temperature while the low temperature α-peak gradually decrease until it is only a shoulder on the other peak.

In the middle row of figure 3.32 the results from the PVD grown nano-particle films are presented. Image d is an STM images of the as deposited 5 nm film. This surface is made of a collection of nano-particles, with a size of 6 ± 2 nm, stacked on

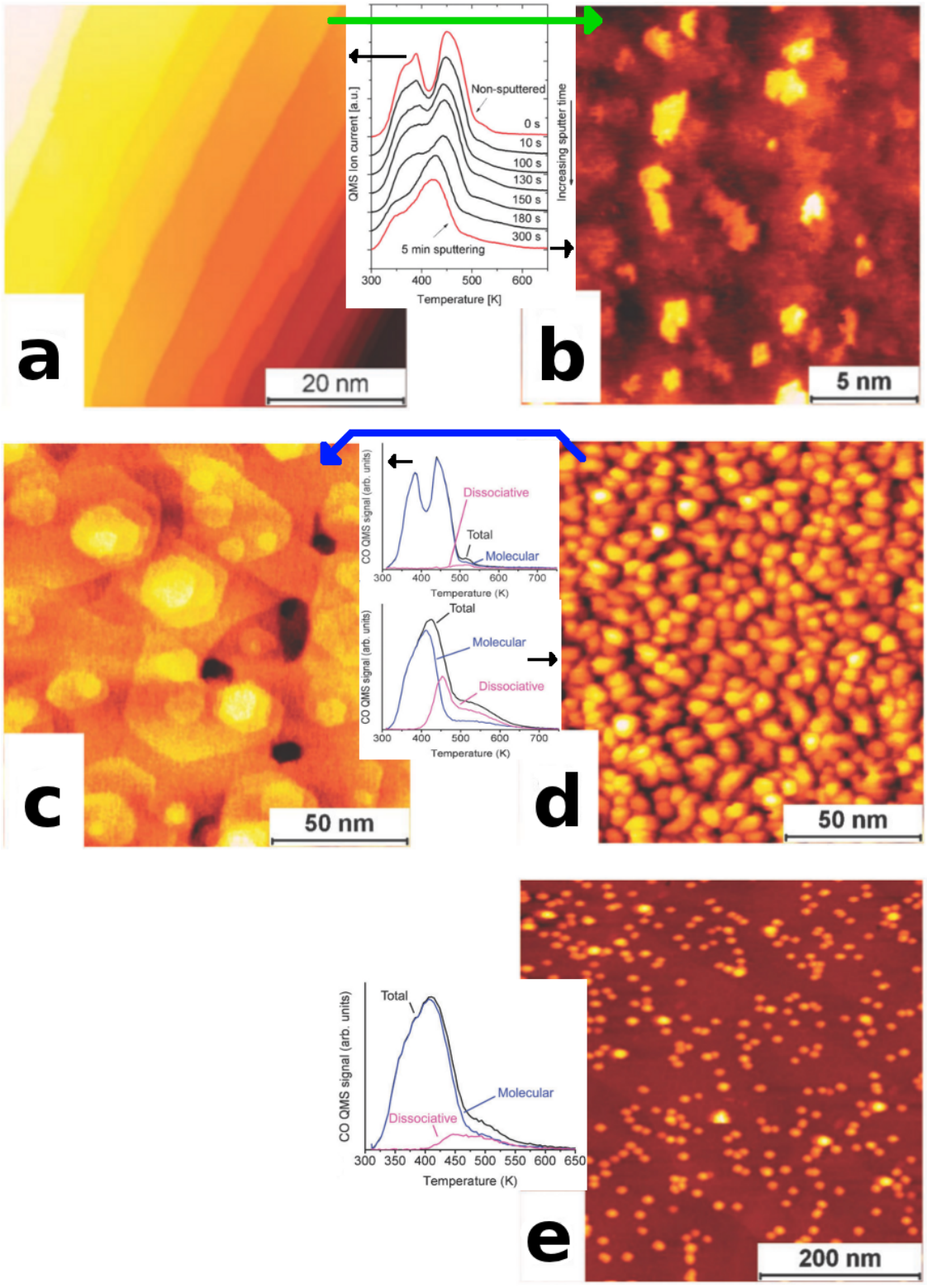

Figure 3.32: STM images of (a) un-sputtered Ru(0 1 54), (b) Ru(0 1 54) after 300 s sputtering, (c) 5 nm PVD ruthenium film as in (d) but annealed at 900 K for 600 s, (e) 9.7 nm mass selected nano-particles. Insets are the TPDs corresponding to the images. Top TPDs in between images belong to the left image and the bottom TPDs to the right image. The figure is assembled from several figures from included article II.

top of each other without any detectable order. Image c is an STM image of the film after 600 s of annealing at 900 K. After this treatment the film has now ordered into a polycrystalline film. It consist of large atomically flat terraces separated by mono-atomic steps. In between the two images are the corresponding TPDs. The lower TPD is from the as-deposited film. It has a single large feature that reaches its maximum at around 420 K and a broad shoulder between 500 K and 600 K. The blue and the pink curve shows the contributions to the TPD that originate from molecular desorption and associative desorption respectively. These curves has been obtained by isotopic scrambling experiments similar to those presented in reference [32]. Two different isotopologues of CO ($^{12}C^{18}O$ and $^{13}C^{16}O$) are dosed in equal amounts and all four possible mixed isotopologues ($^{12}C^{18}O$, $^{13}C^{16}O$, $^{13}C^{18}O$ and $^{12}C^{16}O$) are followed by the mass spectrometer. In this TPD the main peak is due to the molecular desorption and the shoulder is due to associative desorption. The upper TPD is from the annealed film. It has two main features located at 390 K and 450 K and an additional small feature at 530 K. The curves from the isotopic scrambling experiments show that only the little extra feature at 530 K originates from associative desorption.

In the bottom of figure 3.32 is an STM images of 9.7 nm mass selected nano-particles on a sputtered HOPG substrate. The corresponding TPD shown on the left side of the STM image has a single broad feature at around 410 K and a shoulder extending from around 480 K to 600 K.

When comparing these different TPD it becomes apparent that there are two fundamentally different shapes: The single crystal like shape with two main peaks and a small extra peak and the nano-particle like shape with a single broad peak and a broad shoulder. Remembering that the double feature in the single crystal TPD originates from the formation and disruption of an ordered overlayer on the terrace, it is possible that the much smaller areas of terrace like facets on the nano-particles is the reason for this difference in desorption behavior. It has already been shown that on single crystals with much smaller terraces the double peak feature fades[31, 65]. This behavior can be due either to the ordered overlayer not being able to form at all, due to the limited size of the terraces or due to a change in adsorption near steps due to local lattice strain.

The most interesting aspect of the results presented above, is the way it is possible for two different systems to switch the CO desorption spectrum behavior between the two distinct shapes. For the single crystal system it was observed that it was possible to switch the desorption behavior from that characteristic of the single crystal towards that characteristic of the nano-particles by sputtering the surface (following the green arrow in figure 3.32). It was even observed that this change was a very gradual one, that could be applied to many levels depending on the sputtering duration. For the PVD film of nano-particles it was observed that it was possible to shift the behavior the other way, to change the nano-particle shaped TPD for the as-deposited film towards a single crystal shaped TPD by annealing the sample (following the blue arrow in figure 3.32). The fact that this sort of cross-over behavior is possible is important as it allows us, to a certain degree, to related the results from the two different systems to each other, thus bridging some of the structure gap. At the same time it also helps to validate the idea of studying both types of systems to gain the full set of information about the system, as it is

then possible to transfer some information from one system to the other by simple preparation techniques.

3.12 Summary

In the first part of this chapter the results for low doses of CO on the Ru(0 1 54) surface was presented. They showed that after a TPD or after a constant pressure 10^{-8} Torr of CO while cooling down from 700 K to 400 K the surface has elongated decorations on every other step and in some cases these decorations extend onto the terrace in a regular hexagonal lattice. The decorations have a spacing of 0.55 ± 0.05 nm and a unit cell size with the same periodicity when extending onto the steps. These decoration were assigned to rows or patches of atomic oxygen located at the steps. On the terraces a regular hexagonal pattern with a periodicity of 0.47 ± 0.03 nm was observed and assigned to CO in the $(\sqrt{3}\times\sqrt{3})R30^\circ$ overlayer structure. Oxygen titration experiments of these surfaces showed carbon present in amounts between 0.014-0.020 ML, which is roughly consistent with the coverage of one step configuration. These observations strongly indicate that only one of the two step configurations are active for CO dissociation under these conditions.

Another set of experiments with CO dosed at constant temperature showed, that the oxygen structures on every other step was only present when the CO was dosed at 500 K. Neither samples prepared at temperatures above (550 K and 600 K) or below (400 K and 450 K) had any of these structures. From this it was concluded that the dissociation of CO at the active step is an activated process, that needs a temperature somewhere in between 450 K and 500 K to take place.

While the experiments showed that only one step configuration was active for CO dissociation, they unfortunately did not make it possible to determine which one. For the purpose of clarifying this the experiments was compared to simulated STM images and reaction energy level calculations, both based of DFT. The simulated STM images showed that oxygen adsorbed on top of the steps resembled the oxygen structures we observed experimentally, but the images of the oxygen at the two different steps were too similar to make a distinction between them based only on this. The reaction energy calculations showed that on the A-step and on the terraces the CO molecules are more likely to desorb than dissociate and that for the dissociated species, the most stable configuration is on the B-step where the oxygen atom move one hcp 3-fold hollow site over along the step and the carbon atom is located in the 4 fold site at the step. These results clearly indicate a preference for dissociation on the B-step.

From the preliminary results where the sample was exposed to high doses of CO, at a CO pressure of 10^{-5} and a temperature of 550 K, it was apparent that also in this case does the steps show different behavior. The 7 min exposure showed, that in particular one of the steps was very rough. At the 14 min exposure this step-roughening was not nearly as evident. These observations could be in line with the observations of Vendelbo, that the relative area of the β-peak, peaks at 7 min exposure under these conditions and the hypothesis that this may be due to a reconstructive activation of the in-active step. The 60 min exposure showed that

something, most probably carbon species, was growing at the bottom of the steps. This happened primarily at one kind of step and at under-coordinated sites on the other step. This lends further credence to the idea that only one of the steps work as the primary catalytic site.

In the cross over section three different kinds of samples were investigated, mass selected nano-particles, PVD evaporated nano-particle films and a Ru(0 1 54) single crystal. From these studies it was shown how it was possible to shift the shape of CO TPD's, and thereby the desorption behavior, from one characteristic of single crystal like system to one characteristic of nano-particle like systems. The single crystal type TPDs were found to have two main α-peaks at around 390 K and 450 K-460 K and a β-peak at around 530 K-535 K. The nano-particle type samples were found to have TPDs with a single broad feature at around 410 K-420 K and a broad shoulder between 480 K and 600 K. By sputtering the Ru(0 1 54) single crystal sample for 300 s it was possible to shift the TPD shape from the single crystal type to the nano-particle type and this change was gradual as a function of the sputtering time. Likewise for the system that consisted of a 5 nm PVD nano-particle film, it was possible to shift the TPD behavior from the nano-particle type to the single crystal type by annealing it for 600 s at 900 K. These observations are believed to be important for the prospect of relating studies to each other at varying model systems complexities, thus helping to bridge some of the structure gap.

Chapter 4

Bi/Pt(111)

In this chapter the results of an STM study of bismuth overlayer structures on a Pt(111) surface will be described. This projects was carried out partially during my masters thesis work and during the first 6 months of my PhD project period.

4.1 Introduction

Platium is known to be a good catalyst for several different reaction, including the hydrogen evolution reaction and the oxidation of several small organic compounds. Even though platinum is a excellent catalyst for many of these reactions, there is still room for improvement. For this reason, it has been investigated extensively in literature, whether it is possible to enhance the catalytic abilities by modifying platinum with other elements. For the particular case of modifying platinum with bismuth, these studies range all the way from electrochemistry studies on single crystals e.g. in references [66, 67, 68, 69, 70, 71], UHV studies on single crystals[72, 73], electrochemistry studies on ordered bulk inter-metallic compounds[74], and DFT calculations and electrochemistry experiments on surface alloys[7].

When changes in the reactivity are observed, it is always interesting to figure out how, why and if these changes correlate to changes in structure. Restricting our perspective to the single crystals only, the literature on the structure of these systems is more limited. In a recent study the authors have investigated the structure sensitivity of formic acid electro-oxidation with an electrochemical STM[71]. This reaction is known as a very structure sensitive reaction on platinum, and it has been shown that it is possible to enhance this reaction by deposition of bismuth on the platinum surface. The mechanism behind this has been concluded to be mainly an ensemble effect (but there is also a smaller electronic effect), that shifts the reaction pathway towards dehydrogenation (direct oxidation) instead of dehydration. The latter poisons the surface as a side effect and therefore the overall effect of this partial blocking of the surface is positive even though sites are blocked[66, 69, 70]. In the study by J. Kim and C.K. Rhee they were able to elegantly investigate the relation between ensemble size and oxidation activity, by determination of the ensemble size from STM images such as the one shown in figure 4.1. From this study it was concluded that the poison formation was inhibited with ensembles of less than 2 nm and that at the right ensemble size the turnover frequency was enhanced 100-200 times[71].

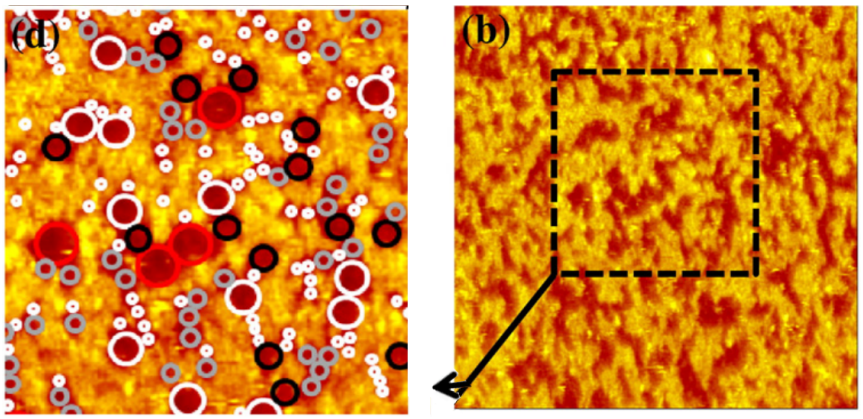

(a) **(b)** $100\times100\,\mathrm{nm}^2$

Figure 4.1: EC-STM images of the Bi-modified Pt(111) surface. **(a)** is a zoom in of a region of **(b)**, in which the ensembles are shown as circles. The ensembles were marked by first fitting in the largest possible circles and then filling in the gaps with succesively smaller circles. Adapted from [71].

In terms of UHV structure studies these has so far only been performed with averaging reciprocal space structure techniques. By far the most relevant work for the present study is that by M.T. Paffet *et al*[75, 76]. In these studies the structures of bismuth overlayers on a Pt(111) single crystal were studied extensively by LEED, AES and TPD. The main conclusion was, that the bismuth overlayers will adopt a range of different overlayer structures depending on the coverage, as summarized in figure 4.2(a). In the beginning the bismuth will adopt a multilayer structure, but as soon as the temperature crosses ∼300 K it will change into a structure with just a single overlayer and the rest of the bismuth gathered in large 3D-islands. Proceeding up in temperature the surface enters into a regime where a p(4×4) structure can be observed, and at slightly higher temperatures (680 K) bismuth will start to desorb from the surface. At approximately 800 K only a single layer of bismuth remains on the surface and when heating further, the bismuth overlayer then adopts the p(3×3), $(\sqrt{3}\times\sqrt{3})R30°$ and p(2×2) structures as the coverage go down[76]. In the figure, the temperatures we have investigated in this study are highlighted with blue lines. Figure 4.2(b) shows structural models for all the LEED patterns that have been observed during Paffett's work. The explanation given as to why bismuth will adopt so many different sub-monolayer structures is that bismuth is slightly repulsive of itself on a Pt(111) surface, and it will therefore always seek to maximize the distance to its neighbors. A similar explanation was given to explain similar observations for the bismuth on Pt(110) system[72].

We wish to further extend the knowledge about the overlayer structures of bismuth on Pt(111) by an UHV STM study. This projects was originally motivated by the results of Greeley and co-workers[7], in which it was shown that a surface alloy of bismuth into platinum gave an activity for the hydrogen evolution reaction that was superior to that of pure platinum and platinum with a bismuth overlayer. Thus the purpose was to try and produce this alloy in UHV and study its characteristics. Unfortunately, we did not manage to prove that we could produce the surface alloy

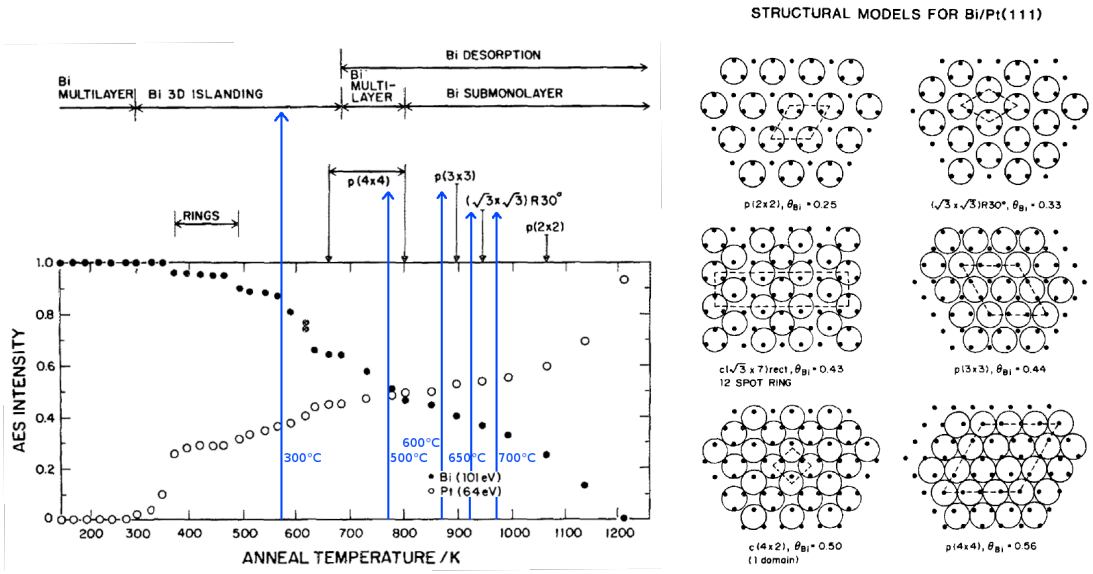

(a) (b)

Figure 4.2: **(a)** shows the range of structures that the bismuth overlayers adopt in a Pt(111) single crystal surface, as a function of the annealing temperature. The main features will be described in the text. The blue lines are added and shows the temperatures that we have investigated with STM. **(b)** shows the structure models proposed for the observed LEED patterns. Both figures are adapted from [76].

within the time allocated for the project, but we did obtain a lot of information and STM images of the overlayer structures. Thus in the following we will present XPS results and, what to our knowledge are, the first UHV STM images of UHV prepared bismuth overlayers on a Pt(111) crystal.

4.2 Experimental details

The sample that was used for this study is a Pt(111) single crystal, as described in section 2.2. The sample was cleaning by a cleaning procedure inspired by those presented in references [77, 78] and consist of:

- 1 or 2 keV Ar^+ sputtering at 600°C for 900 s
- Oxidation at 600°C in $1.2 \cdot 10^{-6}$ Torr oxygen
- Annealing at 950°C for 600 s

After several of these cleaning cycles the cleanliness was checked with XPS and STM.

Bismuth deposition is done by PVD from a resistively heated crucible doser, and the deposition rate is monitored by a quartz crystal microbalance. The bismuth used for dosing is 99.999% pure and from Aldrich.

The XPS spectra was fitted with the CasaXPS program[79] with a set of Gaussian-Lorentzian peaks. The Pt $4f$ doublet was fitted with a set of peaks with an asymmetry ratio of 0.45 super-imposed on a Shirley background. The peak fitting was restricted with a peak splitting value of 3.35 eV and an intensity ratio of 4:3. All XPS energies were calibrated to a Pt $4f_{7/2}$ value of 70.9 eV in correspondence with reference [25]. The Bi $4f$ doublet was fitted with a peak set with an asymmetry ratio of 0.46 also super-imposed on a Shirley background. For this doublet the peak splitting did not exactly match that from the reference [25] (5.39 eV) for which reason it was decided not to restrict it, but instead to monitor it for consistency.

The experiments were performed in the following manner. After cleaning the sample a multi-layer of bismuth was dosed onto it. Thereafter it was heated following a 1°C/s heating ramp up to the annealing temperature, where it was kept for a specific amount of time. Annealing temperatures was in the range from 300-700°C and annealing times in the range from 3-30 min. After annealing the sample was cooled down along a 1°C/s heating ramp until the cooling became diffusion limited. After cooling, the sample was characterized with XPS and STM.

4.3 Results and discussion

4.3.1 XPS results

Coverages

Figure 4.3 contains coverage information in the form of bismuth to platinum XPS ratios. The black and the gray lines represent the values for a Bi(111) and Bi(100) monolayer, calculated from equation 2.22. The thicknesses used in the calculation are 0.197 and 0.186 nm for the Bi(111) and Bi(100) monolayer respectively. These two surfaces are the lowest energy surfaces of bulk bismuth with a hexagonal symmetry[80], which is what we observe in the STM measurements (section 4.3.2). Furthermore, since Bi(111) is the preferred direction for epitaxial growth[80], these two surfaces form the most likely candidate structures for the overlayers. The first points are from data obtained immediately after deposition and have values in the range $0.26-0.38 \pm 0.02$. After the first heat treatment at 300°C for 3 min the values increase to between $0.34-0.40 \pm 0.02$. No bismuth is added at this point, so it is speculated that the observed increase in bismuth to platinum signal is due to a structural change, which is known from the STM data to take place during this first heat treatment. The values stay pretty stable until a significant drop appears when going from the heat treatment at 400°C for 3 min to the one at 500°C for 3 min. After this drop the values are in between $0.11-0.12 \pm 0.02$ which is below that which would be expected for a single layer of bismuth and it is therefore assumed that at this point all bismuth in excess of one layer has left the sample. This point is also in good correspondence with the value obtained by Paffett, who observed the intensities going down to a single layer at roughly 507°C[76]. During the remaining heat treatments up to 700°C for 30 min the intensities slowly drop down to around 0.05 ± 0.02.

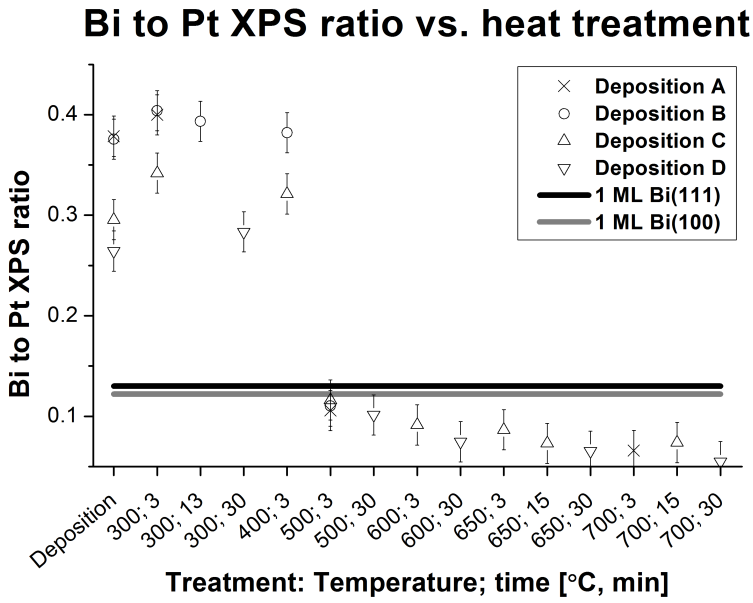

Figure 4.3: The XPS ratio of Bi to Pt. A through D are different experiments. The black and the grey line represent the 1 ML value for the Bi(111) and Bi(100) surface respectively. Values for layer thicknesses are from reference [80]. The thickness for the Bi(111) layer was set to (0.197 nm), which is the average between the intra and inter bilayer distance and the Bi(100) distance which was set to (0.186 nm) is the average distance between layers.

Binding energy shifts

When observing the binding energy values of the Bi $4f_{7/2}$ peak as a function of the heat treatments there seems to be a development, where they fall in basically three groups. The value obtained right after deposition has a value of $E_{\text{binding}} = 156.87 \pm 0.02\,\text{eV}$. For the heat treatments between 300°C 3 min and up to 500°C 3 min the binding energies values are $E_{\text{binding}} = 156.96 \pm 0.02\,\text{eV}$. For all the remaining heat treatments from 500°C 30 min up to 700°C 30 min the values are $E_{\text{binding}} = 156.86 \pm 0.02\,\text{eV}$. These observations are different from those reported in the work by D.C. Godfrey *et al.* on the Pt(110) surface, where the binding energy was reported to always lie at 156.8 eV[72]. For our system we observe two shifts in the binding energy, first a shift up by $0.08 \pm 0.02\,\text{eV}$ (not 0.09 eV due to rounding) and later a shift down by $0.10 \pm 0.02\,\text{eV}$. A shift of about 0.1 eV is small compared to the normal accuracy of XPS, but these peak values are not found as absolute values. Due to the calibration they are found as the difference between two peaks (between this one and the Pt $4f_{7/2}$-peak which is assumed to be constant) and such a difference is much more accurate that the absolute values. We are assuming that it is indeed possible to measure differences of this size in the way described above. The next subject is the uncertainty in the fitting. On this subject it has been tested extensively what kind of uncertainties the fitting procedure brings into the data processing, this has been done by studying the consequence of varying peak shapes, constrictions and background and fitting ranges. The results show that within the ranges where these can be expected to vary, the resulting differences in the results are indeed very small and it is those values that has been provided as uncertainties on the values above.

Returning to the interpretation of these shifts it is noticed that the first shift coincides with the increase in Bi to Pt ratio, which from the STM images can be seen to coincide with a change in the bismuth layer from an unordered to an ordered overlayer. It is hypothesized that this shift might originate from the change in electronic structure that follows from an organization into a more crystalline structure. The second shift is observed to almost coincide with the drop in Bi to Pt intensity associated with the removal of bismuth in excess of the first layer. The points that does not match are the 500°C 3 min points where the intensity ratio has already dropped but the binding energy value has not. There can be two different possible explanations for this shift. It could be associated with the reduction to a single overlayer, as it is very likely that the first layer of bismuth has a different electronic environment than the rest, but the 500°C 3 min values seems to disagree with this interpretation. The other possibility is that the change in binding energy is due to alloying, in which case the point at which the value drops is simply the value where there is energy enough available to facilitate the change. In literature it is seen, that e.g. in the work by Greeley *et al.* the electro-deposited samples were heated in air at 500°C for 12 hours to make the alloy[7]. However Paffett *et al.* mentions the possibility of an alloy on the UHV Bi/Pt(111) system already at ∼370°C[76]. This information does however not make it possible to conclude whether an alloying actually takes place or not, so at this point it is only possible to say that it is a possibility.

4.3.2 STM results

Overview

In figure 4.4 a set of $50 \times 50\,\mathrm{nm}^2$ STM images are collected to give an overview of the structure development as a function of increasing heat treatments. In the image of the sample after deposition it is seen, that the surface has a very rough look and there are no indications of the overlayers being crystalline. In the image after the lowest temperature heat treatment at 300°C for 3 min the surface structure now looks quite different. It displays large islands with flat terraces separated by well defined steps. Furthermore, there is also a periodic structure visible on the terraces (described in detail later). This all indicate that the surface has now rearranged itself into a crystalline structure. The heights of the steps on the islands span a wide range from 0.15 nm to 13.0 nm. These observations fit very well with the "3D-island" structure previously proposed by Paffett *et al.* to exits under these conditions. Between 27°C and 407°C they observed a increase in the Pt AES signal, but no bismuth left the surface. This lead to the hypothesis that either the bismuth alloyed into the surface or it rearranged itself into high 3D-islands, thus leaving large areas with much less bismuth covering the platinum[76]. This 3D-island hypothesis including the temperature range fits well with our observations.

In the 500°C images there are no longer any islands visible. This corresponds nicely with the coverage decrease that was observed when going to this temperature. According to the XPS measurements this is where the coverage should be down to about 1 ML. Furthermore, the height of the steps are measured to 0.22 ± 0.01 nm which is very close to the Pt(111) step height of 0.23 nm, suggesting that the observed steps

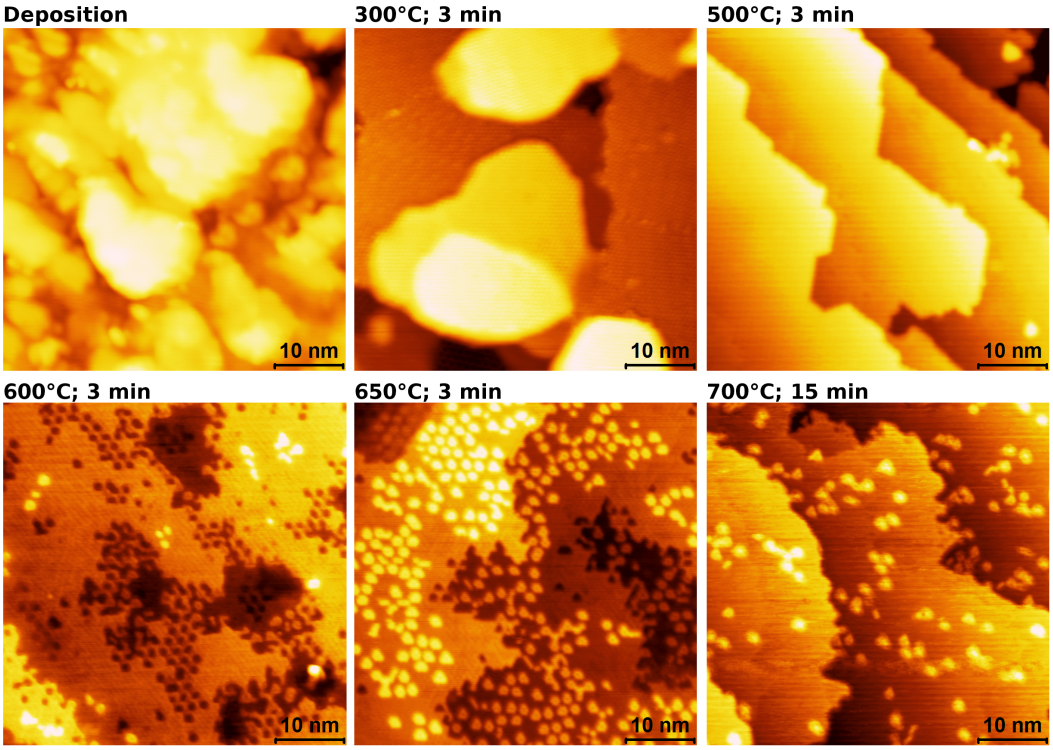

Figure 4.4: 50×50 nm^2 STM images after deposition and after different heat treatments. The image parameters are: Top left) 1.24 V, 0.54 nA; top middle) 1.25 V, 0.26 nA; top right) 1.25 V, 0.49 nA; bottom left) -0.30 V, -0.44 nA; bottom middle) 0.32 V, 0.41 nA; bottom right) 0.05 V, 0.38 nA.

might indeed be the steps of the substrate. It should however be noticed, that the steps are not nearly as smooth and parallel as the substrate was before deposition. This could indicate that either there is still slightly more bismuth present than what is needed for a single layer or that the substrate has gone through a structure change during the process.

The bottom three images in figure 4.4 are of the surface after the 600°C 3 min, 650°C 3 min and 700°C 15 min heat treatments. These images shows a continued development of the surface. In the 600°C 3 min images, holes have started to form. Some of these holes have gathered into larger holes and in a few places there also appear to be small particles, having roughly the same size as the holes. Proceeding to the 650°C 3 min image, there are now only large holes, indicating that the small ones that were present in the previous images have now joined. It is also seen that there are now many more of the particles present. At 700°C 15 min there are no more holes and only very few particles left. Remembering from XPS results that this is the heat treatment regime in which the coverage drops from 1 ML and downwards these observations could correspond to this single bismuth overlayer dissolving. The fate of the bismuth however is still uncertain. Both evaporation and alloying would be observed as a drop in XPS intensity and these images does not allow us to make the distinction. From the work of Paffett it is known however that bismuth does leave the surface in the temperature regime[76], which would indicate evaporation. An interesting feature of these images is the way that the bismuth layer dissolves, whether it is due to alloying or evaporation. Instead of this process taking place

from a step, holes are observed to form in the surface, some times in the middle of the terraces and they do so at a semi-regular distances in a pattern. At the same time particles are observed to form, but they are often observed to form from a hole, indicating that they are in fact not being formed on the terraces, but are simply what is left after the layer has become sufficiently full of holes. It is worth remembering at this point that a structure with holes in a bismuth overlayer has been observed before in the electrochemical STM work by Kim *et al*[71]. In that work however the holes were not nearly as regularly shaped as on our surfaces, which is not surprising as there is much more interaction with the environment in an electrochemical cell.

In the following sections a set a images with atomic resolution of these surfaces will be presented, to shed more light on the structure of them.

300°C 3 min

Figure 4.5(a) shows an atomic resolution image of the surface after the 300°C 3 min heat treatment. Here two different periodic structures are observed. At the bottom level there is a regular hexagonal structure with a periodicity of 1.03-1.04×1.15-1.16 nm and an angle between unit cell vectors of 62.7-62.8°. At all the higher levels a second regular hexagonal structure is observed with a periodicity of 0.62-0.70×0.67-0.70 nm and an angle between unit cell vectors of 64.0-69.8°. Looking back at the literature, it is noticed that the structure at the bottom level corresponds nicely with the p(4×4) structure observed by M.T. Paffett. This structure has a unit cell size of 1.11×1.11 nm and an angle between unit cell vectors of 60° and corresponds to the highest amount of bismuth that can be present in a single layer $\theta_{Bi} = 0.56$ relative to the atoms in the Pt(111) surface[76] (see also figure 4.2(b)). Clearly there is much more than a single layer of bismuth present on this surface, but if the bismuth gathers in islands, leaving areas of just a single layer exposed, then it is also likely that it will be possible to observe this most densely packed bismuth overlayer structure in these regions.

The periodicity on the higher levels of this image have we unfortunately not been able to identify. The periodicity of 0.67-0.70 nm does match with any superstructure distances relative to the Pt(111) surface, nor does it match with any of the low index surfaces of bismuth that has a hexagonal structure. Therefore, we have no structure model to propose for this other than a speculation of a form of superstructure between the p(4×4) overlayer and the extra bismuth overlayers.

Unfortunately the structures observed in this image has only been observed on multiple regions on the same sample, but not on several samples. The lack of proper reproduction means that one should be cautious about drawing any conclusions based purely on them. However, the structures observed at the bottom level has also been observed on the samples after the 500°C 3 min heat treatment. These have been properly reproduced and so lends credibility to the observations above.

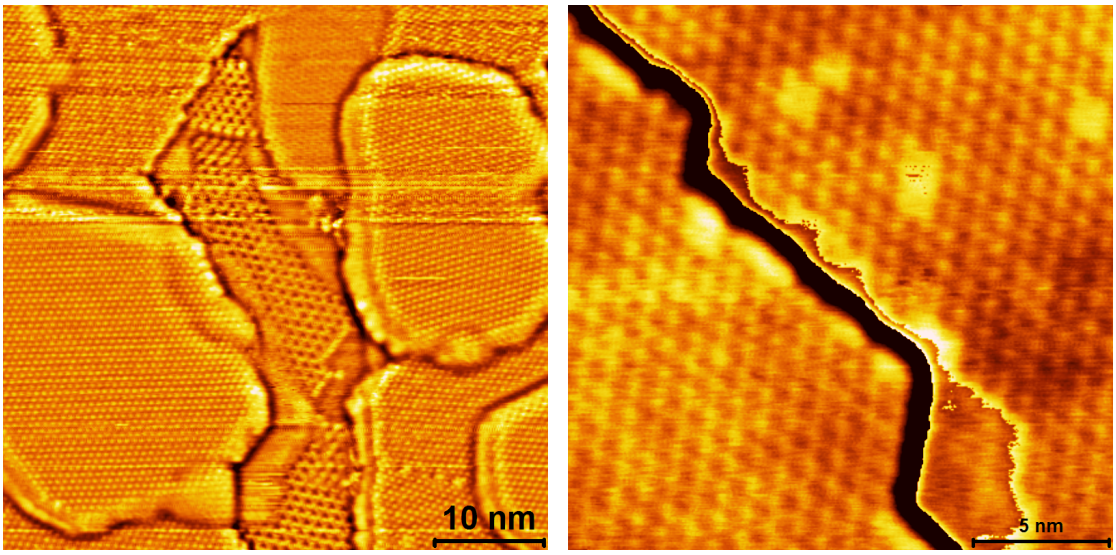

(a) $50\times50\,\mathrm{nm}^2$ **(b)** $20\times20\,\mathrm{nm}^2$

Figure 4.5: **(a)** and **(b)** are STM images after the 300°C 3 min and 500°C 3 min heat treatments respectively. Image parameters are 1.25 V, 0.26 nA for **(a)** and 0.19 V, 0.54 nA for **(b)**. In image **(b)** the average height has been set to zero in three different regions to highlight the details without the use of a derivative image.

500°C 3 min

Figure 4.5(b) shows an STM image of the surface after the 500°C 3 min heat treatment. This surface has an regular hexagonal structure measured to 1.05-1.07×1.07-1.08 nm and an angle between unit cell vectors of 62.2-65.8°. This periodicity is similar to the structure observed at the bottom level of the 300°C 3 min image, and therefore also to the p(4×4) structure observed by Paffett[76]. It is remembered from figure 4.3 that the XPS results indicate that this surface is the first one with only a single layer of bismuth present and that the overview STM image indicates a much lower coverage than before, but not quite a single layer. Comparing this with the observations of Paffett we see that this matches very well with the placement of this surface in figure 4.2(a) (highlighted by the blue 500°C line). In terms of coverage the 500°C line is a little before the single monolayer point and it is well with the range in which the p(4×4) structure was observed with LEED[76].

650°C 15 min

Figure 4.6(a) shows an STM image of the surface after the 650°C 15 min heat treatment. In this image the particles can be viewed with near atomic resolution. Besides that, there is also a region in the center bottom part, that shows near atomic resolution on the step and a structure that seems to extend out into a particle from the step. From this part of the step where we have good resolution, it appears as if it is breaking up. If this process causes the inter-atomic distance to expand that might

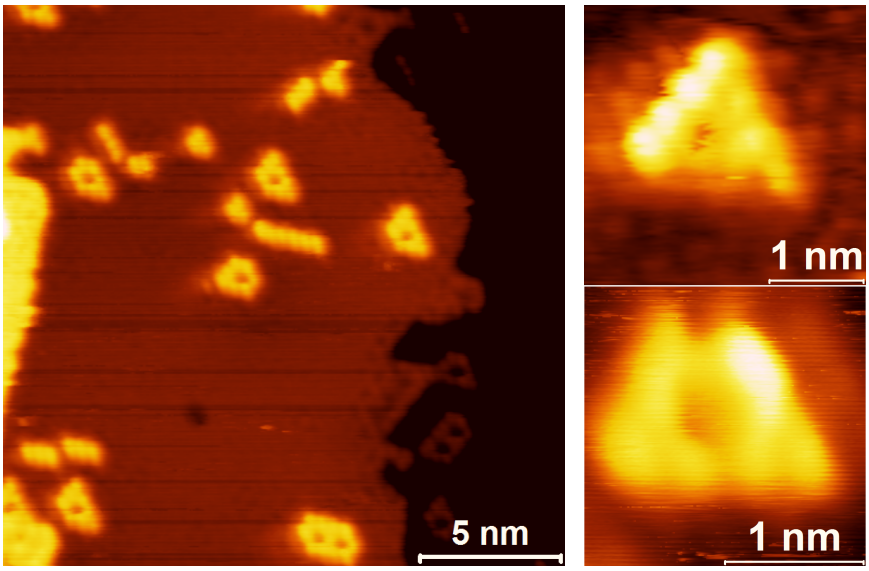

(a) $20\times20\,\mathrm{nm}^2$ **(b)**

Figure 4.6: (a) is an STM image of the surface after the 650°C 15 min heat treatment. Image parameters are 0.34 V, 0.41 nA. **(b)** are a few close up images of the particles with (near) atomic resolution.

explain why this good resolution is only observed at the edge of the step. Furthermore, the part of the image where the step seems to extend into a particle could support the idea of these particles form when the bismuth layer dissolves enough so that it is not coherent anymore.

There are a few images of the sample in the heat treatment range from 600°C 3 min to 650°C 30 min (see figure 4.6(b)) that has good enough resolution to make it possible to fit a hexagonal grid to the atoms in the particles. These measurement gave an angle between unit cell vectors of 57.0-66.3° and an inter-atomic distance of 0.33-0.46 nm. Looking back at the interatomic distances of the LEED structures proposed by Paffett, they are 0.37, 0.42 and 0.48 nm for the p(4 × 4), p(3 × 3) and $(\sqrt{3}\times\sqrt{3})R30°$ structures, which correspond to the 377-507°C, ∼623°C and ∼671°C temperature ranges respectively[76]. The observation we make are close to the range of inter-atomic distances previously reported for these temperatures. Unfortunately we do not have enough images of sufficient quality to make a proper statistical determination about whether our measurement show a larger portion of inter-atomic distances around the overlayer LEED value reported by Paffett. At this point it is then only possible to say that these results raise the possibility that the periodicities reported from the LEED studies might in fact also partially be formed by particles and not only by complete overlayers.

4.4 Summary

In this study the bismuth overlayers on Pt(111) after different heat treatments were studied with STM and XPS. The ratio of bismuth to platinum from XPS intensi-

ties was seen to increase from the measurement after deposition to the first heat treatment at 300°C 3 min, and it was hypothesized that this increase was due to a structure change of the overlayers. The XPS ratio remains roughly constant until the heat treatment to 500°C 3 min at which point it drops to about 1 ML and then continues to drop with higher heat treatments. The observed binding energies of the Bi $4f_{7/2}$ peak was seen to go through two small shifts. It was observed to shift up by 0.08 eV±0.02 between the deposition measurement and the first heat treatment and shift down 0.10 eV±0.02eV between the heat treatments of 500°C 3 min and 500°C 30 min. For the first shift it was hypothesized, that it originated from the same structure change that was hypothesized from the coverage measurements and which is visible in the STM images. For the second shift two possibilities was presented. Either it originates from the reduction of the coverage to just a single layer or it originate from an alloying. The coverage possibility suffers because the shift and the coverage drop does not exactly correspond, with the 500°C 3 min treatment being the point of conflict. Therefore, the strongest possibility is the alloying, but since we have no extra results to back it up, it remains a hypothesis.

From the overview STM images it was observed that the deposition resulted in a rough surface and that this surfaces was straightened out into a crystalline surface at the first heat treatment to 300°C 3 min. This surface also showed islands formation in correspondence with previous reports[76] and as a preliminary results showed two periodicities. At the lower levels was a hexagonal 1.03-1.04×1.15-1.16 nm 62.7-62.8° structure that matches nicely with the p(4×4) overlayer structure and at the higher levels an unidentified hexagonal 0.62-0.70×0.67-0.70 nm 64.0-69.8° structure. In the 500°C 3 min sample there is no longer any islands and the surface is reduced to a flat layer with the step heights of the underlying platinum, which indicates just a single layer. It also shows a hexagonal periodicity of 1.05-1.07×1.07-1.08 nm 62.2-65.8° once again indicative of the p(4×4) structure. On the higher heat treatment samples, a continued development is observed, in which the overlayer seem to dissolve by forming holes until the holes become connected and the remaining material appears as particles. This is consistent with the slow decrease in coverage observed from the XPS coverage measurements, but it is uncertain whether this reduction in observed coverage is due purely to evaporation, which is known to take place[76], or also due to alloying. As preliminary results it is observed in some images with atomic resolution of the particles, that they have an inter-atomic distance close to those reported previously from LEED studies for overlayer structures[76]. This therefore raises the possibility that some of the LEED observations were in fact due not only to complete layers but also has a contribution from particles.

Chapter 5

Summary and outlook

As mentioned in the general introduction, the main theme and common component throughout the different projects, has been the real space identification of catalytically relevant surface structures and the correlation between such structures and the catalytic activity. This has been achieved by the use of STM as the primary technique. Since the individual results for the different projects has already been summarized in sections 3.12 and 4.4, here only the main points, and the way in which the STM has contributed to these results will be summarized and possible future research within these subjects will be proposed.

In the low CO dose work on the Ru(0 1 54) sample it was possible, by means of the STM, to provide real space image evidence to support the conclusion that only one of the two step configurations is active for CO dissociation under the applied conditions. Even though is was one of the desired goals, it has not so far been possible to directly identify the active site purely by the use of STM. For that we needed the assistance of the theoreticians, in the form of DFT calculations, but it is still a goal and hopefully it can be achieved in the future. To achieve this it will either be necessary to continue the current line of research and hope to get images of even better quality, or to think of another kind if system where the identification of the step types is easier.

In the high CO dose work on the Ru(0 1 54) sample unfortunately only preliminary results was obtained. But even with the preliminary status of these results it seems clear, that the STM images can provide unique insight into the difference in behavior between the steps and how this difference correlate with the carbon uptake results (described in detail in sections 3.1 and 3.10). For future work it is proposed to continue along the current line of experiments, to confirm the current observations and to achieve more results for more different dose lengths. It would also be very interesting to extend the study with high pressure doses, where the carbon uptake has previously been shown to have a significantly different behavior (see previously mentioned sections).

The ruthenium structure cross over work concerned itself mainly with correlating the structures of samples with the CO desorption behavior, and to show that this behavior could be shifted between two different characteristic states. As such, STM played an instrumental role in characterization of the sample structures, which was necessary in order to make this kind of study. In the future it would be interesting to study the transitions from one behavior to the other in more detail. But of much

more general interest, it would be interesting to see if the conclusions drawn in this study extends to other catalytically relevant materials as well.

In the Bi/Pt(111) study, the circumstances of the results transformed the project from a structure vs. reactivity study to a more fundamental structure study, but still of a catalytically relevant system. In terms of the application of STM it proved helpful in confirming some of the structures that had previously been reported from the averaging structure technique LEED, but it also potentially, if the preliminary results hold through, provided knowledge about the high temperature sample structure that is not possible to obtain with LEED. In order to extend and support the conclusion drawn here, the study should be expanded to include more different temperatures in the high temperature regime.

Bibliography

[1] I. Chorkendorff and J.W. Niemantsverdriet. *Concepts of Modern Catalysis and Kinetics*. Wiley-VCH GmbH & Co., student edition, 2003.

[2] J.K. Nørskov and C.H. Christensen. Toward efficient hydrogen production at surfaces. *Science*, 312(5778):1322–1323, 2006.

[3] T. Bligaard, J.K. Nørskov, S. Dahl, J. Matthiesen, C.H. Christensen, and J. Sehested. The Bronsted-Evans-Polanyi relation and the volcano curve in heterogeneous catalysis. *JOURNAL OF CATALYSIS*, 224(1):206–217, MAY 15 2004.

[4] B. Hammer and J.K. Norskov. Electronic factors determining the reactivity of metal surfaces. *SURFACE SCIENCE*, 343(3):211–220, DEC 10 1995.

[5] A. Groß. Reactivity of Bimetallic Systems Studied from First Principles. *Topics in Catalysis*, 37(1):29–39, 2006.

[6] F. Besenbacher, I. Chorkendorff, and B.S. Clausen. Design of a Surface Alloy Catalyst for Steam Reforming. *Science*, 279(5358):1913–1915, 1998.

[7] J. Greeley, T.F. Jaramillo, J. Bonde, I. Chorkendorff, and J.K. Nørskov. Computational high-throughput screening of electrocatalytic materials for hydrogen evolution. *Nature Materials*, 5(11):909–13, 2006.

[8] N. Schumacher, K. Andersson, L.C. Grabow, M. Mavrikakis, J. Nerlov, and I. Chorkendorff. Interaction of carbon dioxide with Cu overlayers on Pt(111). *Surface Science*, 602(3):702–711, 2008.

[9] M. Mavrikakis, B. Hammer, and J.K. Nørskov. Effect of Strain on the Reactivity of Metal Surfaces. *Phys. Rev. Lett.*, 81(13):2819–2822, Sep 1998.

[10] S. Dahl, A. Logadottir, R.C. Egeberg, J.H. Larsen, I. Chorkendorff, E. Törnqvist, and J.K. Nørskov. Role of steps in N_2 activation on Ru(0001). *Physical Review Letters*, 83(9):1814–17, 1999.

[11] J.V. Lauritsen, M. Nyberg, J.K. Nørskov, B.S. Clausen, H. Topsoe, E. Lægsgaard, and F. Besenbacher. Hydrodesulfurization reaction pathways on MoS_2 nanoclusters revealed by scanning tunneling microscopy. *JOURNAL OF CATALYSIS*, 224(1):94–106, MAY 15 2004.

[12] T.F. Jaramillo, K.P. Jørgensen, J. Bonde, J.H. Nielsen, S. Horch, and I. Chorkendorff. Identification of Active Edge Sites for Electrochemical H_2 Evolution from MoS_2 Nanocatalysts. *Science*, 317(5834):100–102, 2007.

[13] M. Bowker. Catalysis resolved using scanning tunnelling microscopy. *Chem. Soc. Rev.*, 36:1656 – 1673, 2007.

[14] F. Besenbacher, K. Laegsgaard, K. Mortensen, U. Nielsen, and I. Stensgaard. Compact high-stability 'thimble-size' scanning tunneling microscope. *Review of Scientific Instruments*, 59(7):1035–8, 1988.

[15] K. Nielsen. Characterization of nanoscale structure of surfaces using scanning tunnel microscopy. Master's thesis, Technical University of Denmark (DTU), 2008.

[16] G. BINNIG and H. ROHRER. SCANNING TUNNELING MICROSCOPY. *HELVETICA PHYSICA ACTA*, 55(6):726–735, 1982.

[17] J. Tersoff and D.R. Hamann. Theory and application for the scanning tunneling microscope. *Physical Review Letters*, 50(25):1998–2001, 1983.

[18] J. Tersoff and D.R. Hamann. Theory of the scanning tunneling microscope. *Physical Review B (Condensed Matter)*, 31(2):805–13, 1985.

[19] J. Bardeen. Tunnelling from a many-particle point of view. *Physical Review Letters*, 6(2):57–59, 1961.

[20] N.D. Lang. Theory of single-atom imaging in the scanning tunneling microscope. *Physical Review Letters*, 56(11):1164–7, 1986.

[21] Århus University SPM group.
Website: http://phys.au.dk/forskning/condensed-matter-physics/spm/.

[22] SPIP software, Image metrology website.
Website:http://www.imagemet.com/.

[23] J.M. Thomas and W.J. Thomas. *Principles and Practice of Heterogeneous Catalysis* . VCH Verlagsgesellshaft mbH, Weinheim and VCH Publishers Inc., New York, NY, 1997.

[24] I. Chorkendorff. Experimental Surface Physics, 2004.

[25] C.D. Wagner, Riggs W.M., Davis L.E., and Moulder J.F. *Handbook of X-ray photoelectron spectroscopi.* Perkin-Elmer Corporation, 1978.

[26] NIST X-ray Photoelectron Spectroscopy Database.
Website: http://srdata.nist.gov/xps/.

[27] J.L. Olsen. *Heterogeneous catalysis in highly sensitive microreactors.* PhD thesis, Technical University of Denmark (DTU), 2010. Section 2.4.

[28] S.B. Vendelbo. *Structure Sensitivity of CO Dissociation and the Methanation Reaction of a Ruthenium Single Crystal.* PhD thesis, Technical University of Denmark (DTU), 2010.

[29] H. Pfnur, P. Feulner, H.A. Engelhardt, and D. Menzel. Example of fast desorption - anomalously high pre-exponentials for CO desorption from Ru (001). *CHEMICAL PHYSICS LETTERS*, 59(3):481–486, 1978.

[30] H. Pfnur, P. Feulner, and D. Menzel. The influence of adsorbate interactions on kinetics and equilibrium for CO on Ru(001) .2. desorption-kinetics and equilibrium. *JOURNAL OF CHEMICAL PHYSICS*, 79(9):4613–4623, 1983.

[31] E. Shincho, C. Egawa, S. Naito, and K. Tamaru. The behavior of CO adsorbed on Ru(1,1,10) and Ru(001) - the dissociation of CO at the step sites of the Ru(1,1,10) surface, 1985.

[32] T. Zubkov, G.A. Morgan, J.T. Yates, O. Kuhlert, M. Lisowski, R. Schillinger, D. Fick, and H.J. Jansch. The effect of atomic steps on adsorption and desorption of CO on Ru(109). *SURFACE SCIENCE*, 526(1-2):57–71, FEB 20 2003.

[33] S. Vendelbo, M. Johansson, D. Mowbray, M. Andersson, F. Abild-Pedersen, J. Nielsen, J. Nørskov, and I. Chorkendorff. Self Blocking of CO Dissociation on a Stepped Ruthenium Surface. *Topics in Catalysis*, 53:357–364, 2010. 10.1007/s11244-010-9445-4.

[34] H. Schulz. Short history and present trends of Fischer-Tropsch synthesis. *APPLIED CATALYSIS A-GENERAL*, 186(1-2):3–12, OCT 4 1999.

[35] E.D. WILLIAMS and W.H. WEINBERG. GEOMETRIC STRUCTURE OF CARBON-MONOXIDE CHEMISORBED ON THE RUTHENIUM (001) SURFACE AT LOW-TEMPERATURE. *SURFACE SCIENCE*, 82(1):93–101, 1979.

[36] G. MICHALK, W. MORITZ, H. PFNUR, and D. MENZEL. A LEED DETERMINATION OF THE STRUCTURES OF RU(001) AND OF CO/RU(001)-SQUARE-ROOT 3X SQUARE-ROOT 3 R30-DEGREES. *SURFACE SCIENCE*, 129(1):92–106, 1983.

[37] H. Pfnur and D. Menzel. The influence of adsorbate interactions on kinetics and equilibrium for CO on Ru(001) .1. adsorption-kinetics. *JOURNAL OF CHEMICAL PHYSICS*, 79(5):2400–2410, 1983.

[38] F.B. de Mongeot, M. Scherer, B. Gleich, E. Kopatzki, and R.J. Behm. CO adsorption and oxidation on bimetallic Pt/Ru(0001) surfaces - a combined STM and TPD/TPR study. *SURFACE SCIENCE*, 411(3):249–262, AUG 25 1998.

[39] P. Jakob, M. Gsell, and D. Menzel. Interactions of adsorbates with locally strained substrate lattices. *The Journal of Chemical Physics*, 114(22):10075–10085, 2001.

[40] K. Meinel, H. Wolter, Ch. Ammer, A. Beckmann, and H. Neddermeyer. Adsorption stages of O on Ru(0001) studied by means of scanning tunnelling microscopy. *Journal of Physics: Condensed Matter*, 9(22):4611, 1997.

[41] J. Wintterlin, J. Trost, S. Renisch, R. Schuster, T. Zambelli, and G. Ertl. Real-time STM observations of atomic equilibrium fluctuations in an adsorbate system: O/Ru(0001). *Surface Science*, 394(1-3):159 – 169, 1997.

[42] M. Gsell, P. Jakob, and D. Menzel. Effect of substrate strain on adsorption. *SCIENCE*, 280(5364):717–720, MAY 1 1998.

[43] J. Trost T. Zambelli, J. Wintterlin and G. Ertl. Identification of the "Active Sites" of a Surface-Catalyzed Reaction. *Science*, 273:1688–1690, 1996.

[44] J. Wintterlin and T. Zambelli. Active sites at finite coverages - an STM investigation of the dissociation of NO on Ru(0001). *ZEITSCHRIFT FUR PHYSIKALISCHE CHEMIE-INTERNATIONAL JOURNAL OF RESEARCH IN PHYSICAL CHEMISTRY & CHEMICAL PHYSICS*, 219(7):997–1017, 2005.

[45] C. Corriol, F. Calleja, A. Arnau, J.J. Hinarejos, A.L. Vázquez de Parga, W.A. Hofer, and R. Miranda. Role of surface geometry and electronic structure in STM images of O/Ru(0 0 0 1). *Chemical Physics Letters*, 405(1-3):131 – 135, 2005.

[46] T.K. Shimizu, A. Mugarza, J.I. Cerda, and M. Salmeron. Structure and reactions of carbon and hydrogen on Ru(0001): A scanning tunneling microscopy study. *JOURNAL OF CHEMICAL PHYSICS*, 129(24):244103, DEC 28 2008.

[47] M.C. WU, Q. XU, and D.W. GOODMAN. INVESTIGATIONS OF GRAPHITIC OVERLAYERS FORMED FROM METHANE DECOMPOSITION ON RU(0001) AND RU(11(2)OVER-BAR-0) CATALYSTS WITH SCANNING-TUNNELING-MICROSCOPY AND HIGH-RESOLUTION ELECTRON-ENERGY-LOSS SPECTROSCOPY. *JOURNAL OF PHYSICAL CHEMISTRY*, 98(19):5104–5110, MAY 12 1994.

[48] S. Marchini, S. Gunther, and J. Wintterlin. Scanning tunneling microscopy of graphene on Ru(0001). *Physical Review - Section B - Condensed Matter*, 76(7):75429, 2007.

[49] K. Donner and P. Jakob. Structural properties and site specific interactions of Pt with the graphene/Ru(0001) moire overlayer. *JOURNAL OF CHEMICAL PHYSICS*, 131(16):164701, OCT 28 2009.

[50] Z. Zhou, F. Gao, and D.W. Goodman. Deposition of metal clusters on single-layer graphene/Ru(0001): Factors that govern cluster growth. *SURFACE SCIENCE*, 604(13-14):L31–L38, JUL 15 2010.

[51] D.W. Goodman. Model catalytic studies over metal single-crystals. *ACCOUNTS OF CHEMICAL RESEARCH*, 17(5):194–200, 1984.

[52] R.D. Kelley and D.W. Goodman. Catalytic methanation over single-crystal nickel and ruthenium - reaction-kinetics on different crystal planes and the correlation of surface carbide concentration with reaction-rate. *SURFACE SCIENCE*, 123(2-3):L743–L749, 1982.

[53] M.P. Andersson, E. Abild-Pedersen, I.N. Remediakis, T. Bligaard, G. Jones, J. Engbæk, O. Lytken, S. Horch, J.H. Nielsen, J. Sehested, J.R. Rostrup-Nielsen, J.K. Nørskov, and I. Chorkendorff. Structure sensitivity of the methanation reaction: H_2-induced CO dissociation on nickel surfaces. *JOURNAL OF CATALYSIS*, 255(1):6–19, APR 1 2008.

[54] T. Zubkov, G.A. Morgan, and J.T. Yates. Spectroscopic detection of CO dissociation on defect sites on Ru(109): implications for Fischer-Tropsch catalytic chemistry. *CHEMICAL PHYSICS LETTERS*, 362(3-4):181–184, AUG 19 2002.

[55] S.B. Vendelbo, M. Johansson, J.H. Nielsen, and I. Chorkendorff. Is the methanation reaction over Ru single crystals structure dependent? *PHYSICAL CHEMISTRY CHEMICAL PHYSICS*, 13(10):4486–4493, 2011.

[56] M. Mavrikakis, M. Baumer, H.J. Freund, and J.K. Nørskov. Structure sensitivity of CO dissociation on Rh surfaces. *CATALYSIS LETTERS*, 81(3-4):153–156, 2002.

[57] S. Dahl, E. Törnqvist, and I. Chorkendorff. Dissociative Adsorption of N_2 on Ru(0001): A Surface Reaction Totally Dominated by Steps. *Journal of Catalysis*, 192(2):381, 2000.

[58] C.J.H. Jacobsen, S. Dahl, P.L. Hansen, E. Tornqvist, L. Jensen, H. Topsoe, D.V. Prip, P.B. Moenshaug, and I. Chorkendorff. Structure sensitivity of supported ruthenium catalysts for ammonia synthesis. *JOURNAL OF MOLECULAR CATALYSIS A-CHEMICAL*, 163(1-2):19–26, DEC 4 2000.

[59] C. Holse. Investigation of Gas Induced Step Changes on Ruthenium Single Crystal Surfaces. Master's thesis.

[60] DACAPO Simulation Code. Available from: https://wiki.fysik.dtu.dk/dacapo.

[61] B. Hammer, L. B. Hansen, and J. K. Nørskov. Improved adsorption energetics within density-functional theory using revised Perdew-Burke-Ernzerhof functionals. *Phys. Rev. B*, 59(11):7413–7421, Mar 1999.

[62] D. Vanderbilt. Soft self-consistent pseudopotentials in a generalized eigenvalue formalism. *Phys. Rev. B*, 41(11):7892–7895, Apr 1990.

[63] I.M. Ciobica and R.A. van Santen. Carbon monoxide dissociation on planar and stepped Ru(0001) surfaces. *JOURNAL OF PHYSICAL CHEMISTRY B*, 107(16):3808–3812, APR 24 2003.

[64] B. Hendriksen. *Model Catalysts in Action - High-Pressure Tunneling Microscopy*. PhD thesis, Leiden University, 2003.

[65] T. Yamada, Y. Iwasawa, and K. Tamaru. The isotope exchange reaction of carbon monoxide on Ru(0001), single crystal surfaces. *Surface Science*, 223(3):527 – 550, 1989.

[66] T.J. Schmidt, V.R. Stamenkovic, C.A. Lucas, N.M. Markovic, and P.N. Ross Jr. Surface processes and electrocatalysis on the Pt(hkl)/Bi-solution interface. *Physical Chemistry Chemical Physics*, 3(18):3879–3890, 2001.

[67] R. Gómez, A. Fernandezvega, J.M. Feliu, and A. Aldaz. Hydrogen Evolution on Pt Single Crystal Surfaces - Effects of Irreversibly Adsorbed Bismuth and Antimony on Hydrogen Adsorption and Evolution on Pt(100). *Journal of Physical Chemistry*, 97:4769–4776, 1993.

[68] R. Gómez, J.M. Feliu, and A. Aldaz. Effects of irreversibly adsorbed bismuth on hydrogen adsorption and evolution on Pt(111). *Electrochimica Acta*, 42(11):1675–1683, 1997.

[69] J. CLAVILIER, A. FERNANDEZVEGA, J.M. FELIU, and A. ALDAZ. HETEROGENEOUS ELECTROCATALYSIS ON WELL DEFINED PLATINUM SURFACES MODIFIED BY CONTROLLED AMOUNTS OF IRREVERSIBLY ADSORBED ADATOMS .1. FORMIC-ACID OXIDATION ON THE PT (111) - BI SYSTEM. *JOURNAL OF ELECTROANALYTICAL CHEMISTRY*, 258(1):89–100, JAN 10 1989.

[70] J. CLAVILIER, A. FERNANDEZVEGA, J.M. FELIU, and A. ALDAZ. HETEROGENEOUS ELECTROCATALYSIS ON WELL-DEFINED PLATINUM SURFACES MODIFIED BY CONTROLLED AMOUNTS OF IRREVERSIBLY ADSORBED ADATOMS .3. FORMIC-ACID OXIDATION ON THE PT(100)-BI SYSTEM. *JOURNAL OF ELECTROANALYTICAL CHEMISTRY*, 261(1):113–125, MAR 24 1989.

[71] J. Kim and C.K. Rhee. Ensemble size estimation in formic acid oxidation on Bi-modified Pt(111). *Electrochemistry Communications*, 12:1731–1733, 2010.

[72] D.C. Godfrey, B.E. Hayden, A.J. Murray, R. Parsons, and D.J. Pegg. Bismuth adsorption on Pt(110) and the coadsorption of carbon monoxide. *Surface Science*, 294(1-2):33–42, 1993.

[73] M.T. Paffett, C.T. Campbell, R.G. Windham, and B.E. Koel. A multitechnique surface analysis study of the adsorption of H_2, CO and O_2 on Bi/Pt(111) surfaces. *Surface Science*, 207(2-3):274–296, 1989.

[74] E. Casado-Rivera, D.J. Volpe, L. Alden, C. Lind, C. Downie, T. Vazquez-Alvarez, A.C.D. Angelo, F.J. DiSalvo, and H.D. Abruna. Electrocatalytic Activity of Ordered Intermetallic Phases for Fuel Cell Applications. *Journal of the American Chemical Society*, 126(12):4043–4049, 2004.

[75] M.T. Paffett, C.T. Campbell, and T.N. Taylor. The influence of adsorbed Bi on the chemisorption properties of Pt(111): H_2, CO, and O_2. *Journal of Vacuum Science & Technology A (Vacuum, Surfaces, and Films)*, 3(3):812–16, 1985.

[76] M.T. Paffett, C.T. Campbell, and T.N. Taylor. Adsorption and growth modes of Bi on Pt(111). *Journal of Chemical Physics*, 85(10):6176–85, 1986.

[77] M.T. Paffett, C.T. Campbell, T.N. Taylor, and S. Srinivasan. Cu adsorption on Pt(111) and its effects on Chemisorption: A comparison with electrochemistry. *Surface Science*, 154(1):284–302, 1985.

[78] T. Michely and G. Comsa. Temperature dependence of the sputtering morphology of Pt(111). *Surface Science*, 256(3):217–226, 1991.

[79] http://www.casaxps.com/.

[80] Ph. Hofmann. The surfaces of bismuth: Structural and electronic properties. *Progress in Surface Science*, 81(5):191–245, read 194–197 and 202–207, 2006.

Included papers

Paper I:

STM evidence for the dissociation of carbon monoxide on ruthenium steps

Yann Tison, **Kenneth Nielsen**, Lone Bech, Christian Holse, and Jane H. Nielsen
CINF
Duncan J. Mowbray, Federico Calle Vallejo, Kirsten Andersen,
Jens J. Mortensen, and Karsten W. Jacobsen
CAMd
In preparation (included lastest version)

Paper II:

Probing the crossover in CO desorption from single crystal to nanoparticulate Ru model catalysts

S. Murphy, C. Strebel, S. B. Vendelbo, C. Conradsen, Y. Tison,
K. Nielsen, L. Bech, R. M. Nielsen, M. Johansson, I. Chorkendorff
and J. H. Nielsen
Published in Phys. Chem. Chem. Phys. **13**, 10333-10341 (2011)

Paper III:

Dissolution structures of Bi overlayers on Pt(111)

Kenneth Nielsen, Yann Tison, Lone Bech, Jane H. Nielsen
In preparation, abstract included

Other publications

Paper IV:

Combined spectroscopy and microscopy of supported MoS_2 nanoparticles

J.H. Nielsen, L. Bech, **K. Nielsen**, Y. Tison, K.P. Jørgensen, J.L. Bonde,
S. Horch, T.F. Jaramillo and I. Chorkendorff
Published in Surface Science **603**, 1182-1189 (2009)

STM evidence for the dissociation of carbon monoxide on ruthenium steps

Yann Tison, Kenneth Nielsen, Lone Bech, Christian Holse, and Jane H. Nielsen

CINF

Duncan J. Mowbray,* Federico Calle Vallejo, Kirsten Andersen, Jens J. Mortensen, and Karsten W. Jacobsen

CAMd

(Dated: July 7, 2011)

Abstract

In heterogeneous catalysis, identifying the active site for key reaction steps is necessary for optimising industrial synthesis. For instance, the structure sensitivity of CO dissociation on a metal catalyst, which is the rate limiting step for the methanation and the Fischer-Tropsch processes, has been debated for years. Here, scanning tunnelling microscopy and density functional theory are used in order to clarify the role of monoatomic steps in the splitting of CO on a stepped Ru(0 1 54) crystal, which displays alternating steps with either 4-fold or 3-fold symmetry. After CO doses at elevated temperatures, the STM images reveal step decorations characteristic of atomic oxygen resulting from CO dissociation on every second step. The confrontation of the STM images with the results of DFT calculations showed that the step decorations occur on the steps displaying the 4-fold symmetry. Hence, the active sites for CO dissociation on ruthenium are located on this type of monoatomic steps.

*Now at: Nano-bio spectroscopy Group and ETSF scientific Development Center, Depto. Física de Materiales, Universidad del País Vasco and DIPC, E-20018, San-Sebastian, Spain

I. INTRODUCTION

CO dissociation is considered to play an important role in industrially relevant reactions such as the methanation reaction or the Fischer-Tropsch process, involved in the preparation of synthetic fuels [1][2][3]. Various metal catalysts such as iron, cobalt, nickel or ruthenium can be used in those processes, usually in the form of nanoparticles supported on a carbon or a metal oxide substrate [1]. Despite the scarcity of ruthenium [4], it is of interest to elucidate the mechanism of these chemical reactions on a ruthenium surface since this metal is known for being a better catalyst than the more widely used cobalt or nickel for both the Fischer-Tropsch [1] and the methanation reactions. In early studies, Goodman and co-workers measured the rate of methane formation for various facets of nickel and ruthenium, as well as for supported catalysts [5][6]. For both metals, these authors did not notice any significant change between the activation energies obtained for the different facets and the supported particles. This observation lead them to suggest that the methanation reaction is not structure sensitive. However, later studies, based on catalytic tests, scanning tunnelling microscopy (STM) and density functional theory (DFT) calculations have highlighted the importance of monoatomic steps for CO dissociation on Ni(111) under ultra high vacuum conditions [3]. In the case of ruthenium, isotopic scrambling experiments on stepped surfaces clearly showed that step sites are more efficient at splitting CO than terraces [7][8]. Recently, in our group, Vendelbo *et al.* highlighted the role of steps and the accumulation of carbon on the surface by means of temperature programmed desorption (TPD) and carbon uptake measurements on a Ru(0 1 54) single crystal, together with DFT calculations [9]. These results were further confirmed by high pressure methanation and step blocking experiments [10].

It is of interest to mention that ruthenium is also a good catalyst for other processes such as ammonia synthesis. For instance, Dahl *et al.* used thermal rate measurements combined with step blocking experiments to demonstrate that the active site for N_2 dissociation, which is the rate limiting step for ammonia synthesis, is located at the monoatomic steps on a Ru(0 0 1) surface [11]. Furthermore, in the same work, DFT calculations allowed to identify particular sites, the so-called B5 sites, as the sites responsible for the activation of N_2 on the surface of a ruthenium single crystal. Later studies also revealed the importance of steps for supported Ru catalysts, suggesting an optimum ac-

tivity for 2 nm Ru nanoparticles, for which the abundance of step-like sites is the highest [12].

The aforementioned studies are based on averaging techniques and do not bring a localized experimental insight into individual catalytic processes. This crucial information could nevertheless be provided by microscopy techniques. The use of scanning probe microscopies, and more particularly STM, have been extremely fruitful at bringing insight into catalytic processes [13]. Diverse types of samples have been considered, such as low Miller indices surfaces on single-crystals, nanoparticles on various atomically flat substrates and thin films of oxides. High pressure STM measurements have been used to show the effect of reactive gases on the catalyst surface; as an example, Tao *et al.* evidenced the reconstruction of the Pt(5 5 7) and Pt(3 3 2) surfaces into clusters as an effect of the exposure to high pressures of CO (above 0.1 bars). These observations were supported by high-pressure XPS and DFT calculations [14]. Another success of STM in reference to catalysis was, for example, to demonstrate that, for MoS_2 nanoclusters, the catalytic sites for the hydrodesulfurization process [15] and for the hydrogen evolution reaction are located on the edges of the particles [16][17].

In the case of ruthenium, STM was used by Neddermeyer's group in order to investigate the different structures adopted by an oxygen overlayer as a function of coverage. This study showed that a p(2×2) structure dominates for coverages below 0.35 ML, with a perfect ordering at 0.25 ML. For higher coverages, p(2×1) domains appear until the saturation coverage of 0.5 ML, for which these domains cover the entire surface [18]. Menzel and co-workers showed the effect of lattice strain on the adsorption of oxygen atoms at room temperature showing in particular that the p(2×2) structure is favored if the lattice spacing is slightly expanded [19][20]. Ertl and co-workers studied the behaviour of nitrogen and oxygen atoms after NO dissociation on a Ru(0 0 1) surface [21][22][23]. Their work gave evidence of the high mobility of adsorbed oxygen at low coverages, compared to nitrogen, unless an oxygen atom is either located in the vicinity of a monoatomic step or included within a cluster of oxygen atoms adopting a p(2×2) periodicity with respect to the ruthenium lattice [21]. It also allowed for the identification of the monoatomic steps as the active site for NO dissociation in UHV conditions [22][23]. During this study, the authors also observed a different behaviour depending on whether the step presents a 4-fold or a 3-fold symmetry. Although both types of steps seem to be active, a rim of oxygen

atoms is accumulated at the top of the steps with a 4-fold symmetry and progressively de-activates these steps whereas the steps with a 3-fold symmetry remain active [22]. More recently, in a series of low temperature STM experiments, Shimizu *et al.* observed the formation of C-H_x species after the dissociative adsorption of either H_2 or H_2O on a Ru(0 0 1) surface containing up to 0.03 ML of carbon impurities [24]. It is also of interest to note that defect-free graphene layers can grow over a large area of a Ru(0 0 1) single crystal and that STM was used to study the structural and electronic modifications induced by the lattice mismatch between the graphene layer and the ruthenium substrate [25][26]. An interesting aspect is the possible use of the moiré pattern observed for graphene overlayers on Ru(0 0 1) as a template for the deposition of transition metal nanoparticles [27][28].

Regarding CO adsorption, early LEED studies gave evidence that CO molecules adsorb preferably on atop sites on the Ru(0 0 1) terraces [29]. Furthermore, several periodical structures have been observed at low temperature ($110\,K$), including a $\left(\sqrt{3}\times\sqrt{3}\right)R30°$ lattice for coverages up to one third of a monolayer (ML) [29][30][31] and a $\left(2\sqrt{3}\times 2\sqrt{3}\right)R30°$ structure for coverages varying between 0.33 and 0.58 ML [30][31]. At room temperature, only the $\left(\sqrt{3}\times\sqrt{3}\right)R30°$ structure is observed and the CO overlayer is believed to be disordered for coverages higher than 0.33 ML [30][31]. The $\left(\sqrt{3}\times\sqrt{3}\right)R30°$ CO structure has also been identified in two independant STM studies [20][32]. Moreover, it is found that the images of dense CO layers (with a coverage higher than 0.33 ML) do not exhibit any discernable feature because of a weak corrugation [20]. In (CO + O) coadsorption experiments, also in ref. [20] the $\left(\sqrt{3}\times\sqrt{3}\right)R30°$ CO lattice is observed in the vicinity of monoatomic steps, on the top terrace, while a $p(2\times 2)$ periodicity corresponding to oxygen atoms with CO impurities is present further away from the step edges. This behaviour was assigned to modifications of the adsorbates' binding energies as a function of the compressive or extensive lattice strain induced by the presence of steps.

The aim of the work presented here is to directly observe the results of CO dissociation on a ruthenium catalyst under UHV conditions. Since monoatomic steps are suggested as the active sites according to several studies [7][8][9][10], special attention was devoted to these low coordination sites. In particular, we investigate whether the different step geometries (i.e. 3-fold versus 4-fold geometry) affect the reactivity towards CO splitting. For this purpose, we performed STM studies of CO dissociation on a Ru(0 1 54) stepped

surface. Theoretical STM images, calculated using DFT, were used to support our interpretation.

II. METHODS

The sample is a vicinal Ru(0 1 54) single crystal from Mateck, GmbH. Its surface presents (0 0 1) terraces with an average width of 7 nm, corresponding to 27 atomic rows, separated by monoatomic steps (figure 1). According to the hexagonal close packed structure of ruthenium, one can observe alternating structures for the monoatomic steps, namely the A-type and B-type steps. As evidenced by the close-ups in figure 1, the A steps present a 3-fold symmetry whereas a 4-fold symmetry is observed for the B steps.

All experiments were performed in a UHV chamber equipped with a STM, together with facilities for X-ray photoelectron spectroscopy (XPS), ion scattering spectroscopy (ISS) and temperature programmed desorption (TPD). The background pressure was 7×10^{-11} torr. The sample was cleaned via repeated cycles involving Ar^+ sputtering at 800 K (30 min., 1.5×10^{-7} torr), surface oxidation (O_2, 10^{-7} torr, 1100 K, 10 min.), surface reduction (H_2, 2×10^{-6} torr, 500 K, 20 min.) and annealing to 1400 K for 2 min. Sample heating is provided by an electron beam heater implemented within the manipulator. The sample cleanliness was regularly controlled with XPS and CO-TPD. All STM measurements were perfomed at room temperature in a Århus-type STM [33] working in constant current mode. STM images were typically recorded at a bias voltage of 1 V or lower and tunnelling currents of 0.4-1 nA. The software package SPIP [34] was used to process the images. Typical image treatment include plane correction, noise removal using a median filter and derivation of the height along the fast-scan axis in order to emphasize small features on the image. Atomic resolution on either HOPG(0 0 1) or Au(1 1 1) were used as references to calibrate the STM images in the horizontal plane while the height measurements were calibrated against the step height obtained for Au(1 1 1).

The DFT calculations were performed with the plane wave code DACAPO [35], us-

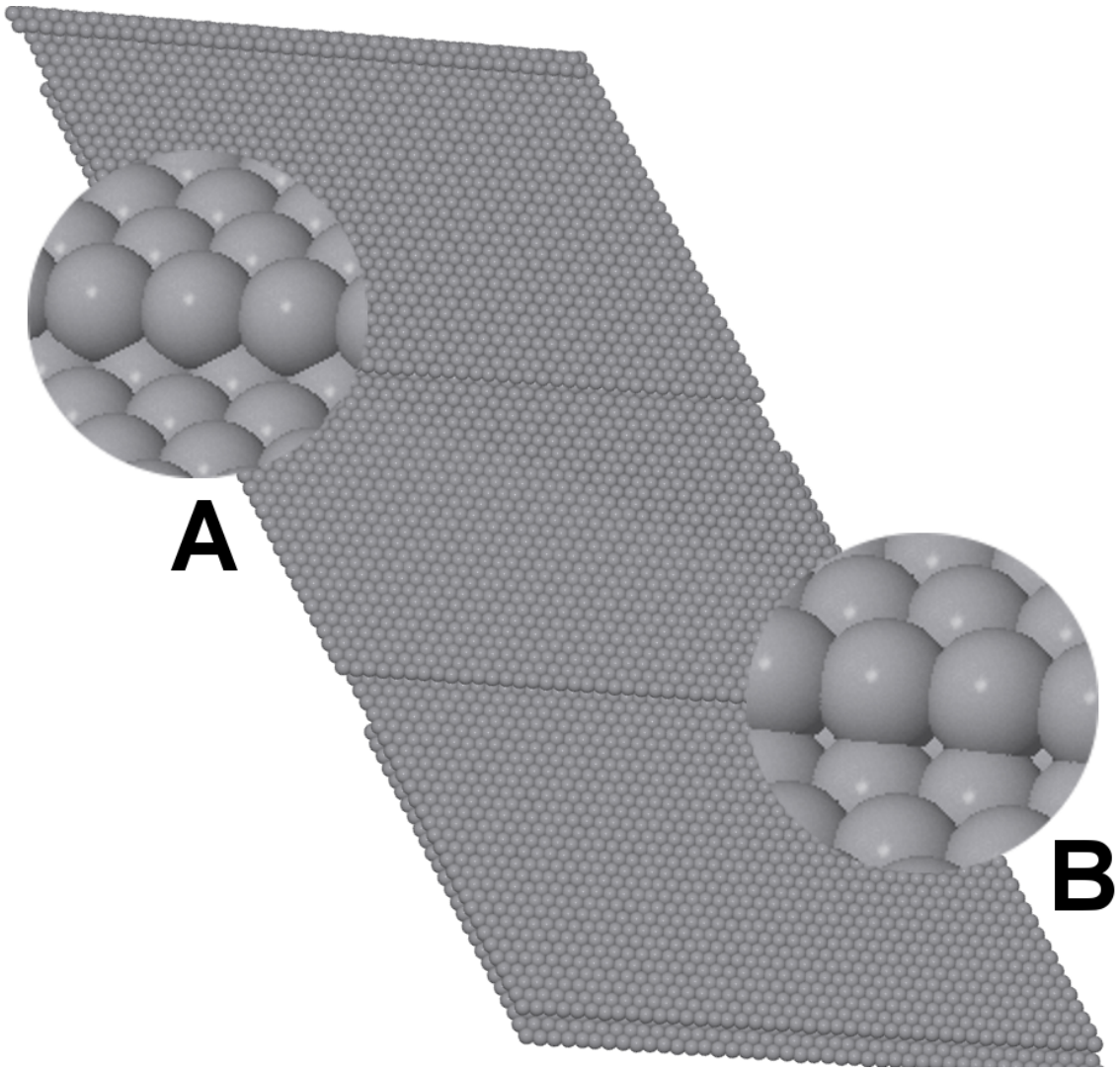

Figure 1: Ball-model of the Ru(0 1 54) surface, the close-ups highlight the structure of the A steps with a 3-fold symmetry (top left) and the B steps presenting a 4-fold symmetry (bottom right).

ing the RPBE exchange-correlation functional [36], a converged plane wave cutoff of 340 eV and a density cutoff of 400 eV. DACAPO uses ultrasoft pseudopotentials to represent the ion-electron interaction [37]. The Brillouin zone of all slabs was sampled with 4x1x1 Monkhorst-Pack grids, which guarantees that the product of the supercell dimensions and the k-points was approximately 20 Å in all directions. The vertical separation between consecutive slabs was in all cases more than 12 Å and dipole corrections were applied. Only atoms in the topmost layer were free to move and the atomic relaxations were done with the quasi-Newton minimization scheme, until the maximum force between atoms was below 0.05 eV.$Å^{-1}$. The self-consistent RPBE density was determined by iterative diagonalization of the Kohn-Sham Hamiltonian at an electronic temperature of $k_B T = 0.1$ eV, using Pulay

mixing of densities, and all total energies were extrapolated to $k_B T = 0\,eV$. We used the Ru(1 0 9) system, with a 4 layers thick 2×1 supercell, which is described in more destails in ref. [9] to model the surfaces. The simulated STM images were made within the Tersoff-Hamann approach as implemented in the Atomic Simulation Environment (ASE) package [38] with the GPAW code using non-orthogonal unit cells [39]. The coupling channel between the surface and STM tip was modeled using an s orbital. The tomograph was generated with a density of states of 10^{-3} at the Fermi level. A grid spacing of 0.2 Å was used to produce the STM image, with a bicubic interpolation.

III. EXPERIMENTAL RESULTS

Figure 2 displays STM images of the freshly cleaned Ru(0 1 54) surface,with line profiles as inserts, as a reference for the images after CO exposure. This surface in figure 2a exhibits straight, parallel monoatomic steps. Kinks can be observed along the steps. The height of the monoatomic steps is measured at 0.21 ± 0.1 nm (figure 2b), which is consistent with the value extracted from the crystallographic structure of ruthenium (0.214 nm). In general, the terrace width varies between 4 and 10 nm, in agreement with the expected average value of 7 nm. On some occasions, we also observed regions displaying some step bunching, characterized by 5 to 8 monoatomic steps separated by narrow terraces (1 to 2 nm wide). Next to these areas with step bunching, we usually find relatively broad terraces, with a typical width of 15 to 25 nm. It is of interest to note that none of our STM experiments show the presence of double steps on the freshly cleaned Ru(0 1 54) surface, unlike the observations made by Yates' group on the Ru(1 0 9) surface [8]. Furthermore, we occasionally observed the presence of locally strained areas (2-3 nm wide) which have previously been assigned to subsurface argon bubbles trapped a few atomic layers below the surface [19][20]. Although the lattice stress induced by those bubbles has been shown to locally modify adsorption energies [20], we estimate that, due to a very low density, it does not significantly influence the results from averaging experiments such as the TPD. Furthermore, during STM measurements, we ensured that the areas we studied after CO exposures did not contain such local area of lattice strain.

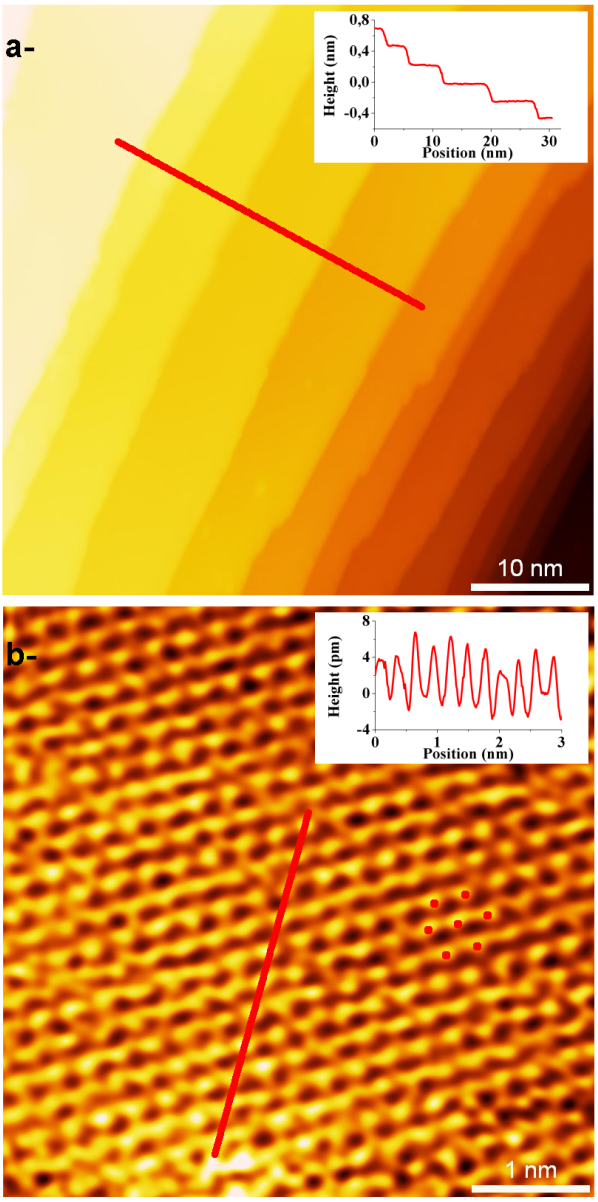

Figure 2: a- $50 \times 50\,\mathrm{nm}^2$ STM image of the clean Ru(0 1 54) surface, b- $5 \times 5\,\mathrm{nm}^2$ atomically resolved STM image of the ruthenium lattice, the red dots on the image are highlighting the hexagonal array. For both images, height profiles extracted along the red markers are presented as inserts.

If the ruthenium surface is exposed to CO while cooling down (typically $5{\times}10^{-8}\,\mathrm{torr}$, 1000 seconds, at a cooling rate of ca. $0.4\,\mathrm{Ks}^{-1}$) from 700 K to 400 K or after a CO TPD, we observe a partial decoration of the monoatomic steps. On the STM image presented in figure 3, one can distinguish periodical features on every second step. Furthermore a faint hexagonal lattice is observed on the terraces which can be seen more easily on figure 3b

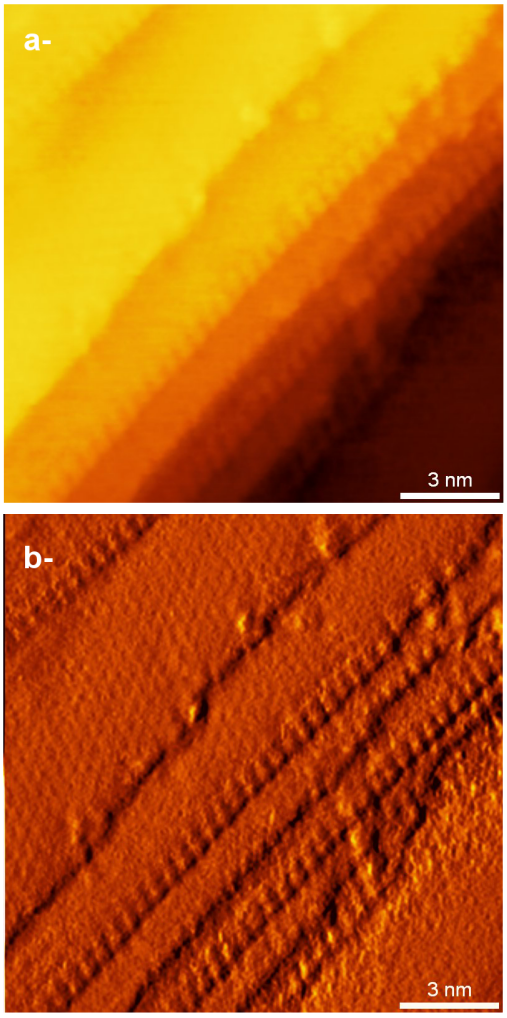

Figure 3: a- $20 \times 20\,\mathrm{nm}^2$ STM image of the Ru(0 1 54) surface after a CO-TPD, b- gradient image of figure 3a, further highlighting the step decoration.

where we show a derivative image of the picture presented on figure 3a.

Figure 4 exhibits STM images recorded on two different areas of the same sample. In order to evidence the periodical feature, a cyclic color scale has been applied. On both

pictures, the hexagonal lattice on the terraces is highlighted by a series of blue dots. It is rotated by 30° with respect to the ruthenium lattice (see figure 2b) and we measure a spacing of 0.47 ± 0.03 nm, much larger than the interatomic distance between Ru atoms (0.27 nm). We assign this structure to the $\left(\sqrt{3} \times \sqrt{3}\right) R30°$ superlattice ($\sqrt{3}\times$ 0.27 nm = 0.47 nm) adopted by CO molecules for coverages lower than 0.33 ML, previously observed using LEED [31] and STM [20][32]. The partial step decoration is highlighted by green dots; it is observed on every second step edge and can be described as "fingers" separated by 0.55 ± 0.05 nm. On a few occasions, we observe that this structure is extended into a hexagonal lattice with a 0.55 nm spacing. It is the case, for instance, on the terrace on the left-hand side of figure 4b. This periodicity corresponds to twice the interatomic distance on ruthenium (0 0 1) terrace. Previous STM studies [18][19][20] have shown that adsorbed oxygen atoms adopt a $p(2 \times 2)$ superstructure at coverages lower than 0.35 ML. The adsorbed oxygen atoms are located in hcp 3-fold hollow sites. They are observed as dark spots on the STM image since their presence leads to a decrease of the density of states at the Fermi level for the neighbouring ruthenium atoms [40]. Furthermore, Ertl and co-workers [21] have shown that, for coverages of the order of 0.01 to 0.02 ML, isolated oxygen atoms adsorbed on the Ru(0 0 1) surface are extremely mobile and only appear as "dashes" when imaged wih usual STM conditions. However, these authors also demonstrated that the adsorbed oxygen atoms included in a cluster of oxygen atoms (with a $p(2 \times 2)$ periodicity with reference to the ruthenium lattice) or located in a 3-fold hollow site next to a monoatomic step, are far less mobile and they are also observed as dark spots on the ruthenium surface [21]. As a consequence, we attribute the presence of the "fingers" decorating every other steps to oxygen atoms located in 3-fold hollow sites next to the top of a step edge. Since no oxygen is present on the surface before the CO exposure, we suggest that these oxygen atoms are provided by CO splitting occurring on step sites. The fate of the carbon atoms is more questionable. CO-TPDs and measurements of oxygen titration of carbon have been performed after dosing CO at high temperatures. The results of the titration experiments are shown in the supplementary information. The CO-TPD spectra usually exhibit the presence of a peak with a maximum at 480-500 K corresponding to molecularly adsorbed CO, and a shoulder appearing at 550-600 K which has been assigned to CO dissociated at step sites [7][8]. Furthermore, the carbon content measured using oxygen titration is approximately 0.02 ML, in agreement with the observations made by Vendelbo and co-workers [9]. These experiments confirm the presence of carbon at the step

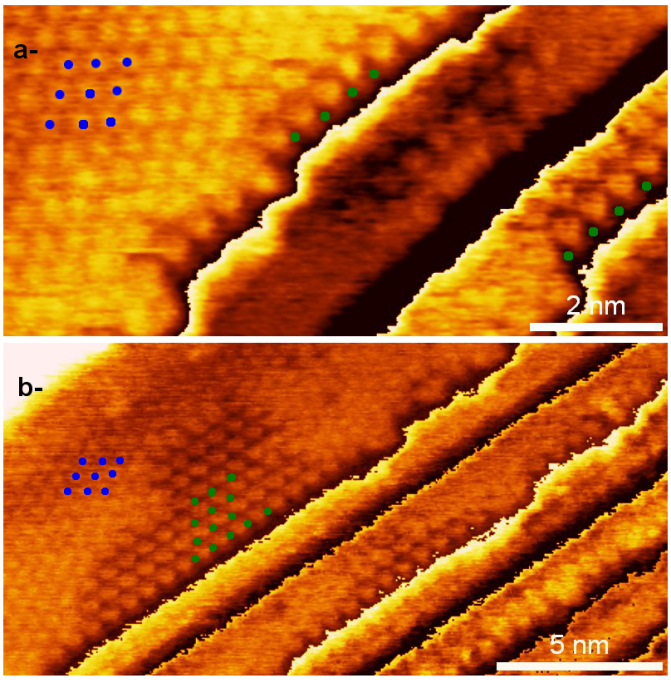

Figure 4: a- $10 \times 5\,\mathrm{nm}^2$ STM image of the Ru(0 1 54) surface after a CO-TPD, b- $20 \times 10\,\mathrm{nm}^2$ STM image of another area of the Ru(0 1 54) surface after a CO-TPD. For both images, a cyclic color scale is optimised in order to further highlight the periodical lattices, especially at the step edge. The blue dots correspond to the the periodicity observed on the terraces and the green dots are used to evidence more clearly the periodical features observed at the steps and their vicinity.

edges of our Ru crystal after dosing CO while the sample cools down from 700 K to 400 K. In STM, the presence of isolated carbon atoms has been observed at low temperatures (6 K) on the terraces of a Ru(0 0 1) crystal [24]. Like in the case of oxygen atoms, carbon atoms are characterized by dark spots due to a lowering of the density of states for the neighbouring Ru atoms, as compared to unmodified Ru atoms. This is not observed in our STM experiments, probably because the carbon atoms resulting from CO dissociation are located at the bottom of the steps, in areas which are screened by tip convolution effects.

IV. THEORETICAL MODELLING

In order to confirm our interpretation, a theoretical study based on DFT calculations has been undertaken. The Ru(1 0 9) surface, exhibiting the same succession of A and B monoatomic steps but narrower terraces of approximately 1 nm than the Ru(0 1 54) surface, was chosen as it is a good compromise between a reasonable calculation time and a good description of our experimental data. The geometry of the clean Ru(1 0 9), and that of the same system with diverse adsorbates (molecular CO, dissociated CO and adsorbed atomic oxygen) on both types of steps were optimized. We present theoretical STM images calculated for each optimized structure using a method derived from the Tersoff-Hamann model [41] in figure 5.

Figure 5a exhibits the simulated STM image of the clean Ru(1 0 9) surface, it shows no significant difference between the two types of monoatomic steps, aside form the registry between the (0 0 1) terraces. Furthermore, the small variations in apparent height between ruthenium atoms and the interatomic space is consistent with the low corrugations observed experimentally.

The case of CO molecules adsorbed on the B-type steps is presented on figure 5b. We find that CO molecules adsorb preferentially on bridge sites at the step edge, with the carbon atom binding to the surface, and are tilted towards the bottom part of the step. A similar calculation has been performed for molecular CO adsorbed on the A step; in this case, the CO molecule is also located on a bridge site at the step edge and tilted towards the lowest part of the step. This orientation is in good agreement with the observations made by Shincho *et al.* [42] during an investigation of CO adsorption on a stepped Ru(1 1 10) using angle resolved ultra-violet photoemission spectroscopy. These authors find that the CO molecules adsorbed at the step edge are tilted by approximately 30° with respect to the direction normal to the (0 0 1) plane. The adsorption on a bridge site at the steps might seem in contradiction with the adsorption on atop sites on the terraces. In fact, we find that a bridge site is a more favorable adsorption site than a step atom by very small margin of approximately 30 meV. For both the A and the B steps, the theoretical STM images display very prominant CO molecules at the step edge, contrary to the experimental data. As a consequence, the step edges would appear as bright rims

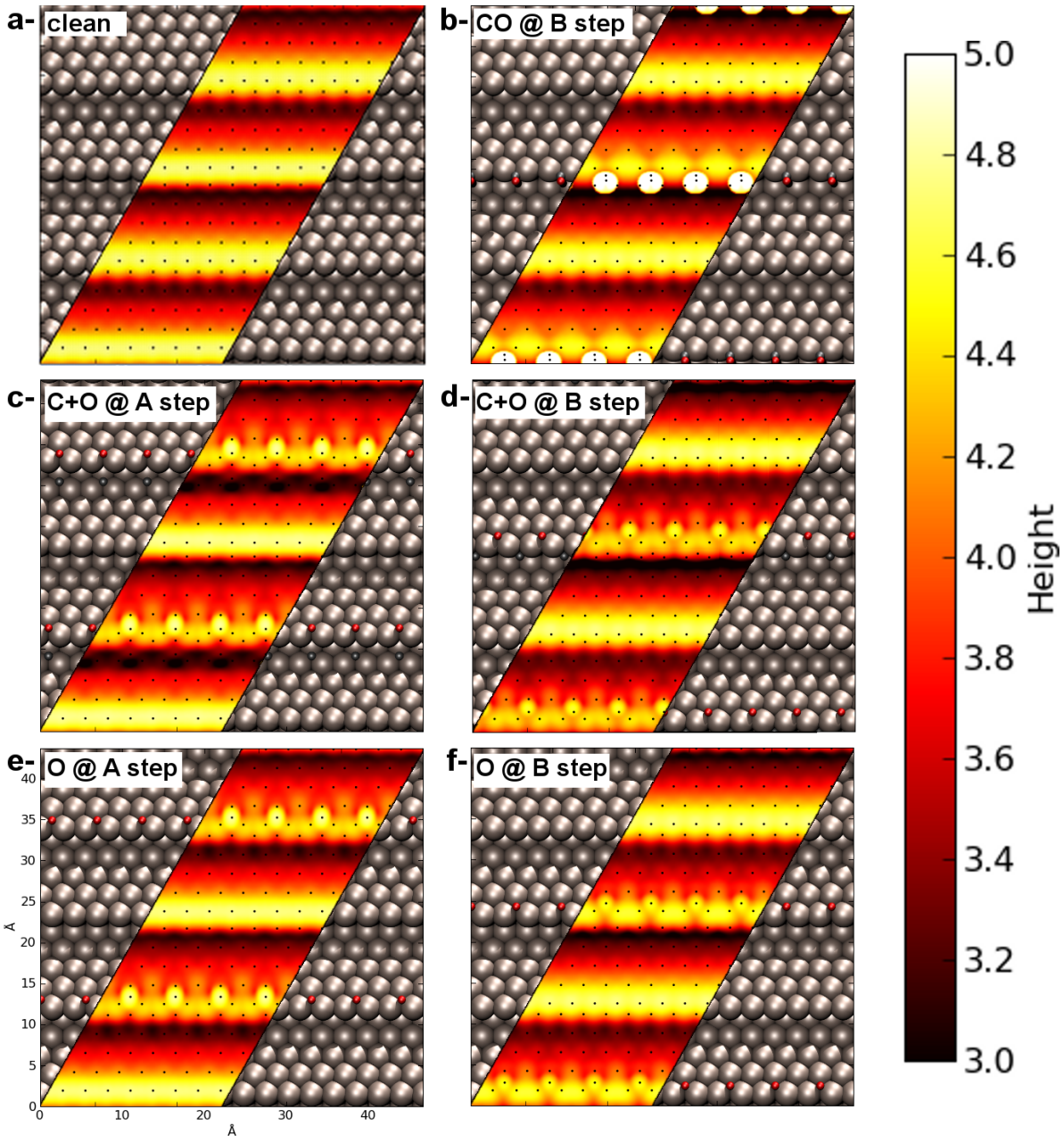

Figure 5: Simulated STM images of the Ru(1 0 9) surface with various adsorbates: a- clean surface; b- with molecular CO adsorbed on B steps; c- with CO dissociated on A steps; d- with CO dissociated on B steps; e- with atomic oxygen adsorbed at the top of A steps; f- with atomic oxygen adsorbed at the top of B steps. On the ball models, ruthenium atoms are represented in gray, carbon atoms in black and oxygen atoms in red. On the model images, the orange color scale corresponds to apparent height (in Å with respect to the bottom of the cell) in the simulated STM image and the black dots indicate the position of the surface atoms.

on the STM images of a ruthenium surface with CO adsorbed at the step edges and clean terraces. One also needs to consider the case of CO adsorbed on both steps and terraces. Previous STM experiments, performed on ruthenium covered with 0.33 ML of CO, did not show significant height difference between the CO molecules adsorbed on either the step edges or the terraces [20][32]. Therefore, we conclude that the molecular adsorption of CO on the ruthenium steps does not explain the step decoration presented on figures 3 and 4.

On figures 5c and 5d, we consider the case of CO dissociated on the A and B steps, respectively. For the A steps (figure 5c), the most stable structure corresponds to the oxygen atom located in a fcc 3-fold hollow site next to the step edge, on the top terrace, with the carbon atom also sitting in a fcc 3-fold hollow site located in the vicinity of the bottom of the step. On the theoretical STM image, the oxygen atom appears slightly higher than the neighbouring ruthenium atoms: A lower density of states, hence a lower apparent height, is observed at the step edge, in the area located between the adsorption sites of the carbon and oxygen atoms. In the case of CO dissociation on the B step, we first considered the case with the carbon atom is found in the 4-fold sites at the bottom of the step and the oxygen atom located in the hcp 3-fold hollow site closest to the carbon adsorption site. This structure was found to be less stable than the structure with CO adsorbed at the step edge, which will be discussed later. Another structure was then considered in which the oxygen atom is found in a hcp 3-fold hollow site further away from the carbon atom, this so-called "cross structure" is more favorable than both the initial adsorbed state and the dissociated state. It probably results of a migration of the oxygen atoms immediately after the dissociation, thanks to the low diffusion barrier for oxygen atoms, estimated at 0.7 eV by Wintterlin et al. [21]. The model STM image, in a similar fashion than that obtained for CO dissociated at the A step, displays a lower density of states in the areas located next to the oxygen atoms. The oxygen atom, however, is not as prominent as it is in the case of the A step. The presence of the carbon atoms also seems to induce a small decrease of the density of states, probably negligible compared to that induced by the oxygen atoms. On the basis of our calculation, both these configurations could explain our STM images, with a small preference for the case of the dissociation on the B step, since the oxygen atoms do not appear higher than their neighbouring ruthenium atoms on the experimental data.

As we mentioned earlier, similar step decoration has been observed in previous works

for low coverages of oxygen, after dissociation of NO or O_2 [22][21][23], which suggests that the presence of oxygen atoms at the top of the step edge is the main factor contributing to the formation of the "fingers" at the step edges as observed in our STM investigation. As a verification, we performed calculations with oxygen atoms adsorbed in the sames sites than in the case of the dissociated CO, namely the fcc 3-fold hollow site closest to the top of the step edge for the A step (figure 5e) and the hcp 3-fold hollow site closest to the top of the step edge for the B step (figure 5f), in the absence of carbon. The model STM images are very similar to those obtained for dissociated CO, hence confirming that the oxygen atoms have a larger influence than the carbon atoms on the STM images. As a further verification, Theoretical STM images with carbon atoms at the bottom of the steps have been calculated (see supplementary information) and clearly show that these carbon atoms have little influence on the STM images.

In order to help identifying the type of step on which the decoration occurs, we present an energy diagram comparing the role of the (0 0 1) terraces, the A steps and the B steps for the dissociation of CO (figure 6). For these three types of structures, all energies have been calculated with respect to a cell containing the Ru slab as described in the methods section and one CO molecule in the gas phase (i.e not interacting with the surface).

First, this calculation shows that the adsorption energies of molecular CO are approximately 1.5 eV for the three types of adsorption site we consider, with CO adsorbed on the B step being slightly more stable than CO on the A step or on the terrace (the difference in energy is approximately 0.1 eV). Moreover, if one focuses on the transition states, one will notice that the energy barrier is significantly lower for CO dissociation on the B step, as compared to the A step (by 0.4 eV) or to the terraces (by 1.2 eV), suggesting that the dissociation is more likely to occur on this type of step. In addition, for the A step and the terraces, the transition states are found to be less stable than the ruthenium surface with a CO molecule in the gas phase, meaning that CO desorption is more probable than CO dissociation on these sites. As a consequence, the step decoration resulting from CO dissociation would only be observed on B steps.

After dissociation, we find that the configuration with a carbon sitting at the bottom of the step and an oxygen atom in the first available 3-fold hollow site at the top of the step is

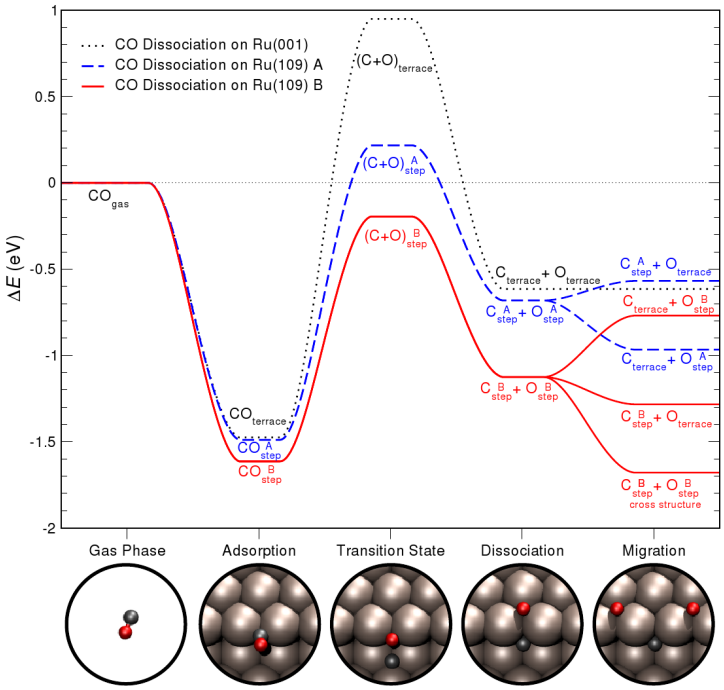

Figure 6: Energy diagram for CO dissociation on the Ru(1 0 9) surface, the dissociation on the A step is represented by the blue dashed line and the solid red line corresponds to dissociation on the B step. For comparison, the black dotted line illustrates CO dissociation on the Ru(0 0 1) terraces. The thumbnails show a CO molecule in the gas phase and in various consecutive configurations on a B step: adsorbed, in the transition state, dissociated and in the cross structure obtained after migration.

more stable for the B step than the equivalent structure for the A step (by approximately 0.45 eV). Furthermore, the "cross structure", obtained after migration of the oxygen atoms at the top of steps, is 0.55 eV more favorable than the dissociated state. It appears to be slightly lower in energy than the surface with a CO molecule adsorbed at the B-step. On the contrary, for both the A step and the (0 0 1) terraces, the dissociated state is less favored than the molecularly adsorbed state. This further confirms that the step decoration resulting from CO dissociation is more likely to be observed on the B steps.

Another interesting aspect is the discrepancy between the preferred site for oxygen atoms next to the monoatomic steps. In the case of the A-type steps, our calculations show that the oxygen atoms sit preferentially in the fcc 3-fold hollow site in the immediate vicinity of the step edge whereas, for B steps, the most favorable adsorption site for oxygen is the hcp

3-fold hollow site, also located in the immediate vicinity of the step edge. Previous works [18][22][21][23][40] show that the adsorption site for oxygen atoms on the (0 0 1) terraces is the hcp 3-fold hollow site and that, for low oxygen coverages, the adsorbed oxygen atoms are organized according to a $p(2 \times 2)$ superstructure with reference to the ruthenium lattice. As a consequence, if the CO molecules were dissociated on the A steps, there would be a lattice mismatch between the adsorption sites of oxygen atoms at the A step and the preferred $p(2 \times 2)$ oxygen overlayer on the terraces, while they would be a lattice match in the case of a dissociation on the B steps. Experimentally (figure 4b), we observe that the $p(2 \times 2)$ overlayer and the step decoration are well aligned, which, again, suggests that the CO molecules dissociates on the B steps in our experimental conditions.

Finally, on the right-hand side of the diagram on figure 6, we consider the migration of carbon and oxygen atoms away from the step sites to the terraces. For the A steps, we find that, if CO dissociation were to occur on these steps, the carbon atom would preferably migrate to the neighbouring terrace whereas the oxygen atoms would tend to remain at the step. The behaviour of CO dissociated on the B step is quite different; it is energetically favorable for the oxygen atoms to move away from the dissociation site in order to form the "cross structure". The structure corresponding to the carbon atom remaining at the B step and the oxygen atom located on the terraces (resp. the configuration with the oxygen atom at the B step and the carbon atom on the terraces) is approximately 0.4 eV (resp. 0.9 eV) less stable than the "cross structure" [49]. The latter case is consistent with the observation of carbon poisoning at the ruthenium steps after exposure to CO at 550 K [9]. It also accounts for the formation of a rim of oxygen atoms at the top of the steps for CO dissociation on ruthenium. Moreover, a similar behaviour has also been observed for isolated oxygen atoms after NO dissociation on Ru(0 0 1) [22][21][23].

To summarize, the simulation of STM images confirms that our experimental data can be explained by the dissociation of CO on step edges with a main contribution coming from oxygen atoms located in 3-fold hollow sites in the immediate vicinity of the step. Furthermore, when considering the total energies for the transition states and for the system after dissociation, we conclude that CO dissociation occurs preferentially on the B-type steps, which is further confirmed by registry between the $p(2 \times 2)$ oxygen overlayers and the step decoration. Furthermore, our calculations are also consistent with both the

high mobility of oxygen atoms on the surface of ruthenium and the accumulation of carbon on step sites observed earlier in our group.

V. DISCUSSION

As mentioned in the introduction, the identification of the active site for CO dissociation has been an open question for decades. While early measurements suggested that the reaction rate for methanation was independent of the nature of the ruthenium surface (Ru(0 0 1) compared with Ru(1 1 0) and with supported particles) [6], several experimental studies based on stepped crystals lead to the conclusion that the active site for CO activation is located on steps. For instance, Shincho *et al.* used TDS, AES, XPS and UPS to investigate the adsorption of CO on Ru(1 1 10) and Ru(0 0 1) [42]. The comparison between the results obtained for the stepped (1 1 10) surface and those gathered for the basal plane demonstrated that CO is adsorbed in the molecular state on the (0 0 1) terraces and that the CO molecules dissociate on step sites, provided that the adsorption temperature is high enough (approx. 500 K). Later, Yates' group used another route, involving IR spectroscopy and isotopic exchange experiments, to demonstrate that the steps, which appear to be two atomic rows thick after reconstruction, are responsible for the dissociation of CO on a Ru(1 0 9) surface. More recently, Vendelbo *et al.* also showed the importance of steps for the dissociation of CO, together with carbon accumulation at the steps, by the means of temperature programmed desorption and carbon uptake measurements performed on a Ru(0 1 54) surface [9]. The step decoration we observed using STM, after exposing ruthenium to CO at temperatures varying from 700 K down to 400 K or after a CO-TPD, provides further evidence that CO adsorbs dissociatively on monoatomic steps at elevated temperature. Moreover, our STM data shows that CO is dissociated on every other step in our experimental conditions (figures 3 and 4), demonstrating that either the A steps or the the B steps are more active at activating CO. DFT calculations were performed in order to rationalize this observation (figures 5 and 6) and, based on the comparison between the results of this theoretical modelling and the experimental data, we suggest that the actives sites are located at the B steps. This is also in agreement with the predictions, based upon DFT calculations, that CO dissociation would preferably occur on the so-called B5 site in the case of ruthenium [43], nickel [3] and rhodium [44]. It is worth mentioning that

the B5 site is considered as the active site for several structure sensitive reactions such as N_2 dissociation [11].

In terms of reactivity, the stability of the "cross structure" (see figures 5 and 6) is of importance. Firstly, because of the migration of the oxygen atoms in order to form this configuration, these atoms are at equal distance from two equivalent carbon atoms. Thus, during TPD experiments, the recombination can occur either between C and O atoms resulting from a single CO molecule or between atoms arising from two different molecules, with equal probability. This observation is in very good agreement with the results of isotopic exchange measurements reported by Yates and co-workers [7][8] and Shincho *et al.* [42] which both show random mixing of the different isotopes in the peak corresponding to the dissociative adsorption at steps. Secondly, for the "cross structure", the adsorption sites located just above the carbon atoms; namely the step brige site, the closest hcp 3-fold hollow site and several atop sites, are available for other reactants. As a consequence, the reactivity for processes involving the dissociation of carbon monoxide (methanation, Fischer-Tropsch) may be enhanced.

Interestingly, in a study of the interaction of adsorbates on a ruthenium surface presenting local strain induced by Ar "bubbles" trapped a few atomic layers below the surface, Jakob and coworkers used STM and infrared spectroscopy to describe the behaviour of co-adsorbed CO molecules and oxygen atoms, with a deposition performed at room temperature [20]. Their results show that a pure $\left(\sqrt{3}\times\sqrt{3}\right)R30^\circ$ CO phase prevails at the vicinity of the steps, on the upper terrace, while a $p(2\times2)$ superstructure characteristic of adsorbed oxygen, probably with CO impurities, is observed further away from the step edge. This results from a local lattice compression in the proximity of a step (upper terrace) which leads to a more favorable adsorption for the $\left(\sqrt{3}\times\sqrt{3}\right)R30^\circ$ CO overlayer in this area. On the contrary, the $p(2\times2)$-$(O+CO)$ phase is more favorable for an unstrained or an expanded ruthenium lattice. Furthermore, their interpretation is consistent with previous theoretical studies [45]. The behaviour we observe after CO deposition at high temperature (figures 3 and 4), with a $p(2\times2)$ oxygen overlayer next to a step on the upper terrace and $\left(\sqrt{3}\times\sqrt{3}\right)R30^\circ$ CO phase in the unstrained areas further from the step edge is opposite to that reported by Jakob *et al.*[20]. In our opinion, this discrepancy can only be explained if, in our experiment, the oxygen atoms are generated at the steps while the $\left(\sqrt{3}\times\sqrt{3}\right)R30^\circ$ CO overlayer is forming (or is already formed). Thus, it confirms the hypothesis that CO molecules adsorb dissociatively at step sites on the ruthenium

surface, provided the temperature is sufficiently high. It is here of interest to mention that lattice strain can also be induced by depositing pseudomorphic layers on a substrates or by preparing surface alloys. For instance, Mongeot *et al.* showed that the adsorption energy of CO on platinum islands grown on a Ru(0 0 1) surface or on a PtRu surface alloy is lower than on either Pt(111) or Ru(0 0 1) [32]. In addition, in the same work, they demonstrated that the barrier for CO oxidation was reduced in the case of the PtRu surface alloy, as compared with Pt(1 1 1).

Recent studies evidenced that the surface of metal catalysts could be strongly modified in the presence of reactive gases at the relatively high temperatures necessary for the catalysed reactions to take place. As an example, Somorjai's group has demonstrated that stepped platinum surfaces (Pt(5 5 7) and Pt (3 3 2)) undergo drastic restructuring leading to the formation of triangular or parallelogram-shaped nanocluster when exposed to CO at a high pressure (1 torr) [14]. In the case of ruthenium, STM measurements performed in CO rich environment at high temperatures by Frenkel's group at Leiden University exhibited the formation of "clusters" on the Ru(0 0 1) surface [46]. Since the density and the shape of these clusters evolve with the gas composition, they were assigned to carbonaceous species able to react with H_2 or O_2 in the gas phase. Furthermore, these authors also observed a step roughening during CO oxidation. Such a phenomenon could be involved in the modified reactivity of the Ru(0 1 54) surface after exposure to CO (10^{-5} torr) [9]. We are currently performing STM experiments in order to clarify this behaviour.

Contrary to our experiments performed in UHV on model crystals, industrial catalysis is usually performed using supported metal particles at high pressures and temperatures [1]. As a consequence, one compares the behaviour of a well characterized crystalline surface in the model experiments to a juxtaposition of various facets, steps and kinks in the case of nanoparticles. Despite this so-called structure gap, our observations, especially the fact that the B steps are more active at dissociating CO, are relevant to the industry. In particular, this could lead to developing new strategies aiming at optimising the density of active sites at the surface of supported particles.

Furthermore, recent work suggests that the role of the substrate in the catalytic process is not negligible [47]. In our opinion, two approaches could help clarifying this question. The first concerns the surface science study of nanoparticles on a crystalline substrate such as HOPG [48] or metal oxides [13]. The second approach is based on the concept of reverse

catalysts: nanoparticles of substrate material grown at the surface of a catalytically active species [13]. We believe that both these approaches would be bring insight into phenomena such as charge transfer or spill over effects.

VI. CONCLUSIONS

STM results obtained after exposing a stepped Ru(0 1 54) surface to carbon monoxide in UHV conditions exhibit step decorations. We assign this decoration to CO dissociated at step sites and more particularly to the presence of oxygen atoms in 3-fold hollow sites in the immediate vicinity of the step, on the upper terrace. DFT calculation have been performed in order to rationalize our observation and the comparison between the experimental data and the theoretical results lead us to confirm our interpretation. Moreover, we observe that the step decoration occurs on every second step, which demonstrates that CO dissociation is surface sensitive since the hcp structure of ruthenium results in alternating A (3-fold symmetry) and B (4-fold symmetry) steps. An energy diagram calculated for CO dissociation, together with some considerations about the organization of the adsorbates, suggest that the active site is located on the B steps, in agreement with theoretical predictions concerning CO activation on ruthenium and other metal catalysts. Finally, our results are discussed with regards to the literature and we propose to extend this work towards the influence of CO exposures on the reactivity, towards nanoparticles studies and finally towards a reverse catalyst approach.

[1] H. Schulz, APPLIED CATALYSIS A-GENERAL **186**, 3 (1999), ISSN 0926-860X.

[2] J. COENEN, P. VANNISSELROOY, M. DECROON, P. VANDOOREN, and R. VANMEERTEN, APPLIED CATALYSIS **25**, 1 (1986), ISSN 0926-860X.

[3] M. P. Andersson, E. Abild-Pedersen, I. N. Remediakis, T. Bligaard, G. Jones, J. Engbæk, O. Lytken, S. Horch, J. H. Nielsen, J. Sehested, et al., JOURNAL OF CATALYSIS **255**, 6 (2008), ISSN 0021-9517.

[4] E. David R. Lide, *Handbook of Chemistry and Physics, 89th Edition* (CRC Press/Taylor and Francis, Boca Raton, FL., 2009).

[5] D. Goodman, ACCOUNTS OF CHEMICAL RESEARCH **17**, 194 (1984), ISSN 0001-4842.

[6] R. Kelley and D. Goodman, SURFACE SCIENCE **123**, L743 (1982), ISSN 0039-6028.

[7] T. Zubkov, G. Morgan, and J. Yates, CHEMICAL PHYSICS LETTERS **362**, 181 (2002), ISSN 0009-2614.

[8] T. Zubkov, G. Morgan, J. Yates, O. Kuhlert, M. Lisowski, R. Schillinger, D. Fick, and H. Jansch, SURFACE SCIENCE **526**, 57 (2003), ISSN 0039-6028.

[9] S. Vendelbo, M. Johansson, D. Mowbray, M. Andersson, F. Abild-Pedersen, J. Nielsen, J. Nørskov, and I. Chorkendorff, Topics in Catalysis **53**, 357 (2010), ISSN 1022-5528, 10.1007/s11244-010-9445-4, URL `http://dx.doi.org/10.1007/s11244-010-9445-4`.

[10] S. Vendelbo, M. Johansson, J. Nielsen, and I. Chorkendorff (2010), submitted.

[11] S. Dahl, A. Logadottir, R. C. Egeberg, J. H. Larsen, I. Chorkendorff, E. Törnqvist, and J. K. Nørskov, Phys. Rev. Lett. **83**, 1814 (1999).

[12] C. Jacobsen, S. Dahl, P. Hansen, E. Tornqvist, L. Jensen, H. Topsoe, D. Prip, P. Moenshaug, and I. Chorkendorff, JOURNAL OF MOLECULAR CATALYSIS A-CHEMICAL **163**, 19 (2000), ISSN 1381-1169.

[13] M. Bowker, Chem. Soc. Rev. **36**, 1656 (2007).

[14] F. Tao, S. Dag, L.-W. Wang, Z. Liu, D. R. Butcher, H. Bluhm, M. Salmeron, and G. A. Somorjai, Science **327**, 850 (2010), http://www.sciencemag.org/cgi/reprint/327/5967/850.pdf, URL `http://www.sciencemag.org/cgi/content/abstract/327/5967/850`.

[15] J. Lauritsen, M. Nyberg, J. Norskov, B. Clausen, H. Topsoe, E. Laegsgaard, and F. Besenbacher, JOURNAL OF CATALYSIS **224**, 94 (2004), ISSN 0021-9517.

[16] T. F. Jaramillo, K. P. Jorgensen, J. Bonde, J. H. Nielsen, S. Horch, and I. Chorkendorff, SCIENCE **317**, 100 (2007), ISSN 0036-8075.

[17] J. H. Nielsen, L. Bech, K. Nielsen, Y. Tison, K. P. Jorgensen, J. L. Bonde, S. Horch, T. F. Jaramillo, and I. Chorkendorff, SURFACE SCIENCE **603**, 1182 (2009), ISSN 0039-6028.

[18] K. Meinel, H. Wolter, C. Ammer, A. Beckmann, and H. Neddermeyer, Journal of Physics: Condensed Matter **9**, 4611 (1997), URL `http://stacks.iop.org/0953-8984/9/i=22/a=013`.

[19] M. Gsell, P. Jakob, and D. Menzel, SCIENCE **280**, 717 (1998), ISSN 0036-8075.

[20] P. Jakob, M. Gsell, and D. Menzel, The Journal of Chemical Physics **114**, 10075 (2001), URL `http://link.aip.org/link/?JCP/114/10075/1`.

[21] J. Wintterlin, J. Trost, S. Renisch, R. Schuster, T. Zambelli, and G. Ertl, Surface Science **394**, 159 (1997), ISSN 0039-6028, URL http://www.sciencedirect.com/science/article/B6TVX-3SYPH4W-4M/2/76930945d72429c0aae1b62def251140.

[22] J. T. T. Zambelli, J. Wintterlin and G. Ertl, Science **273**, 1688 (1996).

[23] J. Wintterlin and T. Zambelli, ZEITSCHRIFT FUR PHYSIKALISCHE CHEMIE-INTERNATIONAL JOURNAL OF RESEARCH IN PHYSICAL CHEMISTRY & CHEMICAL PHYSICS **219**, 997 (2005), ISSN 0942-9352.

[24] T. K. Shimizu, A. Mugarza, J. I. Cerda, and M. Salmeron, JOURNAL OF CHEMICAL PHYSICS **129**, 244103 (2008), ISSN 0021-9606.

[25] M. WU, Q. XU, and D. GOODMAN, JOURNAL OF PHYSICAL CHEMISTRY **98**, 5104 (1994), ISSN 0022-3654.

[26] S. Marchini, S. Guenther, and J. Wintterlin, PHYSICAL REVIEW B **76**, 075429 (2007), ISSN 1098-0121.

[27] K. Donner and P. Jakob, JOURNAL OF CHEMICAL PHYSICS **131**, 164701 (2009), ISSN 0021-9606.

[28] Z. Zhou, F. Gao, and D. W. Goodman, SURFACE SCIENCE **604**, L31 (2010), ISSN 0039-6028.

[29] G. MICHALK, W. MORITZ, H. PFNUR, and D. MENZEL, SURFACE SCIENCE **129**, 92 (1983), ISSN 0039-6028.

[30] E. WILLIAMS and W. WEINBERG, SURFACE SCIENCE **82**, 93 (1979), ISSN 0039-6028.

[31] H. Pfnur and D. Menzel, JOURNAL OF CHEMICAL PHYSICS **79**, 2400 (1983), ISSN 0021-9606.

[32] F. de Mongeot, M. Scherer, B. Gleich, E. Kopatzki, and R. Behm, SURFACE SCIENCE **411**, 249 (1998), ISSN 0039-6028.

[33] E. LAEGSGAARD, F. BESENBACHER, K. MORTENSEN, and I. STENSGAARD, JOURNAL OF MICROSCOPY-OXFORD **152**, 663 (1988), ISSN 0022-2720.

[34] *Spip software, image metrology a/s, denmark.*

[35] *Dacapo simulation code. available from: https://wiki.fysik.dtu.dk/dacapo.*

[36] B. Hammer, L. B. Hansen, and J. K. Nørskov, Phys. Rev. B **59**, 7413 (1999).

[37] D. Vanderbilt, Phys. Rev. B **41**, 7892 (1990).

[38] S. Bahn and K. Jacobsen, COMPUTING IN SCIENCE & ENGINEERING **4**, 56 (2002), ISSN 1521-9615.

[39] J. Enkovaara, C. Rostgaard, J. J. Mortensen, J. Chen, M. Dulak, L. Ferrighi, J. Gavnholt, C. Glinsvad, V. Haikola, H. A. Hansen, et al., JOURNAL OF PHYSICS-CONDENSED MATTER **22**, 253202 (2010), ISSN 0953-8984.

[40] C. Corriol, F. Calleja, A. Arnau, J. Hinarejos, A. V. de Parga, W. Hofer, and R. Miranda, Chemical Physics Letters **405**, 131 (2005), ISSN 0009-2614, URL http://www.sciencedirect.com/science/article/B6TFN-4FK42P6-6/2/b83f6645dc7d250ca42faf663ef2e352.

[41] J. Tersoff and D. R. Hamann, Phys. Rev. B **31**, 805 (1985).

[42] E. Shincho, C. Egawa, S. Naito, and K. Tamaru, SURFACE SCIENCE **149**, 1 (1985), ISSN 0039-6028.

[43] I. Ciobica and R. van Santen, JOURNAL OF PHYSICAL CHEMISTRY B **107**, 3808 (2003), ISSN 1520-6106.

[44] M. Mavrikakis, M. Baumer, H. Freund, and J. Nørskov, CATALYSIS LETTERS **81**, 153 (2002), ISSN 1011-372X.

[45] M. Mavrikakis, B. Hammer, and J. K. Nørskov, Phys. Rev. Lett. **81**, 2819 (1998).

[46] B. Hendriksen, Ph.D. thesis, Leiden University (2003).

[47] P. Panagiotopoulou, D. I. Kondarides, and X. E. Verykios, APPLIED CATALYSIS B-ENVIRONMENTAL **88**, 470 (2009), ISSN 0926-3373.

[48] R. M. Nielsen, S. Murphy, C. Strebel, M. Johansson, I. Chorkendorff, and J. H. Nielsen, JOURNAL OF NANOPARTICLE RESEARCH **12**, 1249 (2010), ISSN 1388-0764.

[49] A small difference can be observed between the energies of the migrated state in figure 6 and the comparable graph presented in figure 3 in ref. [9]. This is due to the fact that, in the original calculation, the adsorption site for the oxygen atoms was considered as the fcc 3-fold hollow site which is les favorable than the hcp 3-fold hollow site. This mistake has been corrected in the calculation presented here. Furthermore, it is a more refined calculation since the co-adsorption energies of carbon and oxygen have been taken into account in the present calculation.

PCCP

View Online
Dynamic Article Links

Cite this: *Phys. Chem. Chem. Phys.*, 2011, **13**, 10333–10341

www.rsc.org/pccp

PAPER

Probing the crossover in CO desorption from single crystal to nanoparticulate Ru model catalysts

S. Murphy, C. Strebel, S. B. Vendelbo, C. Conradsen, Y. Tison, K. Nielsen, L. Bech, R. M. Nielsen, M. Johansson, I. Chorkendorff and J. H. Nielsen*

Received 11th February 2011, Accepted 1st April 2011
DOI: 10.1039/c1cp20371a

Using model catalysts, we demonstrate that CO desorption from Ru surfaces can be switched from that typical of single crystal surfaces to one more characteristic of supported nanoparticles. First, the CO desorption behaviour from Ru nanoparticles supported on highly oriented pyrolytic graphite was studied. Both mass-selected and thermally evaporated nanoparticles were deposited. TPD spectra from the mass-selected nanoparticles exhibit a desorption peak located around 410 K with a broad shoulder extending from around 480 K to 600 K, while spectra obtained from thermally evaporated nanoparticles exhibit a single broad feature from ~350 K to ~450 K. A room temperature deposited 50 Å thick Ru film displays a characteristic nanoparticle-like spectrum with a broad desorption feature at ~420 K and a shoulder extending from ~450 K to ~600 K. Subsequent annealing of this film at 900 K produced a polycrystalline morphology of flat Ru(001) terraces separated by monatomic steps. The CO desorption spectrum from this surface resembles that obtained on single crystal Ru(001) with two large desorption features located at 390 K and 450 K due to molecular desorption from terrace sites, and a much smaller peak at ~530 K due to desorption of dissociatively adsorbed CO at step sites. In a second experiment, ion sputtering was used to create surface defects on a Ru(0 1 54) single crystal surface. A gradual shift away from the desorption spectrum typical of a Ru(001) surface towards one resembling desorption from supported Ru nanoparticles was observed with increasing sputter time.

I. Introduction

While surface science studies of macroscopic single crystal surfaces have yielded much valuable insight into the fundamental principles of heterogeneous catalysts, the well-known materials gap between surface science and industrial catalysis exists.[1–4] Typically, industrial catalysts are much more complex in nature than the single crystal surfaces encountered in many surface science studies. A better representation of these materials can be obtained by studying an ensemble of nanoparticles supported on a well-defined planar substrate.[5–7] Such model systems can be used to investigate the effect of the particle size and the influence of the support material on reactivity. Moreover, nanoparticulate model catalysts are more suited to studying the correlation between structure and activity in structure-sensitive reactions because of the resemblance to industrial catalysts, which comprise a high density of various active sites such as edge or corner sites, as compared to single crystal surfaces where the number of equivalent step or kink sites can be outweighed by several orders of magnitude by less-active terrace sites.[8,9] As part of our efforts to understand the materials gap we have been investigating the crossover in desorption behaviour between the two model catalyst systems, *i.e.* single crystal surfaces *versus* supported nanoparticles. Here we present details of our investigation of the thermal desorption of CO from a Ru(0 1 54) single crystal surface and from Ru nanoparticles supported on highly oriented pyrolytic graphite (HOPG).

Ruthenium is a versatile catalyst, which has been particularly investigated with respect to methanation and Fischer–Tropsch synthesis.[10–12] As an elementary step in this process the adsorption of CO on single crystal Ru(001) has been studied extensively by various surface science methods.[13–22] CO adsorbs on the Ru(001) basal surface in an upright position *via* the carbon atom at all coverages up to saturation at around 2/3 of a monolayer.[23–25] The CO molecules adsorb in on-top positions up to a coverage of 1/3 of a monolayer, forming a $(\sqrt{3}\times\sqrt{3})R30^\circ$ adlayer structure.[26–28] At higher coverages, the $(\sqrt{3}\times\sqrt{3})R30^\circ$ structure is disrupted as strong repulsive interactions cause CO molecules to be displaced from on-top positions (though the exact microstructure of the higher coverage overlayers is still debated[29]).

Center for Individual Nanoparticle Functionality, Department of Physics, Technical University of Denmark, 2800 Kgs. Lyngby, Denmark. E-mail: jane@fysik.dtu.dk; Fax: +45 4593 2399

The change in adlayer structure is reflected in the CO desorption behaviour. For coverages up to 1/3 of a monolayer CO desorbs in a single peak decreasing from 480 K to 450 K with increasing coverage (α_1 peak), while for higher coverages a second peak develops around 350–400 K (α_2 peak).[18,22,30,31] In addition to these peaks, which are due to desorption of molecularly adsorbed CO, an additional much smaller peak may also be observed at around 530 K, arising from the desorption of CO that has been dissociatively adsorbed at step sites (β peak).[13,19,21,22,32] This was demonstrated by Shincho *et al.*,[13] Yamada *et al.*[19] and Zubkov *et al.*[21,22] using isotopic scrambling experiments, which rely on the recombination and desorption of atomic carbon and oxygen originating from the dissociative adsorption of CO. It was furthermore demonstrated that deposition of carbon at surface steps blocked them for dissociative adsorption of CO and resulted in the disappearance of the β peak from CO desorption spectra.[22,32]

The CO desorption from more open Ru single crystal surfaces has also been investigated and displays similarities to TPD spectra obtained from the Ru(001) plane.[33–37] For the Ru(110) plane, for example, the α_1 and α_2 peaks at similar temperatures were observed along with two β peaks attributed to dissociation of CO at different sites. The desorption of CO_2 from the Ru(110) surface at 380–450 K was furthermore observed.

If we consider the information available with regard to CO desorption from supported Ru nanoparticles, a number of studies have investigated CO desorption from Ru catalysts prepared by chemical impregnation of SiO_2 and Al_2O_3 supports.[38–42] Typically, two main features were observed in these studies, a low temperature feature located between 350 K and 475 K, and a higher temperature feature located between 600 K and 700 K.[38–42] The two features at lower temperatures agree well with the double-peak spectrum obtained from Ru(001)[18,22,30,31] and the variation in the temperatures recorded for the desorption features in the different studies could be attributed to the different heating rates used. Moreover, where desorption experiments were performed in reactors under a He carrier gas flow,[38–41] the measured desorption temperatures could also be influenced by readsorption of CO, which was found to shift desorption peaks to higher temperatures.[39] The desorption of CO_2 was also observed in some of these studies, which could be taken as evidence of CO dissociation occuring over the Ru nanoparticles.[39,40,42]

Here, we demonstrate that it is possible to link the desorption behaviour of supported nanoparticles (both mass-selected particles formed in a magnetron-sputter gas-aggregation source and vapour-deposited particles) and that of the single crystal surface using two approaches. In the first case, we demonstrate the transition from nanoparticle-like CO desorption behaviour to single-crystal surface behaviour in Ru nanoparticles supported on HOPG. In the second case, we demonstrate the reverse transition from single-crystal surface to nanoparticle-like CO desorption behaviour by means of Ar^+ ion pre-sputtering of the Ru(0 1 54) surface.

II. Experimental

The experiments were performed in three separate UHV systems. The experiments on Ru nanoparticles were performed in a multichamber ultrahigh vacuum (UHV) system (Omicron, Multiscan Lab) with a base pressure in the low 10^{-11} mbar region.[43,44] This system is equipped with facilities for combined scanning tunneling microscopy (STM) and scanning electron microscopy (SEM), as well as Auger electron spectrsocopy (AES), ion scattering spectroscopy (ISS) and temperature programmed desorption (TPD) measurements. The thermal desorption experiments on the Ru(0 1 54) surface were performed in a UHV chamber with a base pressure below 10^{-10} mbar, which is equipped with facilities for TPD and AES, as well as a high-pressure cell.[32] STM measurements on the Ru(0 1 54) surface were performed in a UHV chamber with a base pressure below 10^{-10} mbar,[45] which is equipped with X-ray photoelectron spectroscopy (XPS) and an Aarhus-type STM.[46]

A Ru nanoparticles on HOPG

The HOPG substrates (SPI-1, 7 mm × 7 mm × 0.5 mm) were cleaved in air and mounted in sample holders incorporating a pyrolytic boron nitride (PBN) radiative heater, which is capable of heating the sample to temperatures in excess of 975 K. A C-type thermocouple (W-5 at.% Re/W-26 at.% Re) was placed in contact with the substrate in order to monitor and control the sample temperature *via* a PID controller (Eurotherm 2408). Upon insertion into UHV, the samples were outgassed for several hours at 775 K to outgas adsorbed contaminants prior to use. Two different methods were used to deposit Ru nanoparticles.

In the first method, mass-selected nanoparticles were deposited from an inert-gas aggregation source (Mantis Deposition Ltd.), which is described in detail elsewhere.[43,44] Briefly, a flux of Ru atoms is produced by a magnetron sputter head, which is condensed into nanoparticles upon contact with cooled Ar gas atoms. The ionised fraction of the nanoparticle beam is filtered to select the mass of the nanoparticles to be deposited using a quadrupole mass filter, before the nanoparticles are soft-landed (*i.e.* they have a kinetic energy of $\leq$0.1 eV atom^{-1}) onto HOPG substrates. For these studies, we have investigated both as-cleaved HOPG and surfaces that have been sputtered for 15 min with 500 eV Ar^+ ions at a current density of $\sim$1 μA cm^{-2} and subsequently outgassed at 935 K. The 15 min sputtering causes defects in at least the first two layers of the surface.[47]

In the second method, Ru films were deposited on HOPG by electron-beam evaporation of a 99.99% purity Ru rod. The substrates were either as-cleaved or sputtered for 30 s with 500 eV Ar^+ ions under the same conditions as those given above. Sputtering for only 30 s produces approximately 5% of defects in the topmost surface layer. The substrate was grounded while the Ru rod was held at a positive bias of 500 V.[48] A quartz crystal balance was used to monitor the deposition rate (typically 0.46–0.9 Å min^{-1}) and estimate the final film thickness.

Ion Scattering Spectroscopy (ISS) was used to confirm the cleanliness of the HOPG substrate and the deposited Ru nanoparticles and thin films. The ISS spectra were recorded using 1 keV He^+ ions produced by a differentially pumped electron impact ion source (ISE 100, Omicron Nanotechnology). The reflected ions were detected at a 147° scattering angle with a hemispherical energy analyser.

TPD experiments were performed in the preparation chamber of the UHV system. The samples were dosed with a 1 : 1 mixture of two different isotopically labeled CO molecules, namely $^{13}C^{16}O$ (CIL, 99% ^{13}C, $<10\%$ ^{18}O)[49] and $^{12}C^{18}O$ (CIL, 2% ^{16}O). Both gases were dosed simultaneously using separate leak valves until a total chamber pressure of 2×10^{-8} mbar was attained. The ratio of the two gases was held constant by monitoring the mass spectrometer signal for each component. The samples were dosed in this manner for 10 min, corresponding to an exposure of nine Langmuir, which was sufficient to saturate the surface. It was possible to observe the saturation in the CO uptake during dosing with the mass spectrometer. The sample temperature was then ramped at a rate of 1 K s^{-1} in UHV and the CO desorption from the substrate was analysed using a differentially pumped Balzers QMA 125 quadrupole mass spectrometer. The spectrometer was equipped with an oxygen-free high conductivity (OFHC) copper sniffer tip with a 1 mm diameter aperture, which is positioned within 0.5 mm of the sample surface. This arrangement allows the local gas composition above the sample surface to be measured with negligible contribution from the sample holder or surroundings.

The isotope exchange reaction ($^{12}C^{18}O + {}^{13}C^{16}O \rightarrow {}^{12}C^{18}O + {}^{13}C^{16}O + {}^{13}C^{18}O + {}^{12}C^{16}O$) allows us to determine the relative amount of CO that has been dissociated on the surface from the TPD spectra. If the adsorbed $^{13}C^{16}O$ and $^{12}C^{18}O$ molecules dissociate on the surface, the dissociated species can scramble and recombine into the four possible CO isotopologues $^{12}C^{16}O$, $^{13}C^{16}O$, $^{12}C^{18}O$ and $^{13}C^{18}O$. The TPD mass spectrometer signals of 28 amu, 29 amu, 30 amu and 31 amu were background subtracted and integrated to find the total desorption of each isotopologue. Particular attention was paid to the $^{13}C^{18}O$ signal as this does not have a high natural background in the UHV chamber like $^{12}C^{16}O$, and does not contribute to molecular desorption like either $^{13}C^{16}O$ or $^{12}C^{18}O$. Assuming an equal probability for scrambling into each of the four products, the amount of desorbed $^{13}C^{18}O$ will account for approximately one quarter of the total amount of adsorbed CO molecules that have been dissociated.

STM was performed at room temperature in constant current mode, using electrochemically etched W tips without any in-vacuum treatments other than applying a series of voltage pulses (typically 4–9 V for 10–100 ms) or scanning for several lines with increased bias ($U \approx 2$ V) in order to condition the tip. The typical tunnel parameters used to image the particles in this study were $U = 10$–600 mV for the gap bias and $I = 0.1$–0.8 nA for the tunnel current. Slow scan speeds were adopted with a typical line scan frequency of about 0.5–1 Hz.

B Ru(0 1 54) surface

The samples used for these experiments are Ru(0 1 54) single crystals (Mateck GmbH.), which on average expose 27-atom wide (001) terraces separated by monatomic steps. Due to the hexagonal close-packed structure of Ru, the steps will be of two alternating structures, one with three-fold symmetry and the other with four-fold symmetry.[22] For the TPD experiments presented here, a Ru(0 1 54) sample was cleaned by repeated cycles of sputtering with 1 keV Ar^+ ions at 800 K for 30 min, oxidation in 10^{-7} mbar O_2 at 1100 K for 10 min, reduction in 10^{-6} mbar H_2 at 500 K for 30 min, and finally annealing to 1200 K in UHV for 1 min. The cleanliness of the sample was checked by AES and CO TPD and oxygen titration measurements (which were used to check for carbon contamination).[32] TPD measurements were performed using a (Balzers 125) quadrupole mass spectrometer fitted with a differentially pumped OFHC copper sniffer tip with a 2 mm diameter circular aperture. This orifice was positioned at a distance of 0.5 mm from the sample surface, so that only desorption from the front side of the single crystal was measured. The sample temperature was measured by means of a C-type thermocouple spot-welded to the side of the crystal. The crystal was mounted on tungsten filaments which were used to provide direct current heating. During TPD measurements the sample temperature was ramped linearly at a rate of 2 K s^{-1}. The sample was mounted in the UHV chamber out of direct line-of-sight of the ionisation gauge in order to avoid hot-filament induced chemistry.

A second Ru(0 1 54) sample was used for the STM measurements, which was cleaned using a similar procedure to that described above.[50] The sample was sputtered using 1 keV Ar^+ ions by quickly rastering a 3 mm diameter ion beam with a current density of 18 μA cm^{-2} across the sample surface. The cleanliness was checked using STM, XPS and CO TPD measurements (the TPD setup was similar to the one described above). STM measurements were performed at room temperature in constant current mode, using electrochemically etched W tips. Images were typically recorded with a gap bias of 1 V and a tunneling current of 0.4–1 nA.

III. Results

A Ru nanoparticles on HOPG

The morphology of the mass-selected nanoparticles has been described in detail elsewhere.[43,44] Depositions were carried out so that between 10% and 40% of the HOPG surface was covered by a monodisperse distribution of nanoparticles with a mean diameter in the range from 2 nm to 15 nm.[51] Transmission electron microscopy (TEM) was used to measure the particle size distributions obtained after mass filtering and it was found that the diameters of the nanoparticles were distributed within ±15% of the mean diameter. TEM measurements revealed that smaller nanoparticles displayed more well-defined facets, while larger nanoparticles were found to be irregular in shape with evidence of significant surface roughness.[44] An example of a STM image of mass-selected 9.7 nm Ru nanoparticles on HOPG is shown in Fig. 1(a). We have previously established that the morphology of nanoparticles supported on sputtered or as-cleaved HOPG is basically the same.[43] Fig. 1(b) shows the total CO desorption spectrum obtained from 9.7 nm Ru nanoparticles. The TPD spectrum is characterised by a desorption peak located around 410 K, followed by a broad shoulder extending from around 480 K to 600 K. The molecularly- and dissociatively-adsorbed components of the TPD spectrum [also shown in Fig. 1(b)] can be deconvoluted by utilising the isotope exchange reaction,

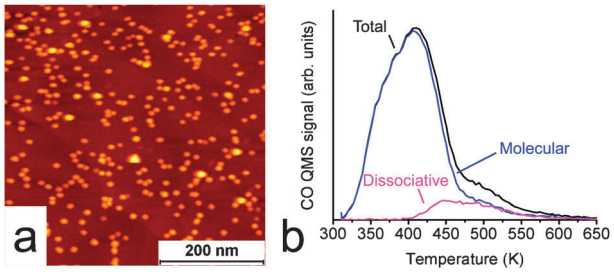

Fig. 1 STM and CO desorption from size-selected Ru nanoparticles on HOPG. (a) STM image of 9.7 nm Ru nanoparticles on sputtered HOPG. (b) CO TPD spectrum obtained from 9.7 nm Ru nanoparticles on as-cleaved HOPG, showing the total CO desorption, as well as the contributions from molecularly- and dissociatively-adsorbed CO.

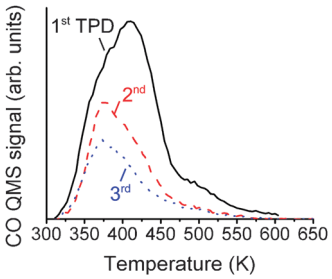

Fig. 2 Three successive CO TPD spectra obtained from 9.7 nm mass-selected Ru nanoparticles on as-cleaved HOPG, showing a drop in the desorption area.

$^{12}C^{18}O + {}^{13}C^{16}O \rightarrow {}^{12}C^{18}O + {}^{13}C^{16}O + {}^{13}C^{18}O + {}^{12}C^{16}O$, which is expected to occur after CO dissociation. It is clear that the large desorption peak located around 410 K corresponds to the molecularly desorbed component (*i.e.* mass-29 and mass-30 CO), while desorption of dissociatively adsorbed CO (here only mass-31 CO is used in the analysis), which displays peaks at 450 K and 530 K, is largely responsible for the broad shoulder up to 600 K seen in the total CO desorption spectrum.

Fig. 2 shows three successive CO TPD spectra obtained from 9.7 nm Ru nanoparticles on as-cleaved HOPG. The main desorption feature, which is located around 410 K in the first TPD, shifts to 375 K in the second and third spectra. There is also a substantial loss in the CO desorption area (63%) between the first and second TPD, and a smaller drop (30%) between the second and third TPD. This behavior was consistently observed for different nanoparticle sizes on as-cleaved and sputtered HOPG. It was usually found that the loss in desorption area became small or negligible after the second or third TPD. Three mechanisms can be identified as candidates for this deactivation: (1) sintering, (2) poisoning by loose carbon from the support, and (3) annealing-out of the initial surface roughness of the as-deposited nanoparticles. We have previously confirmed by STM that small nanoparticles (*e.g.* ~3 nm) deposited onto as-cleaved HOPG do sinter at elevated temperatures (775–975 K).[43] We have also performed oxygen titration experiments (not presented here), which indicate that carbon is present at the surface of the nanoparticles after heating to temperatures comparable to those encountered during the desorption experiments. We can therefore confirm that both of these mechanisms contribute to the deactivation of the nanoparticles, while the third proposed mechanism requires further investigation by performing annealing experiments in the TEM.

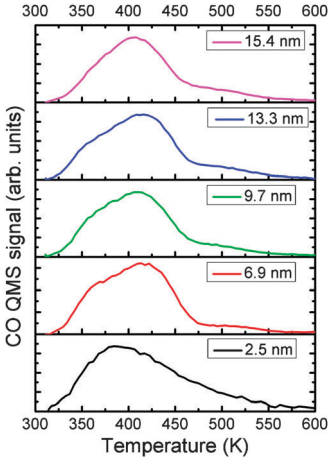

Fig. 3 CO TPD spectra obtained for different sized Ru nanoparticles supported on as-cleaved HOPG. The curves have been normalised to the same peak height.

Fig. 3 compares the total CO TPD spectra obtained from nanoparticles of different sizes supported on as-cleaved HOPG. The curves have been normalised to the same peak height in order to compare their shape. The TPD spectra are qualitatively similar being characterised by a broad desorption feature with a peak around 410–420 K and a broad shoulder extending from ~450 K to ~600 K. The low-temperature shoulder along with the high-temperature tail seems to increase as the nanoparticle size decreases, being most prominent for the 2.5 nm size. In previous studies of PVD grown Ru nanoparticles on mica, the position of the CO desorption feature was not observed to change substantially with the mean particle size.[52]

In addition to investigating the CO desorption behavior from mass-selected nanoparticles produced using the inert-gas aggregation source, we have also investigated the CO desorption behavior of PVD-grown Ru nanoparticles on HOPG. The morphology of these nanoparticles has been discussed in detail elsewhere.[43] Briefly, Ru films deposited onto as-cleaved HOPG at room temperature were found to display bimodal growth with small round nanoparticles decorating the substrate step edges and large flat nanoparticles formed on the terraces. The mean diameter of these nanoparticles was between 3 nm and 5.5 nm and their mean height was around 1.5 nm, while the spread in the measured size distributions was of the order of ±30%. On sputtered HOPG, room temperature deposition of Ru results in the formation of small round nanoparticles with a narrow size distribution. In this case, the mean particle diameter was approximately 2.3 nm and the mean height was close to 1.3 nm, while the spread in the measured particle size was ±20%. Examples of these two nanoparticle morphologies are shown in Fig. 4(a) and (c), which show STM images of 1 Å Ru films deposited on as-cleaved and sputtered HOPG, respectively. These images were obtained after CO TPD measurements were made. The average diameter of the nanoparticles from the 1 Å deposition was 5.2 ± 2.1 nm on the terraces

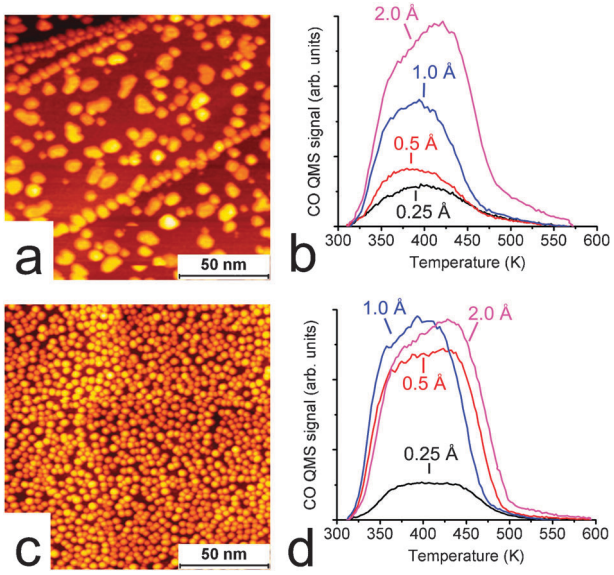

Fig. 4 STM and CO TPD measurements of Ru films deposited onto HOPG. (a) STM image of a 1 Å Ru film deposited onto as-cleaved HOPG. The average diameter of the terrace nanoparticles was 5.2 nm and their average height was 1.7 nm. (b) CO TPD spectra from 0.25–2.0 Å Ru films on as-cleaved HOPG. (c) STM image of a 1 Å Ru film deposited onto HOPG that has been pre-sputtered with 500 eV Ar^+ ions for 30 s. The average nanoparticle diameter was 2.1 nm and the average height was 1.1 nm. (d) CO TPD spectra from 0.25–2.0 Å Ru films on sputtered HOPG.

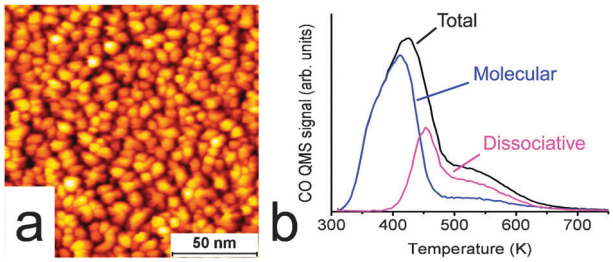

Fig. 5 (a) STM image of a 50 Å Ru film deposited on as-cleaved HOPG at room temperature. (b) The corresponding CO TPD spectrum obtained from the film, showing the total CO desorption, as well as the contributions from molecularly- and dissociatively-adsorbed CO.

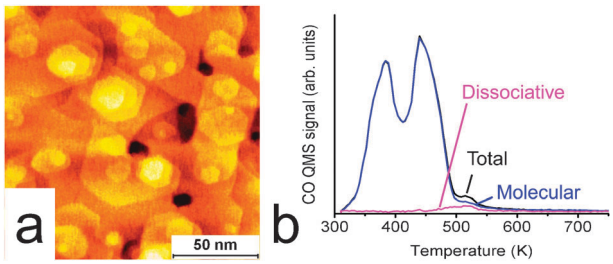

Fig. 6 (a) STM image of a 50 Å Ru film deposited on as-cleaved HOPG after annealing in UHV at 900 K for 10 min. (b) The corresponding CO TPD spectrum obtained from the film, showing the total CO desorption, as well as the contributions from molecularly- and dissociatively-adsorbed CO.

and 3.9 ± 1.0 nm along the steps, in the case of deposition on the as-cleaved HOPG surface [*cf.* Fig. 4(a)], and 2.1 ± 0.5 nm in the case of deposition on the pre-sputtered HOPG [*cf.* Fig. 4(c)]. The heights of the nanoparticles were on the order of 1–2 nm.[43] Fig. 4(b) and (d) show CO desorption spectra for different nominal film thicknesses deposited on (b) as-cleaved HOPG and (d) HOPG sputtered for 30 s with 500 eV Ar^+ ions. The desorption spectra are characterised by a single broad feature from ~350 K to ~450 K. For Ru nanoparticles deposited on as-cleaved HOPG the CO desorption area increases continuously with increasing nominal film thickness in the thickness range investigated here [see Fig. 4(b)]. This reflects the fact that the HOPG surface is gradually covered by Ru nanoparticles with increasing film thickness. By contrast, there is a substantial jump in the CO desorption area from the 0.25 Å to 0.5 Å Ru films on sputtered HOPG, after which the amount of CO desorbing from the surface remains approximately constant. In this case, the HOPG surface is partially exposed for the 0.25 Å film, but is almost completely saturated by Ru nanoparticles at a nominal film thickness of 0.5 Å [see Fig. 4(d)]. Thereafter, the total Ru surface area exposed to CO remains approximately constant for thicker films.[43] As was the case for the mass-selected nanoparticles, successive TPD spectra of the vapour-deposited nanoparticles (not shown here) also displayed deactivation of the nanoparticles between the first and second TPD measurements.

We have examined the CO desorption behaviour of these PVD-grown Ru films up to the extreme case of a 50 Å Ru thin film. Fig. 5(a) shows an image of a 50 Å Ru film deposited on as-cleaved HOPG at room temperature. The surface morphology of the film comprises nanoparticles with a mean diameter of 6 ± 2 nm. The substrate cannot be imaged by STM as the film is several layers thick. Fig. 5(b) shows the corresponding CO desorption spectrum, which shows a single broad desorption feature centered around 420 K and a broad shoulder from 500 K to 600 K. After obtaining this spectrum the film was annealed for 10 min at 900 K in UHV. The resulting film morphology, shown in Fig. 6(a), is polycrystalline with large flat terraces separated by monatomic steps. The corresponding CO desorption spectrum is shown in Fig. 6(b), and shows two desorption features at ~390 K and ~450 K. An additional, smaller peak can be seen at ~530 K. This spectrum agrees well with the typical desorption spectrum obtained from the Ru(001) facet.[18,22,30–32] The two principal peaks can be attributed to desorption of molecularly adsorbed CO from the terraces (α peaks), while the smaller peak can be attributed to desorption of dissociatively adsorbed CO from step sites (β peak).[13,22]

B Ru (0 1 54) surface

Fig. 7(a) and (b) show STM images of the non-sputtered Ru (0 1 54) surface and the same surface after sputtering for 5 min, respectively. The non-sputtered surface is characterised by terraces with a width varying between 4 nm and 10 nm, encompassing the expected average terrace width of 6.5 nm (corresponding to 27 atoms), and separated by straight monatomic steps with a measured height of 0.21 ± 0.01 nm, which is in good agreement with the distance between the (001) planes of ruthenium. In comparison, the steps on the sputtered surface display a high degree of roughness, while small islands are

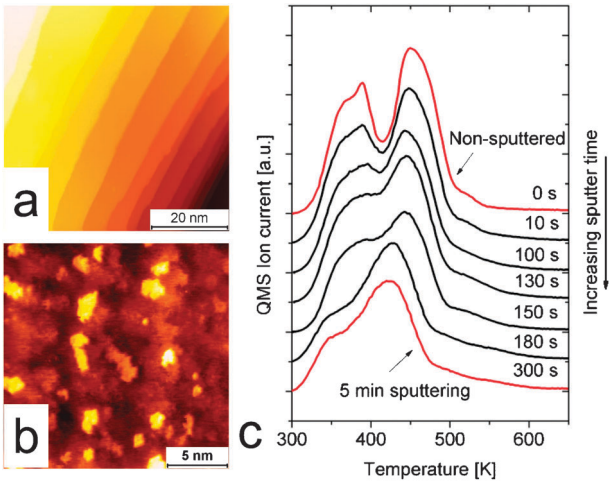

Fig. 7 STM and CO TPD measurements from a Ru(0 1 54) single crystal surface before and after Ar^+ ion sputtering. (a) STM image of the clean non-sputtered Ru(0 1 54) surface. (b) STM image of the same surface after sputtering with 1 keV Ar^+ ions for 5 min. (c) Sequence of CO TPD spectra obtained from the Ru(0 1 54) surface after sputtering with 1 keV Ar^+ ions for increasing periods of time.

evident on the terraces, which are presumably formed by surface restructuring as a result of the sputtering process.

Fig. 7(c) shows a sequence of CO desorption spectra obtained from the Ru(0 1 54) surface after different periods of sputtering with 1 keV Ar^+ ions at room temperature. The CO desorption spectrum from the non-sputtered surface shows two desorption peaks located at 390 K and 460 K that are characteristic of CO desorption from (001) terraces (α_1- and α_2-peaks) and a peak at $\sim$535 K corresponding to the dissociative adsorption at step sites (β-peak).[18,22,30–32] However, with increased surface sputtering a gradual transition is observed between the double-peak spectrum towards a single broad feature centered around 420 K. The desorption feature seen at 390 K on the non-sputtered surface gradually disappears with increased sputtering time until it is no more than a shoulder on the low-temperature side of the main desorption feature seen for the 5 min sputtered surface. In addition, the peak at 460 K on the non-sputtered surface gradually shifts down in temperature with increased sputtering time until the feature is located around 420 K.

It should be pointed out once again that the STM and TPD data of the Ru(0 1 54) surface presented here were obtained in two different UHV systems. However, in both cases the cleanliness of the surface before and after sputtering was confirmed (by XPS in the case of the STM measurements, and by AES and oxygen titration measurements in the case of the TPD experiments) to ensure that a contamination level below $\sim$1% was obtained. Moreover, CO TPD measurements were also performed in the STM system, which yielded qualitatively similar results to those presented here.

IV. Discussion

A Comparison of desorption energies

As demonstrated in Section IIIA the isotope exchange reaction unambiguously identifies molecular desorption being responsible for the main desorption feature at 410–420 K, while dissociative adsorption is responsible for smaller features at 430 K and 500 K. For comparison, Table 1 gives a summary of the CO desorption features reported from various studies (including this study) of supported Ru nanoparticles and single crystal surfaces. For the purposes of comparing our results to literature values, desorption energies based on the data presented in Table 1 are calculated and presented together in Fig. 8. The desorption features were classified into two categories corresponding to molecular (first-order) and dissociative (second-order) adsorption on the basis of the literature surveyed in Section I. The first-order desorption energies were calculated using the Redhead equation[53] and assuming a pre-exponential factor of 10^{13} s^{-1}. The second-order desorption energies were solved iteratively using the equation:[54]

$$E_{\mathrm{des}}(\theta) = RT_{\mathrm{p}} \ln\left(\frac{2\theta\nu(\theta)RT_{\mathrm{p}}^2}{E_{\mathrm{des}}(\theta)\beta}\right) \quad (1)$$

where T_{p} is the desorption peak temperature, θ is the remaining CO coverage (assumed to be half the initial coverage) and R is the gas constant. The desorption energy E_{des} and the pre-exponential factor ν are both assumed to be constant with coverage, where $\nu = 10^{13}$ s^{-1}.

From our CO TPD experiments on graphite-supported nanoparticles, we calculate desorption energies of 112–113 kJ mol^{-1}, which agree reasonably well with the values calculated from previous studies of oxide-supported nanoparticles,[38–42] particularly

Table 1 Summary of CO desorption features from saturation coverages of CO on various supported Ru nanoparticles and single crystal surfaces. The peak temperatures for the different desorption features and the heating rate are listed. Temperature intervals for some features have been indicated by hyphenated values. The desorption features have been classified into two categories; T_α representing molecular desorption and T_β representing dissociative adsorption

System	T_α/K	T_β/K	Heating rate/K s^{-1}
Ru NPs/HOPG[a]	410-420	450, 530	1
50 Å Ru/HOPG (as-deposited)[a]	420	450, 530	1
50 Å Ru/HOPG (annealed)[a]	390, 450	530	1
Ru/mica[52]	$\sim$410		1.5
Ru/Al_2O_3[38]	375	475, 600–630	1
Ru/Al_2O_3[39]	460	620	1
Ru/SiO_2[40]	450	650	1.5
Ru/SiO_2[41]	405, 473	698	0.17
(001)[18,30]	405-420, 465-480		5
(109)[22]	400, 450	535	2
(0 1 54)[32]	$\sim$390, $\sim$460	535	2
(0 1 54) non-sputtered[a]	$\sim$390, $\sim$460	535	2
(0 1 54) sputtered[a]	$\sim$420		2
Ru(S)-[15(001)×2(100)][20]	400, 470	520	9
(1 $\bar{1}$ 10)[13]	460	$\sim$580	15
(2 $\bar{1}$ 10)[19]	$\sim$460	$\sim$530	7.7
(2 $\bar{1}$ 22)[19]	$\sim$470	$\sim$530	5.2
(101)[33]	$\sim$480	$\sim$520	30
(100)[34]	$\sim$403, $\sim$495		8
(100)[35]	350, 380, 500		4
(100)[36]	375, $\sim$400, $\sim$500		8.7
(110)[37]	400, 440-460	500, 540	3

[a] This work.

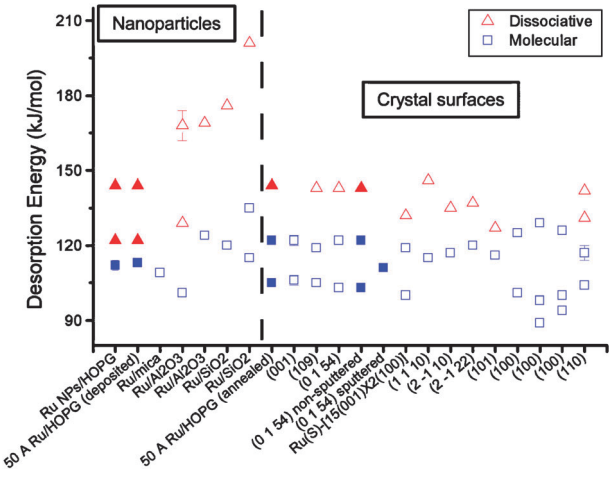

Fig. 8 Summary of the desorption energies calculated using the data presented in Table 1. Open symbols are data taken from previous studies, while filled symbols are taken from the present study. Temperature intervals for certain features are indicated by error bars.

with the case of PVD-grown nanoparticles on mica, see Fig. 8.[52] On the other hand, the desorption energies for dissociatively adsorbed CO (122 kJ mol^{-1} and 144 kJ mol^{-1}) calculated for our graphite supported nanoparticles are much lower than those estimated from the data available from these other studies, where a high temperature desorption feature was typically observed between 600 K and 700 K, corresponding to desorption energies around 164–201 kJ mol^{-1}. The origins of these high temperature peaks were investigated by McCarty and Wise[38] who used isotopic scrambling of $^{13}C^{16}O$ and $^{12}C^{18}O$ to investigate the dissociation of CO over Ru/Al_2O_3. While they observed isotope exchange at ~475 K (129 kJ mol^{-1}), which is in reasonable agreement with the results obtained in the present study, they also observed an unusual behaviour at ~600 K where the levels of ^{18}O containing isotopologues ($^{12}C^{18}O$ and $^{13}C^{18}O$) were found to decrease, while the levels of ^{16}O containing isotopologues ($^{12}C^{16}O$ and $^{13}C^{16}O$) increased. This indicated that an excess of ^{16}O was being derived from some source, though the Al_2O_3 support was ruled out as a potential source on the basis of blank TPD measurements. As a result, the nature of the higher temperature desorption feature observed between 600 K and 700 K in most of these studies has not been adequately explained and may be linked to the method of preparing the catalyst, *i.e.* wet impregnation.

B Origins of the nanoparticle desorption spectra

Compared to the single crystal surfaces, the desorption energies calculated for both molecularly- and dissociatively-adsorbed CO on the supported nanoparticles in the present study generally fall within the range of energies calculated for both the basal Ru surface and for more open surfaces. This may be attributed to the fact that the nanoparticles expose facets with different orientations. In the simplest representation of the nanoparticle shape, *i.e.* the Wulff construction, the nanoparticles will principally comprise (001), (101) and (100) facets, as these have the lowest surface free energy.[44,55] Consequently, the desorption spectra should mainly contain contributions from these facets. However, we have previously shown that the shape of the mass-selected Ru nanoparticles departs from the Wulff construction,[44] and consequently the CO desorption behaviour is expected to be more complex than one based on this simple model. In addition to the orientation of the facets exposed on the nanoparticle surface, their size may also influence the desorption spectra. For example, it has been shown that the double-peak molecular desorption feature characteristic of the Ru(001) facet appears to be inhibited on stepped Ru single crystal surfaces when the average terrace width is sufficiently narrow.[13,19] Shincho *et al.*[13] found a single desorption feature during CO desorption from a Ru(S)-[5(001)×(110)] surface comprising five-atom wide (001) terraces,[56] whereas Westre *et al.*[20] and Zubkov *et al.*[22] observed two desorption features during desorption from saturated CO coverages on Ru(S)-[15(001)×2(100)] and Ru(S)-[9(001)×2(101)] surfaces comprising fifteen- and nine-atom wide (001) terraces, respectively. There are two possible explanations for this: (1) the terraces are too small to accommodate the ordered overlayer structures found on extended (001) facets and (2) a localised lattice strain is produced in the vicinity of steps, which has been shown to influence CO adsorption.[57] In the case of nanoparticles, where facet sizes can be comparably small to the terrace widths found on highly stepped single crystal surfaces, both of these mechanisms may play a role in determining the CO desorption behaviour from the nanoparticle surface. In Fig. 4, a change in the desorption spectrum may be present for the smallest (*i.e.* 2.5 nm) of the nanoparticles with an increase in the low-temperature shoulder and in the high-temperature tail. This suggests that different sites are relatively more abundant on the very small nanoparticles. Detailed investigations of several mass-selected nanoparticle sizes in the 1–5 nm range are needed before conclusions can be made, but it is interesting to note that carbon-supported cobalt nanoparticles, which—just like ruthenium—are catalysts for the Fischer–Tropsch (FT) reaction, show an increase in FT activity for the very small sizes.[58]

It should also be pointed out that pre-adsorption of a small amount of O_2 or H_2O onto the Ru(001) surface prior to CO adsorption can substantially shift the TPD spectrum from the double-peak spectrum to a spectrum similar to that obtained from supported nanoparticles.[59,60] However, in the present study ISS measurements performed on the nanoparticles both before and after the TPD experiments showed no evidence of oxygen (*i.e.* below the detection limit of 1% of a monolayer). This indicates that the shape of the TPD spectra is related to the structure of the clean nanoparticle surface. We therefore conclude that the TPD spectrum obtained from the nanoparticles can be linked to a combination of the compact facet size on the nanoparticle surface, and the fact that more open facets may be exposed. This is particularly true when the shape of the nanoparticles departs from the equilibrium shape. Moreover, we observe two features corresponding to desorption of dissociatively adsorbed CO at 450 K and 530 K (desorption energies of 122 kJ mol^{-1} and 144 kJ mol^{-1}, respectively), which point to the presence of two main dissociation sites for CO on the nanoparticle surface.

C Crossover in desorption behaviour

A key result of the present study is that we have been able to demonstrate the crossover in CO desorption behaviour between Ru nanoparticles and the basal Ru surface simply by annealing a PVD-grown thin film to high temperature. The fact that we observe dissociative CO adsorption both before and after annealing the film proves that the surface remains free of carbon from the support, which would otherwise block the undercoordinated sites responsible for CO dissociation on the surface.[22,32] A key element in the formation of the polycrystalline film in Fig. 6 is that an epitaxial relationship exists between the vapour deposited Ru and the HOPG surface. In the case of the mass-selected nanoparticles discussed earlier, no such epitaxial relationship is obtained since the nanoparticles are formed before deposition and assume random orientations when landed on the surface. As expected, it was therefore not possible to obtain a morphology like that shown in Fig. 6(a) by annealing a thin film of mass-selected nanoparticles at 900 K. However, we believe that this should in principle be possible if higher anneal temperatures are used, which was not possible with the existing experimental set-up.

It was also possible to demonstrate the reverse transition in desorption behaviour between that of the basal Ru surface and that of Ru nanoparticles by sputtering a single crystal surface. As the amount of sputtering increases the amount and type of surface sites change as probed by the CO TPDs in Fig. 7(c). It is seen that the amount of step sites giving rise to the small shoulder at 510 K for the non-sputtered surface increases with more sputtering and changes into a broad feature ranging from below 500 K to at least 600 K for the most sputtered surface. This indicates that the sputtering introduces more undercoordinated sites, and that different kinds of sites exist giving rise to different desorption temperatures of dissociatively adsorbed C and O. More detailed STM studies of the sputtered surface would be required to identify the different site configurations.

It was found that the molecular desorption feature at 390 K gradually disappears, while the desorption feature at 460 K, corresponding to more strongly bound molecular CO, shifts downwards in temperature with increased sputtering. This can be rationalized as an effect of having smaller average terrace sizes on the sputtered surface. As mentioned earlier, the terraces may be too small to accommodate the ordered overlayer structures found on extended (001) facets. Also, it has previously been suggested by Jakob *et al.*[57] that the region 1–2 nm from the step exhibits a compressed lattice, which would result in a weaker binding of CO.[61] With a higher abundance of terrace sites in close proximity to a step, more weakly bonded CO would be expected, in excellent agreement with our CO TPDs.

It is observed that desorption of CO from the sputtered surface starts immediately upon heating from room temperature, whereas the desorption from the non-sputtered surface does not start until around $\sim$20 K above room temperature. This indicates that our CO TPD spectra from the sputtered surfaces do not probe all sites available on the surface, as the TPD spectrum from the non-sputtered surface appears to do. As such, one should not attempt to rationalise the apparent trend in Fig. 7(c) that the total CO desorption area decreases with increased sputtering time, until TPD experiments starting from below room temperature are performed.

V. Summary

We have compared the CO desorption characteristics of a stepped Ru(001) single crystal with Ru nanoparticles supported on graphite and have established the crossover in CO desorption behaviour between the two. Our main findings were:

- Mass-selected Ru nanoparticles deposited on HOPG display a single CO desorption feature around 410–420 K followed by a broad shoulder from 480 K to 600 K. Utilising the isotope exchange reaction we have established that the larger peak at 410–420 K is principally due to molecularly desorbing CO, while the shoulder is due to desorption of dissociatively adsorbed CO.
- Successive TPD measurements result in deactivation of the nanoparticles due to sintering and/or poisoning of the catalyst surface by carbon from the support. A possible third deactivation mechanism involves annealing-out the non-equilibrium surface features of the nanoparticles.
- Ru nanoparticles grown on HOPG by vapour deposition display broadly the same characteristics as the mass-selected nanoparticles. Moreover, by annealing a PVD-grown thin film we demonstrate a crossover in CO desorption spectra from that characteristic of supported nanoparticles to one characteristic of a stepped Ru(001) single crystal surface.
- Starting from a stepped Ru(001) single crystal surface we have also demonstrated the reverse transition from single crystal to nanoparticle-like CO desorption behaviour by means of Ar^+ ion sputtering.

We have shown that it is possible to vary the desorption behaviour between the two model catalyst systems by using straightforward sample preparation methods. These results demonstrate the complementary nature of both model catalyst systems and affirm the validity of studying both in order to narrow the materials gap to more complex industrial catalysts. With further work, for example using more well-defined Wulff constructed nanoparticles or mesoscale crystals,[62] even greater insight into the crossover between the desorption behavior of single crystal surfaces and supported nanoparticles can be obtained.

This work was supported by the Danish National Research Foundation and the EU FWP7 Marie Curie Intra-European Fellowship ESRCN (PIEF-GA-2008-220055).

References

1 D. W. Goodman, *Chem. Rev.*, 1995, **95**, 523.
2 G. A. Somorjai, R. L. York, D. Butcher and J. Y. Park, *Phys. Chem. Chem. Phys.*, 2007, **9**, 3500.
3 H. Oosterbeek, *Phys. Chem. Chem. Phys.*, 2007, **9**, 3570.
4 J. Assmann, V. Narkhede, N. A. Breuer, M. Muhler, A. P. Seitsonen, M. Knapp, D. Crihan, A. Farkas, G. Mellau and H. Over, *J. Phys.: Condens. Matter*, 2008, **20**, 184017.
5 C. R. Henry, *Surf. Sci. Rep.*, 1999, **31**, 231.
6 H. J. Freund, H. Kuhlenbeck, J. Libuda, G. Rupprechter, M. Bäumer and H. Hamann, *Top. Catal.*, 2001, **15**, 201.
7 S. Haq and R. Raval, *Phys. Chem. Chem. Phys.*, 2007, **9**, 3641.
8 S. Dahl, P. A. Taylor, E. Törnqvist and I. Chorkendorff, *J. Catal.*, 1998, **178**, 679.

9 S. Dahl, A. Logadottir, R. C. Egeberg, J. H. Larsen, I. Chorkendorff, E. Törnqvist and J. K. Nørskov, *Phys. Rev. Lett.*, 1999, **83**, 1814.
10 R. A. Dalla'Betta and M. Shelef, *J. Catal.*, 1977, **48**, 111.
11 H. Abrevaya, M. J. Cohn, W. M. Targos and H. J. Robota, *Catal. Lett.*, 1990, **7**, 183.
12 R. J. Madon, S. C. Reyes and E. Iglesia, *J. Phys. Chem.*, 1991, **95**, 7795.
13 E. Shincho, C. Egawa, S. Naito and K. Tamaru, *Surf. Sci.*, 1985, **149**, 1.
14 J. C. Fuggle, E. Umbach, P. Feulner and D. Menzel, *Surf. Sci.*, 1977, **64**, 69.
15 H. Pfnür, P. Feulner, H. A. Engelhardt and D. Menzel, *Chem. Phys. Lett.*, 1978, **59**, 481.
16 P. Feulner, H. A. Engelhardt and D. Menzel, *Appl. Phys.*, 1978, **15**, 355.
17 J. A. Schwarz and S. R. Kelemen, *Surf. Sci.*, 1979, **87**, 510.
18 H. Pfnür, P. Feulner and D. Menzel, *J. Chem. Phys.*, 1983, **79**, 4613.
19 T. Yamada, Y. Iwasawa and K. Tamaru, *Surf. Sci.*, 1989, **223**, 527.
20 E. D. Westre, D. E. Brown, J. Kutzner and S. M. George, *Surf. Sci.*, 1994, **302**, 280.
21 T. Zubkov, G. A. Morgan and J. T. Yates, *Chem. Phys. Lett.*, 2002, **362**, 181.
22 T. Zubkov, G. A. Morgan, J. T. Yates, O. Kühlert, M. Lisowski, R. Schillinger, D. Fick and H. J. Jänsch, *Surf. Sci.*, 2003, **526**, 57.
23 T. E. Madey, *Surf. Sci.*, 1979, **79**, 575.
24 G. E. Thomas and W. H. Weinberg, *J. Chem. Phys.*, 1979, **70**, 1437.
25 H. Pfnür, D. Menzel, F. M. Hoffmann, A. Ortega and A. M. Bradshaw, *Surf. Sci.*, 1980, **93**, 431.
26 E. D. Williams and W. H. Weinberg, *Surf. Sci.*, 1979, **82**, 93.
27 G. Michalk, W. Moritz, H. Pfnür and D. Menzel, *Surf. Sci.*, 1983, **129**, 92.
28 H. Pfnür and D. Menzel, *Surf. Sci.*, 1984, **148**, 411.
29 P. Jakob, *J. Chem. Phys.*, 2004, **120**, 9286.
30 S. Kneitz, J. Gemeinhardt and H. P. Steinrück, *Surf. Sci.*, 1999, **440**, 307.
31 S. H. Payne, J. S. McEwen, H. J. Kreuzer and D. Menzel, *Surf. Sci.*, 2005, **594**, 240.
32 S. B. Vendelbo, M. Johansson, D. J. Mowbray, M. P. Andersson, F. Abild-Pedersen, J. H. Nielsen, J. K. Nørskov and I. Chorkendorff, *Top. Catal.*, 2010, **53**, 357.
33 P. D. Reed, C. M. Comrie and R. M. Lambert, *Surf. Sci.*, 1976, **59**, 33.
34 R. Ku, N. A. Gjostein and H. P. Bonzel, *Surf. Sci.*, 1977, **64**, 465.
35 G. Lauth, T. Solomun, W. Hirschwald and K. Christmann, *Surf. Sci.*, 1989, **210**, 201.
36 G. Rotaris, A. Baraldi, G. Comelli, M. Kiskinova and R. Rosei, *Surf. Sci.*, 1996, **359**, 1.
37 J. Wang, Y. Wang and K. Jacobi, *Surf. Sci.*, 2001, **488**, 83.
38 J. G. McCarty and H. Wise, *Chem. Phys. Lett.*, 1979, **61**, 323.
39 G. G. Low and A. T. Bell, *J. Catal.*, 1979, **57**, 397.
40 E. Zağli and J. L. Falconer, *J. Catal.*, 1981, **69**, 1.
41 H. M. Miura, M. L. McLaughlin and R. D. Gonzalez, *J. Catal.*, 1983, **79**, 227.
42 N. Kakuta and J. M. White, *J. Catal.*, 1986, **97**, 150.
43 R. M. Nielsen, S. Murphy, C. Strebel, M. Johansson, J. H. Nielsen and I. Chorkendorff, *Surf. Sci.*, 2009, **603**, 3420.
44 R. M. Nielsen, S. Murphy, C. Strebel, M. Johansson, I. Chorkendorff and J. H. Nielsen, *J. Nanopart. Res.*, 2010, **12**, 1249.
45 J. H. Nielsen, L. Bech, K. Nielsen, Y. Tison, K. P. Jørgensen, J. L. Bonde, S. Horch, T. F. Jaramillo and I. Chorkendorff, *Surf. Sci.*, 2009, **603**, 1182.
46 F. Besenbacher, E. Lægsgaard, K. Mortensen, U. Nielsen and I. Stensgaard, *Rev. Sci. Instrum.*, 1988, **59**, 1035.
47 S. Murphy, R. M. Nielsen, M. Johansson and J. H. Nielsen, *Carbon*, 2011, **49**, 376.
48 Therefore, some surface defects may have been formed on the HOPG by accelerated positive Ru ions coming from the electron-beam evaporator.
49 Our measurements indicated a concentration of approximately 1% $^{13}C^{18}O$ in the $^{13}C^{16}O$ dosing gas.
50 The only differences were that the reduction step was carried out for 20 min and the final anneal step in UHV was carried out at 1400 K for 2 min.
51 The corresponding diameter of a sphere with the selected mass is used to identify the nanoparticles.
52 C. Park, W. G. Durrer, H. Poppa and J. T. Dickinson, *J. Catal.*, 1985, **95**, 361.
53 P. A. Redhead, *Vacuum*, 1962, **12**, 203.
54 I. Chorkendorff and J. W. Niemantsverdriet, *Concepts of Modern Catalysis and Kinetics*, Wiley, 2007.
55 J. Gavnholt and J. Schiøtz, *Phys. Rev. B: Condens. Matter*, 2008, **77**, 035404.
56 Here we have used the notation for stepped surfaces to describe the Ru(1 1 10) surface.
57 P. Jakob, M. Gsell and D. Menzel, *J. Chem. Phys.*, 2001, **114**, 10075.
58 G. L. Bezemer, J. H. Bitter, H. P. C. E. Kuipers, H. Oosterbeek, J. E. Holewijn, X. Xu, F. Kapteijn, A. J. van Dillen and K. P. de Jong, *J. Am. Chem. Soc.*, 2006, **128**, 3956.
59 H. I. Lee, B. E. Koel, W. M. Daniel and J. M. White, *J. Catal.*, 1982, **74**, 192.
60 K. L. Kostov, H. Rauscher and D. Menzel, *Surf. Sci.*, 1992, **278**, 62.
61 M. Mavrikakis, B. Hammer and J. K. Nørskov, *Phys. Rev. Lett.*, 1998, **81**, 2819.
62 N. Tian, Z. Y. Zhou, S. G. Sun, Y. Ding and Z. L. Wang, *Science*, 2007, **316**, 732.

Dissolution structures of Bi overlayers on Pt(111)

Kenneth Nielsen, Yann Tison, Lone Bech, Jane H. Nielsen

September 1, 2011

1 Abstract

The work presented in this articles is an UHV STM and XPS study of the dissolution structures of bismuth overlayers on a Pt(111) single crystal. Samples were prepared by multilayer PVD of bismuth on the Pt(111) sample at room temperature, after which it was heated to a temperature in the range from 300°C to 700°C for a duration between 3 and 30 min. After the heat treatment the sample was characterized by XPS and STM.

The XPS results showed an increase in between the deposition and the first heat treatment at 300°C for 3 min, probably associated with an ordering of the overlayers. A heat treatment to 500°C for 3 min was sufficient to evaporate all bismuth in excess of the first overlayer. Two small shifts was observed for the XPS binding energy of the Bi $4f_{7/2}$ peak. It shifted up by 0.08 eV±0.02 between deposition and the first heat treatment at 300°C 3 min, probably due to an ordering of the overlayer. It also shifted down by 0.10 eV±0.02eV between the heat treatments of 500°C 3 min and 500°C 30 min. The last shift can be due either to the evaporation of the bismuth layer in excess of 1 ML or due to alloying.

From the STM images it was observed that the bismuth is deposited as an amorphous overlayer. After the first heat treatment at 300°C 3 min these

overlayers ordered themselves into a crystalline island structure with islands as high as 13.0 nm. After the heat treatment to 500°C 3 min the images show a surface without any islands and step heights comparable to the substrate, indicative of a single monolayer, and a hexagonal periodicity of 1.05-1.07×1.07-1.08 nm 62.2-65.8° which is consistent with a p(4 × 4) overlayer. In all higher heat treatments the surface went through a continuous dissolution of the single monolayer. In this process holes were formed in the surface in a semi-regular pattern, until these holes became interconnected, at which point the remaining bismuth appear as particles.

Surface Science 603 (2009) 1182–1189

Contents lists available at ScienceDirect

Surface Science

journal homepage: www.elsevier.com/locate/susc

Combined spectroscopy and microscopy of supported MoS_2 nanoparticles

J.H. Nielsen [a,*], L. Bech [a], K. Nielsen [a], Y. Tison [a,b], K.P. Jørgensen [a,1], J.L. Bonde [a,2], S. Horch [a,b], T.F. Jaramillo [a,3], I. Chorkendorff [a]

[a] Center for Individual Nanoparticle Functionality (CINF), Department of Physics, Nano-DTU, Building 312, Technical University of Denmark, 2800 Kgs. Lyngby, Denmark
[b] Center for Atomic-scale Materials Design (CAMD), Department of Physics, Nano-DTU, Building 307, Technical University of Denmark, 2800 Kgs. Lyngby, Denmark

ARTICLE INFO

Article history:
Received 28 November 2008
Accepted for publication 24 February 2009
Available online 18 March 2009

Keywords:
Scanning tunneling microscopy
X-ray photoelectron spectroscopy
Au(1 1 1)
Molybdenum-sulfide
Supported nanoparticle

ABSTRACT

Supported molybdenum-sulfide nanoparticles are known catalysts for petroleum hydrodesulfurization as well as for electrochemical hydrogen evolution. In this study, we investigate molybdenum-sulfide nanoparticles supported on Au(1 1 1) using X-ray photoelectron spectroscopy (XPS) and scanning tunneling microscopy (STM), aiming to correlate spectroscopically determined chemical states with atomically resolved nanostructure. The results of this study allow us to conclude the following: (1) the XPS results from our model system are in good agreement with previously published results on supported MoS_2 for industrial applications, validating in part the fidelity of the model system; (2) STM reveals that catalytically active, crystalline MoS_2 nanoparticles exhibiting the well-known metallic edge state are only present after a post-deposition annealing step in the synthesis procedure, without which the particles exhibit amorphous shapes and incomplete sulfidation; and (3) the sulfided nanoparticles are found to be stable in air at room temperature.

1. Introduction

MoS_2 catalysts are most commonly investigated in relation to the hydrodesulfurization (HDS) process used for petroleum feedstocks [1]. A number of experimental methods have been employed in previous work to show that MoS_2 particles supported on high surface area, industrially-relevant substrates like carbon or alumina are present as nano-crystals [2,3], primarily as single S–Mo–S trilayers in the shape of slightly truncated triangles [4]. The edges of the nanoparticles play a critical role in the desulfurization of crude oils, as their sulfur-containing organics are believed to adsorb at the edge via the sulfur atom immediately prior to bond cleavage [1].

In order to better understand this catalyst, ultra-high vacuum (UHV) surface science methods have been employed in studying model systems consisting of MoS_2 or MoS_x nanoparticles supported on defect-induced highly ordered pyrolytic graphite (HOPG) [5,6] and Au(1 1 1) [7–10]. Scanning tunneling microscopy (STM) of MoS_2 on Au(1 1 1) has provided images of triangular shaped, single-layered MoS_2 particles, giving insight into the catalyst surface structure on the atomic scale. STM images of the nanoparticles exhibited a bright edge state running along their perimeters, the origin of which was ultimately explained by density functional theory (DFT) calculations: the edges of these nanoparticulate semiconductors are in fact metallic [7,8,11]. X-ray photoelectron spectroscopy (XPS) of supported MoS_x systems has been performed previously [12–15] and a clear influence of the degree of sulfidation on Mo and S binding energies is observed. However, the exceptional structure information obtained by STM has not yet been supplemented with spectroscopic measurements on those same samples; such a study would give insight into the local chemical environment of Mo and S on well-defined nanoparticulate systems.

Linking results from UHV-studied model catalysts to those of commercial catalysts operating at high pressures and temperatures is an important undertaking, bridging the gap between the fields of surface science and heterogeneous catalysis. One aim of the present work is to improve links in our understanding of the model MoS_2 catalyst studied by UHV surface science methods to that of MoS_2 catalysts deposited on high surface area, industrially-relevant supports such as alumina or particulate carbon. XPS measurements have not yet been reported on the model catalysts, preventing a direct comparison to their industrial counterparts for which data has been collected previously [15–17]. In the following, we report a combined XPS and STM study of different low-coverage preparations (<0.2 ML) of MoS_2 nanoparticles supported on Au(1 1 1) and draw comparisons to previous work on planar model

* Corresponding author. Tel.: +45 45 25 32 22.
E-mail address: jane@fysik.dtu.dk (J.H. Nielsen).
[1] Present address: Haldor Topsøe A/S, Nymøllevej 55, 2800 Kgs. Lyngby, Denmark.
[2] Present address: IRD Fuel Cell, Kullingade 31, 5700 Svendborg, Denmark.
[3] Present address: Department of Chemical Engineering, 381 North-South Mall, Stauffer III, Stanford University, Stanford, CA 94305-5025, USA.

0039-6028/$ - see front matter © 2009 Elsevier B.V. All rights reserved.
doi:10.1016/j.susc.2009.02.039

systems and supported nano-catalysts for HDS. The present study also aims to elucidate effects of varying the sulfidation process conditions.

Another important aspect to explore is the stability of the MoS_2/Au(1 1 1) nano-catalysts upon exposure to atmospheric air. We also employ XPS for this study, inspired by recent results in which a well-characterized model system consisting of supported MoS_2 nanoparticles was shown to be catalytically active for the hydrogen evolution reaction (HER). This was concluded based on electrochemical measurements on STM-imaged samples, whose results were consistent with predictions made by DFT calculations [5,18]. STM-imaging the catalysts allowed the MoS_2 electrocatalytic activity to be correlated to its surface structure, and it was found that the active site for the hydrogen evolution was the edge [18]. Linking UHV studies to reactions at ambient conditions have clearly pointed to the edge as the key feature for MoS_2's catalytic activity, whether for HDS or the HER [1,16,18,19]. However, only for the aforementioned HER studies were the MoS_2 nano-catalysts the same exact samples as those prepared and characterized using UHV surface science methods and studied as catalysts under ambient-pressure reaction conditions. This was accomplished by transferring the UHV-prepared and characterized samples out of vacuum and into an electrochemical cell. Thus exploring their stability in the oxidizing environment of atmospheric air is of direct relevance.

2. Experimental

The experiments are performed in two ultra-high vacuum (UHV) chambers with base pressures below $1{\cdot}10^{-10}$ mbar, both normally equipped with an STM of the Aarhus type [20]. We have chosen to use a gold surface as support for the MoS_2 nanoparticles. The Au(1 1 1), supplied by MaTeck, is aligned to within 0.4° of the (1 1 1) direction and is cleaned immediately prior to MoS_2 deposition by cycles of 2 keV Ar^+ sputtering at room temperature and at elevated temperatures, followed by annealing at 650 °C. The sample is heated by electron bombardment from a tungsten filament on to the backside of the single crystal. The cleanliness is checked by XPS using a commercial Specs system consisting of a Specs RQ 20/38 X-ray gun and a 100 mm Phoibos hemispherical analyzer. All measurements are performed with Mg Kα radiation. The energy calibration of the photoelectrons is performed against the Au $4f_{7/2}$ line (E_B = 84.0 eV). We estimate that the binding energies are accurate within ±0.2 eV. No traces of carbon, oxygen or sulfur are detectable with XPS after the cleaning procedure described above. The cleanliness of the Au(1 1 1) surface is confirmed with STM, and the well-known herringbone reconstruction is observed [21]. The XPS spectra of the Mo 3*d* and S 2*p* lines are fitted using CasaXPS with a series of peaks superimposed on a Shirley or a linear background, respectively.

The H_2S gas is of purity 99.5% (N25) and it is dosed through a directed doser in order to maintain an overall lower chamber pressure, which is continuously monitored during synthesis with an ion gauge. The local pressure over the sample is estimated to be approximately a factor of ten higher.

The Mo is deposited by physical vapor deposition (PVD) from a home-made evaporator consisting of a resistively heated high purity Mo filament (99.95%). The cleanliness of the evaporated Mo was verified by XPS. A shutter flag allows for accurate dosing times.

The preparation of the MoS_2 nanoparticles is inspired by the procedure described in Ref. [22]. Alternatives to this synthesis procedure exist, e.g. using Mo carbonyls and S_2 precursors [10]. Our clean Au(1 1 1) is pre-annealed to 600 °C and allowed to cool. Once the Au(1 1 1) crystal reaches 177 °C, the H_2S gas is introduced to the chamber, resulting in a steady-state overall pressure of $1.3{\cdot}10^{-7}$ mbar and a pressure at the sample surface of approximately $1{\cdot}10^{-6}$ mbar. Once the sample temperature reaches 147 °C, the evaporator shutter flag is opened allowing Mo deposition for 0.5–3 min at a Mo flux on the order of 0.1 ML/min. Three different treatments after the evaporation are employed in this work: (A) no post-deposition annealing, (B) annealing at 400 °C for 15 min in H_2S (this is the procedure described in Ref. [22]), and (C) annealing at 550 °C for 15 min in H_2S. Following the annealing step, the sample is allowed to cool down to 95 °C before the H_2S exposure is terminated. After synthesis, the sample is characterized with XPS.

In the UHV chamber, where the synthesis of the MoS_2 nanoparticles is performed, the STM had to be removed in order to avoid exposure to the H_2S gas, which degrades certain mechanical parts of the STM. For imaging, the sample is transferred under vacuum ($p < 10^{-7}$ mbar) to a different UHV chamber where STM measurements are performed. Image analysis was performed using SPIP [23]. Some of the synthesized MoS_2 samples were transferred in air to electrochemical measurements after the STM investigation. The results of the electrochemical measurements are reported elsewhere [18].

3. Results

3.1. XPS on MoS_x/Au(1 1 1)

In Fig. 1, a representative XPS broad spectrum of Au(1 1 1) supported MoS_2 nanoparticles annealed to 400 °C is shown. All Au peaks are indicated, as are the energy positions for O 1*s*, C 1*s*, Mo 3*d* and S 2*p*. Furthermore, each inset in Fig. 1 exhibits the corresponding high resolution spectra comparing clean Au(1 1 1) (bottom) to the MoS_2/Au(1 1 1) spectra (top). The coverage of MoS_2 is estimated to be ~0.1 ML as determined by XPS. Neither C nor O is observed before or after synthesis, indicating that the support was clean and that no contamination had been inadvertently deposited during MoS_2 synthesis. Also note that the S 2*p* signal is present only after synthesis, as expected. A small Mo signal, however, is detected for the clean Au(1 1 1) sample; this is attributed to the surrounding sample holder which is made of molybdenum and lies within the field of view of the detector. This unwanted background signal can be significantly reduced by adjusting the iris set-

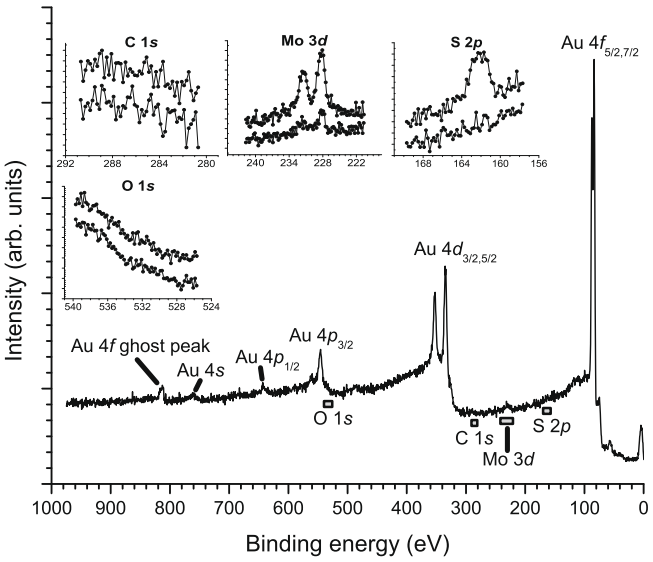

Fig. 1. XPS spectra of ~0.1 ML MoS_2 supported on Au(1 1 1), after post-deposition annealing to 400 °C. The dominant Au features and the key binding energy regions for Mo, C, O, and S are indicated in the full spectrum, with selected elemental lines shown with higher resolution in the insets. For comparison, the corresponding measurements for the clean Au(1 1 1) are shown as the lower spectra in the insets. The small Mo 3*d* signal from the sample plate is also visible.

ting of the analyzer, however such a setting would also severely reduce signal intensity from the MoS_2/Au(1 1 1) sample. Thus, we use the wider aperture and subtract the background Mo signal for coverage determinations of deposited Mo and MoS_2.

In order to vary the size and shape of the sulfided Mo particles on the surface, different post-deposition treatments are employed as described in Section 2. Representative XPS spectra of Mo 3*d* and S 2*p* for the three synthesis procedures following evaporation of Mo in an atmosphere of H_2S are shown in Fig. 2: (A) no post-deposition annealing, (B) annealing in H_2S gas at 400 °C (two different coverages are shown), and (C) annealing in H_2S gas at 550 °C. The Mo 3*d* spectra are fitted with asymmetric peaks based on the Gaussian–Lorentzian line shape with asymmetry parameter of 0.33, consistent with Fermi sea screening of the core hole [24,25] due to the coupling to the gold substrate's free electrons and possibly some contribution from the metallic edge state. The splitting between the Mo $3d_{3/2}$ and $3d_{5/2}$ peaks was fixed to 3.15 eV, consistent with literature [16,26], and the intensity ratio was fixed to 2:3 according to the quantum numbers. The small peak around 226.5 eV is attributed to the S 2*s* line in agreement with previous reports [27,28]. The S 2*s* is set to scale with the S 2*p* area (2*p*:2*s* = 1.63), in agreement with their sensitivity factors [29]. The Mo $3d_{5/2}$ binding energies extracted from the deconvolution are 228.2 eV (A, no annealing), 228.7 eV (i) and 228.5 eV (ii) (B, annealing at 400 °C), and 228.5 eV (C, annealing at 550 °C). The S 2*p* lines are fitted with Gaussian–Lorentzian line-shapes with spin-orbit splitting of 1.2 eV in agreement with literature [26] and intensity ratio fixed to 0.5, and we extract binding energies of 161.6 eV (A), 162.0 eV (B (i) and (ii)), and 162.1 eV (C).

3.2. XPS on Mo/Au(1 1 1)

In order to establish the line positions for metallic Mo for our experimental conditions, Mo is deposited for 33 min in the absence of H_2S, with intermittent stops after 1 and 3 min to characterize the sample by XPS as shown in Fig. 3. In order to stay close to the MoS_2 synthesis conditions, a similar flux is used, and the Mo is deposited on a heated Au substrate, initially at 147 °C from which the sample is allowed to cool during each deposition. Surface alloying is known to take place for the Mo–Au system however not at deposition temperatures below 250 °C [30], so we do not expect any intermixing in the experiments for Fig. 3. The first spectrum was obtained after 1 min in the presence of the Mo flux, Fig. 3(I). The next deposition added 2 min of Mo with a similar flux to the sample. After XPS characterization, shown in Fig. 3(II), a large amount was added by depositing Mo for 30 min, and the XPS spectrum divided by ten is shown in Fig. 3(III). Using the same fitting parameters and constraints as in the previous section (except for a slightly higher asymmetry parameter of 0.45, consistent with a more metallic character of the Mo deposits), binding energies of the Mo $3d_{5/2}$ lines are found to be at 228.0 eV (I), 227.9 eV (II) and 227.7 eV (III). This is in good agreement with literature values for metallic Mo 3 $d_{5/2}$, which are reported to be in the range of 227.5–227.9 eV [31–33].

3.3. STM on MoS_x/Au(1 1 1)

After characterization with XPS, the samples are investigated with STM. In Fig. 4, STM images of 47 nm × 47 nm are shown for MoS_x/Au(1 1 1) samples, prepared using A: no post-deposition annealing, B: annealing at 400 °C, and C: annealing at 550 °C. In all three cases, the particles are well-dispersed on the Au(1 1 1) surface, aided by the herringbone reconstruction which serves to keep the particles separated [7]. No sign of incorporation of Mo or alloying is observed even after the highest post-deposition annealing temperature, which we attribute to the presence of the reactive

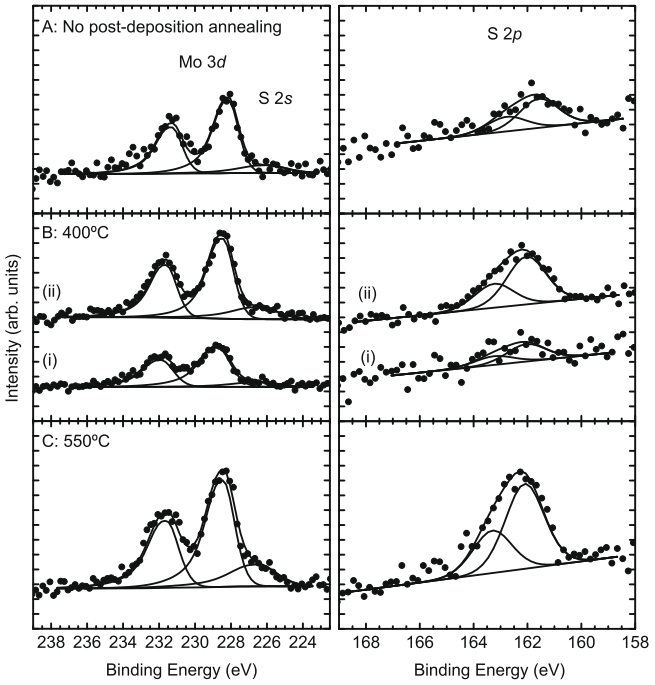

Fig. 2. XPS measurements of the Mo 3*d* (left) and S 2*p* (right) lines of Mo deposited in H_2S as described in the text. The post-deposition annealing conditions differ: (A) no annealing, (B) post-deposition annealing in H_2S at 400 °C, and (C) post-deposition annealing in H_2S at 550 °C. Using the fits shown as solid lines, the MoS_2 coverages are estimated to be 0.09 ML(A), 0.04 ML (B(i)), 0.11 ML (B(ii)), and 0.16 ML (C).

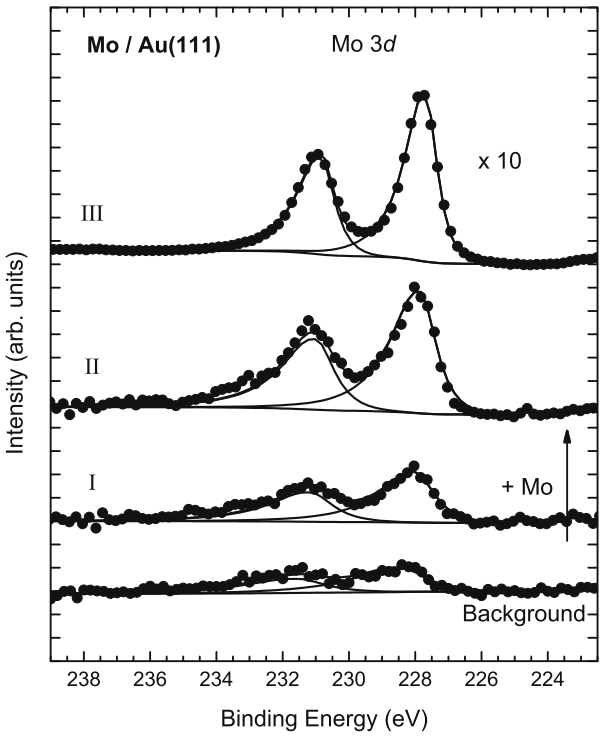

Fig. 3. XPS measurements of the Mo 3*d* line for increasing amounts of Mo deposited on Au(1 1 1) at 147 °C. The lowest spectrum is a background measurement of the clean Au(1 1 1) surface attached to a Mo sample plate, and the three spectra above (I–III) are recorded after depositing increasing amounts of Mo. The topmost spectrum (III) has been scaled down by a factor 10. The estimated Mo coverages are 0.06 ML (I), 0.2 ML (II) and 3.1 ML (III). The solid lines are fits to the data.

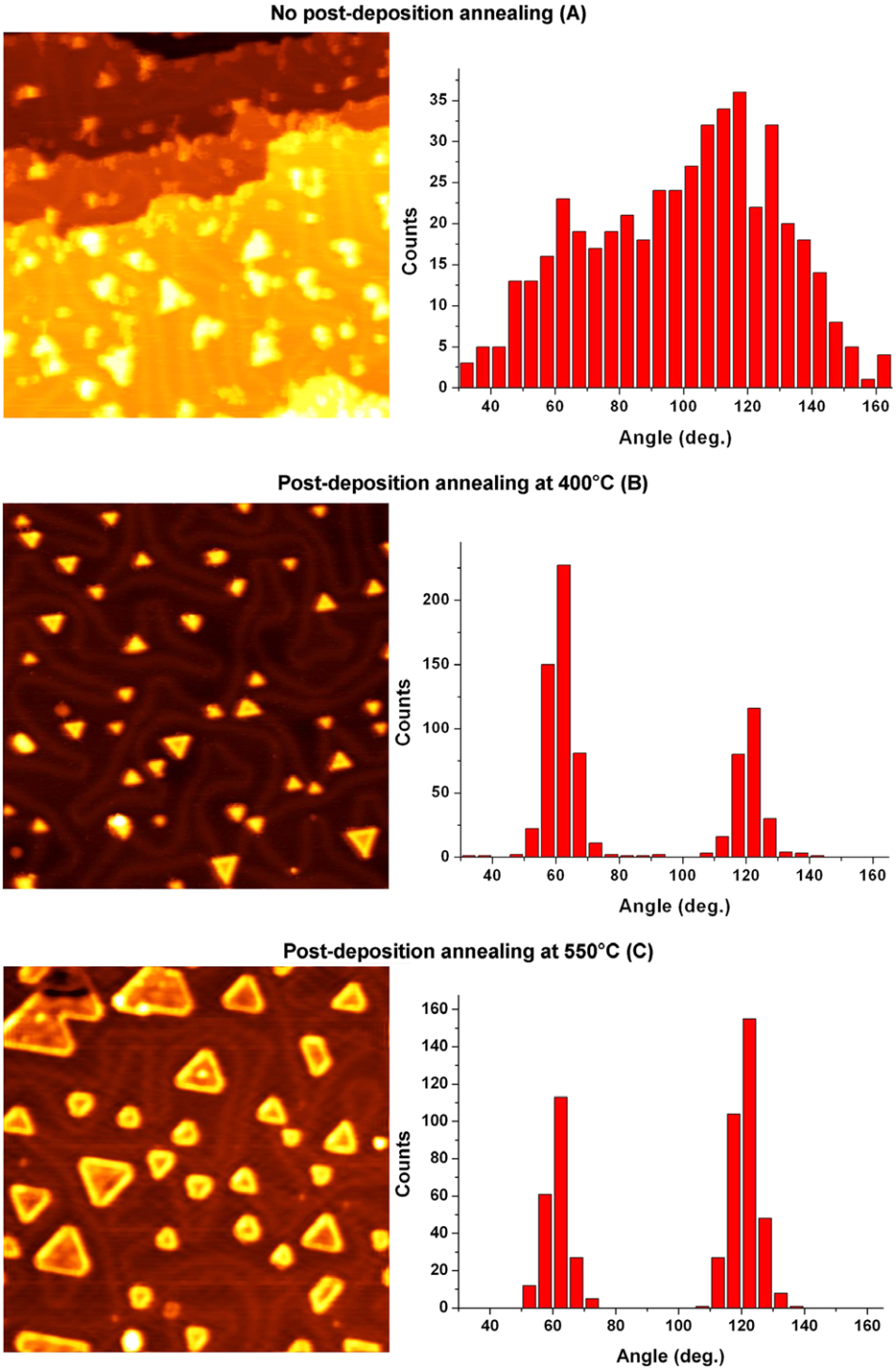

Fig. 4. STM of Mo deposited in H_2S on Au(1 1 1). Mo was deposited in an H_2S atmosphere followed by no post-deposition annealing (A), annealing in H_2S at 400 °C (B), and annealing in H_2S at 550 °C (C). Fig. 4(A) and (B) were obtained on the same samples as the XPS spectra presented in Fig 2(A) and (B(i)), respectively. All STM images are 47 nm × 47 nm, and the scanning parameters are: (A) V_t = 1.3 V, I_t = −2.9 nA, (B) V_t = 1.4 V, I_t = −4.8 nA, (C) V_t = 1.6 V, I_t = −1.1 nA. The STM-based MoS_2 coverage estimates are 0.1 ML(A), 0.05 ML(B) and 0.14 ML(C), in good agreement with the corresponding coverages estimated from XPS. To the right of each STM image, a distribution of angles measured on the nanoparticles prepared under each of the three conditions is shown, quantifying the effect of post-deposition annealing on particle shape.

H_2S gas, preventing intermixing. The nanoparticles synthesized without post-deposition annealing (Fig. 4A) are poorly defined compared to the annealed particles (Figs. 4B and C) – a few unannealed particles exhibit a pseudo-triangular shape (Fig. 4A), but the majority appears as amorphous aggregates of nanometer dimensions. The unannealed nanoparticles are completely unlike those annealed to 400 and 550 °C which exhibit a crisp edge structure.

The shape of the tri-layered MoS_2 nanoparticles and their distinct metallic edge state are, for our 400 °C preparation, in agreement with previous studies [7,8,22]. Our samples annealed to 550 °C exhibit similar characteristics. The height of the annealed MoS_2 islands is measured in the range from 1 to 3 Å depending on bias, indicating single layer MoS_2 slabs as the expected thickness of a single, supported S–Mo–S slab is 3.17 Å [34]. At higher

coverages than those reported in this work (<0.2 ML), coalescence and second layer growth also starts to play a role. For the unannealed samples, the metallic edge state was never observed.

For each of the different preparation procedures, an analysis of the MoS_x nanoparticle size distribution was performed on several STM images. The distributions are all rather broad with mean island sizes of ~3 nm^2 (no post-deposition annealing), ~4 nm^2 (post-deposition annealing at 400 °C), and ~8 nm^2 (post-deposition annealing at 550 °C). Although average island size will generally depend on the coverage, this is not expected here as all samples were prepared at small coverages, below ~0.2 ML, with little interaction between particles. Thus the expected increase in the particle sizes of the annealed samples is clearly observed and is attributed to sintering. For the samples annealed at 550 °C, a few very large islands (up to 110 nm^2) were observed (not shown) which further confirms the presence of sintering at this temperature. The angle distributions shown in Fig. 4 will be discussed below.

3.4. Coverage assignment

Coverages are assigned based on the XPS peak intensities and simple models for the attenuation due to the overlayers. The coverage given in monolayer (ML) is defined as the fractional coverage of the Au(1 1 1) surface area.

The intensity ratio of the Mo $3d_{5/2}$ line to the Au $4f_{7/2}$ line is used to estimate the coverage of the MoS_2 islands. We include the damping of the Molybdenum signal by one overlayer of sulfur, and the damping of the gold signal by the tri-layered S–Mo–S structure. Using appropriate values for the sensitivity factors [29], the mean free paths, and a damping thickness of the MoS_2 tri-layer of 4.8 Å (estimated by multiplying the S–S distance in a MoS_2 slab of 3.17 Å [34] by 1.5 in order to include both sulfur layers) we get MoS_2 coverages of 0.09 ML (A), 0.04 ML (B, i), 0.11 ML (B, ii), and 0.16 ML (C) in Fig. 5. We estimate the uncertainty to ±0.02 ML on the coverage assignments, taking into account contributions related to the subtraction of the Mo 3*d* background signal.

For the Mo/Au(1 1 1) system, only attenuation by the Mo layer is included, yielding Mo coverages of 0.06 ML, 0.2 ML, and 3.1 ML for the XPS spectra I, II, and III presented in Fig. 3, respectively.

Analysis of the STM pictures in Fig. 4 indicates coverages of ~0.10 ML (Fig. 4A), ~0.05 ML (Fig. 4B), and ~0.14 ML (Fig. 4C). The coverages from Figs. 4A and B compare very favorably with the coverages determined by XPS at the same samples: 0.09 ML (Fig. 2A) and 0.04 ML (Fig. 2B(i))[4].

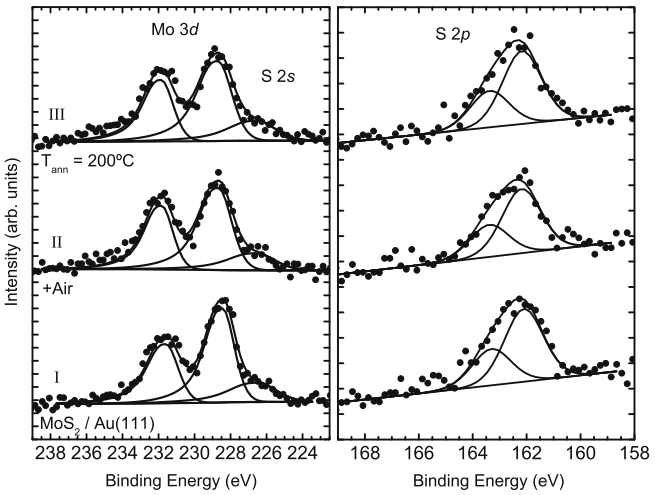

Fig. 5. XPS measurements of the Mo 3*d* and S 2*p* lines for the MoS_2 sample annealed at 550 °C (I, cf. Fig 2C), then exposed to air and reinserted into vacuum (II), and finally annealed to 200 °C in vacuum (III). The Mo and S are seen to be stable to the air exposure. The solid lines are fits to the data.

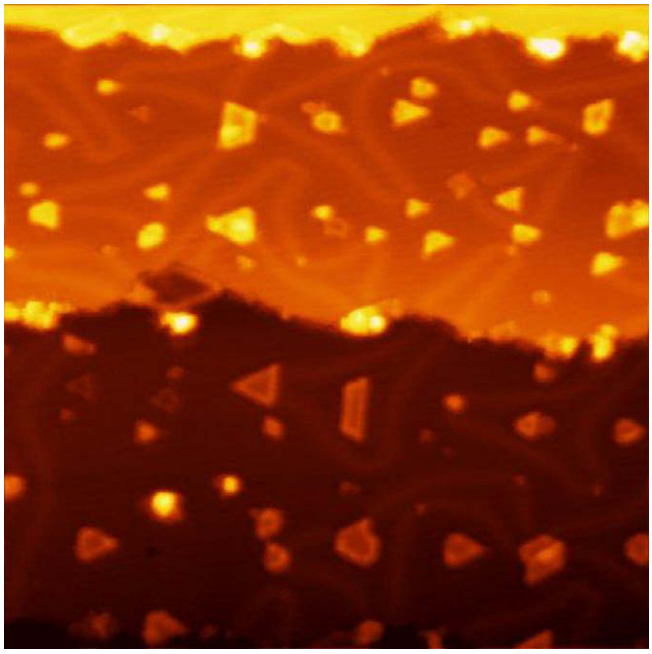

Fig. 6. STM of MoS_2 on Au(1 1 1) after exposure to air. The MoS_2 nanoparticles were synthesized similarly to those shown in Fig. 4B (post-deposition annealing at 400 °C) and subsequently exposed to air for several minutes. The STM-imaging was performed under UHV after reinserting the sample in vacuum and a short anneal at ~200 °C. The morphology is similar to that shown in Fig. 4B, and results of the image analysis (particle size and angle distributions) are also in agreement with the samples that had never been exposed to air. The STM image is 47 nm × 47 nm in size, and the scanning parameters are: V_t = 1.0 V, I_t = −1.0 nA.

3.5. Air exposure

All MoS_x samples that we examined for HER catalytic activity (see Ref. [18] for examples) were exposed to air during transfer to the electrochemical cell. To examine the effects of air exposure on the oxidation state of MoS_2, we measured XPS on the in situ synthesized MoS_2/Au(1 1 1) before and after the sample had been exposed to air, see Fig. 5. The spectrum measured immediately after synthesis, Fig. 5I, is reproduced from Fig. 2C. The sample is then exposed to air at room temperature for several minutes and then reinserted into UHV via the loadlock. XPS is performed after the pressure has reached an appropriate level, shown in Fig. 5II and again after a short annealing in vacuum to 200 °C to remove weakly bonded contaminants, Fig. 5III. Both the Mo $3d_{5/2}$ and the S 2*p* spectra are almost identical for the three experiments, with a negligible effect on the chemical state of molybdenum. Binding energies of the Mo $3d_{5/2}$ line found by fitting the spectrum using an asymmetry parameter of 0.33 are found to be 228.7 eV for both (II) and (III), extremely close to the value of 228.4 eV for (I). Had the molybdenum been oxidized during this procedure, presumably to MoO_3, we would have expected a significant shift of the Mo $3d_{5/2}$ line to higher binding energies around 232–233 eV [13,14,27].

STM was also employed to study the impact of air exposure on gold-supported MoS_2 nanoparticles. In Fig. 6, a STM image of a MoS_2 sample exposed to air is shown. The sample was prepared similarly to that in Fig. 4B, but then exposed to air for several minutes, reinserted into vacuum, and annealed shortly at ~200 °C be-

[4] The data in Figs. 4C and 2C cannot directly be compared since they were not measured on the exact same sample.

fore STM-imaging. As seen in the image, triangles, truncated triangles, and metallic edge states are still present after the air exposure. The particle size and angle distributions (see later) are similar to those measured on samples that had never been exposed to air, leading us to conclude that air has a negligible effect on the sulfide nanoparticles. This is in agreement with a study of graphite-supported MoS_2 which was exposed to air before TEM analysis, revealing primarily truncated triangles [4], however not with a recent TEM study of MoS_2 supported on alumina [35].

4. Discussion

4.1. Annealed samples

The nanoparticles imaged with STM in Fig. 4B and C are similar to the MoS_2-crystallites reported in Refs. [7,8]. By increasing the post-deposition annealing temperature from 400 to 550 °C, we have seen that the particles grow in size while maintaining a similar truncated triangular shape. We have also observed that the important edge state exists within nanoparticles annealed at either temperature. The ability to vary the ratio of the edge length to the area of the particle was exploited in our previous study to identify the edge as the active site for the HER [18]. It is well known that the atomic-scale morphology depends on the synthesis conditions, for example the presence of H_2. Lauritsen et al. found that the equilibrium shape of the MoS_2 is typically hexagonal with both Mo- and S-edges rather than triangular with only Mo-edges when hydrogen is present in partial pressures more than ten times the H_2S partial pressure [36]. This can be explained as an effect of the changed chemical potential of sulfur [36,37]. The chemical potential of sulfur depends both on temperature and gas composition, and an increase in temperature at our synthesis conditions, predicts a lower chemical potential at the higher temperature, making the S-edge slightly more favorable [37,11], which is in agreement with Fig. 4.

From sulfidation studies of Mo–O compounds, it is also known that temperatures above 200 °C are required to obtain the fully sulfided state [15,27]. The binding energies of Mo $3d_{5/2}$ measured by XPS for the annealed samples in Fig. 2B and C (228.4–228.7 eV) are in reasonable agreement with those reported in the literature for MoS_2, in the range from 228.8 to 230.1 eV [38]. In a study by Muijsers et al. of various Mo–sulfur compounds adsorbed on SiO_2, the Mo $3d_{5/2}$ line is observed at 229.0 eV for MoS_2 with Mo in the 4+ oxidation state [13]. Araki et al. report a value of 228.8 eV for the binding energy of Mo $3d_{5/2}$ for MoS_2 supported on TiO_2 [39]. Recently, Bonde et al. found a value of 229.0 eV for carbon supported MoS_2 [14], and for industrially-relevant HDS catalysts, such as MoS_2 on Al_2O_3, the Mo $3d_{5/2}$ line is found at 229.0 eV [15,16]. Our Mo 3*d* binding energy lies in the lower end or slightly below the Mo binding energies measured on more industrially-relevant supports. This could be due to a different influence of the Au substrate compared to an oxide surface or to the small size of the particles, e.g. because of the abundance of edge sites. Supporting the latter, Mattila et al. demonstrated negative binding energy shifts for defect sites with respect to the basal plane of MoS_2 [26]. More detailed discussion of the influence of the support on the binding energy shift is however beyond the scope of this paper.

The S $2p_{3/2}$ lines observed at 162.0–162.1 eV (Fig. 2B and C) are also in reasonable agreement with Muijsers et al. as well as Araki et al. who both report a S $2p_{3/2}$ binding energy around 161.8 eV for adsorbed MoS_2 [13,39]. This suggests that MoS_2 nanoparticles grown on Au(1 1 1) are chemically similar to those grown on more industrially-relevant support materials, in part validating the investigation of the Au(1 1 1) system as a relevant model of the industrial catalyst.

From our XPS data we estimate the S:Mo ratio using the appropriate sensitivity factors [29], and we find values of 2.1, 1.9 and 2.2 for Fig 2B(i), 2B(ii) and 2C. Despite the uncertainty introduced by the subtraction of the Mo signal from the sample plate and the rather small S signals, these values are in excellent agreement with the expected number for MoS_2. Based on our STM and XPS measurements, we conclude that after post-deposition annealing at either 400 or 550 °C in H_2S, we have produced a crystalline MoS_2 particle on the surface with an XPS fingerprint consistent with that of MoS_2 catalysts prepared in a more industrially-relevant fashion.

The metallic edge state was clearly observed by STM, but only on the annealed samples (to either 400 or 550 °C). One question to ask is whether or not the photoelectrons from the Mo or S atoms along the conducting edge state can be distinguished with XPS. With a conducting metallic state, one might expect a different potential around the core electrons as well as better screening of the core hole remaining upon photoelectron emission, resulting in a negative binding energy shift (towards metallic Mo) with respect to typical semiconducting MoS_2. This effect would presumably be most pronounced for the smallest particles as most of their Mo atoms lie along the conducting edge, whereas for larger islands, most Mo atoms reside in the interior of the semiconductor. Our results, however, do not resolve such site-specific lines. Higher intensities and better detector energy resolution appear to be necessary.

In terms of particle size distributions, we have addressed the influence of synthesis conditions on nanoparticle growth on the basis of STM-imaging in Fig. 4. Another important aspect to address is the particle shape, which we quantify in the following by analyzing the distribution of angles measured at corners (e.g. 60° for each vertex of an ideal triangle and 120° for each vertex of a hexagon). To the right of each STM image in Fig. 4 are the results of this analysis performed on a large number (100–400) of particles, corresponding to several images for each sample preparation. All particles counted are from images of identical size (47 nm × 47 nm) and resolution (512 pixels), corresponding to a pixel resolution of ~1 Å/pixel, and only particles from samples with coverages less than ~0.2 ML are included in order to avoid coalescence and second layer growth. The angle distribution of the post-deposition annealed samples (400 and 550 °C) are clearly bimodal, with peaks around 60° and 120° corresponding to triangular and truncated triangular nanoparticles, clearly reflecting what is seen in the adjacent STM images. The fact that all post-deposition annealed nanoparticles (400 or 550 °C) exhibit angle distributions centered around 60° and 120°, shows that the two materials are equally crystalline with only a vanishing number of amorphous particles observed.

Closer examination of the angle distributions for each temperature reveals a slight difference between the two post-annealed samples; the angle distribution for 400 °C annealed nanoparticles reveals slightly more 60° angles than 120° (with a ratio of approximately 60:40), while the inverse is true for the angle distribution for nanoparticles annealed to 550 °C (with a ratio of approximately 40:60). Particles smaller than 1 nm^2 corresponding to approximately 10 pixels along the edges are omitted from this analysis since the pixel resolution does not allow for unambiguous distinction between 60° and 120° angles. These omitted particles correspond to less than 1% of the total particle coverage. For particles slightly larger than this ~1 to 2 nm^2 – the shape appears to be triangular and they are analyzed as such. Short truncations of the particle vertices, however, might be present in these particles but not visible in the STM due to the pixel resolution. The amount of these apparently triangular particles is estimated to be 1–2% of the coverages shown. The potential overpopulation of the 60° angle is therefore not expected to significantly change the overall distribution.

The measured angle distribution of the MoS_2 particles does not uniquely determine particle shape and edge terminations, however it does provide a basis for discussion. The statistics reveal that more truncated triangles appear in the samples which have experienced a higher annealing temperature. One possible interpretation of this result is that the ratio of S-terminated edges to the Mo-terminated edges increases in samples with have been exposed to higher temperatures, which would be consistent with results reported in Ref. [22]. But as other effects such as annealing time and MoS_2 coverage may also influence the particle morphology, a dedicated study based on direct edge type identification and quantification is required in order to draw strict conclusions on this matter.

4.2. Non-annealed samples

The MoS_x particles that have not been annealed after deposition in H_2S have a slightly lower Mo $3d_{5/2}$ binding energy (228.2 eV) than the annealed ones (228.5–228.7 eV). This indicates that Mo could be at a lower valence than 4+, reflecting an incomplete sulfidation of the Mo. This is supported by our finding of a S:Mo ratio of 1.6 for the unannealed sample.

The particle shape angle measurement on the same sample (Fig. 4A) exhibits a broad, continuous distribution, ranging from 30° to 160°. Local maxima around 60° and 120° could indicate that there is some tendency towards triangles and truncated triangles, respectively, but only a small portion of the particles can be characterized as one or the other. Instead, most are amorphous aggregates whose edges form angles of all kinds, with few features that correspond to any defined shape.

The formation of fully sulfided MoS_2 from Mo–O compounds has previously been found to be an activated process, requiring temperatures above 200 °C in the presence of H_2S [15,27]. This is in good agreement with our results where we see that deposition at ~147 °C in H_2S is not sufficient to form crystalline MoS_2 structures without annealing to higher temperatures.

We further studied these unannealed MoS_x nanoparticles as catalysts by measuring electrochemical activity for the HER, following the exact same procedure as in Ref. [18]. It was found that they exhibited a much lower activity than their annealed counterparts. In fact, the activity is comparable to that of the reference activity of the background sulfided Au(1 1 1). This data is consistent with the previous identification of the edge of crystalline MoS_2 islands being the active site for the HER. The STM studies in this work have shown that without the post-deposition annealing step this active site is not present, and the MoS_x sample is thus not active for hydrogen evolution.

4.3. Stability upon air exposure

The direct comparison of our UHV and electrochemical measurements depends on the sample stability against exposure to ambient air. Considering Fig. 5, the similarity of the Mo 3*d* and the S 2*p* spectra before and after air exposure supports the notion that the MoS_2 nanoparticle structure remains intact after exposure to air and even after subsequent annealing to 200 °C in vacuum. No significant features appeared in the Mo $3d_{5/2}$ spectra in the high binding energy region characteristic of oxidized Mo (5+ or 6+), demonstrating that all Mo remains in the 4+ oxidation state. This is supported by STM in which the same characteristic features as before the air exposure is seen, see Fig. 6. Some ill-defined features are also observed on this surface. These are believed to be carbon contamination caused by the air exposure. A blind experiment on a sulfided Au(1 1 1) also exposed to air shows that these air-induced contaminations are not electrochemically active. We therefore conclude that the electrochemical measurements were indeed conducted on the same MoS_2 nanostructures as those imaged by STM [18].

5. Conclusions

Heterogeneous catalysis is highly sensitive to the geometric arrangement and electronic structure of surface sites. STM and XPS are powerful methods to characterize these properties, and combining these two methods in the same study ultimately allows one to establish the correlation between the geometric and electronic factors that govern catalysis. In this work, we have examined supported MoS_2 nanoparticles on Au(1 1 1), correlating structural and chemical information for these important model catalysts under various synthesis conditions. We conclude that:

- Without post-deposition annealing the MoS_2 nanoparticles appear as amorphous aggregates without a metallic edge state. Post-deposition annealing to 400 °C and 550 °C in H_2S induces crystallinity and the existence of the metallic edge state. The higher annealing temperature (550 °C) results in a larger average particle size.
- The Mo 3*d* line positions for the post-deposition annealed MoS_2 nanoparticles are very similar to those reported in the literature for supported MoS_2 nanoparticles in industrially-relevant catalysts, indicating that the MoS_2 particles grown on Au(1 1 1) constitute a realistic model system upon which fundamental studies may be pursued under well-defined conditions.
- When exposed to ambient air and subsequently heating under UHV to 200 °C, the MoS_2 nanoparticles do not alter their chemical state nor composition, as measured by XPS. STM images agree, and furthermore show that their size distribution also remains the same. This legitimizes conclusions previously drawn regarding the relationship between structure and catalytic activity, as the detailed structural and chemical information obtained in UHV is also pertinent under ambient conditions.

Having shown that the model MoS_2 catalysts are structurally and chemically similar to industrially-relevant MoS_2 catalysts, and that the model catalysts change negligibly upon exposure to air, one may find it fruitful to pursue direct studies of this model catalyst for numerous hydrotreating reactions.

Acknowledgements

S.H. and Y.T. acknowledge support from the Danish Research Agency (grant 26-04-0047), J.B. acknowledges the support of the Danish Strategic Research Council and T.F.J acknowledges an H. C. Ørsted postdoctoral Fellowship from the Technical University of Denmark. CINF is supported by the Danish National Research Foundation, and CAMD is supported by the Lundbeck Foundation.

References

[1] H. Topsøe, B.S. Clausen, F.E. Massoth, in: J.R. Anderson, M. Boudart (Eds.), Hydrotreating Catalysis, Science and Technology, vol. 11, Springer, Berlin, 1996.
[2] B.S. Clausen, H. Topsøe, R. Candia, J. Villadsen, B. Lengeler, J. Als-Nielsen, F. Christensen, J. Phys. Chem. 85 (1981) 3868.
[3] S.M.A.M. Bouwens, R. Prins, V.H.J. de Beer, D.C. Koningsberger, J. Phys. Chem. 94 (1990) 3711.
[4] M. Brorson, A. Carlsson, H. Topsøe, Catal. Today 123 (2007) 31.
[5] B. Hinnemann, P.G. Moses, J. Bonde, K.P. Jørgensen, J.H. Nielsen, S. Horch, I. Chorkendorff, J.K. Nørskov, J. Am. Chem. Soc. 127 (2005) 5308.
[6] J. Kibsgaard, J.V. Lauritsen, E. Lægsgaard, B.S. Clausen, H. Topsøe, F. Besenbacher, J. Am. Chem. Soc. 128 (2006) 13950.
[7] S. Helveg, J.V. Lauritsen, E. Lægsgaard, I. Stensgaard, J.K. Nørskov, B.S. Clausen, H. Topsøe, F. Besenbacher, Phys. Rev. Lett. 84 (2000) 951.
[8] M.V. Bollinger, J.V. Lauritsen, K.W. Jacobsen, J.K. Nørskov, S. Helveg, F. Besenbacher, Phys. Rev. Lett. 87 (2001) 196803.

[9] J.V. Lauritsen, J. Kibsgaard, S. Helveg, H. Topsøe, B.S. Clausen, E. Lægsgaard, F. Besenbacher, Nature Nanotech. 2 (2007) 53.
[10] J.A. Rodriguez, J. Dvorak, T. Jirsak, J. Hrbek, Surf. Sci. 490 (2001) 315.
[11] M.V. Bollinger, K.W. Jacobsen, J.K. Nørskov, Phys. Rev. B 67 (2003) 085410.
[12] W. Jaegermann, D. Schmeisser, Surf. Sci. 165 (1986) 143.
[13] J.C. Muijsers, Th. Weber, R.M. van Hardevel, H.W. Zandbergen, J.W. Niemantsverdriet, J. Catal. 157 (1995) 698.
[14] J. Bonde, P.G. Moses, T.F. Jaramillo, J.K. Nørskov, I. Chorkendorff, Faraday Discuss. 140 (2008) 219.
[15] L.P. Nielsen, M. Schønning, S.V. Christensen, S.V. Hoffmann, Z. Li, P. Hofmann, F. Besenbacher, B.S. Clausen, Cat. Lett. 73 (2001) 85.
[16] P. Beccat, P. Da Silva, Y. Huiban, S. Kasztelan, Oil Gas Sci. Technol. – Rev. IFP 54 (1999) 487.
[17] N. Frizi, P. Blanchard, E. Payen, P. Baranek, C. Lancelot, M. Rebeilleau, C. Dupuy, J.P. Dath, Catal. Today 130 (2008) 32.
[18] T.F. Jaramillo, K.P. Jørgensen, J. Bonde, J.H. Nielsen, S. Horch, I. Chorkendorff, Science 317 (2007) 100.
[19] J.V. Lauritsen, M. Nyberg, R.T. Vang, M.V. Bollinger, B.S. Clausen, H. Topsøe, K.W. Jacobsen, E. Lægsgaard, J.K. Nørskov, F. Besenbacher, Nanotechnology 14 (2003) 385.
[20] F. Besenbacher, E. Lægsgaard, K. Mortensen, U. Nielsen, I. Steensgaard, Rev. Sci. Instrum. 59 (1988) 1035.
[21] Ch. Wöll, S. Chiang, R.J. Wilson, P.H. Lippel, Phys. Rev. B 39 (1989) 7988.
[22] Stig Helveg, PhD thesis 2000; J.V. Lauritsen, PhD thesis 2002, Århus University.
[23] SPIP software, Image metrology A/S, Denmark.
[24] S. Doniach, M. Šunjić, J. Phys. C: Solid State Phys. 3 (1970) 285.
[25] S. Hüfner, G.K. Wertheim, J.H. Wernick, Solid State Commun. 17 (1975) 417.
[26] S. Mattila, J.A. Leiro, M. Heinonen, T. Laiho, Surf. Sci. 600 (2006) 5168.
[27] Th. Weber, J.C. Muijsers, J.H.M.C. van Wolput, C.P.J. Verhagen, J.W. Niemantsverdriet, J. Phys. Chem. 100 (1996) 14144.
[28] W. Grünert, A. Yu Stakheev, R. Feldhaus, K. Anders, E.S. Shpiro, Kh.M. Minachev, J. Phys. Chem. 95 (1991) 1323.
[29] C.D. Wagner, L.E. Davis, M.V. Zeller, J.A. Taylor, R.M. Raymond, L.H. Gale, Surf. Interface Anal. 3 (1981) 211.
[30] M.M. Biener, J. Biener, R. Schalak, C.M. Friend, Surf. Sci. 594 (2005) 221.
[31] C.D. Wagner, W.M. Riggs, L.E. Davis, J.F. Moulder, G.E. Muilenberg, Handbook of X-ray Photoelectron Spectroscopy, Perkin–Elmer Corporation Physical Electronics Division, 1979.
[32] XPS binding energy database. <www.lasurface.com>.
[33] N.V. Alov, Nucl. Instrum. Methods Phys. Res. B 256 (2007) 337.
[34] Th. Böker, R. Severin, A. Müller, C. Janowitz, R. Amnzke, D. Voss, P. Krüger, A. Mazur, J. Pollmann, Phys. Rev. B 64 (2001) 235305.
[35] P.J. Kooyman, J.A. Rob van Veen, Catal. Today 130 (2008) 135.
[36] J.V. Lauritsen, M.V. Bollinger, E. Lægsgaard, K.W. Jacobsen, J.K. Nørskov, B.S. Clausen, H. Topsøe, F. Besenbacher, J. Catal. 221 (2004) 510.
[37] H. Schweiger, P. Raybaud, G. Kresse, H. Toulhoat, J. Catal. 207 (2002) 76.
[38] NIST Standard Reference Database 20, Version 3.5. <http://srdata.nist.gov/xps/>.
[39] Y. Araki, K. Hinna, H. Shimada, J. Catal. 207 (2002) 361.